Neutrino Radiation Transport
And Other Topics in High Energy Density Astrophysics

Thesis by

Sherwood Richers

In Partial Fulfillment of the Requirements for the
degree of
Doctor of Philosophy

CALIFORNIA INSTITUTE OF TECHNOLOGY
Pasadena, California

2018
Defended June 29 2017

Sherwood Richers
ORCID: orcid.org/0000-0001-5031-6829

ACKNOWLEDGEMENTS

I would like to thank my advisor Christian Ott for his scientific guidance and for his tireless attention to detail. I would also like to thank Daniel Kasen and Josh Dolence for hosting me in their labs for several months and exposing me to new directions of research. This work would not be possible without them.

I am also extremely grateful for the opportunities afforded by the Department of Energy Computational Science Graduate Fellowship and the Blue Waters Graduate Fellowship. They sparked collaborations that shaped my scientific interests.

Most importantly, I would like to thank Krister Lagergren for his never-ending support.

ABSTRACT

Neutron star mergers and the collapse of massive stars result in some of the universe's most violet explosions. However, the detailed mechanisms behind all of these astrophysical explosions remain elusive. Their strongly nonlinear and complicated nature makes them difficult and expensive to simulate, and the properties of matter in these extreme conditions are poorly constrained. I use a variety of computational tools to understand the detailed mechanisms behind both types of events.

I describe my relativistic time-independent multidimensional Monte Carlo neutrino radiation transport code Sedonu that provides an accurate account of the neutrino radiation fields and the interaction with neutrinos and background fluid. Though Sedonu calculations are time-independent, I demonstrate their utility in dynamical general relativistic variable Eddington tensor radiation hydrodynamics simulations.

I apply Sedonu to simulations of accretion disks following neutron star mergers to demonstrate that more realistic disk cooling and neutrino-driven mass ejection rates are larger than is predicted using approximate transport methods. I also reinforce that neutrino pair annihilation from these disk configurations is unlikely to be able to energize a gamma-ray burst jet.

I subject Sedonu to the first thorough comparison of Boltzmann neutrino radiation transport methods in multiple spatial dimensions in the context of core-collapse supernovae. The comparisons with the other highly accurate discrete ordinates-based transport scheme show remarkably similar results, verifying the accuracy of both methods and underscoring the importance of numerical fidelity.

I perform the first broad parameter study on how different descriptions of dense nuclear matter and star rotation rates influence the dynamics of, and hence gravitational waves from, the bounce and early post-bounce phase of rapidly rotating core collapse supernovae. Using the results of 1824 two-dimensional general relativistic core-collapse simulations, I demonstrate that the equation of state is unlikely to be constrained by LIGO observations. I show that the effect of the equation of state on the gravitational wave frequency can be described by a single universal relation.

Finally, I use results of three-dimensional general relativistic magnetohydrodynamics simulations of rapidly rotating core collapse to demonstrate that the polar magnetic structures that form are destroyed by a magnetohydrodynamic kink instability.

PUBLISHED CONTENT AND CONTRIBUTIONS

Philipp Mösta, Sherwood Richers, Christian D. Ott, Roland Haas, Anthony Piro, Kristen Boydstun, Ernazar Abdikamalov, Christian Reisswig and Erik Schnetter (2014). "Magnetorotational Core Collapse Supernovae in Three Dimensions". ***The Astrophysical Journal Letters*** **785, 2. DOI:10.1088/2041-8205/785/2/L29**

I heavily contributed to data analysis and interpretation of simulations performed by Philipp Mösta and performed much of the visualization. I demonstrated that the magnetic outflows are crippled by $m = 1$ (kink) instabilities that are well-known in the fusion reactor and AGN jet literature.

Sherwood Richers, Daniel Kasen, Evan O'Connor, Rodrigo Fernández, and Christian D. Ott (2015). "Monte Carlo Neutrino Transport through Remnant Disks from Neutron Star Mergers". ***The Astrophysical Journal*** **813,1. DOI:10.1088/0004-637X/813/1/38**

I revamped a stripped version of the Sedona Monte Carlo photon transport code from Daniel Kasen and coupled it to the NuLib neutrino reaction rate library from Evan O'Connor to make the specialized neutrino transport code Sedonu. I verified the code performance against several tests, imported simulation data from Rodrigo Fernandez, ran the time-independent MC transport calculations, reduced the data, and wrote the text.

Sherwood Richers, Christian D. Ott, Ernazar Abdikamalov, Evan O'Connor, and Chris Sullivan (2017). "Equation of State Effects on Gravitational Waves from Rotating Core Collapse". *Physical Review D* 95, 063019. DOI:10.1103/PhysRevD.95.063019

I ran the simulations using a version of the CoCoNuT code from Nazarbayev University Professor Ernazar Abdikamalov, the GR1D code from North Carolina State University postdoc Evan O'Connor, and detailed electron capture rates from Michigan State University graduate student Chris Sullivan. I performed the data analysis and wrote the text.

Sherwood Richers, Hiroki Nagakura, Christian D. Ott, Joshua Dolence, Kohsuke Sumiyoshi, and Shoichi Yamada (2017). "A Detailed Comparison of Multi-Dimensional Boltzmann Neutrino Transport Methods in Core-Collapse Supernovae". Submitted to *The Astrophysical Journal Supplement Series*.

I designed and implemented a special relativistic, time-independent version of the Monte Carlo random walk approximation in Sedonu, restructured Sedonu for modularity and speed, ran the Monte Carlo calculations, and wrote most of the text. This was in close collaboration with Hiroki Nagakura, who contributed results, data analysis, and text related to his discrete ordinates code.

TABLE OF CONTENTS

LIST OF ILLUSTRATIONS

LIST OF TABLES

Chapter 1

INTRODUCTION

1.1 Overview

Core-collapse supernovae (CCSNe) and gamma-ray bursts (GRBs) are among the most brilliant explosions in the universe, and the mechanisms driving both are deeply interrelated. As the name suggests, CCSNe result from the collapse of massive stars. The explosion expels matter that forms the vast majority of elements heavier than helium but lighter than iron and leaves behind an incredibly dense neutron star. Though supernovae have been seen throughout history and the modern theory of CCSNe began in the 1960s, simulations show that our understanding is still incomplete. Since we cannot see into the depths of exploding stars (except for exceedingly rare galactic events, where we would observe a neutrino and potentially a gravitational wave signal), we rely on simulations to understand what can and what can not cause a star to explode. But these simulations, too, suffer from an incomplete understanding of the properties of matter at high densities and the highly nonlinear processes and instabilities in neutrino radiation magentohydrodynamics. Explanations of exotic, extremely energetic supernovae ("hypernovae") and their long-duration GRB counterparts are particularly elusive, as they also launch a hyper-relativistic and tightly collimated jet. In parts of this thesis, I use simulations of CCSNe to further our theoretical understanding of how each of these elements contributes to CCSNe and to predict what we might observe from future nearby CCSNe.

Short-duration GRBs, on the other hand, are thought to be the result of a neutron star merging with another neutron star or a black hole. This has not yet been confirmed, as we will need corroborating evidence, such as a kilonova afterglow or a gravitational wave signal, before knowing with certainty. Interestingly, this model may explain not only the origin of short-duration GRBs, but also of most of the elements heavier than iron (though AGB stars play a role, too). The same issues exist with the theory of neutron star mergers (NSMs) as with CCSNe, which makes sense given that the neutron stars and stellar-mass black holes are themselves the result of CCSNe. This system also requires an as of yet incomplete understanding of matter at extreme densities and of strongly nonlinear dynamics. In the remaining

parts of this thesis, I use simulations of neutrino radiation transport to work towards a more robust understanding of how neutrinos influence the dynamics and ejecta composition in NSMs.

Neutrinos are at first glance extremely weakly interacting particles that have no relevance to every day life. After all, there are hundreds of billions from the sun passing through each person each second, day and night, and we never take notice. However, with the extremely dense matter in CCSNe and NSMs, the neutrinos interact strongly and even get trapped within the newly-formed neutron star or hypermassive neutron star. Neutrinos are thought to be the primary driving force behind CCSNe, they drive outflows from NSMs, and how matter interacts with neutrinos determines which elements eventually form from ejected matter. Clearly, including an accurate account of neutrino effects in models of CCSNe and NSMs is an important component of understanding the real thing. Classical radiation transport is a seven-dimensional (3 for space, 3 for momentum, one for time) sometimes very stiff integro-differential problem and is an area of active research in many fields of physics. A central focus of this thesis is developing methods to accurately simulate neutrino transport, and using these methods to improve models and understand what they tell us about the nature of these explosions.

In the remainder of this chapter, I provide the astrophysical background for CCSNe and NSMs to set the stage for the remainder of the thesis. In Chapter 2, I provide an outline of the detailed concepts and computational components that go into modeling these systems. Since much of this thesis is based on results from my Monte Carlo neutrino transport code Sedonu, I describe the method and the code in more detail in Chapter 3. I also show some code tests that demonstrate the code's self consistency in time-independent calculations, and provide some new proof of concept tests of a time-dependent Monte Carlo variable Eddington tensor method. Then following four chapters (Chapters 4-7) are very closely tied to previously published papers, though information has been rearranged to make the thesis more cohesive. Each of these chapters has a complete introduction to set the stage for that particular project. In Chapters 4 and 5, I use Sedonu in the context of NSMs and CCSNe, respectively, to better understand how far reality lies from simulation results. In the next two chapters, I study rapidly rotating CCSNe from two vantage points. In Chapter 6, I explain why strongly magnetized rotating core collapse is unable to produce coherent polar magnetic structures once thought to form based on axisymmetric simulations. In Chapter 7, I perform a broad parameter study over descriptions of nuclear matter

and the rotation rates of collapsing stars to understand how the nuclear matter properties might imprint themselves on the gravitational wave signals. Finally, I summarize my conclusions and provide some outlook in Chapter 8.

1.2 Core-Collapse Supernovae

Observational Signature

Long before it was known that supernovae are distant stellar explosions, the first supernovae were observed as bright celestial objects easily visible to the naked eye for several months. In recorded history, only six such explosions have been sufficiently nearby (in the Milky Way galaxy or in the Large Magellanic Cloud) to be so obviously visible and to have been recorded (Bethe, 1990; Burrows, 2000). The most recent such SN occurred in 1987. Many more nearby explosions are likely to have occurred, but were hidden by dust in the galaxy. On average, it is estimated that there are 1-2 SNe in our galaxy per century (van den Bergh and Tammann, 1991; Tammann, Loeffler, and Schroeder, 1994; Cappellaro, R. Evans, and Turatto, 1999; Ando, Beacom, and Yüksel, 2005). Fortunately, modern telescopes (SDSS, PTF, Gaia, and CSS, to name a few) make it possible to observe hundreds of extragalactic SNe per year.

SNe are most commonly classified according to their spectral properties, and further classified according to their light curves. These classifications have only a loose connection to what causes the explosion, but the terminology is ubiquitous. Type II SNe contain hydrogen lines, while type I do not. Type Ia contain silicon lines and are the result of a thermonuclear detonation of a white dwarf. Type Ia SNe Type Ia SN are tremendously important for our understanding of the universe, but I limit the scope of this thesis to only core-collapse supernovae (CCSNe). All types of SNe other than Ia are the result of an implosion of massive stellar core. Type II SNe are generally the result of the explosion of intact stars including the hydrogen and helium envelopes. Type Ib contain helium lines and no silicon lines, and result from the collapse of a star that has lost its outer hydrogen envelope by stellar winds or binary interactions. Type Ic contain no helium or silicon lines, indicating that the progenitor star lost both they hydrogen and helium layers before explosion. All of the light observed from SNe is emitted either by recombination of ejected matter or interaction of the ejecta with its surroundings. Though electromagnetic supernova observations shed light onto the stellar evolution processes leading up to the explosion and the environment around the explosion, they do not say much about the internals launching the explosion. However, neutrinos and gravitational

waves can offer a window right down to the engines themselves.

SN 1987a was the first and only SN to occur after the invention of neutrino detectors that was nearby enough to provide a detectable flux of neutrinos. Between observations using the Kamiokande II detector in Japan (Hirata et al., 1987) and the IMB in Ohio (Bionta et al., 1987), 20 neutrinos were detected, though modern detectors would observe tens of thousands from a similar event (e.g., Abbasi et al. [IceCube Collaboration] 2011). Since neutrinos interact with matter much more weakly than photons, the neutrinos come from deep within the core, offering a much more direct view of the thermodynamic conditions of the interiors. This observation was fundamentally important to confirming that (non-Ia) supernovae are indeed caused by stellar core collapse (e.g., Bethe 1990).

The recent discovery of gravitational waves from a binary black hole merger (Abbott, 2016b) is encouraging for the exciting prospect of detecting gravitational waves from CCSNe. Various instabilities in CCSNe are expected to emit potentially observable gravitational waves. This would provide a second direct line to the CCSN internals, but for the most probable gravitational wave emission mechanisms, the supernova must be within the Milky Way or Large Magellanic Cloud for current detectors (e.g., Ott 2009; S. E. Gossan et al. 2016; Abbott 2016a).

Canonical Explosion Mechanism

The modern theory of CCSNe extends back to 1934, when Baade and Zwicky supposed that supernovae represent the transition of a star to a neutron star (Baade and Zwicky, 1934b; Baade and Zwicky, 1934a). Since then, the mechanisms by which stars can explode have been fleshed out in much more detail, but simulations show that our understanding still remains incomplete (see, e.g., Bethe 1990; Kotake, Sato, and Takahashi 2006; H.-T. Janka, Langanke, et al. 2007; Ott 2009; H.-T. Janka 2012; Kotake, Sumiyoshi, et al. 2012; Foglizzo et al. 2015 for reviews).

Stars are energized by the fusion of hydrogen into heavier elements that require higher and higher pressures and temperatures to fuse. Only stars with initial masses of $M \gtrsim 10\,M_\odot$ are heavy enough to drive the central pressure and temperature sufficiently high to eventually form significant amounts of iron. After $\sim 10^7$ years of evolution, such a star ends up with an iron core of $\sim 1.4\,M_\odot$ that is surrounded by shells of silicon, oxygen, carbon, helium, and hydrogen. Once the iron core reaches a critical mass, photodissociation of nuclei and electron capture onto nuclei soften the equation of state just enough that pressure can no longer support the star and the

core begins to collapse under its own gravity.

Within a few tenths of a second, the core's density exceeds nuclear densities ($\sim 10^{14}\,\mathrm{g\,cm^{-3}}$), at which point nuclear forces prevent further collapse. The subsonically-infalling *inner core* rebounds into the now supersonically infalling *outer core*, launching a shock wave outward through the core. The shock stalls after a few tens of milliseconds at a radius of $\sim 100\,\mathrm{km}$, as it cannot move through the stellar matter as quickly as the matter is falling.

Understanding the mechanism that causes this shock to blow through the rest of the star has been the primary goal of CCSN theory for half of a century. The *neutrino mechanism* (Colgate and Johnson, 1960) is the strongly favored candidate for ordinary CCSNe. Theoretical estimates confirmed by the SN 1987a neutrino detection confirmed that $\sim 10^{53}\,\mathrm{erg}$ of energy is emitted in neutrinos during the CCSN, which matches the gravitational energy difference between an extended iron core and a compact neutron star. This is much more energy than the $\sim 10^{51}\,\mathrm{erg}$ of kinetic energy observed in the explosion. If even a small amount of the neutrino energy is deposited in the stellar matter, this could drive an explosion. Simulations have shown that the explosion is not a spherical process, and that complex multi-dimensional dynamics like turbulence (e.g., Burrows and van Riper 1995; Murphy, Dolence, and Burrows 2013; Couch and Ott 2015; Radice, Couch, and Ott 2015) and the standing accretion shock instability (Blondin, Mezzacappa, and DeMarino, 2003) are important parts of the process. Precisely how the neutrino radiation, gravity, hydrodynamics, and nuclear forces conspire to explode the star is still uncertain, given that theoretical models from first principles do not yet consistently exhibit realistic explosions and there is little data from direct observations of the engines.

Exotic CCSNe

Of course, nature is far more rich than this single theory, and many CCSNe do not fit into the canonical mold. The lowest-mass CCSN progenitor stars are sufficiently supported by electron degeneracy that pressures and temperatures are not high enough to fuse elements beyond oxygen, neon, and magnesium. Electron captures on magnesium reduce the pressure support and collapse to a neutron star ensues (Nomoto, 1984; Nomoto, 1987). In a similar situation, an oxygen-neon-magnesium white dwarf accreting matter from a binary companion star could undergo the same process, but whether the white dwarf collapses into a neutron star or explodes as a

type Ia supernova depends on a sensitive competition between the electron capture process and energy generation by oxygen deflagration (Nomoto and Kondo, 1991). The steep density gradient at the edge of the core does allow for spherical explosions without multi-dimensional dynamics, but this produces an explosion an order of magnitude weaker than a canonical CCSN. These weak explosions are consistent with some observed CCSNe (e.g., Nomoto, Sugimoto, et al. 1982; Hillebrandt 1982; Wanajo, Tamamura, et al. 2003, though see Kitaura, H.-T. Janka, and Hillebrandt 2006; Dessart, Burrows, Ott, et al. 2006).

In very low-metallicity environments, stars with initial masses of greater than 100 $M_\odot$ can form (e.g., Heger, C. L. Fryer, et al. 2003). The temperatures in the core as it contracts after burning carbon is high enough to form electron-positron pairs, effectively removing thermal pressure support by turning the energy into mass. Stars with initial masses in the range of $140\ M_\odot \lesssim M \lesssim 260\ M_\odot$ may have enough nuclear fuel and little enough mass that when the fuel ignites during collapse it completely unbinds the star and releases $\sim 10^{53}$ erg of kinetic energy (e.g., Woosley, Heger, and Weaver 2002; Heger, C. L. Fryer, et al. 2003; C. L. Fryer and Kalogera 2001). This mechanism has been suggested for several candidate explosions, but interactions with the surrounding circumstellar material could have produced the same signal (e.g., Smith, W. Li, Foley, et al. 2007; Gal-Yam et al. 2009).

Hypernovae are a rare ($\sim 1\%$) kind of supernova with kinetic energies of up to around an order of magnitude higher than typical supernovae (e.g., Soderberg et al. 2006; Drout et al. 2011). They are also associated with long-duration ($\gtrsim 2$ s) gamma-ray bursts from hyper-relativistic jets (see Section 1.3, and Woosley and Bloom 2006 and Hjorth and Bloom 2012 for reviews). The spectral properties are classified as type Ic-bl (broad-line), indicating a stripped-envelope progenitor star and spectral lines Doppler-broadened by high ejecta velocities (Iwamoto et al., 1998). The neutrino mechanism lacks the efficiency to create such high explosion energies, so the extra energy is usually ascribed to rotational kinetic energy. A protoneutron star rotating at a near-Keplerian rate could wind up magnetic fields that tie the protoneutron star to the surrounding matter during the supernova, transferring enough energy to drive the explosion (e.g., LeBlanc and Wilson 1970; Meier et al. 1976; J. C. Wheeler, Meier, and Wilson 2002; Burrows, Dessart, et al. 2007). I investigate this possibility in Chapter 6. Alternatively, the protoneutron star could eventually collapse to a black hole, which subsequently launches a jet through the star (e.g., Woosley 1993; MacFadyen and Woosley 1999).

1.3 Neutron Star Mergers

Observational Motivation

Gamma-ray bursts (GRBs) are short flashes of gamma rays lasting from under a second to thousands of seconds (see Piran, 2004; Mészáros, 2006 for older, but rather comprehensive reviews). These flashes are known to come from cosmological distances (e.g., Fong and Berger 2013). The distribution of durations is bimodal, with a division between short and long bursts at $\sim 2\,\mathrm{s}$ (Kouveliotou et al., 1993). GRBs are strongly beamed in one direction. A combination of the jet energy and the time of the *jet break*, when the jet luminosity begins fading more rapidly, shows that the opening angles are $\theta \sim 10^\circ$ (Rhoads, 1999; Sari, Piran, and Halpern, 1999; Berger, 2014). Accounting for this opening angle, typical jet energies are on the order of $\sim 10^{51}$ erg, though much more energy may be emitted in neutrinos and gravitational waves (Frail et al., 2001; Panaitescu and Kumar, 2001).

The spectra are non-thermal and have tails that can extend up to GeV energies. The fact that such high-energy photons escape implies that their energy in the comoving frame of the jet must be small enough that they do not form electron-positron pairs. Photon energies high enough to create pairs do so, and hence do not escape the jet. This puts a lower limit on individual GRB jet Lorentz factors, which are on the order of $\Gamma \gtrsim 100$ (Lithwick and Sari, 2001). GRBs are also often accompanied by an x-ray, optical, and/or radio afterglow following interaction between the jet and the circumstellar medium and lasting on the timescale of weeks to months (e.g., Nousek et al. 2006; B. Zhang et al. 2006).

Long-duration GRBs are convincingly linked to the hypernovae discussed in Section 1.2 (see Woosley and Bloom 2006; Hjorth and Bloom 2012 for reviews). Long GRBs are found in galaxies where young massive stars are being formed, which is also true for CCSNe (e.g., Paczyński 1998; Fruchter et al. 2006; Savaglio, Glazebrook, and Le Borgne 2009). Even more importantly, there are several GRBs that have been observed coincidentally with type Ic-bl supernovae, and several other GRBs in which evidence of a supernova appeared in the afterglow light curve. Eight of these are "ironclad" GRB-SN associations with trong spectroscopic and photometric evidence (see, e.g., Hjorth and Bloom 2012; Cano et al. 2017 for more details).

Short-duration GRBs have no such connection to CCSNe. The differences in the populations of GRBs and in the properties of the emission indicate that they form in very different environments (see Berger 2014 and D'Avanzo 2015 for recent

reviews). Short GRBs occur in both young and old stellar populations (e.g., Bloom et al. 2006). A few data points indicate the possibility of an optical or infrared afterglow (Tanvir et al., 2013; Berger, Fong, and Chornock, 2013; Yang et al., 2015), but the paucity of data is difficult to interpret. There is a great deal of work being done, including some of this thesis, to definitively determine the origin of both classes of GRBs.

Another related observational puzzle is the presence of elements heavier than $A \sim 200$ in the universe. CCSNe are the dominant source of elements up to iron and asymptotic giant branch stars can provide elements up to $A \sim 200$ (e.g., Woosley, Heger, and Weaver 2002), but an environment that is neutron-rich or has very high entropy is required to allow nuclei to capture neutrons rapidly enough to form the heaviest elements (the r-process, Burbidge et al. 1957; Arnould, Goriely, and Takahashi 2007).

Canonical Theory

The favored story behind short GRBs begins with the merger of a neutron star and another neutron star or a black hole (Paczynski, 1986; D. Eichler et al., 1989; Meszaros and Rees, 1992; Narayan, Paczynski, and Piran, 1992). This provides large amounts of gravitational energy to liberate into jets, neutrinos, and gravitational waves, in a small enough package to create the observed rapid variations in the jet. This also provides a great deal of very neutron rich ejecta in which the r-process could operate to create heavy elements. As two orbiting NSs slowly approach each other as the orbital energy is dissipated by gravitational waves, one or both of the neutron stars gets tidally shredded. This launches upwards of a solar mass of relatively cold, neutron-rich matter mostly in the equatorial plane. The remaining mass merges into either a black hole, a temporarily-stable hypermassive neutron star (HMNS), or a permanent remnant neutron star surrounded by a hot, magnetized accretion disk. Magnetic instabilities in the disk drive aggressive heating, accretion, and outflows. Neutrinos emitted from the hot disk and possibly the central HMNS also heat the disk and drive outflows, which I touch on in Chapter 4. If there is a central black hole, the relativistic jet may be launched by the Blandford-Znajeck (Blandford and Znajek, 1977) process, in which magnetic fields threading through the disk and coupled to a rotating black hole create an immense Poynting flux that drives a relativistic jet along the rotation axis. Shocks within the jet emit radiation in the comoving frame that is boosted to gamma-ray energies and relativistically beamed in the direction of the jet. Eventually, the relativistic jet interacts with the

interstellar medium, creating a long-lived x-ray, optical, and radio afterglow (Sari, Piran, and Narayan, 1998).

Alternatively, neutrinos and anti-neutrinos could annihilate in the polar regions and deposit enough energy to drive the jet (D. Eichler et al., 1989; Meszaros and Rees, 1992; Popham, Woosley, and C. Fryer, 1999; Zalamea and Beloborodov, 2011), though this is more difficult to justify. Estimates and simulations of energy deposition by neutrino annihilation suggest the amount of energy is only marginally, if at all, comparable to a GRB jet kinetic energy (e.g., Setiawan, Ruffert, and H.-T. Janka 2006; Dessart, Ott, et al. 2009; Leng and Giannios 2014). In addition, the density of baryons where the neutrinos annihilate and deposit energy most likely prevent outflows from reaching ultra-relativistic speeds (e.g., Levinson and D. Eichler 2003; Fujibayashi et al. 2017). I also touch on this issue in Chapter 4.

Though this theory is an interesting explanation of multiple astrophysical problems, there is yet no conclusive observational evidence. However, two types of smoking-gun evidence may be in our immediate future. First, based on estimates of stellar populations, Advanced LIGO should be able to detect gravitational waves from a neutron star merger, which would be identifiably different from binary black hole signals due to tidal dissipation (Abadie et al., 2012). Second, if a optical or infrared *kilonova* counterpart of a short GRB is conclusively observed, this would corroborate the story of neutron-rich mass ejection that forms r-process elements (e.g., Metzger, Martínez-Pinedo, et al. 2010). These observations would be especially powerful in conjunction (Nissanke, Kasliwal, and Georgieva, 2013).

1.4 Computational Approach

CCSNe and NSMs involve an intricate interplay between many areas of physics and a multitude of nonlinear dynamical phenomena. As such, analytic techniques are insufficient for understanding the detailed explosion mechanism, and computation has become the dominant tool for modeling CCSN and NSM engines (e.g., Ott 2016). The results of simulations depend in general on how the physics is discretized and which approximations are assumed, but the huge computational cost of these simulations will require the use of approximations for the foreseeable future. It must be *verified* that simulation methods accurately represent the physics they encode, and the outputs must be *validated* against nature (Calder et al., 2002). There is much work, including parts of this thesis, dedicated to understanding which aspects of the models are realistic and which are numerical or approximation artifacts. These

efforts are what give scientific value to simulation results.

Computational science in general requires knowing what processes to simulate and how to discretize the processes so they can be solved on a computer. I give a flash briefing here on conceptually how this is done, and expand on details relevant to this thesis in Chapter 2. The bulk of the matter in both systems can be modeled with general relativistic, inviscid, non-resistive magnetohydrodynamics. This is generally done in a *finite-volume* scheme by discretizing the domain into a grid of fluid cells and computing the fluxes of mass, energy, momentum, and magnetic field between adjacent cells (e.g., Baumgarte and Shapiro 2010). Alternatively, some simulations use the Lagrangian approach of *smoothed particle hydrodynamics*, where the fluid is broken up into smoothed spheres that interact with each other (e.g., citealtrosswog:09). Neutrino radiation transport can also be discretized in a finite-volume scheme similar to the hydrodynamics, or by simulating a statistical sample of individual *Monte Carlo* sample neutrinos (e.g., H.-T. Janka 1991). The microphysics, including nuclear forces, composition, and thermodynamics, are accounted for in simulations via an approximate equation of state, which relates the pressure to the fluid density, temperature, and electron fraction (e.g., J. M. Lattimer and Prakash, 2016). In the explosive engines themselves, the nucleons, nuclei, photons, and leptons are assumed to be in nuclear statistical equilibrium, though a nuclear reaction network can be used in regions where this is not the case, such as in ejecta from CCSNe and NSMs (e.g., Timmes and Arnett 1999; Timmes and Swesty 2000). Each of these physical and numerical approximations are well-motivated, but it is not uncommon to find that simulation outcomes depend very senstiviely on both.

Chapter 2

TECHNICAL BACKGROUND

In this chapter, I outline the notation, definitions, and assumptions used in the rest of the thesis. I briefly describe each of the major components that go into general relativistic radiation magnetohydrodyamics (GRRMHD) simulations of CCSNe and NSMs. In Section 2.1, I introduce the conventions I and my collaborators use for the 3+1 decomposition of general relativity, on top of which the simulations are built. In Section 2.2, I introduce the evolution scheme for fluid quantities in GRHD and GRMHD. I discuss the neutrino radiation component in Section 2.3. Finally, I describe the microphysical equation of state in Section 2.4. A far more complete introduction to GRRMHD can be found in Baumgarte and Shapiro, 2010. This chapter also makes extensive use of ideas outlined by Ott, 2007, Mösta, Mundim, et al., 2014, M. Shibata, Kiuchi, et al., 2011, Cardall, Endeve, and Mezzacappa, 2013, and E. O'Connor, 2015.

2.1 Numerical Relativity

Throughout this thesis, I adopt Einstein summation notation and the (-+++) metric signature convention. Since these equations are intended to be discretized for computational calculations, I also write all geometric quantities in a coordinate basis unless otherwise bolded. Greek indices carry values of (0,1,2,3), while Latin indices only carry values of (1,2,3).

Einstein Equations

The fundamental equation describing the dynamics of spacetime and mass-energy are the Einstein field equations

$$G_{\alpha\beta} = 8\pi T_{\alpha\beta} \ . \tag{2.1}$$

$T_{\alpha\beta}$ is the stress-energy tensor that describes mass and energy, which I will define in detail later in this section. The Einstein tensor is defined as

$$G_{\alpha\beta} = R_{\alpha\beta} - \frac{1}{2} g_{\alpha\beta} R - \Lambda g_{\alpha\beta} \ , \tag{2.2}$$

where the Ricci scalar is $R = R^{\alpha}{}_{\alpha}$, the Ricci tensor is $R_{\alpha\beta} = R^{\gamma}{}_{\alpha\gamma\beta}$, and the Riemann tensor is

$$R^{\alpha}{}_{\beta\gamma\delta} = \partial_{\gamma}\Gamma^{\alpha}{}_{\beta\delta} - \partial_{\delta}\Gamma^{\alpha}{}_{\beta\gamma} + \Gamma^{\alpha}{}_{\eta\gamma}\Gamma^{\eta}{}_{\beta\delta} - \Gamma^{\alpha}{}_{\eta\delta}\Gamma^{\eta}{}_{\beta\gamma} \ . \tag{2.3}$$

Of course, on the non-cosmological length scales associated with CCSNe and NSMs, we can safely take the cosmological constant to be $\Lambda = 0$. The Christoffel symbols are defined by

$$\Gamma^{\alpha}{}_{\beta\gamma} = \frac{1}{2} g^{\alpha\delta} \left(\partial_\gamma g_{\beta\delta} + \partial_\beta g_{\delta\gamma} - \partial_\delta g_{\beta\gamma} \right) \ . \tag{2.4}$$

The metric tensor is

$$g_{\alpha\beta} = \mathbf{e}_{(\alpha)} \cdot \mathbf{e}_{(\beta)} \ , \tag{2.5}$$

where $\mathbf{e}_{(\alpha)}$ are a set of four coordinate basis vectors. The subscript on the basis vectors specifies the basis vector and is not a component index.

3+1 Decomposition

In order to construct a Cauchy (i.e., initial value) problem, we follow the ADM 3+1 decomposition of spacetime (Arnowitt, Deser, and C. W. Misner, 1962; York, 1979). The evolved quantities (metric tensor and mass-energy sources) are specified on a three-dimensional spacelike hypersurface Σ_t defined by constant coordinate $x^0 = t$. The spatial coordinates x^i label the location on the hypersurface. We can define a vector n_α that is future-pointing ($n^0 > 0$), timelike normal ($n^\alpha n_\alpha = -1$), and is orthogonal to the hypersurface Σ_t ($n_\alpha e^\alpha_{(i)} = 0$). A *normal observer* is one that is moving with four-velocity n^α. The four-vector connecting points of the same spatial coordinate on nearby time slices is in general

$$dt^\alpha = d\tau(\alpha n^\alpha + \beta^\alpha) \ . \tag{2.6}$$

The *lapse function* α allows the rate of change of coordinate time to differ from the rate of change of the normal observer's proper time. The *shift vector* β^α, defined to be tangent to Σ_t, indicates that the spatial coordinates are also constructed to be able to slide normal to n^α with time. These coordinate freedoms are afforded by several gauge freedoms in the Einstein equations. One can choose to use Gaussian-normal coordinates which enforce $dt^\alpha = n^\alpha d\tau$, but this is unsuitable for computation because coordinate singularities quickly form. The orthogonality of n^α to $e^\alpha_{(i)}$ imply that $n_i = 0$, and since β^α is tangent to Σ_t we know that $\beta^0 = 0$. This, together with the normalization condition for n^α, implies that

$$\begin{aligned} n_\alpha &= \alpha(-1, 0, 0, 0) \ , \\ n^\alpha &= \alpha^{-1}(1, -\beta^i) \ . \end{aligned} \tag{2.7}$$

We can use this to define a spatial metric $\gamma_{\alpha\beta} = g_{\alpha\beta} + n_\alpha n_\beta$, so that $\gamma_{\alpha\beta} n^\beta = 0$. That is, γ_{ij} defines the dot product for spatial vectors, and $\gamma_{\alpha\beta}$ projects four-vectors

onto Σ_t. This defines the form of the metric tensor to be

$$\begin{aligned} g_{\alpha\beta} &= \begin{bmatrix} -\alpha^2 + \beta_\alpha \beta^\alpha & \beta_i \\ \beta_j & \gamma_{ij} \end{bmatrix} , \\ g^{\alpha\beta} &= \begin{bmatrix} -\alpha^{-2} & \alpha^{-2}\beta^i \\ \alpha^{-2}\beta^j & \gamma^{ij} - \alpha^{-2}\beta^i\beta^j \end{bmatrix} . \end{aligned} \tag{2.8}$$

Einstein's equations are a set of second order differential equations for the metric tensor, which has ten independent components. However, only six of the ten Einstein equations are evolution equations, the rest being constraint equations associated with a four-fold gauge freedom. Conceptually, the above 3+1 formalism allows the equations to be recast into a set of second order differential equation for only the six spatial components of the metric tensor. The other components (α and β^α) are determined by gauge choices. In practice, the six second order equations are implemented as a set of 12 first order equations, similar to how the second order equation for the position of a particle $d^2x/dt^2 = a$ can be recast into a first order equation for the position $dx/dt = v$ and a first order equation for the velocity $dv/dt = a$. The analog to the velocity in the above analogy in the context of numerical relativity is the extrinsic curvature

$$K_{\alpha\beta} = -\gamma_\alpha{}^\gamma \gamma_\beta{}^\delta \nabla_\gamma n_\delta , \tag{2.9}$$

which measures the rate at which the hypersurface Σ_t deforms with coordinate time. Furthermore, in the BSSN (Nakamura, Oohara, and Kojima, 1987; M. Shibata and Nakamura, 1995; Baumgarte and Shapiro, 1999) formulation, both the spatial metric and extrinsic curvature are reorganized into different evolution variables to ensure that the equations are well-posed and significantly more stable. However, since the focus of this thesis is on radiation magnetohydrodynamics on not techniques of numerical relativity, I again refer the interested reader to Baumgarte and Shapiro, 2010.

The Lorentz factor W of an object moving with four-velocity u^α relative to a normal observer (i.e., a reference frame with four-velocity n^α) is simply the dot product between the two velocity vectors $W = -n^\alpha u_\alpha = \alpha u^0$. To get the three-velocity v^i that a normal observer sees, we project the four-velocity into Σ_t and normalize by the Lorentz factor:

$$v^i = \frac{\gamma^i{}_\beta u^\beta}{-n_\beta u^\beta} = \frac{u^i}{W} + \frac{\beta^i}{\alpha} . \tag{2.10}$$

The Lorentz factor can then also be expressed as $W = (1 - v^i v_i)^{-1/2}$. We can also define an operator that transforms any four-vector from the normal frame to a frame moving at velocity u (i.e., a Lorentz transformation) as

$$L^{\alpha\beta} = -\frac{1}{n_\gamma u^\gamma}\left(g^{\alpha\beta} + u^\alpha u^\beta\right) \ . \tag{2.11}$$

Gravitational Waves

In a vacuum far from the source, the metric can be described by a linearized metric, consisting of the Minkowski metric with a linear perturbation:

$$g_{\alpha\beta} = \eta_{\alpha\beta} + h_{\alpha\beta} \ . \tag{2.12}$$

The gauge can be uniquely defined with the Lorentz gauge condition ($\nabla_\alpha \bar{h}^{\alpha\beta} = 0$) and the transverse-traceless (TT, $h_{\alpha 0} = 0$ and $h^\alpha_\alpha = 0$) gauge. In this gauge, the perturbation h_{ij} represents the relative strain between nearby particles. The Einstein equations then reduce to

$$\Box h_{\alpha\beta} = \nabla^\gamma \nabla_\gamma h_{\alpha\beta} = 0 \ . \tag{2.13}$$

There are two degrees of freedom in the gravitational wave, so it is commonly decomposed into + and × polarizations as

$$h_{ij} = h_+ e^+_{ij} + h_\times e^\times_{ij} \ , \tag{2.14}$$

where $e^+_{12} = \mathbf{e}_{(1)} \otimes \mathbf{e}_{(1)} - \mathbf{e}_{(2)} \otimes \mathbf{e}_{(2)}$ and $e^\times_{12} = \mathbf{e}_{(1)} \otimes \mathbf{e}_{(2)} + \mathbf{e}_{(2)} \otimes \mathbf{e}_{(1)}$ for two orthonormal basis vectors $\mathbf{e}_{(1,2)}$ orthogonal to the direction of propogation $\mathbf{e}_{(3)}$.

A time-retarded solution to a non-vacuum form of Equation 2.13 in the limits of weak gravitational field and slow motion within the source yields the approximate *quadropole formula* (e.g., C. W. Misner, Thorne, and J. A. Wheeler 1973):

$$h_{ij}(t, \mathbf{x}) \approx \frac{2G}{c^4 r} \ddot{\mathcal{I}}^{TT}_{ij}\left(t - \frac{r}{c}\right) \ , \tag{2.15}$$

where r is the distance to the source. The reduced quadrupole moment tensor is

$$\mathcal{I}_{ij} = \int \rho \left(x_i x_j - \frac{1}{3}\delta_{ij} r^2\right) W \sqrt{\gamma} d^3 x \tag{2.16}$$

and is projected into the TT gauge using

$$\begin{aligned} \mathcal{I}^{TT}_{jk} &= \left(P_{jl} P_{km} - \frac{1}{2} P_{jk} P_{lm}\right) \mathcal{I}_{lm} \ , \\ P_{ij} &= \delta_{ij} - e_{(3)i} e_{(3)j} \ . \end{aligned} \tag{2.17}$$

The rest mass continuity equation ($\nabla_\alpha \rho u^\alpha = 0$) can be used to turn one time derivative into a spatial derivative:

$$\dot{\mathcal{I}}_{ij} = \int \rho \left(v_i x_j + v_j x_i - \frac{2}{3}\delta_{ij} v_m x^m \right) W \sqrt{\gamma} d^3x \ . \tag{2.18}$$

An explicit time derivative can be taken of this quantity and plugged into Equation 2.15. The resulting gravitational wave signature is dependent on the gauge and on boundary conditions, but has been shown to compare very favorably against full numerical relativity calculations in the context of oscillating neutron stars (e.g., Balbinski 1985; M. Shibata, Karino, and Eriguchi 2003). This is the method used to extract gravitational waves from the axisymmetric core-collapse simulations in Chapter 7.

Conformally Flat Approximation

The metric is considered *conformally flat* if the spatial metric can be related to the flat spacetime metric with a single scalar, i.e.,

$$\gamma_{ij} = \psi^4 \eta_{ij} \ . \tag{2.19}$$

In spherical symmetry, this expression is automatically true. However, in two and three spatial dimensions, this is only true for metrics that contain no gravitational wave component. Since ordinary CCSNe are largely spherical, are slowly rotating, and lack strong spacetime variability (as in, for example, merging BHs or NSs), approximating the metric as conformally flat is a good approximation for simulating the hydrodynamics (Ott, Dimmelmeier, Marek, H.-T. Janka, Zink, et al., 2007). Doing so greatly simplifies the Einstein equations into a set of elliptic equations with no explicit time derivatives. Thus, the spacetime metric can be determined at each time step, independent of the previous time step. Since a conformally flat metric does not admit gravitational waves, the quadrupole formula above must be used to estimate the GW signal from these simulations. The conformally flat approximation us used to evolve the spacetime quantities in the CoCoNuT code used in Chapter 7.

2.2 General Relativistic Magnetohydrodynamics

In order to make equations suitable for computation, we recast them in conservative form

$$\partial_t \left(\sqrt{\gamma} \mathbf{U} \right) + \partial_i \left(\sqrt{\gamma} \mathbf{F}^i \right) = \sqrt{-g} \mathbf{S} \ . \tag{2.20}$$

$\mathbf{U} = \{\mathcal{U}\}$ is the set of evolved conserved variables, $\mathbf{F}^i = \{\mathcal{F}^i\}$ is the corresponding set of fluxes, and $\mathbf{S} = \{\mathcal{S}\}$ is the corresponding set of source terms. Here, $\gamma = \det(\gamma_{ik})$ and $g = \det(g) = -\alpha^2\gamma$. $\sqrt{\gamma}\mathbf{U}$ are referred to as *densitized* variables.

Taking the gradient of the Einstein equations gives the equations for the conservation of energy-momentum that govern the flow of all non-gravitational mass and energy:

$$\nabla_\beta T^{\alpha\beta} = 0 \ . \tag{2.21}$$

In general, $\mathbf{U} = T^0{}_\alpha$, $\mathbf{F}^i = T^i{}_\alpha$, and $\mathbf{S} = T^{\beta\gamma}\partial_\alpha g_{\beta\gamma}/2$ (i.e., a set of four quantities). However, it is useful to separate the conserved quantities into a part projected tangent to Σ_t and a part projected in the normal direction. The conserved energy- and momentum-like variables can be written as and the source terms as

$$\mathbf{U} = \begin{bmatrix} S_j \\ \tau \end{bmatrix} = \begin{bmatrix} \alpha T^0{}_j \\ \alpha^2 T^{00} \end{bmatrix} \ , \tag{2.22}$$

$$\mathbf{F} = \begin{bmatrix} \alpha T^i{}_j \\ \alpha^2 T^{0i} \end{bmatrix} \ . \tag{2.23}$$

$$\mathbf{S} = \begin{bmatrix} T^{\alpha\beta}\left(\partial_\alpha g_{\beta j} - \Gamma^\lambda{}_{\alpha\beta} g_{\lambda j}\right) \\ T^{\alpha 0}\partial_\alpha \alpha - T^{\alpha\beta}\Gamma^0{}_{\alpha\beta} \end{bmatrix} \ . \tag{2.24}$$

The stress-energy tensor can be conceptually split into three separate components,

$$T^{\alpha\beta} = T^{\alpha\beta}_{\rm HD} + T^{\alpha\beta}_{\rm EM} + T^{\alpha\beta}_{\rm neutrinos} \ . \tag{2.25}$$

Additional variables introduced in the specific forms of these tensors must be evolved with additional equations.

Hydrodynamics (HD)

The equations of inviscid compressible hydrodynamics are an excellent approximation of the behavior of neutrons, protons, electrons, and nuclei in the dense matter of NSMs and CCSNe (e.g., E. Flowers and Itoh, 1976; E. Flowers and Itoh, 1979). Classical hydrodynamics is described in terms of the rest mass density ρ, the pressure P, the thermal energy density ϵ, and three velocities v^i. The fluid stress energy tensor is written

$$T^{\alpha\beta}_{\rm HD} = \rho h u^\alpha u^\beta + P g^{\alpha\beta} \ , \tag{2.26}$$

where the relativistic specific enthalpy is $h = 1 + \epsilon + P/\rho$.

The matter in CCSNe and NSMs that is dynamically relevant (i.e., neglecting ejected matter and the sparse region between merging NSs) is in nuclear statistical equilibrium, which allows us to parameterize the composition of the matter in terms of the ratio of electron number density to baryon number density Y_e (assuming no

charge separation). There are now seven variables to evolve and only four evolution equations from the energy-momentum conservation equations. The first additional equation is the mass continuity equation that implements the hypothesis that rest mass is conserved:

$$\nabla_\alpha \left(\rho u^\alpha\right) = 0 \,, \tag{2.27}$$

The second is the proton (or, equivalently, electron) number continuity equation:

$$\nabla_\alpha \left(Y_e \frac{\rho}{m_u} u^\alpha\right) = 0 \,, \tag{2.28}$$

where m_u is the atomic mass unit. The third is the equation of state

$$P = P(\rho, \epsilon, Y_e) \ . \tag{2.29}$$

The equation of state is in general very complicated, and I discuss it separately in Section 2.4.

In addition to the equation of state, the terms in the hydrodynamic evolution equations can be written as

$$\mathbf{U}_{\rm HD} = \begin{bmatrix} D \\ DY_e \\ S_j \\ \tau - D \end{bmatrix} = \begin{bmatrix} \rho W \\ Y_e \rho W \\ \rho h W^2 v_j \\ \rho h W^2 - P - D \end{bmatrix} \,, \tag{2.30}$$

$$\mathbf{F}^i_{\rm HD} = \alpha \times \begin{bmatrix} D\tilde{v}^i \\ DY_e\tilde{v}^i \\ S_j\tilde{v}^i + P\delta^i_{\ j} \\ \tau\tilde{v}^i + Pv^i \end{bmatrix} \,, \tag{2.31}$$

$$\mathbf{S}_{\rm HD} = \alpha \times \begin{bmatrix} 0 \\ 0 \\ T^{\alpha\beta}_{\rm HD}\left(\partial_\alpha g_{\beta j} - \Gamma^\lambda_{\ \alpha\beta} g_{\lambda j}\right) \\ T^{\alpha 0}_{\rm HD}\partial_\alpha \alpha - T^{\alpha\beta}_{\rm HD}\Gamma^0_{\ \alpha\beta} \end{bmatrix} \,, \tag{2.32}$$

where $\tilde{v}^i = (v^i - \beta_i/\alpha)$. The spherically symmetric version of this formalism is used in the GR1D calculations in Chapter 7.

Magnetohydrodynamics (MHD)

The Faraday tensor describing the electromagnetic fields is

$$F^{\alpha\beta} = n^\alpha E^\beta - n^\beta E^\alpha + n_\delta \epsilon^{\delta\alpha\beta\gamma} B_\gamma \,, \tag{2.33}$$

where E^α and B^α are the electric and magnetic fields seen by a normal observer and are tangent to Σ_t. $\epsilon_{\alpha\beta\gamma\delta}$ is the anti-symmetric Levi-Civita tensor where $\epsilon_{0123} = \sqrt{\gamma}$. The dual of the Faraday tensor is denoted $F^{*\alpha\beta} = 1/2\epsilon^{\alpha\beta\gamma\delta}F_{\gamma\delta}$, and the general relativistic Maxwell equations are

$$\begin{aligned} \nabla_\alpha F^{\alpha\beta} &= 4\pi J^\beta \,, \\ \nabla_\alpha F^{*\alpha\beta} &= 0 \,, \end{aligned} \tag{2.34}$$

where J^α is the four-current. We can define a comoving-frame magnetic field, normalized by $\sqrt{4\pi}$ for future convenience, to be

$$b^\alpha = \frac{L^{\alpha\beta}B_\beta}{\sqrt{4\pi}} \,, \tag{2.35}$$

where the Lorentz transformation operator $L^{\alpha\beta}$ is shown in Equation 2.11.

In the ideal MHD approximation, written as $F^{\alpha\beta}u_\beta = 0$, the fluid conductivity is infinite and the electric field is zero in the fluid rest frame. Using this, the Faraday tensor to reduces to $F^{\alpha\beta} = n^\beta B^\alpha - n^\alpha B^\beta = \sqrt{4\pi}\left(u^\beta b^\alpha - u^\alpha b^\beta\right)$. The electromagnetic stress-energy tensor can then be written as

$$T^{\alpha\beta}_{\rm EM} = \frac{1}{4\pi}F^{\alpha\gamma}F^{\beta}_{\ \gamma} + \frac{1}{16\pi}g^{\alpha\beta}F_{\gamma\delta}F^{\gamma\delta} \xrightarrow[\rm MHD]{} b^2u^\alpha u^\beta - b^\alpha b^\beta + \frac{1}{2}b^2 g^{\alpha\beta} \,, \tag{2.36}$$

where $b = b^\alpha b_\alpha$. The first Maxwell equation is not needed, as it now only provides a description of the current density given the magnetic field. The MHD energy-momentum equations use the stress-energy tensor $T^{\alpha\beta}_{\rm MHD} = T^{\alpha\beta}_{\rm HD} + T^{\alpha\beta}_{\rm EM}$.

In addition to the equation of state, the MHD evolution equations become

$$\mathbf{U}_{\rm MHD} = \begin{bmatrix} D \\ DY_e \\ S_j \\ \tau - D \\ B^k \end{bmatrix} = \begin{bmatrix} \rho W \\ Y_e \rho W \\ \rho h^* W^2 v_j - \alpha b^0 b_j \\ \rho h^* W^2 - P^* - (\alpha b^0)^2 - D \\ B^k \end{bmatrix} , \tag{2.37}$$

$$\mathbf{F}^i_{\rm MHD} = \alpha \times \begin{bmatrix} D\tilde{v}^i \\ DY_e\tilde{v}^i \\ S_j\tilde{v}^i + P^*\delta^i_j - b_j B^k/W \\ \tau\tilde{v}^i + P^* v^i - \alpha b^0 B^k/W \\ B^k\tilde{v}^i - B^i\tilde{v}^k \end{bmatrix} , \tag{2.38}$$

$$\mathbf{S}_{\rm MHD} = \alpha \times \begin{bmatrix} 0 \\ 0 \\ T^{\alpha\beta}_{\rm MHD}\left(\partial_\alpha g_{\beta j} - \Gamma^{\lambda}{}_{\alpha\beta} g_{\lambda j}\right) \\ T^{\alpha 0}_{\rm MHD}\partial_\alpha \alpha - T^{\alpha\beta}_{\rm MHD}\Gamma^{0}{}_{\alpha\beta} \\ 0 \end{bmatrix} , \tag{2.39}$$

where $P^* = P + b^2/2$ and $h^* = 1 + \epsilon + (P + b^2)/\rho$. The second Maxwell equation also provides the "no magnetic monopoles" condition $\partial_i \left(\sqrt{\gamma} B^i\right) = 0$, which, though guaranteed analytically, must be enforced explicitly on a computer. This is the basis of the GRMHD code GRHYDRO (Mösta, Mundim, et al., 2014) used in Chapter 6.

2.3 Neutrino Transport

There are six neutrino species (ν_e,ν_μ,ν_τ and their anti-species) corresponding to the six lepton species. I assume that neutrinos are Dirac fermions with zero mass and behave as classical, ultra-relativistic particles following the electroweak theory of Glashow, Weinberg and Salam (e.g., Glashow 1961; Weinberg 1967; Weinberg 1972; Salam 1980).

The neutrino distribution function $f(x^\alpha, p^\alpha)$ of any species, where p^α is the momentum-space coordinate, is the phase-space neutrino number density. That is,

$$dN = -\frac{1}{hc} p_\alpha u^\alpha f \, dV \, dP \, , \tag{2.40}$$

where $dV = W\sqrt{-g}d^3x$ is the invariant volume element and $dP = \sqrt{-g}d^3p/(-h^2 p_0)$ is the invariant phase-space volume element. Since everything else in the equation is invariant, f is also invariant. Since this conserves energy and momentum in a relativistic sense, the equations $\nabla_\alpha T^{\alpha\beta} = 0$ are satisfied.

Neutrinos interact through a variety of processes with electrons (e^-), positrons (e^+), neutrons (n), protons (p), nuclei (A, Z) with atomic mass A and atomic charge Z, and other neutrinos. Interactions for all neutrino species are mediated by the exchange of a neutral boson (*neutral-current* reactions), whereas in the temperature and energy ranges relevant to CCSNe and NSMs, only electron neutrinos and anti-neutrinos can interact with their respective leptons (electrons) by the exchange of a charged boson (*charged-current* reactions). The masses of μ and τ leptons are too high to be produced in large number. This effectively causes electron neutrinos and anti-neutrinos to interact much more strongly with the fluid. For more detailed derivations and reviews of these interactions, see the works by Bruenn, 1985 and Burrows, Reddy, and Thompson, 2006. The simplest reactions to treat from the

point of view of radiation transport are absorption processes, since they involve only one type of neutrino and only on one side of the reaction. The most relevant are electron neutrino and anti-neutrino absorption onto nucleons and nuclei, along with their inverse reactions:

$$\begin{aligned} \nu_e + n &\rightleftharpoons e^- + p \\ \bar{\nu}_e + p &\rightleftharpoons e^+ + n \\ \nu_e + (A, Z) &\rightleftharpoons e^- + (A, Z+1) \end{aligned} \quad . \tag{2.41}$$

The degeneracy of the neutrino field can be accounted for either by blocking neutrino emission, or more simply via the concept of stimulated absorption (e.g., Burrows, Reddy, and Thompson 2006). Scattering processes have neutrinos on both sides of the reaction:

$$\begin{aligned} \nu + \{n, p, e^\pm\} &\rightleftharpoons \nu + \{n, p, e^\pm\} \\ \nu + (A, Z) &\rightleftharpoons \nu + (A, Z) \end{aligned} \quad . \tag{2.42}$$

In this case, Fermi blocking of the final neutrino state must be taken into account explicitly, complicating the transport equations. Pair proceses involve a neutrino and its anti-neutrino on one side of the reaction. The most relevant are neutrino pair annihilation into electron-positron pairs, nucleon-nucleon bremsstrahlung, and their inverses:

$$\begin{aligned} \nu + \bar{\nu} &\rightleftharpoons e^+ + e^- \\ \nu + \bar{\nu} + \{n, p\} + \{n, p\} &\rightleftharpoons \{n, p\} + \{n, p\} \end{aligned} \quad . \tag{2.43}$$

Fermi blocking must then be explicitly accounted for for both species in the neutrino emission direction, and the effective absorption opacity depends on both fluid *and* neutrino field properties. Finally, there are other neutrino reactions with multiple types of neutrinos on both sides of the reaction, including neutrino pair annihilation into neutrino pairs and neutrino-neutrino scattering. In this thesis I ignore them as is commonly done, but they may be important for helping heavy lepton neutrinos escape the protoneutron star (e.g., E. G. Flowers and Sutherland 1976; Keil, Raffelt, and H.-T. Janka 2003).

Neutrino interactions with the fluid are most easily described in local orthonormal frame at rest with the fluid, where the timelike unit vector is the fluid velocity u^α. For brevity, I do not describe the transformations into and out of this basis, but details can be found in, for example, Lindquist, 1966; Dolence, Gammie, et al., 2009; Cardall, Endeve, and Mezzacappa, 2013. In this frame, I choose the neutrino momentum space coordinates to be the neutrino comoving frame energy $\epsilon = -p_\alpha u^\alpha$ and the unit direction vector in spherical-polar coordinates $\Omega = (\bar{\theta}, \bar{\phi})$.

There are three separate formulations of neutrino transport that I make use of in this thesis. All three are formally equivalent, but have very different implementations and are conducive to different types of approximations. Rather than incorporate the neutrino field into the left hand side of the (magneto-)hydrodynamic evolution equations, interactions between neutrinos and hydrodynamics are placed in the source terms on the right hand side of those equations.

Boltzmann Transport

The stress-energy tensor from radiation can be written

$$T^{\alpha\beta}_{\text{neutrinos}} = \frac{1}{hc}\int p^\alpha p^\beta f dP \ . \tag{2.44}$$

The Boltzmann equation that governs the evolution of the distribution function is essentially a restatement of the Liouville theorem and reads:

$$\frac{df}{d\lambda} = p^\alpha \frac{\partial f}{\partial x^\alpha} - \Gamma^i{}_{\alpha\beta} p^\alpha p^\beta \frac{\partial f}{\partial p^i} = -\frac{p_\alpha u^\alpha}{c}\left[\left(\frac{df}{cd\tau}\right)_{\text{em-abs}} + \left(\frac{df}{cd\tau}\right)_{\text{scat}} + \left(\frac{df}{cd\tau}\right)_{\text{pair}}\right], \tag{2.45}$$

where τ is the proper time in an orthonormal frame moving with four-velocity u^α. The source terms on the right hand side in general depends on value of the fluid properties and of all six neutrino distribution functions at the same spatial location.

In a comoving orthonormal coordinate system, the emission and absorption term takes the form of

$$\left(\frac{df}{cd\tau}\right)_{\text{em-abs}} = R_{\text{em}}(\epsilon)(1-f) - R_{\text{abs}}(\epsilon) f \ , \tag{2.46}$$

where R_{em} and R_{abs} are the emission and absorption reaction rates, respectively. We can also take advantage of the concept of stimulated absorption to account for final-state neutrino blocking (Burrows, Reddy, and Thompson, 2006), in which the effective absorption reaction rate is $\widetilde{R}_{\text{abs}} = R_{\text{abs}} + R_{\text{emis}}$. This removes the need to treat final-state blocking explicitly in the neutrino emission process.

The scattering term accounts for neutrinos scattering into and out of a given direction according to

$$\begin{aligned}\left(\frac{df}{cd\tau}\right)_{\text{scat}} = \int d\mathbf{\Omega}' \int d\left(\frac{\epsilon'^3}{3}\right) [&R_{\text{scat}}(\epsilon', \epsilon, \mathbf{\Omega}'\cdot\mathbf{\Omega}) f'(1-f) \\ &- R_{\text{scat}}(\epsilon, \epsilon', \mathbf{\Omega}\cdot\mathbf{\Omega}') f(1-f')] \ .\end{aligned} \tag{2.47}$$

The primed variables are the neutrino final-state quantities and R_{scat} is the scattering reaction rate. If we assume isotropic, isoenergetic scattering, so the scattering

reaction rate becomes $R_{\text{scat}}(\epsilon', \epsilon, \mathbf{\Omega}' \cdot \mathbf{\Omega}) = \delta(\epsilon, \epsilon')\widetilde{R}_{\text{scat}}(\epsilon)$. Under this assumption, the scattering source term reduces to

$$\left(\frac{df}{cd\tau}\right)_{\text{scat}} = \int d\mathbf{\Omega}' \widetilde{R}_{\text{scat}}(\epsilon)(f' - f) \ . \tag{2.48}$$

Finally, pair annihilation and neutrino bremsstrahlung source terms take the form of

$$\begin{aligned}\left(\frac{df}{cd\tau}\right)_{\text{pair}} = \int d\bar{\mathbf{\Omega}} \int d\left(\frac{\bar{\epsilon}^3}{3}\right) [R_{\text{pair,em}}(\epsilon, \bar{\epsilon}, \mathbf{\Omega} \cdot \bar{\mathbf{\Omega}})(1 - f)(1 - \bar{f}) \\ - R_{\text{pair,abs}}(\epsilon, \bar{\epsilon}, \mathbf{\Omega} \cdot \bar{\mathbf{\Omega}}) f \bar{f}] \ .\end{aligned} \tag{2.49}$$

The barred variables are the neutrino anti-species quantities and $R_{\text{pair,em}}$ is the reaction rate for pair and and bremsstrahlung processes. This is the basis for the discrete ordinates scheme of Nagakura, Iwakami, Furusawa, Sumiyoshi, et al., 2017 used in Chapter 5.

Moment Transport

The stress-energy tensor can be written in a frame moving with velocity u^α as

$$T^{\alpha\beta}_{\text{neutrinos}} = E\frac{1}{c^2}u^\alpha u^\beta + \frac{1}{c}F^\alpha u^\beta + \frac{1}{c}F^\beta u^\alpha + P^{\alpha\beta} \ , \tag{2.50}$$

where E, F^α, and $P^{\alpha\beta}$ are the zeroth, first, and second angular moments, respectively. The energy-dependent angular moments projected into Σ_t are defined as

$$\begin{aligned} E_{(\epsilon)} &= \epsilon \int d\mathbf{\Omega} f \ , \\ F^\alpha_{(\epsilon)} &= \epsilon \int d\mathbf{\Omega} f l^\alpha \ , \\ P^{\alpha\beta}_{(\epsilon)} &= \epsilon \int d\mathbf{\Omega} f l^\alpha l^\beta \ , \\ &\cdots \end{aligned} \tag{2.51}$$

The ellipsis denotes that there is an infinite list of moments that can be used to reconstruct the two-dimensional angular dependence of the distribution function, much like an infinite list of terms in a Taylor series can be used to reconstruct a one-dimensional function. Here, l^α are define to split the neutrino four-momenta into timelike and spacelike components as

$$p^\alpha = \frac{-p^\beta u_\beta (u^\alpha + l^\alpha)}{c^2} \ . \tag{2.52}$$

For any moment $M_{(\epsilon)}$, the energy-integrated moment is

$$M = \frac{1}{(hc)^3} \int d\left(\frac{\epsilon^3}{3}\right) M_{(\epsilon)} \ . \tag{2.53}$$

In the same light, one can take moments of the Boltzmann equation and write the results in conservative form to arrive at (M. Shibata, Kiuchi, et al., 2011; Cardall, Endeve, and Mezzacappa, 2013):

$$\begin{aligned}
&\partial_t(\sqrt{\gamma}\mathbf{U}_{\rm rad}) + \partial_j\left(\sqrt{\gamma}\mathbf{F}_{\rm x,rad}\right) + \partial_\epsilon\left(\sqrt{\gamma}\mathbf{F}_{\epsilon,\rm rad}\right) = \sqrt{-g}\mathbf{S}_{\rm rad} \ , \\
&\mathbf{U}_{\rm rad} = \begin{bmatrix} E_{(\epsilon)} \\ F_{(\epsilon),i} \\ \cdots \end{bmatrix} \ , \\
&\mathbf{F}_{x,\rm rad} = \alpha \times \begin{bmatrix} F^j_{(\epsilon)} - \frac{\beta^j}{\alpha} E_{(\epsilon)} \\ P^j_{(\epsilon),i} - \frac{\beta^j}{\alpha} F_{(\epsilon),i} \\ \cdots \end{bmatrix} \ , \\
&\mathbf{F}_{\epsilon,\rm rad} = \epsilon\alpha M^{\alpha\beta\gamma}_{(\epsilon)} \nabla_\gamma u_\beta \begin{bmatrix} n_\alpha \\ \gamma_{i\alpha} \\ \cdots \end{bmatrix} \ , \\
&\mathbf{S}_{\rm rad} = \begin{bmatrix} \alpha P^{ij}_{(\epsilon)} K_{ij} - F^j_{(\epsilon)} \partial_j \alpha \ln\alpha - \alpha S^\alpha_{(\epsilon)} n_\alpha \\ -\alpha E_{(\epsilon)} \ln\alpha + F_{(\epsilon),k} \partial_i \beta^k + \frac{\alpha}{2} P^{jk}_{(\epsilon)} \partial_i \gamma_{jk} + \alpha S^\alpha_{(\epsilon)} \gamma_{i\alpha} \\ \cdots \end{bmatrix} \ .
\end{aligned} \tag{2.54}$$

Notice that the evolution equation for each moment depends on higher-order moments.

The so-called local two-moment transport method (G. C. Pomraning, 1969; J. L. Anderson and Spiegel, 1972; Thorne, 1981; M. Shibata, Kiuchi, et al., 2011; Cardall, Endeve, and Mezzacappa, 2013) is the current state of the art method for time-dependent multi-dimensional simulations of neutrino radiation hydrodynamics (e.g., E. O'Connor and Couch 2015; Just, Obergaulinger, and H.-T. Janka 2015; Foucart, E. O'Connor, L. Roberts, Kidder, et al. 2016; L. F. Roberts, Ott, et al. 2016; Kuroda, Takiwaki, and Kotake 2016; Radice, Burrows, et al. 2017)[1].

In the two-moment method, only the first two moments are evolved and are assumed to provide a good enough representation of the full distribution function. The

[1] Higher-order transport calculations (e.g., B. Müller, H.-T. Janka, and Dimmelmeier 2010) are used in multiple dimensions via the ray-by-ray approximation (e.g., Burrows, J. Hayes, and Fryxell 1995; Buras et al. 2006)

evolution equations for each moment depend on higher-order moments. In a *local* two-moment scheme, the pressure tensor and higher-order moments are estimated based on the energy density and flux at the same spatial location. This estimate is referred to as a closure relation, many of which have been proposed based on various motivations (e.g., Smit, van den Horn, and Bludman 2000; Murchikova, E. Abdikamalov, and Urbatsch 2017 and references therein).

Three particular choices of approximate closure relations based on different physical motivations are the maximum entropy closure of Minerbo, 1978 in the classical limit (Minerbo), the isotropic rest-frame closure of Levermore, 1984 (Levermore), and the closure of H.-T. Janka, 1991 in the form presented in Just, Obergaulinger, and H.-T. Janka, 2015 that is empirically based on MC calculations of neutrino transport in protoneutron stars. In all three cases, the pressure tensor is expressed as an interpolation between optically thick and thin limits where the solution is known analytically:

$$P^{ij}_{\epsilon} = \frac{3\chi_{\epsilon} - 1}{2} P^{ij}_{\epsilon,\text{thin}} + \frac{3(1-\chi_{\epsilon})}{2} P^{ij}_{\epsilon,\text{thick}} \,, \tag{2.55}$$

where

$$\begin{aligned} P^{ij}_{\epsilon,\text{thin}} &= E_{\epsilon} \frac{F^i_{\epsilon} F^j_{\epsilon}}{\mathbf{F}_{\epsilon} \cdot \mathbf{F}_{\epsilon}} \,, \\ P^{ij}_{\epsilon,\text{thick}} &= \frac{E_{\epsilon}}{3} I^{ij} + O\left(\frac{v}{c}\right) \,, \end{aligned} \tag{2.56}$$

and I is the 3×3 identity matrix. The different closure relations are defined by

$$\begin{aligned} \chi_{\epsilon,\text{Minerbo}} &= \frac{1}{3} + \frac{2}{15}\zeta_{\epsilon}^2 \left(3 - \zeta_{\epsilon} + 3\zeta_{\epsilon}^2\right) \,, \\ \chi_{\epsilon,\text{Levermore}} &= \frac{3 + 4\zeta_{\epsilon}^2}{5 + 2\sqrt{4 - 3\zeta_{\epsilon}^2}} \,, \\ \chi_{\epsilon,\text{Janka}} &= \frac{1}{3}\left(1 + \zeta_{\epsilon}^{1.31} + 1.5\zeta_{\epsilon}^{3.56}\right) \,. \end{aligned} \tag{2.57}$$

$\zeta_{\epsilon} = \sqrt{\mathbf{F}_{\epsilon} \cdot \mathbf{F}_{\epsilon} / E_{\epsilon}^2}$ is referred to as the the flux factor. P^{ij}/E is referred to as the Eddington tensor, and in the context of spherically-symmetric radiation transport, P^{rr}/E is referred to as the Eddington factor.

I briefly discuss methods for using Monte Carlo transport to estimate the higher-order moments in dynamical simulations in Chapter 3. I evaluate the accuracy of several closures in the context of time-independent core-collapse calculations in Chapter 5. The spherically symmetric form of these equations are used in the GR1D calculations in Chapter 7.

Particle Transport

The stress-energy tensor can be written in frame moving with velocity u^α as

$$T^{\alpha\beta}_{\text{neutrinos}} = c^2 n \sum \frac{p^\alpha p^\beta}{p^\gamma u_\gamma} \,, \tag{2.58}$$

where the sum is over all particles and n is the particle number density. That is, a neutrino can be described by a single null four-momentum $p^\alpha = dx^\alpha/d\lambda$, where λ is an affine parameter that I choose here to be $\lambda = c\tau$ and τ is the proper time in the same frame. Except when undergoing a collision, neutrinos follow null geodesics:

$$\begin{aligned} \frac{dx^\alpha}{cd\tau} &= c\frac{p^\alpha}{p^\gamma u_\gamma} \\ \frac{dp^\alpha}{cd\tau} &= -\Gamma^\alpha{}_{\beta\gamma} p^\beta p^\gamma \end{aligned} \,, \tag{2.59}$$

The emissivity $j(\epsilon)$ with units of (erg cm^{-3} s^{-1} MeV^{-1}) can be related to the emission reaction rate via

$$\begin{aligned} j(\epsilon) = \frac{\epsilon^2}{c^2 h^3} &\int d\mathbf{\Omega} R_{\text{em}}(\epsilon)(1-f) \\ &+ \int d\mathbf{\Omega} \int \bar{\mathbf{\Omega}} R_{\text{pair,em}}(\epsilon, \bar{\epsilon}, \mathbf{\Omega}\cdot\bar{\mathbf{\Omega}})(1-f)(1-\bar{f}) \,. \end{aligned} \tag{2.60}$$

In a comoving orthonormal coordinate system, neutrinos are emitted isotropically, and the probability density of a neutrino being emitted with energy ϵ is

$$p(\epsilon) = \frac{j(\epsilon)}{\int d\epsilon j(\epsilon)} \,. \tag{2.61}$$

A neutrino moving in a certain direction $\mathbf{\Omega}$ with a certain energy ϵ will move a random distance s between scattering/absorption events, according to the probability distribution function

$$p(s) = \sigma e^{-\sigma s} \,, \tag{2.62}$$

where σ is the net opacity given by

$$\begin{aligned} \sigma(\epsilon, \mathbf{\Omega}) = R_{\text{abs}}(\epsilon) &+ \int d\mathbf{\Omega}' \int d\epsilon' R_{\text{scat}}(\epsilon, \epsilon', \mathbf{\Omega}\cdot\mathbf{\Omega}')(1-f') \\ &+ \int d\bar{\mathbf{\Omega}} \int d\bar{\epsilon} R_{\text{pair,abs}}(\epsilon, \bar{\epsilon}, \mathbf{\Omega}\cdot\bar{\mathbf{\Omega}})\bar{f} \,. \end{aligned} \tag{2.63}$$

When the neutrino does interact, the probability of each of these types of reactions is proportional to the respective opacity. If the particle undergoes a scatter, the probability density of the particle scattering into final energy ϵ' and direction $\mathbf{\Omega}'$ is

$$p(\epsilon', \mathbf{\Omega}') = \frac{R_{\text{scat}}(\epsilon, \epsilon', \mathbf{\Omega}\cdot\mathbf{\Omega}')(1-f')}{\int d\epsilon' \int d\mathbf{\Omega}' R_{\text{scat}}(\epsilon, \epsilon', \mathbf{\Omega}\cdot\mathbf{\Omega}')(1-f')} \,. \tag{2.64}$$

If the neutrino is absorbed, its energy and momentum are transferred to the fluid. This formalism is the basis for the Monte Carlo neutrino transport scheme used by Sedonu, which I describe in more detail in Chapter 3 and which is used in Chapters 4 and 5.

Beyond the Standard Model

In the standard model, which I use throughout this thesis, neutrinos are massless fermions. Though this is a common assumption in simulations of CCSNe and NSMs, neutrinos are now known to have mass and *oscillate* between flavor states. There is also the possibility of additional non-interacting *sterile* neutrino flavors. In this section, I will briefly present the modern description of neutrino oscillations, describe how well these properties are known, and lay out the state of the art of the computational tools used to simulate neutrino oscillations. This section is based largely on the reviews of Duan, G. M. Fuller, and Qian, 2010, Bellini et al., 2014, Chakraborty et al., 2016, and Mirizzi et al., 2016.

Neutrino masses and oscillations lie outside of the standard model and as of yet lack a consistent theoretical underpinning (e.g., Lobanov 2015). However, we can take a phenomenological approach using the language of nonrelativistic quantum mechanics that yields results that match experimental and observational data (e.g., Esteban et al. 2017). In this approach, the quantum state of a neutrino can be expressed in a *flavor basis* $|\nu_\alpha\rangle$ where $\alpha = \{e, \mu, \tau, ...\}$, or a *mass basis* $|\nu_i\rangle$ where $i = \{1, 2, 3, ...\}$. The ellipses indicate the possibility of sterile neutrino flavors, though from this point on we assume for simplicity that there are only three neutrino flavors. Flavor eigenstates are different from mass eigenstates, such that

$$\begin{aligned} |\nu_\alpha\rangle &= U^*_{\alpha i}|\nu_i\rangle \ , \\ |\bar{\nu}_\alpha\rangle &= U_{\alpha i}|\bar{\nu}_i\rangle \ . \end{aligned} \tag{2.65}$$

$U_{\alpha i}$ is a unitary matrix. U can be expressed in terms of three *mixing angles* θ_{12}, θ_{23}, and θ_{13}, and a phase $\delta_{\rm CP}$ as

$$U = \begin{bmatrix} 1 & 0 & 0 \\ 0 & c_{32} & s_{23} \\ 0 & -s_{23} & c_{23} \end{bmatrix} \cdot \begin{bmatrix} c_{13} & 0 & s_{13}e^{-i\delta_{\rm CP}} \\ 0 & 1 & 0 \\ -s_{13}e^{i\delta_{\rm CP}} & 0 & c_{13} \end{bmatrix} \cdot \begin{bmatrix} c_{12} & s_{12} & 0 \\ -s_{12} & c_{12} & 0 \\ 0 & 0 & 1 \end{bmatrix} \cdot \mathcal{P} \tag{2.66}$$

where $c_{ij} = \cos\theta_{ij}$, $s_{ij} = \sin\theta_{ij}$. If neutrinos are Dirac neutrinos, $\mathcal{P}$ is the identity matrix, and if neutrinos are Majorana particles, $\mathcal{P}$ is a diagonal matrix with two additional phases that do not affect neutrino oscillations. In Table 2.3, I list the

Parameter	Normal Hierarchy	Inverted Hierarchy
θ_{12} [°]	$33.56^{+0.77}_{-0.75}$	$33.56^{+0.77}_{-0.75}$
θ_{23} [°]	$41.6^{+1.5}_{-1.2}$	$50.0^{+1.1}_{-1.4}$
θ_{13} [°]	$8.46^{+0.15}_{-0.15}$	$8.49^{+0.15}_{-0.15}$
δ [°]	261^{+51}_{-59}	277^{+40}_{-46}
Δm^2_{21} [10^{-5} eV^2]	$7.50^{+0.19}_{-0.17}$	$7.50^{+0.19}_{-0.17}$
Δm^2_{3x} [10^{-3} eV^2]	$2.524^{+0.039}_{-0.040}$	$-2.514^{+0.038}_{-0.041}$

Table 2.1: **Neutrino Oscillation Parameters** from Esteban et al., 2017 based on an analysis of results from several experiments. θ_{ij} are the mixing angles, δ is the CP phase, and $\Delta m^2_{ij} = m^2_i - m^2_j$. In the final row, $x = 1$ for the normal hierarchy and $x = 2$ for the inverted hierarchy.

neutrino oscillation parameters from Esteban et al., 2017, who synthesize results from several experiments. Though experiments constrain the mass differences between neutrinos, they do not constrain the sign of the mass differences with the third mass eigenstate. Thus, the neutrino masses can be ordered as $m_1 < m_2 < m_3$ (Normal Hierarchy) or as $m_3 < m_1 < m_2$ (Inverted Hierarchy).

A neutrino state $|\nu(t)\rangle$ then evolves according to a Schrödinger-like equation

$$i\hbar\frac{d}{dt}|\nu(t)\rangle = \mathcal{H}|\nu(t)\rangle \,, \tag{2.67}$$

where $\mathcal{H} = \mathcal{H}_{\rm vac} + V$ is the Hamiltonian operator composed of a vacuum Hamiltonian $\mathcal{H}_{\rm vac}$ and an effective matter interaction potential V. The Hamiltonian can, of course, be transformed between the mass basis (m) and the flavor basis (f) as $\mathcal{H}^{(f)} = U\mathcal{H}^{(m)}U^\dagger$. Under the assumption that neutrinos are ultrarelativistic ($mc^2 \ll \epsilon$), the vacuum Hamiltonian is written in the mass basis as

$$\mathcal{H}^{(m)} \approx \epsilon + \frac{c^4}{2\epsilon}\text{diag}\left[m_1^2, m_2^2, m_3^2\right] \,. \tag{2.68}$$

In the flavor basis, the effective potentials resulting from interactions with matter are different for each species:

$$V^{(f)} = \text{diag}\left[V_e, V_\mu, V_\tau\right] \,. \tag{2.69}$$

The potentials depend in general on the density of nucleons, leptons, and their anti-particles, along with an integral over the phase-space density of all six neutrino

species and anti-species (see Duan, G. M. Fuller, and Qian, 2010 for a review and examples). The contribution to this potential from matter in astrophysical sources is predominantly due to interaction of electron anti/neutrinos with electrons and positrons (assuming a dearth of heavy leptons), known as the MSW potential (Wolfenstein, 1978). This yields a potential contribution in the form of

$$V_{\mathrm{MSW}}^{(f)} = \sqrt{2} G_F (n_{e^-} - n_{e^+}) \ , \tag{2.70}$$

where $G_f/(\hbar c)^3 = 1.1663787 \times 10^{-5}\,\mathrm{GeV}^{-2}$ is the Fermi coupling constant (Mohr, Newell, and Taylor, 2016). Given that neutrinos can also scatter off other neutrinos, we can apply the same process to neutrino-neutrino interactions that we did to neutrino-electron interactions for the MSW potential. This yields

$$V_{q,\mathrm{self}}^{(f)} = \sqrt{2} G_F \int \frac{d^3\mathbf{q}'}{(hc)^3} (\rho_{\mathbf{q}'} - \bar{\rho}_{\mathbf{q}'})(1 - \cos\theta_{qq'}) \ , \tag{2.71}$$

where q is the neutrino three-momentum, q' is the three-momentum of other neutrino species that is doing the scattering, and $\theta_{qq'}$ is the angle between the two momenta. $\rho_{q'}$ ($\bar{\rho}_{q'}$) is the density matrix of (anti-) neutrinos.

The probability of the neutrino being in a particular flavor eigenstate is

$$P_\alpha = |\langle \nu(t) | \nu_\alpha \rangle|^2 \ . \tag{2.72}$$

If we consider only vacuum oscillations between two neutrino flavors, the probability of transition from one flavor eigenstate to another can be simply written as

$$P(\nu_\alpha \to \nu_\beta) = \sin^2(2\theta_{ij}) \sin^2\left(2\pi \frac{x}{L_{ij}}\right) \ , \tag{2.73}$$

where the characteristic oscillation length is

$$L_{ij} = \frac{2ch\epsilon}{\Delta m_{ij}^2} = 2.5 \left(\frac{\epsilon}{\mathrm{MeV}}\right)\left(\frac{10^{-3}\mathrm{eV}^2}{c^4 \Delta m_{ij}^2}\right) \mathrm{km} \ . \tag{2.74}$$

Since heavy lepton neutrinos decouple from the fluid at a smaller radius than electron anti/neutrinos, their average energies are higher. If heavy lepton neutrinos oscillate into electron type neutrinos under the shock, the large cross section accompanying the higher energy could conceivably enhance the neutrino heating rate in CCSNe and help drive out the shock. The relative relevance of the MSW and self-induced components of the potential is roughly determined by the relative sizes of $n_{e^-} - n_{e^+}$ and $n_{\bar{\nu}_e} - n_{\bar{\nu}_x}$. In regions where the former dominates, neutrinos follow essentially

pure MSW oscillations (e.g., Esteban-Pretel et al. 2008). This is the case under a CCSN shock during the leptonization burst and the accretion phase for all but the smallest collapsing stars. Even with the help of MSW and self-induced potentials, the oscillation length is larger than the distance from the neutrinosphere to the shock radius, resulting in a small effect on the net heating rate under the shock of a few percent (e.g., Dasgupta, E. P. O'Connor, and Ott 2012). There are also possibilities of multi-dimensional multi-angle effects that could enhance the oscillation rates in non-spherical geometries (see Mirizzi et al., 2016 for a review), but the cost of high-dimensional calculations makes these effects only sparsely explored.

Neutrino oscillations can lead to strongly modified neutrino signals, such as the swapping of electron and heavy lepton neutrino spectra at certain energies. Though neutrino oscillations are unlikely to strongly affect the CCSN mechanism, matching observed neutrinos to model predictions could pin down uncertain neutrino physics like the neutrino mass hierarchy (e.g., Duan, G. M. Fuller, Carlson, et al. 2007). Due to the large excess of electron neutrinos, self-induced oscillations do not operate during the neutronization burst of CCSNe. In this phase, MSW effects are expected to cause some mixing of the electron and heavy lepton neutrino fluxes, depending on the neutrino mass hierarchy. Once the density outside the neutrinosphere becomes sufficiently low in the cooling phase of the CCSN (several hundred milliseconds after bounce), self-induced oscillations could result in collective oscillations that lead to similar spectral swapping between electron and heavy lepton neutrinos for certain energy ranges, depending on details like the angular distribution of neutrinos, thee-flavor effects (as reviewed by Mirizzi et al. 2016).

In CCSNe, neutrinos of all flavors and a wide range of energies are present in large quantities, making the evolution equations including self-induced oscillations nonlinear and integro-differential. Neutrino oscillations are generally modeled in CCSNe using a neutrino bulb model in which an inner boundary emits thermal neutrinos of each species at a specified luminosity and temperature. At each location, the neutrino density matrices are discretized in angle and energy and can be integrated out from an inner boundary. Ideally, one would perform time-dependent three-dimensional three-flavor simulations, but this is not currently possible with existing computer hardware and codes. In order to study the phenomenology of neutrino oscillations, common approximations include using a two-flavor neutrino system, simulating one or two spatial dimensions, assuming neutrinos move only radially inward or outward, and simulating a single neutrino energy (e.g., Chakraborty

Name	Model	Nuclei	Reference
LS180	CLD, Skyrme	SNA, CLD	Lattimer and Swesty (1991)
LS220	CLD, Skyrme	SNA, CLD	Lattimer and Swesty (1991)
LS375	CLD, Skyrme	SNA, CLD	Lattimer and Swesty (1991)
HShen	RMF, TM1	SNA, Thomas-Fermi Approx.	H. Shen et al. (1998ab, 2011)
HShenH	RMF, TM1, hyperons	SNA, Thomas-Fermi Approx.	H. Shen et al. (2011)
GShenNL3	RMF, NL3	Hartree Approx., Virial Expansion NSE	G. Shen et al. (2011a)
GShenFSU1.7	RMF, FSUGold	Hartree Approx., Virial Expansion NSE	G. Shen et al. (2011b)
GShenFSU2.1	RMF, FSUGold, stiffened	Hartree Approx., Virial Expansion NSE	G. Shen et al. (2011b)
HSTMA	RMF, TMA	NSE	Hempel et al. (2010, 2012)
HSTM1	RMF, TM1	NSE	Hempel et al. (2010, 2012)
HSFSG	RMF, FSUGold	NSE	Hempel et al. (2010, 2012)
HSNL3	RMF, NL3	NSE	Hempel et al. (2010, 2012)
HSDD2	RMF, DD2	NSE	Hempel et al. (2010, 2012)
HSIUF	RMF, IUF	NSE	Hempel et al. (2010, 2012)
SFHo	RMF, SFHo	NSE	Steiner et al. (2013)
SFHx	RMF, SFHx	NSE	Steiner et al. (2013)
BHBΛ	RMF, DD2-BHBΛ, hyperons	NSE	Banik et al. (2014)
BHBΛΦ	RMF, DD2-BHBΛΦ, hyperons	NSE	Banik et al. (2014)

Table 2.2: **Summary of the employed EOS.** Names of EOS in best agreement with the experimental and astrophysical constraints in Figure 2.1 are in bold font. For each EOS, I list the underlying model and interaction/parameter set, the handling of nuclei in nonuniform nuclear matter, and give the principal reference(s). I use CLD for "compressible liquid drop", RMF for "relativistic mean field", and SNA for "single nucleus approximation". I refer the reader to the individual references and to reviews (e.g., Oertel et al., 2017; J. M. Lattimer, 2012) for more details. Versions of the EOS in simulations should also include contributions from electrons, positrons, and photons.

et al. 2016).

These methods are used to explore the neutrino oscillation phenomenology, but a more realistic (and computationally more challenging) treatment is required for predictive CCSN simulations. It is worth emphasizing that neutrino oscillations are also outside of the standard model, and this phenomenological description bears inconsistencies with fundamental physical principles (e.g., Poincare invariance, Lobanov 2015). Though there are interesting hints from simplified calculations, the effect of neutrino oscillations on the neutrino signals from CCSNe is largely uncertain. For these reasons, neutrino oscillations are ignored throughout the rest of this thesis.

2.4 Nuclear Equations of State

There is substantial uncertainty in the behavior of matter at and above nuclear density, and as such, there are a large number of proposed nuclear EOS that describe the relationship between matter density, temperature, composition (i.e. electron fraction Y_e in nuclear statistical equilibrium [NSE]), and energy density and its derivatives. Properties of the EOS for uniform nuclear matter are often discussed in terms of a

power-series expansion of the binding energy per baryon E at temperature $T = 0$ around the nuclear saturation density n_s of symmetric matter ($Y_e = 0.5$) (e.g., J. M. Lattimer, Pethick, et al., 1985; Hempel, Fischer, et al., 2012; Oertel et al., 2017; J. M. Lattimer, 2012):

$$E(x, \beta) = -E_0 + \frac{K}{18}x^2 + \frac{K'}{162}x^3 + ... + \mathcal{S}(x, \beta) \ , \tag{2.75}$$

where $x = (n - n_s)/n_s$ for a nucleon number density n and $\beta = 2(0.5 - Y_e)$. The saturation density is defined as where $dE(x, \beta)/dx = 0$. The saturation number density $n_s \approx 0.16\,\mathrm{fm}^{-3}$ and the bulk binding energy of symmetric nuclear matter $E_0 \approx 16\,\mathrm{MeV}$ are well constrained from experiments (J. M. Lattimer, 2012; Oertel et al., 2017) and all EOS in this work have a reasonable value for both. K is the nuclear incompressibility, and its density derivative K' is referred to as the skewness parameter. All nuclear effects of changing Y_e away from 0.5 are contained in the symmetry term $\mathcal{S}(x, \beta)$, which is also expanded around symmetric matter as

$$\mathcal{S}(x, \beta) = \mathcal{S}_2(x)\beta^2 + \mathcal{S}_4(x)\beta^4 + ... \approx \mathcal{S}_2(x)\beta^2 \ . \tag{2.76}$$

There are only even orders in the expansion due to the charge invariance of the nuclear interaction. Coulomb effects do not come into play at densities above n_s, where protons and electrons are both uniformly distributed. The $\mathcal{S}_2$ term is dominant and I do not discuss the higher-order symmetry terms here (see J. M. Lattimer, Pethick, et al., 1985; J. M. Lattimer, 2012; Oertel et al., 2017). $\mathcal{S}_2(x)$ is itself expanded around saturation density as

$$\mathcal{S}_2(x) = \left(J + \frac{1}{3}Lx + ...\right) \ . \tag{2.77}$$

J corresponds to the symmetry term in the Bethe-Weizsäcker mass formula (Weizsäcker, 1935; Bethe and Bacher, 1936), so J is what the literature refers to as "the symmetry energy" at saturation density and L is the density derivative of the symmetry term.

It is important to note that none of the above parameters can alone describe the effects an EOS will have on a core collapse simulation. This can be seen, for example, from the definition of the pressure,

$$P(n, Y_e) = n^2 \frac{\partial E(n, Y_e)}{\partial n} \ , \tag{2.78}$$

which depends directly on K and the first derivative of $\mathcal{S}(n)$. Since the matter in core-collapse supernovae and neutron stars is very asymmetric ($Y_e \neq 0.5$), large values for J and L can imply a very stiff EOS even if K is not particularly large.

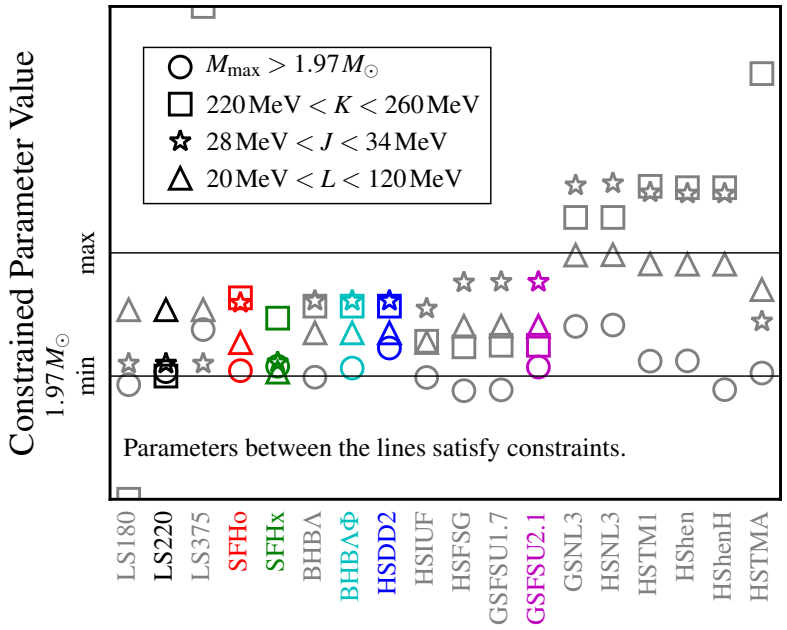

Figure 2.1: **EOS Constraints from experiment and NS mass measurements.** The maximum cold neutron star gravitational mass $M_{\max}$, the incompressibility K, symmetry energy J, and the derivative of the symmetry energy L are plotted. For $M_{\max}$, the bottom of the plot is 0, the min line is at $1.97\,M_\odot$, and the max line is not used. The other constraints are normalized so the listed minima and maxima lie on the min and max lines. EOS that are within all of these simple constraints are colored. Note that there are additional constraints on the NS mass-radius relationship, which I show in Figure 2.2, and joint constraints on J and L (Kolomeitsev et al., 2016) that I do not show.

The incompressibility K has been experimentally constrained to 240±10 MeV (Piekarewicz, 2010), though there is some model dependence in inferring this value, making an error bar of ±20 MeV more reasonable (Steiner, Hempel, and Fischer, 2013). A combination of experiments, theory, and observations of neutron stars suggest that $28\,\text{MeV} \lesssim J \lesssim 34\,\text{MeV}$ (e.g., Tsang et al., 2009). Several experiments place varying inconsistent constraints on L, but they all lie in the range of $20\,\text{MeV} \lesssim L \lesssim 120\,\text{MeV}$ (e.g., Carbone et al., 2010). K' and higher order parameters have yet to be constrained by experiment, though a study of correlations of these higher-order parameters to the low-order parameters (K, J, L) in theoretical EOS models provides some estimates Chen, 2011. Additional constraints on the combination of J and L have been proposed that rule out many of these EOS (most recently, Kolomeitsev et al., 2016). Finally, the mass of neutron star PSR J0348+0432 has been determined to be $2.01 \pm 0.04\,M_\odot$ (Antoniadis et al., 2013), which is the highest

well-constrained neutron star mass observed to date. Any realistic EOS model must be able to support a cold neutron star of at least this mass. Indirect measurements of neutron star radii further constrain the allowable mass-radius region (Nättilä et al., 2016).

I list 18 EOS in Table 2.2, but only SFHo (Steiner, Hempel, and Fischer, 2013; *Equation of state tables by Matthias Hempel* n.d.) appears to reasonably satisfy all current constraints (including the recent constraint proposed by Kolomeitsev et al., 2016). The others satisfy some, but not all, constraints.

Historically, the EOS of Lattimer & Swesty (J. M. Lattimer and Swesty, 1991; *Lattimer-Swesty EOS Webpage* n.d.) (hereafter LS; based on the compressible liquid drop model with a Skyrme interaction) and of H. Shen *et al.* (H. Shen et al., 1998a; H. Shen et al., 1998b; H. Shen et al., 2011; *H. Shen et al. EOS Tables* n.d.) (hereafter HShen; based on a relativistic mean field [RMF] model) have been the most extensively used in CCSN simulations. The LS EOS is available with incompressibilities K of 180, 220, and 375 MeV. There is also a version of the EOS of H. Shen *et al.* (HShenH) that includes effects of Λ hyperons, which tend to soften the EOS at high densities (H. Shen et al., 2011). Both the LS EOS and the HShen EOS treat nonuniform nuclear matter in the single-nucleus approximation (SNA). This means that they include neutrons, protons, alpha particles, and a single representative heavy nucleus with average mass $\bar{A}$ and charge $\bar{Z}$ number in NSE.

Recently, the number of nuclear EOS available for CCSN simulations has increased greatly. Hempel *et al.* (Hempel and Schaffner-Bielich, 2010; Hempel, Fischer, et al., 2012; *Equation of state tables by Matthias Hempel* n.d.) developed an EOS that relies on an RMF model for uniform nuclear matter and nucleons in nonuniform matter and consistently transitions to NSE with thousands of nuclei (with experimentally or theoretically determined properties) at low densities. Six RMF EOS by Hempel *et al.* (Hempel and Schaffner-Bielich, 2010; Hempel, Fischer, et al., 2012; *Equation of state tables by Matthias Hempel* n.d.) (hereafter HS) are available with different RMF parameter sets (TMA, TM1, FSU Gold, NL3, DD2, and IUF). Based on the Hempel model, the EOS by Steiner *et al.* (Steiner, Hempel, and Fischer, 2013; *Equation of state tables by Matthias Hempel* n.d.) require that experimental and observational constraints are satisfied. They fit the free parameters to the maximum likelihood neutron star mass-radius curve (SFHo) or minimize the radius of low-mass neutron stars while still satisfying all constraints known at the time (SFHx). SFH{o,x} differ from the other Hempel EOS only in the choice of RMF parameters.

The EOS by Banik *et al.* (Banik, Hempel, and Bandyopadhyay, 2014; *Equation of state tables by Matthias Hempel* n.d.) are based on the Hempel model and the RMF DD2 parameterization, but also include Λ hyperons with (BHB$\Lambda\phi$) and without (BHBΛ) repulsive hyperon-hyperon interactions.

The EOS by G. Shen *et al.* (G. Shen, Horowitz, and Teige, 2011; G. Shen, Horowitz, and E. O'Connor, 2011; *Equation of state tables by Gang Shen* n.d.) are also based on RMF theory with the NL3 and FSU Gold parameterizations. The GShenFSU2.1 EOS is stiffened at currently unconstrained super-nuclear densities to allow a maximum neutron star mass that agrees with observations. G. Shen *et al.* paid particular attention to the transition region between uniform and nonuniform nuclear matter where they carried out detailed Hartree calculations (G. Shen, Horowitz, and Teige, 2010a). At lower densities they employed an EOS based on a virial expansion that self-consistently treats nuclear force contributions to the thermodynamics and composition and includes nucleons and nuclei (G. Shen, Horowitz, and Teige, 2010b). It reduces to NSE at densities where the strong nuclear force has no influence on the EOS.

Few of these EOS obey all available experimental and observational constraints. In Figure 2.1 I show where each EOS lies within the uncertainties for experimental constraints on nuclear EOS parameters and the observational constraint on the maximum neutron star mass. I color the EOS that satisfy the constraints.

The mass-radius curves of zero-temperature neutron stars in neutrino-less β-equilibrium predicted by each EOS are shown in Figure 2.2. I mark the mass range for PSR J0348+0432 with a horizontal bar. I also include the 2σ semi-empirical mass-radius constraints of "model A" of Nätillä *et al.* (Nättilä et al., 2016). They were obtained via a Bayesian analysis of type-I X-ray burst observations. This analysis assumed a particular three-body quantum Monte Carlo EOS model near saturation density by Gandolfi, Carlson, and Reddy, 2012 and a parameterization of the super-nuclear EOS with a three-piece piecewise polytrope (Steiner, J. M. Lattimer, and E. F. Brown, 2013; Steiner, Gandolfi, et al., 2015). Similar constraints are available from other groups (see, e.g., Özel and Freire, 2016; Özel, Psaltis, et al., 2016; M. C. Miller and Lamb, 2016; Guillot and Rutledge, 2014).

Though more precise neutron star radius measurements would be useful to further constrain the nuclear EOS, the measurements are difficult and suffer from systematic errors or lack of data. These measurements include thermal emission from quiescent low-mass x-ray binaries, geodedic precession and advance of periastron in pulsars

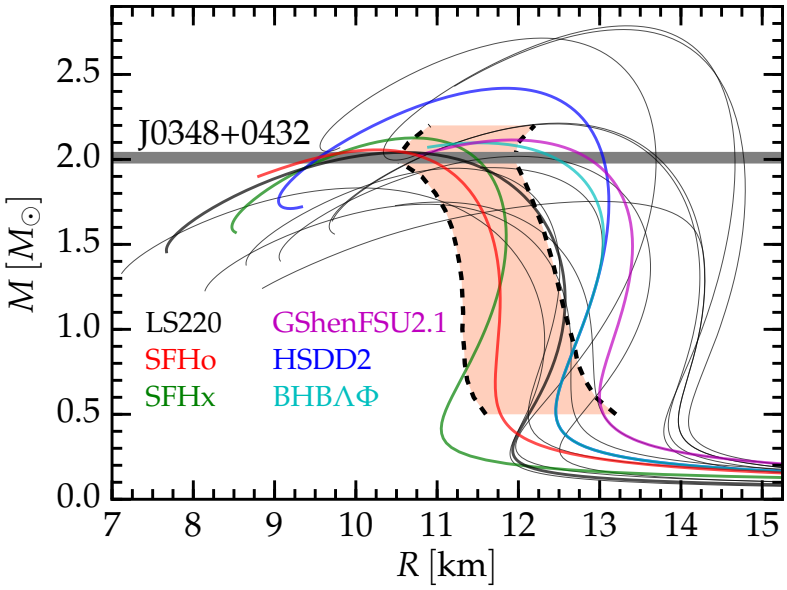

Figure 2.2: **Neutron star mass-radius relations**. The relationship between the gravitational mass and radius of a cold neutron star is plotted for each EOS. EOS that lie within the constraints depicted in Figure 2.1 are colored to match. I show the 2σ mass-radius constraints from "model A" of Nättilä et al., 2016 as a shaded region between two dashed lines. These constraints were obtained from a Bayesian analysis of observations of type-I X-ray bursts in combination with theoretical constraints on nuclear matter. The EOS that agree best with these constraints are SFHo, SFHx, and LS220.

in binary systems, pulsar pulse profiles, gravitational waves from merging neutron stars, the rotation rates of neutron stars, and the net energy released in neutrinos from CCSNe (see J. M. Lattimer and Prakash 2016 for a review). One popular method of simultaneously estimating a neutron star mass and radius is by comparing the luminosity and temperature from a photospheric radius expansion burst. In these bursts, a layer of nuclear fuel on the neutron star ignites with enough power to temporarily lift some of the matter off the neutron star surface. Since the luminosity during the burst exceeds the Eddington luminosity, a measurement of the bolometric flux during the burst relates the mass to the photospheric radius (van Paradijs, 1979; Özel, 2006; Özel, Psaltis, et al., 2016):

$$F_{\mathrm{Edd},\infty} = \frac{cGM}{D^2\kappa}\sqrt{1-\frac{2GM}{R_{\mathrm{phot}}c^2}}\,, \tag{2.79}$$

where R_{phot} is the photosphere radius, which should be equal to R when the matter touches back down. M is the mass of the neutron star, κ is the opacity, and D is the distance to the burst. Given measurements of D along with the bolometric flux F_∞

and the temperature $T_{c,\infty}$ as the burst decays (presumably after the matter touches back down), the angular area of the source is (J. M. Lattimer and Prakash, 2016)

$$A = \frac{F_\infty}{\sigma_B T_{c,\infty}^4} = \frac{1}{f_c^4}\left(\frac{R_\infty}{D}\right)^2 . \tag{2.80}$$

The temperature is deduced from the spectral shape, and nonthermal spectral features are assumed to be known and accounted for by a theoretically estimated f_c. The κ is also determined by theory and $R_\infty = R/\sqrt{2GM/(Rc^2)}$ due to general relativistic effects.

There are a variety of systematic uncertainties due to the model dependence of the derived neutron star properties. For instance, assuming that the photospheric radius is equal to the neutron star radius after the material has landed back on the neutron star leads to inconsistent results, since the photosphere at this point is significantly above the neutron star surface (Steiner, J. M. Lattimer, and E. F. Brown, 2010). The radius constraints plotted in Figure 2.2 come from a modified version of this approach, which makes use of information from the full cooling tail (rather than one discrete point in time) of passive bursts (so there is little uncertainty in the photospheric radius). This approach provides self-consistent results with greater accuracy (Nättilä et al., 2016).

Chapter 3

SEDONU: TIME INDEPENDENT MONTE CARLO NEUTRINO TRANSPORT

Sedonu calculates the steady-state radiative transfer solution for classical neutrinos assuming a fixed fluid background. It is designed to be modular in order to accommodate data structures of any geometry and hopefully enable verification for many neutrino transport codes. Though time-dependent neutrino transport codes exist (e.g., E. Abdikamalov, Burrows, et al. 2012), I made the choice to keep Sedonu's design centered in time-independent radiation transport because of the immensely smaller amount of resources required. Sedonu originates from a version of the photon Monte Carlo (MC) radiation transport code Sedona (Kasen, Thomas, and Nugent, 2006), which I reworked into a neutrino transport code by incorporating neutrino opacities and emissivities from NuLib (E. O'Connor, 2015). I also rewrote and modularized many of the data structures, and the code remains under active development.

In MC radiation transport, the radiation field is discretized into discrete energy packets. In each packet is stored the current location, the single-neutrino four-momentum, the neutrino species, and packet energy E_p denoting how much radiation energy the packet represents. Each of these packets is evolved like an individual neutrino (including motion, absorption, and scattering), and the packet's contribution to fluid heating and leptonization and to the energy- and angle-dependent radiation field is tallied as the packet moves around. The results of many such packet evolutions are then noisy statistical samples of the radiation field behavior. The high cost of MC radiation transport comes from simulating a large number of packets to reduce the noise in the statistical sample. I describe the basis for each element in the code in the following sections, following a brief discussion of random number generation and variance reduction. I present the method in a general relativistic formalism, though Sedonu currently only has special relativistic functionality implemented. However, I designed the infrastructure to extend to the general relativistic version in the future with relative ease.

Random Number Generation

Fundamental to any Monte Carlo method is the ability to generate random numbers with the appropriate probability density function (PDF). Using the method of inverse transform sampling (e.g., Haghighat 2015), it is possible to generate any distribution either analytically or discretely. If we require a random number X with probability density function (PDF) $p(x)$ such that $\int p(x)dx = 1$, we can find the cumulative distribution function (CDF)

$$P(x) = \int_{-\infty}^{x} p(x')dx' \ . \tag{3.1}$$

If $P(x)$ is analytically invertible, we can sample x using

$$X = P^{-1}(U) \ , \tag{3.2}$$

where U is a uniform random number between 0 and 1. If $P(x)$ is not analytically invertible, approximate inversion can be performed numerically. To do this, one must evaluate $P(x_i)$ at a set of discrete points x_i. Since $P(x)$ increases monotonically with x, there is a unique pair $\{P_k, P_{k+1}\}$ at $\{x_k, x_{k+1}\}$ that bracket U. An interpolated function $\widetilde{P}(x)$ can then be defined and inverted. The simplest such interpolation is piecewise constant interpolation:

$$X = \frac{(x_k + x_{k+1})}{2} \ . \tag{3.3}$$

A second choice is linear interpolation:

$$X = x_k + \frac{x_{k+1} - x_k}{P_{k+1} - P_k}(U - P_k) \ . \tag{3.4}$$

A third choice is, cubic interpolation. However, though constant and linear interpolation ensure that the CDF is monotonically increasing given monotonic inputs P_k, standard cubic interpolation does not. Cubic monotone interpolation must be used

to ensure the monotonicity of $P(x)$:

$$
\begin{aligned}
X &= x_k h_{00}(t) + x_{k+1} h_{01}(t) + (P_{k+1} - P_k)\left[m_k h_{10}(t) + m_{k+1} h_{11}(t)\right] \ , \\
m_k &= \begin{cases} \widetilde{m}_k & \alpha^2 + \beta^2 \leq 3^2 \\ \tau_k \alpha_k \Delta_k & \alpha^2 + \beta^2 > 3^2 \end{cases} \qquad m_{k+1} = \begin{cases} \widetilde{m}_{k+1} & \alpha^2 + \beta^2 \leq 3^2 \\ \tau_k \beta_k \Delta_k & \alpha^2 + \beta^2 > 3^2 \end{cases} \\
\widetilde{m}_k &= \begin{cases} \Delta_k & k = 0, k = N \\ \frac{\Delta_{k-1} + \Delta_k}{2} & \text{otherwise} \end{cases} \\
\tau_k &= \frac{3}{\sqrt{\alpha_k^2 + \beta_k^2}} \\
\alpha_k &= \frac{\widetilde{m}_k}{\Delta_k} \qquad \beta_k = \frac{\widetilde{m}_{k+1}}{\Delta_k} \\
\Delta_k &= \frac{x_{k+1} - x_k}{P_{k+1} - P_k} \\
t &= \frac{U - P_k}{P_{k+1} - P_k} \ .
\end{aligned}
\tag{3.5}
$$

All three of these are implemented as options in Sedonu.

Variance Reduction

The expectation value of any quantity $Q(x)$ if x has a PDF $p(x)$ is

$$\langle Q \rangle = \int Q(x) p(x) dx \ . \tag{3.6}$$

The variance of the quantity is $V(Q) = \langle Q^2 \rangle - \langle Q \rangle^2$. The variance is the source of noise in the Monte Carlo results, so if the average quantity $\langle Q \rangle$ is to be determined, many MC packets must be simulated until the variance of the mean $V(\langle Q \rangle) = V(Q)/\sqrt{N}$ is sufficiently small. We can define an arbitrary *biased* PDF $\widetilde{p}(x)$ using

$$p(x) = w(x)\widetilde{p}(x) \ , \tag{3.7}$$

where $w(x)$ is the factor by which the statistical weight (in our case, packet energy) of the packet is multiplied after sampling a random number X from $\widetilde{p}(x)$. As long as Equation 3.7 is true and $w(x)$ is non-singular, $\langle Q \rangle$ remains unchanged. Thus, it is in principle possible to arbitrarily define a $w(x)$ and $\widetilde{p}(x)$ that reduce $V(Q)$ (and thus $V(\langle Q \rangle)$) without having to simulate additional packets. However, care must be taken so numerical issues do not arise. If $w(x)$ is large and the distribution function is sampled many times, the packet weight can quickly exceed the capabilities of numerical precision. For example, one might think to bias the path length of a

packet in an optically deep region to larger values to help it escape more easily. However, this transformation involves and exponential weight, and if the packet samples a path length too many times (depending on how strongly the path length is biased), underflow results. In addition, care must be taken to ensure that the full range of the PDF is adequately sampled. If a PDF is biased so strongly that a part of the distribution function is so rare that it is never actually sampled, this is equivalent to setting that part of the PDF to zero, which violates the requirement for w(x) to be non-singular.

3.1 Neutrino Emission

Just as real neutrinos are emitted from fluid at random locations, with random directions, and with random energies, Sedonu must emit neutrino packets that represent this random behavior with the correct PDFs. In this thesis, neutrino reaction rates are obtained either from the NuLib library (as in Chapter 4) or from the code of Nagakura, Iwakami, Furusawa, Sumiyoshi, et al., 2017 (as in Chapter 5).

Packet Energy

Neutrinos are either emitted from the fluid itself, or from an off-grid source like a central hypermassive neutron star. The neutrinos emitted from a central source are given an isotropically random position on the inner boundary sphere and an isotropically random direction within the outward 2π steradians. Neutrino energies are sampled from a Fermi-Dirac blackbody distribution of a given temperature and chemical potential. Emission from a central object is considered only in Chapter 4.

Within each cell and in the fluid rest frame, the direction and position distribution of spawned neutrinos are isotropically randomly determined. Angle-dependent Fermi blocking could be incorporated via rejection sampling in the future. The net comoving luminosity of a grid cell is determined by numerically integrating the emissivity

$$\mathcal{L}_{\text{cell}} = 4\pi V \sum_{\text{species}} \sum_{i} \eta_i \ , \tag{3.8}$$

where V is the grid cell volume. The bin energy-integrated emissivities are

$$\eta_k = \int_{\epsilon_{k-1/2}}^{\epsilon_{k+1/2}} j(\epsilon) \ , \tag{3.9}$$

where $j(\epsilon)$ is the spectral emissivity (units of erg cm^{-3} s^{-1} MeV^{-1}), and $\epsilon_{k+1/2}$ and $\epsilon_{k-1/2}$ are the upper and lower interfaces of energy bin k, respectively.

In the *emit by energy* model, I emphasize increasing the statistics of the fluid interaction rates by simulating fewer neutrino packets in energy ranges that have little impact on the fluid. Each emitted neutrino packet in a given grid cell has the same packet energy, determined by

$$E_p = \frac{\mathcal{L}_{\text{cell}} \Delta t}{P_{\text{emit}}} \ , \tag{3.10}$$

where Δt is the length of the time step (arbitrary for steady-state calculations like these, as it always cancels out). P_{emit} is the number of neutrino packets to be emitted from the grid cell and is proportional to the cell's neutrino energy emission rate according to

$$P_{\text{emit}} = P_{\text{total}} \frac{\mathcal{L}_{\text{cell}}}{\Sigma_{\text{cells}} \mathcal{L}_{\text{cell}}} \ , \tag{3.11}$$

where P_{total} is the total number of neutrino packets used in the simulation. Though each cell has a different velocity and hence the lab-frame emissivities are modified, Equation 3.11 is used only to distribute computational resources through the disk and has no physical meaning. I use the emit by energy model in Chapter 4.

In the *emit by bin* model, I emphasize improving the statistics of the radiation field uniformly across all energy bins. In this method, the same number N of neutrinos are emitted from each energy bin i in each grid zone and are given packet energy energy

$$E_p = \frac{\eta_i V \Delta t}{N} \ . \tag{3.12}$$

I use the emit by bin model in Chapter 5.

Packet Location

Fluid properties are assumed to be constant within a grid cell, so neutrinos are emitted at uniformly random locations within each cell. For Cartesian coordinates, this is simply

$$X_i = x_i + U(x_{i+1} - x_i) \ . \tag{3.13}$$

However, for a general coordinate system, the three-dimensional probability density for an emission at coordinate location $\mathbf{q}$ is

$$p(q_1, q_2, q_3) = \frac{\sqrt{\gamma}}{\int dV} \ , \tag{3.14}$$

where the volume element is $dV = \sqrt{\gamma} dq_1 dq_2 dq_3$ and γ is the determinant of the 3-metric. If the coordinates are approximately orthogonal, we can approximate the

three-dimensional probability density function as three one-dimensional probability density functions:

$$\begin{aligned} p(q_1) &= \int dq_2 dq_3 p(q_1, q_2, q_3) \ , \\ p(q_2) &= \int dq_1 dq_3 p(q_1, q_2, q_3) \ , \\ p(q_3) &= \int dq_1 dq_2 p(q_1, q_2, q_3) \ . \end{aligned} \tag{3.15}$$

In spherical-polar coordinates in flat spacetime, for example, $\sqrt{\gamma} = r^2$ using the radius r, the cosine of the polar angle μ, and the azimuthal angle ϕ as coordinates. Within a volume defined by coordinate ranges $\{\Delta r, \Delta\mu, \Delta\phi$ and coordinate lower bounds $\{r_0, \mu_0, \phi_0\}$, this comes out to

$$\begin{aligned} p(r) &= \frac{3r^2}{\Delta(r^3)} & R &= \left[r_0^3 + U\Delta\left(r^3\right)\right]^{1/3} \ , \\ p(\mu) &= \frac{1}{\Delta\mu} & M &= \mu_0 + U\Delta\mu \ , \\ p(\phi) &= \frac{1}{\Delta\phi} & P &= \phi_0 + U\Delta\phi \ , \end{aligned} \tag{3.16}$$

where R is a random value of r, M is a random value of μ, and P is a random value of ϕ.

Neutrino Energy

Given a spectral emissivity $j(\epsilon)$ (units of $\mathrm{erg\,cm^{-3}\,s^{-1}\,MeV^{-1}}$), the probability density function for the neutrino energy ϵ is

$$p(\epsilon) = \frac{j(\epsilon)}{\int d\epsilon j(\epsilon)} \ . \tag{3.17}$$

Since the emissivity $j(\epsilon)$ is not necessarily a simple function, we must use numerical inverse transform sampling. The CDF points are defined by the recursive relation

$$\begin{aligned} P_0 &= \eta_0 \\ P_k &= P_{k-1} + \frac{\eta_k}{\sum_k \eta_k} \ . \end{aligned} \tag{3.18}$$

Standard inverse transform sampling can then be performed using these P_k and bin central energies ϵ_k.

Packet Direction

The packet direction is chosen isotropically in a comoving orthonormal tetrad. Since the neutrino momentum properties are always expressed in Cartesian coordinates, a

convenient way to do this is to choose a normal direction 3-vector according to

$$\begin{aligned} \mathbf{D} &= 2\mathbf{U} - 1 \ , \\ \mathbf{D} &\leftarrow \mathbf{D}/D \ , \end{aligned} \tag{3.19}$$

where where $D = \sqrt{\mathbf{D} \cdot \mathbf{D}}$, $\mathbf{U}$ is a vector of three independent uniform random numbers between 0 and 1, and the arrow represents numerical variable assignment rather than a mathematical identity. Given a neutrino energy ϵ, the comoving orthonormal tetrad neutrino four momentum is

$$\widetilde{p}^{\alpha} = \frac{\epsilon}{c}(1, \mathbf{D}) \ . \tag{3.20}$$

The packet is then transformed into the comoving coordinate frame using the tetrad basis vectors $\widetilde{\mathbf{e}}_{(\alpha)}$ as $p^{\alpha} = \widetilde{e}^{\alpha}_{(\beta)} \widetilde{p}^{(\beta)}$. The neutrino can then be Lorentz transformed into the lab frame using Equation 2.11. The packet energy is also transformed between frames according to

$$\frac{E_{p,\mathrm{com}}}{-p^{\alpha} u_{\alpha}} = \frac{E_{p,\mathrm{lab}}}{-p^{\alpha} n_{\alpha}} \ . \tag{3.21}$$

3.2 Neutrino Propagation

The neutrino trajectory is composed of a series of small steps along geodesics (Equation 2.59). The distance the packet moves during each step is $d = \max(\min(d_{\mathrm{interact}}, d_{\mathrm{boundary}}), \chi d_{\mathrm{min}})$, where d_{boundary} is the (non-directional) distance to the nearest grid zone boundary. In order to prevent packets from getting trapped at a single location, the step size is thus always at least χd_{min}, where d_{min} is the current grid cell's smallest dimension and $\chi \ll 1$ is a parameter.

The distance a packet is allowed to move before interacting is $d_{\mathrm{interact}} = \tau/\sigma$, where σ is the transport opacity, which can be either the scattering opacity or the total opacity, depending on the interaction model. Immediately after packet creation or any interaction event, the optical depth τ through which the packet will traverse before the next fluid interaction is chosen randomly according to the probability distribution function $p(\tau)$:

$$\begin{aligned} p(\tau) &= e^{-\tau} \ , \\ T &= -\ln U \ , \end{aligned} \tag{3.22}$$

where T is the sampled value of τ. After each step, the stored value of τ is decreased by $d\sigma$. The distances and opacities can be transformed between frames using the fact that $p^{\alpha} u_{\alpha} \sigma$ and $d\sigma$ are Lorentz invariants.

After each step, the neutrino contributes $E_p d$ to the current grid zone's neutrino distribution function. For an *angular* distribution function, the energy goes into an angle-energy bin corresponding to its direction and energy. For a *native moment* bin, the energy, scaled by dot products indicated by each moment index, goes into a moment-energy bin. For example, for the second moment P^{ij}, the energy accumulated into each moment bin is $E_p d(\mathbf{D} \cdot \mathbf{e}_{(i)})(\mathbf{D} \cdot \mathbf{e}_{(j)})$. At the end of the calculation, the cell energy density can be calculated as

$$E = \frac{\sum_{\text{steps}} E_{\text{dep}}}{c\Delta t V} \ . \tag{3.23}$$

3.3 Scattering and Absorption

In order to reduce noise, absorption is treated continuously in one of two ways. In the first, which I call *exponential decay*, the fluid thermal energy is increased after each step by $E_p[1-\exp(-\sigma_a d)]$ and the packet energy is reduced to $E_p \leftarrow E_p \exp(-\sigma_a d)$. In this case, the transport opacity σ in Section 3.2 is the scattering opacity σ_s. When the packet scatters, the change in its energy is set only by inelastic scattering processes. In this way, scattering determines the rate at which scattering events occur, while absorption simply continuously decreases the packet energy. This effectively describes a packet of neutrinos that are absorbed continuously, but the entire packet is scattered at discrete events.

In the second, which I call *discrete absorption*, the fluid thermal energy is increased by $E_p \sigma_a d$ after each step, but the packet energy is not continuously changed. When an interaction event occurs, the packet energy is reduced to $E_p \sigma_s/(\sigma_a + \sigma_s)$. The transport opacity σ in Section 3.2 is then the total opacity $\sigma_a + \sigma_s$. This effectively describes a packet of neutrinos that undergoes both scattering and absorption in discrete events. Irrespective of which of the three above distances was smallest, the neutrino packet deposits thermal energy continuously into the grid cells it passes through according to $E_{\text{dep}} = E_p \sigma_a d$ and lepton number according to $N_{\text{dep}} = l E_{\text{dep}}/E_\nu$, evaluated in the comoving frame, where $l = 1$ for ν_e, $l = -1$ for $\bar{\nu}_e$, and $l = 0$ for ν_x. Though these quantities may be more or less than the actual packet energy and lepton number, depending on whether the packet moves more than or less than one optical depth, energy and lepton number conservation are well approximated when averaging over many packets. See the code tests below for a test of this algorithm.

When neutrinos scatter, the PDF for a neutrino to be deflected by $\mu = \mathbf{D} \cdot \mathbf{D}'$, where

D and **D′** are the initial and final directions in the comoving frame, respectively, is

$$p(\mu) = \frac{\int_0^\infty d\epsilon' R(\epsilon, \epsilon', \mu)}{\int d\epsilon' \int d\mu R_{\text{scat}}(\epsilon, \epsilon', \mu)} \ . \tag{3.24}$$

This can be inverted via numerical inverse transform sampling for a general scattering kernel. Given this scattering angle, the final energy of the neutrino can be sampled from the probability density function

$$p(\epsilon'|\mu) = \frac{R(\epsilon, \epsilon', \mu)}{\int d\mu R(\epsilon, \epsilon', \mu)} \ . \tag{3.25}$$

If the scattering is approximated as isotropic and elastic, a new direction can instead simply be chosen the same way as in Equation 3.19.

Monte Carlo Random Walk Approximation

In regions where the scattering optical depth $\tau_s = \sigma_s l$ is large, where l is the relevant length scale, direct Monte Carlo radiation transport becomes very inefficient. The path length between scattering events is very small, so a great deal of computer time is spent performing these scattering events while there is little actual movement of energy and lepton number. In these regions, the neutrino transport is very well approximated as a diffusion process, a fact which I use to accelerate the computation.

In the past, Monte Carlo neutrino transport schemes have excluded the inner regions of high optical depth in favor of an inner boundary condition (H.-T. Janka, 1991) or have employed the discrete diffusion Monte Carlo approximation in these regions (Densmore et al., 2007; E. Abdikamalov, Burrows, et al., 2012). In order to keep the neutrino motion free of any specific grid geometry and to prevent a hard spatial boundary between two algorithms, I instead choose to implement the Monte Carlo random walk approximation (J.A Fleck and Canfield, 1984). This treats neutrino motion over a specified distance as a diffusive process, and relies on the assumption of isotropic, elastic scattering. In our implementation, I also assume the fluid is unchanging in space and in time during each diffusion step. Here I modify the method of J.A Fleck and Canfield, 1984 to treat static fluid backgrounds with relativistic fluid velocities.

The approximation accelerates Monte Carlo transport in regions of high scattering optical depth using a solution to the diffusion equation:

$$\partial_t \psi(\mathbf{r}, t) = D\nabla^2 \psi(\mathbf{r}, t) \ . \tag{3.26}$$

In the context of Monte Carlo radiation transport, the solution $\psi(\mathbf{r}, t)$ represents the probability density of the neutrino being at location $\mathbf{r}$ at time t. The first order of business is to determine the diffusion constant D based on the local neutrino opacity. To do this, we compute the solution to the evolution of neutrino field that is initially a delta function in space $\psi(\mathbf{r}, 0) = \delta^3(\mathbf{r})$ in an infinite, uniform medium. It can be easily verified that the solution is

$$\psi(\mathbf{r}, t) = (4\pi Dt) \exp[1 - r^2/4Dt] \ . \tag{3.27}$$

Next, we solve the same problem in the context of a random walk. The probability that a neutrino moves a distance in the range $(x, x+dx)$ between scatters is $f(x)dx = \sigma_s \exp[-\sigma_s x]dx$. Using this, we can calculate the following moments and an expectation value for the net displacement after N scatters $r(N)$:

$$\begin{aligned} \langle x \rangle &= \int_0^\infty x f(x) dx = \sigma_s^{-1} \\ \langle x^2 \rangle &= \int_0^\infty x^2 f(x) dx = 2\sigma_s^{-2} \\ \langle r^2(N) \rangle &= \sum_{i=1}^{N} \sum_{j=1}^{N} \langle \mathbf{x}_i \cdot \mathbf{x}_j \rangle = N \langle x^2 \rangle \ . \end{aligned} \tag{3.28}$$

In the last equation, I used the assumption that each scatter is isotropic, implying that $\langle x_i \cdot x_j \rangle = 0$ if $i \neq j$. This also implicitly assumes elastic scattering, since we assume the opacity remains constant after any number of scatters. derived the probability density function for the net displacement after N steps

$$\psi(r, N) = \frac{2\pi}{3} N \langle x^2 \rangle \exp\left[\frac{-3r^2}{2N\langle x^2 \rangle}\right] \ . \tag{3.29}$$

Comparing this to Equation 3.27 and noting that $t = N\langle x \rangle / c$ demonstrates that $D = c/3\sigma_s$.

Using the diffusion equation with this diffusion constant, we now specify a sphere of radius R in the comoving frame and derive the probability that a neutrino has escaped from the sphere after a certain time t. To do this, we again solve the diffusion equation, but this time with the boundary condition $\psi(R, t) = 0$ to indicate that we are interested only in the *first* time a neutrino leaves the sphere and we do not allow neutrinos to leave and then re-enter the sphere. This can be solved via separation of variables and Sturm-Liouville orthogonality conditions to arrive at

$$\psi(r, t > 0) = \sum_{n=1}^{\infty} \frac{n}{2R^2} \frac{\sin(n\pi r/R)}{r} \exp\left[-\left(\frac{n\pi}{R}\right)^2 Dt\right] \ . \tag{3.30}$$

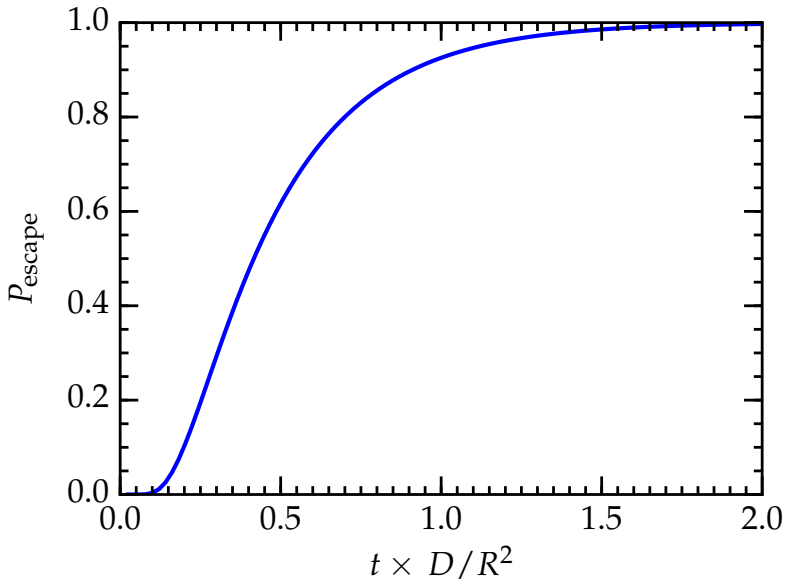

Figure 3.1: **Monte Carlo random walk escape probability:** Probability of escape from a sphere of radius R and diffusion constant D after time t (Equation 3.31). Inverse transform sampling is applied to this function to randomly sample the time it takes a neutrino to reach the edge of a diffusion sphere in the Monte Carlo random walk approximation.

The probability that a neutrino has escaped the sphere after time t is represented by the volume integral of the diffusion solution (Figure 3.1):

$$\begin{aligned} P_{\text{escape}}(R, t > 0) &= 1 - \int_0^R \psi(r,t) 4\pi r^2 dr \\ &= 1 - 2\sum_{n=1}^{\infty} (-1)^{n-1} \exp\left[-\left(\frac{n\pi}{R}\right)^2 Dt \right] . \end{aligned} \tag{3.31}$$

This solution is plotted in Figure 3.1.

The diffusion equation is acausal in that there is a finite probability of a neutrino escaping at times less than the light travel time to the edge of the sphere. Because of this, we set $P_{\text{escape}}(R, t < R/c) = 0$. We can also use the escape probability at $t = R/c$ as an estimate of the accuracy of the approximation. I only use the random walk approximation when

$$P_{\text{escape}}(R, R/c) < tol \ . \tag{3.32}$$

I use $tol = 10^{-3}$ for most applications, which corresponds to only using the random walk approximation when the scattering optical depth of the sphere is $\sigma_s R \geq 12$.

I tabulate $P_{\rm escape}(R,t)$, which can then be inverted via inverse transform sampling to randomly sample the escape time $t_{\rm esc}$. The table extends over the range of $0 \leq \chi \leq \chi_{\rm max}$ using 100 evenly spaced points in χ where $\chi = Dt/R^2$ and, in our calculations, $\chi_{\rm max} = 2$ (corresponding to $P_{\rm escape} = 0.997$). I evaluate the first 1000 terms in the sum in Equation 3.31, which is far more than is necessary for a converged solution, but tabulating $P_{\rm escape}$ is a very cheap one-time calculation.

I restrict the lab-frame radius of the sphere $R_{\rm lab}$ to the largest length scale between (a) the distance to the nearest grid cell boundary and (b) 1% of the grid cell's smallest dimension. However, since the sphere is defined in the fluid rest frame, its size must be further limited when the fluid is moving, since the sphere is effectively advected. The largest restriction occurs in the event that the displacement of the neutrino from its starting position to the surface of the sphere is parallel to the fluid velocity, so we will use this worst-case scenario to set the sphere size limiter. The four-vector $d_{\rm com} = \{t, \mathbf{R}\}$ connecting the neutrino's initial and final positions in the lab frame can be Lorentz-transformed to give the displacement vector in the lab frame $d_{\rm lab} = \{\gamma(t + vR/c^2), \gamma(\mathbf{R} + \mathbf{v}t)\}$. The longest diffusion time the numerical scheme will allow is $t_{\rm max} = R^2\chi_{\rm max}/D$, resulting in a maximum lab-frame displacement of $R_{\rm lab,max} = \gamma R(1 + Rv\chi_{\rm max}/D)$. Inverting this, we set the comoving-frame radius to

$$R = \frac{2R_{\rm lab}}{\gamma}\left(1 + \sqrt{1 + \frac{4R_{\rm lab}v\chi_{\rm max}}{\gamma D}}\right)^{-1} . \tag{3.33}$$

The comoving frame neutrino frequency remains the same throughout the process, since the scattering is assumed to be elastic. Absorption happens continuously throughout the diffusion process. The packet energy is decreased according to

$$E_p(t) = E_p(0)\exp[-\sigma_a ct] , \tag{3.34}$$

and $E_p(0) - E_p(t)$ is added to the fluid energy to account for neutrino absorption. The comoving frame packet energy averaged over the diffusion time is

$$\begin{aligned} \bar{E}_p &= \frac{1}{t}\int_0^t E_{p,0}e^{-\sigma_a ct'}dt' \\ &= \frac{E_{p,0}}{ct\sigma_a}\left(1 - e^{-\sigma_a ct}\right) . \end{aligned} \tag{3.35}$$

If neutrino packets are created assuming the fluid emits for a time of $\delta t_{\rm emit}$, this means that the neutrino contributes $\bar{E}_p t/\delta t_{\rm emit}$ to the fluid cell's steady-state radiation energy content. Averaged over the diffusion process, most of the neutrino energy is

distributed isotropically in direction. However, there is a small asymmetry due to the fact that the neutrino ends up at one point on the edge of the diffusion sphere. Averaged over the duration of the diffusion process, for a neutrino packet with energy E_p, there is a net energy flux of $E_p R/ct$ in the direction of the final displacement vector while $E_p(ct - R)/ct$ is distributed isotropically in direction.

With the theoretical groundwork complete, I now describe the random walk algorithm itself. A comoving frame diffusion sphere size R is first chosen according to Equation 3.33. If the scattering optical depth $\sigma_s R$ is sufficiently large (Equation 3.32), the time the neutrino takes to reach the edge of the sphere t is sampled from Equation 3.31. A location at the edge of the comoving-frame sphere is randomly uniformly chosen, the displacement 4-vector $\{t, \mathbf{R}\}$ is Lorentz transformed into the lab frame, and the neutrino is moved this distance. The new comoving neutrino direction is chosen uniformly in the 2π steradians moving strictly away from the diffusion sphere. The neutrino packet energy is decreased due to absorption according to Equation 3.34 and the absorbed energy is counted toward fluid heating. Comoving radiation energy in the amount of $\bar{E}_p R/c\delta t_{\rm emit}$ moving in the direction of the final displacement is Lorentz transformed into the lab frame and accumulated into the distribution function. The remaining $\bar{E}_p(ct - R)/c\delta t_{\rm emit}$ of comoving radiation energy is divided evenly into N pieces, each is assigned an isotropically uniform random direction in the comoving frame, is Lorentz transformed into the lab frame, and is accumulated into the distribution function. This allows us to self-consistently treat both the isotropic and directional components of the radiation field without making reference to a particular grid structure. I find that $N = 10$ is a reasonable compromise between code performance and noise in the resulting radiation field.

3.4 Equilibrium

After all packets have propagated through the fluid and have left a tally of how much energy and lepton number they deposited in each cell, we can determine what combination of $\{T, Y_e\}$ causes the fluid in each cell to emit the same amount of energy and as many leptons as it absorbed. The equilibrium T and/or Y_e is converged upon using Brent's method (Brent, 1973), which queries the emission rates at successive guesses of $\{T, Y_e\}$ until the integrated emissivities (both energy and lepton number) match the absorption rates calculated during the MC transport. The equilibrium values are physically sensible quantities only where the timescales for such an equilibrium to be reached are short compared with the dynamical timescale. The process of transporting neutrinos and solving for equilibrium can be done iteratively,

allowing temperature and electron fraction changes to affect the neutrino sources, until a truly time-independent equilibrium is reached, as is done in the irradiation tests in the code tests below.

3.5 Code Tests

I perform a pair of related tests to ensure that our transport and equilibrium finding methods arrive at the correct answer. In the first test, I demonstrate that Sedonu is able to recover a blackbody distribution function at high optical depth. In the second, I demonstrate that our equilibrium solver settles to the correct values of temperature and electron fraction.

Blackbody Generation

In this test I use a single unit-volume fluid cell with periodic boundary conditions. I give the cell a density, temperature, and electron fraction, and observe the resulting neutrino radiation that builds up within the cell, similar to Tubbs, 1978. The neutrinos should settle into a Fermi blackbody distribution given by

$$B_\epsilon(\mu, T) = \frac{\epsilon^3/h^3c^2}{e^{(\epsilon-\mu)/kT}+1} \tag{3.36}$$

in CGS units of erg $s^{-1}cm^{-2}MeV^{-1}sr^{-1}$, μ is the neutrino chemical potential, and T is the fluid temperature. This is identical to the photon blackbody, with two exceptions: the sign in the denominator originating from the Fermi-Dirac distribution, and the lack of a factor of 2 in the numerator because there is only a only left-handed neutrino polarization. Integrating over neutrino energy and angle gives the blackbody energy density

$$E = \frac{4\pi}{c}\int_0^\infty B_\epsilon(\mu, T)\, d\epsilon = \frac{4\pi}{(hc)^3}\mathcal{F}_3(\mu)\ , \tag{3.37}$$

where

$$\mathcal{F}_n(\mu) = \int_0^\infty \frac{\epsilon^n\, d\epsilon}{e^{(\epsilon-\mu)/kT}+1} \tag{3.38}$$

are Fermi integrals of order n. In the special case of $\mu = 0$, this has a simple analytic solution akin to the Stefan-Boltzmann law,

$$E = \frac{7\pi^5(kT)^4}{30(hc)^3}\ . \tag{3.39}$$

I let the fluid emit neutrinos and allow them to propagate until they are absorbed and compare the resulting neutrino energy density to Equation 3.37. We expect the net energy density to be the sum of contributions from each of the 6 neutrino species,

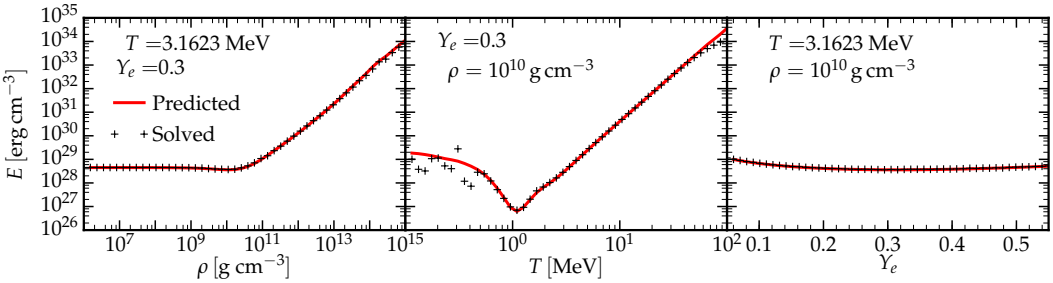

Figure 3.2: **Blackbody generation test:** The equilibrium total neutrino energy density ϵ_ν as a function of fluid density ρ, temperature T, and electron fraction Y_e. The fluid variables are varied around $\rho = 10^{10}\,\mathrm{g\,cm^{-3}}$, $T = 3.1623\,\mathrm{MeV}$, and $Y_e = 0.3$. The Sedonu-calculated energy densities (black crosses) match the theoretical ones (red lines) in a wide range of fluid conditions. Regions of mismatch at low and high temperatures occur as the peak of the neutrino distribution approaches the low and high neutrino energy limits of the NuLib tables.

constrained by $\mu_{\bar{\nu}_e} = -\mu_{\nu_e}$ and $\mu_{\nu_x} = 0$, where ν_x represents any of the four heavy lepton neutrino/anti-neutrino species. The equilibrium μ_{ν_e} can be taken directly from the EOS for a given $\{\rho, T, Y_e\}$. Figure 3.2 demonstrates the match between the predicted energy density and that calculated by Sedonu for many values in each direction of $\{\rho, T, Y_e\}$. The computed and theoretical results disagree at low and high temperatures, where the neutrino distribution functions extend past the energy limits in the NuLib tables.

Blackbody Irradiation

Rather than determining what radiation field is in equilibrium with the input fluid properties as in the previous test, we determine what fluid properties are in equilibrium with the input radiation. That is, we solve for the equilibrium properties of fluid that is allowed to relax in a bath of blackbody neutrinos. I set up a thin shell of fluid ($dr/r = 10^{-4}$), apply a reflective outer boundary condition, and emit blackbody neutrinos from an absorbing inner boundary specified by a neutrino temperature T_{input} and electron neutrino chemical potential $\mu_{\nu_e,\mathrm{input}}$. The chemical potentials of all other neutrino species satisfy the constraints detailed in the previous test, namely that $\mu_{\bar{\nu}_e,\mathrm{input}} = -\mu_{\nu_e,\mathrm{input}}$ and $\mu_{\nu_x,\mathrm{input}} = 0$. Unlike in the main text, the luminosity of each species s is determined by the input temperature and chemical potential of the blackbody neutrinos being emitted from the inner boundary, such that

$$\mathcal{L}_s = 4\pi^2 r^2 \sum_i B_{\epsilon_i}(\mu_{s,\mathrm{input}}, T_{\mathrm{input}})\Delta\epsilon_i \,, \tag{3.40}$$

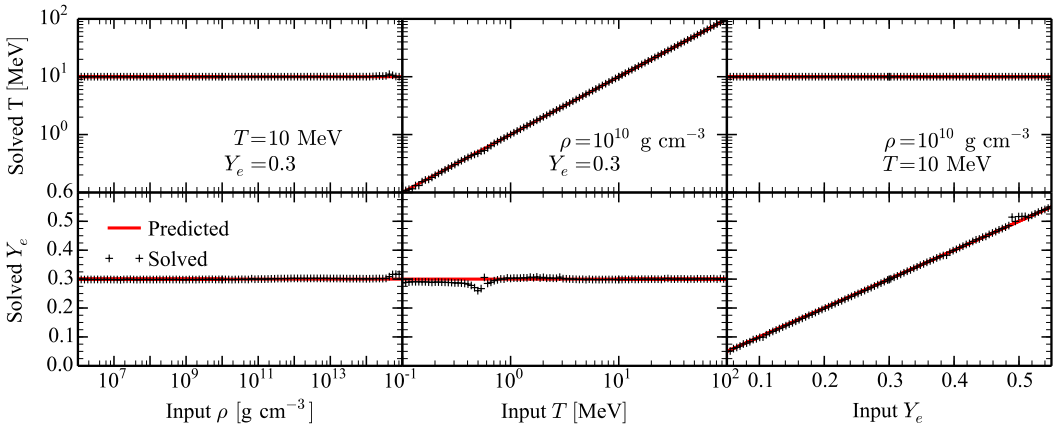

Figure 3.3: **Blackbody irradiation test:** The equilibrium fluid temperature (Solved T) and electron fraction (Solved Y_e) as a function of fluid density (Input ρ), neutrino temperature (Input T), and neutrino chemical potential (via the proxy Input Y_e). The three top panels show results where only fluid temperature is solved for, and the three bottom panels show results where only fluid electron fraction is solved for. The Sedonu-calculated energy densities (black crosses) match the theoretical ones (red lines) in a wide range of fluid conditions. The equilibrium solver has difficulty converging on an electron fraction when the chemical potential is large relative to the temperature (i.e. high ρ or low T), since the neutrino Fermi-Dirac distributions become too sharp to be resolved by the NuLib tables.

where r is the radius of the inner boundary, ϵ_i is the center of energy bin i, and $\Delta\epsilon_i$ is the width of energy bin i.

I then iteratively relax the fluid to its equilibrium temperature and electron fraction as described in the following. Each iteration is done as described in Section 4.2. When solving for temperature, I then set the temperature of each grid cell to $T_{i+1} = T_i + d\Delta T_i$, where T_{i+1} and T_i are the temperatures for the iterations $i + 1$ and i, respectively, $d = 0.3$ is a somewhat arbitrary damping factor, and ΔT_i is the difference between the temperature and the equilibrium temperature. The same process is also applied to the electron fraction if solving for it. Then the new fluid properties are used in another transport and solve iteration. The results presented here are the result of 20 such iterations.

We expect that the equilibrium temperature $T_{\rm eq}$ and electron fraction $Y_{e,\rm eq}$ should settle to values such that $\mu_{\nu_e,\rm EOS}(\rho, T_{\rm eq}, Y_{e,\rm eq}) = \mu_{\nu_e,\rm input}$ and $T_{\rm eq} = T_{\rm input}$, where $\mu_{\nu_e,\rm EOS} = \mu_e + \mu_p - \mu_n$ is given by the EOS. Figure 3.3 demonstrates the estimated and calculated equilibrium temperature and electron fraction at several values of $\{\rho, T_{\rm input}, Y_{e,\rm input}\}$, where $Y_{e,\rm input}$ is a proxy for the chemical potential inputs, such

that $\mu_{\nu_e,\mathrm{EOS}}(\rho, T_{\mathrm{input}}, Y_{e,\mathrm{input}}) = \mu_{\nu_e,\mathrm{input}}$. The equilibrium values of T and Y_e are each determined with independent iterative calculations. There are regions at low temperatures and high densities where the correct solution is not found, as in the previous test. This is a combination of inadequate energy resolution and range in the NuLib tables, as the peaks of the emissivity spectra approach either end of the energy range or become too sharp to resolve. When equilibrium temperature and electron fraction are calculated simultaneously (not plotted), the now two-dimensional solver is less robust and only consistently reaches the correct solution when $\rho \lesssim 3 \times 10^{13}\,\mathrm{g\,cm^{-3}}$ and $T \gtrsim 2\,\mathrm{MeV}$.

3.6 Monte Carlo Closure Proof of Concept

In the two-moment method (Section 2.3), if the estimate of the second and third moments is exact, then the evolution of the zeroth and first moments is also exact. Rather than using an analytic closure in the two-moment method, one could approximate the closure using the result of a time-independent MC simulation. This is a version of a Monte Carlo closure method.

Forcing Consistency with Lower Order Moments

Using a different transport scheme inevitably results in a different estimate of the zeroth and first moments as well. We must therefore force consistency between the two schemes through known identities in contractions of the moments. For the second ($P^{\alpha\beta}$) and third ($W^{\alpha\beta\gamma}$) moments, contracting Equation 2.51 shows that

$$\frac{P^i{}_i}{E} = \frac{W^{ij}{}_j}{F^i} = 1 \ . \tag{3.41}$$

Given moments calculated by the MC method $\widetilde{E}$, $\widetilde{F}^i$, $\widetilde{P}^{ij}$, $\widetilde{W}^{ijk}$, they can be normalized according to

$$\begin{aligned}
P^{mm} &\leftarrow E\frac{\widetilde{P}^{mm}}{\widetilde{P}^j{}_j} \ , \\
W^{1mm} &\leftarrow F^1\frac{\widetilde{W}^{1mm}}{\widetilde{W}^{1j}{}_j} \ , \\
W^{2mm} &\leftarrow F^2\frac{\widetilde{W}^{2mm}}{\widetilde{W}^{2j}{}_j} \ , \\
W^{3mm} &\leftarrow F^3\frac{\widetilde{W}^{3mm}}{\widetilde{W}^{3j}{}_j} \ ,
\end{aligned} \tag{3.42}$$

along with all other components mapped to by symmetries. Contractions of the resulting moments ensure Equation 3.41, even if the MC moments were not calculated in a GR framework. The off-diagonal components of P^{ij} and W^{ijk} are not constrained by the above contractions, but I apply a similar normalization:

$$\begin{aligned} P^{i\neq j} &\leftarrow E\frac{\widetilde{P}^{i\neq j}}{\widetilde{P}^{j}_{\ j}}\ , \\ W^{i\neq j\neq k} &\leftarrow \sqrt{F^a F_a}\frac{\widetilde{W}^{i\neq j\neq k}}{\sqrt{\widetilde{W}^{bn}_{\ \ n}\widetilde{W}_{bm}^{\ \ m}}}\ . \end{aligned} \tag{3.43}$$

In the special case of one spatial dimension in spherical-polar coordinates, the metric reduces to $g_{\alpha\beta} = \mathrm{diag}(-\alpha^2, X^2, r^2, r^2\sin^2\theta)$. The only nonzero flux is F^r, the only nonzero components of P^{ij} are the diagonal terms, and the only nonzero components of the third moment are W^{rrr} and $W^{r\theta\theta} = W^{r\phi\phi}$ (along with the components identified with these by symmetry). The conditions above then become

$$\begin{aligned} P_{rr} &\leftarrow E\frac{\widetilde{P}_{rr}}{X^{-2}\widetilde{P}_{rr} + 2\widetilde{P}^{\theta}_{\ \theta}} \\ P^{\theta}_{\ \theta} &\leftarrow E\frac{\widetilde{P}^{\theta}_{\ \theta}}{X^{-2}\widetilde{P}_{rr} + 2\widetilde{P}^{\theta}_{\ \theta}} \\ W^{rrr} &\leftarrow F^r\frac{\widetilde{W}^{rrr}}{X^2\widetilde{W}^{rrr} + 2\widetilde{W}^{r\theta}_{\ \ \theta}} \\ W^{r\theta}_{\ \ \theta} &\leftarrow F^r\frac{\widetilde{W}^{r\theta}_{\ \ \theta}}{X^2\widetilde{W}^{rrr} + 2\widetilde{W}^{r\theta}_{\ \ \theta}}\ . \end{aligned} \tag{3.44}$$

Smoothing Monte Carlo Results

Monte Carlo results naturally contain a noisy component that seed instabilities. I have found stable evolution to be impossible when using moments calculated by Sedonu directly, at for a reasonable calculation time. However, we can take advantage of the fact that the angular moments do not vary rapidly on the timescale of a single time step or on the length scale of a grid cell. Smoothing can be applied in both the space and time dimensions, and one must in general perform tests with different amounts of smoothing to ensure the evolution is not compromised.

In one spatial dimension, I choose to use a binomial filter. That is, after calculating moments using Sedonu, the moment at each spatial point is replaced by a weighted sum of the moments at nearby points, where the weights are binomial coefficients.

For example, for a second order binomial filter at radial grid m,

$$\begin{aligned}\left(\frac{P^{ij}}{E}\right)_m &\leftarrow \left(\frac{\widetilde{P}^{ij}}{E}\right)_{m-1} + 2\left(\frac{\widetilde{P}^{ij}}{E}\right)_m + \left(\frac{\widetilde{P}^{ij}}{E}\right)_{m+1}, \\ \left(\frac{W^{ijk}}{E}\right)_m &\leftarrow \left(\frac{\widetilde{W}^{ijk}}{E}\right)_{m-1} + 2\left(\frac{\widetilde{W}^{ijk}}{E}\right)_m + \left(\frac{\widetilde{W}^{ijk}}{E}\right)_{m+1},\end{aligned} \tag{3.45}$$

where the quantities with a tilde represent the raw MC moments and those without a tilde are the spatially smoothed moments. In the one-dimensional tests that follow, I use second order binomial spatial smoothing. The amount of noise reduction is comparable to doubling the number of MC packets.

Similarly, we can apply temporal smoothing with a specific timescale by using the MC results, rather than as a direct replacement of moments, as a small nudge in the right direction. More specifically, we set the moments at time step n using the moment from the previous time step $n-1$ according to

$$\begin{aligned}\left(\frac{P^{ij}}{E}\right)_n &\leftarrow \left(1-\frac{\Delta t}{\tau}\right)\left(\frac{P^{ij}}{E}\right)_{(n-1)} + \frac{\Delta t}{\tau}\left(\frac{\widetilde{P}^{ij}}{E}\right)_n, \\ \left(\frac{W^{ijk}}{E}\right)_n &\leftarrow \left(1-\frac{\Delta t}{\tau}\right)\left(\frac{W^{ij}}{E}\right)_{(n-1)} + \frac{\Delta t}{\tau}\left(\frac{\widetilde{W}^{ij}}{E}\right)_n,\end{aligned} \tag{3.46}$$

where quantities with a tilde are MC results after spatial smoothing and consistency enforcement, Δt is the time step size, and τ is the parameter that sets the timescale of the temporal smoothing. Before returning the moments to the dynamical radiation hydrodynamics solver, I once again enforce consistency with the zeroth and first moments. I have found this to be the key to stable evolution; it can immensely improve the statistics from the MC results (depending on τ) and suppresses instabilities.

In summary, the closure cleaning procedure I use is

1. MC transport calculation
2. Spatial binomial or Gaussian smoothing
3. Enforce consistency with zeroth and first moments
4. Temporal smoothing
5. Enforce consistency with zeroth and first moments.

Monte Carlo Closure Test Results

As a simple test case, I evolve the 15 $M_\odot$ progenitor of Woosley and Weaver, 1995 using the $K_0 = 180$ MeV EOS from J. M. Lattimer et al., 1991 until 10 ms after

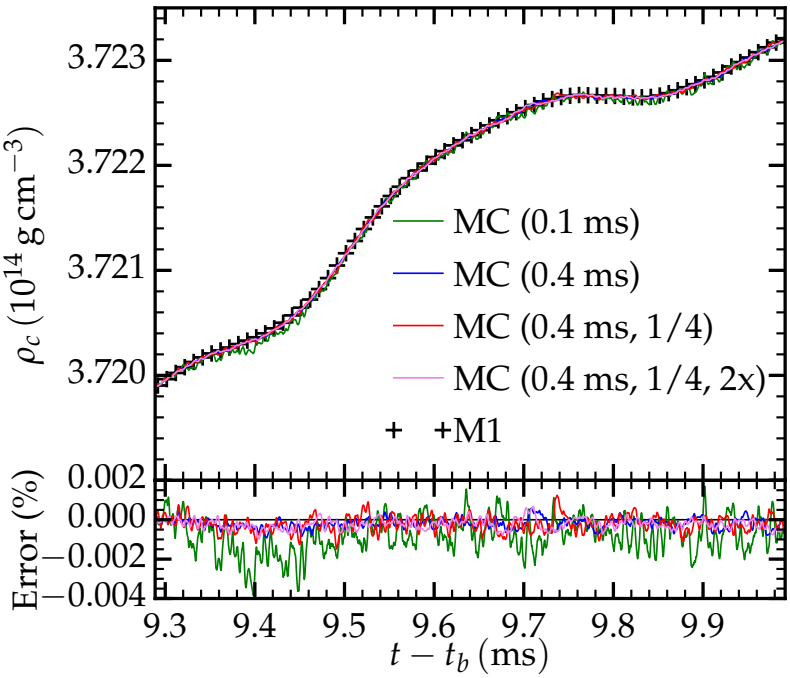

Figure 3.4: **MC closure central density test:** Central density evolution of a 1D 15 $M_\odot$ core collapse simulation in the early post-bounce phase. The crosses are data from the standard M1 evolution. The bottom panel shows the error relative to the standard M1 calculation. The colored curves show results from simulations where the closure was switched from M1 to a MC closure at 9.3 ms after bounce, all of which use second order binomial spatial filtering. The green curve shows data from a simulation that uses $\tau = 0.1$ ms temporal smoothing. The blue curve uses $\tau = 0.4$ ms temporal smoothing. The red curve uses a setup identical to that of the blue curve, except that the closure is recalculated only once every four time steps. The violet curve uses a setup identical to that of the red curve, except uses twice as many MC packets. The results agree well with the M1 results, and show that increasing packet count or smoothing timescale decreases noise.

core bounce using GR1D (E. O'Connor, 2015) with the Minerbo closure (Minerbo, 1978; Pons, Ibáñez, and Miralles, 2000). This is an exact replica of a simulation presented in E. O'Connor, 2015, which was in turn constructed to replicate similar simulations by (Liebendörfer, Rampp, et al., 2005), including neutrino interaction processes. the exact configuration. I then restart the simulation at 9.3 ms after bounce, but replace the closure with the MC procedure outlined above. This phase of the supernova evolution is still very dynamical, and since steady-state neutrino transport is not applicable, it should make differences between the MC closure and M1 methods more clear.

In Figures 3.4 and 3.5, I plot the central density and electron fraction, respectively,

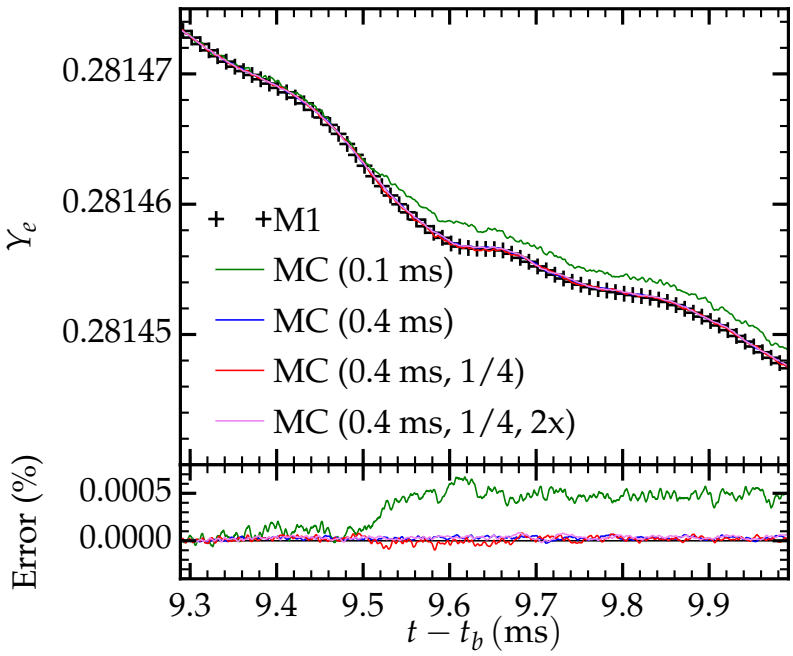

Figure 3.5: **MC closure central electron fraction test:** Central Y_e evolution of a 1D 15 $M_\odot$ core collapse simulation in the early post-bounce phase. The crosses are data from the standard M1 evolution. The bottom panel shows the error relative to the standard M1 calculation. The colored curves show results from simulations where the closure was switched from M1 to a MC closure at 9.3 ms after bounce, all of which use second order binomial spatial filtering. The green curve shows data from a simulation that uses $\tau = 0.1$ ms temporal smoothing. The blue curve uses $\tau = 0.4$ ms temporal smoothing. The red curve uses a setup identical to that of the blue curve, except that the closure is recalculated only once every four time steps. The violet curve uses a setup identical to that of the red curve, except uses twice as many MC packets. The results agree well with the M1 results, and show that increasing packet count or smoothing timescale decreases noise. Small differences of yet undetermined origin appear after a few temporal smoothing timescales.

over the 0.7 s test simulation duration. By this point, neutrinos at the center of the protoneutron star are trapped, and these quantities should be independent of the transport method. Indeed, the density in the MC results oscillates around the M1 result (due to statistical perturbations in the neutrino pressure). As a baseline, the RMS density error integrated over the 0.7 ms evolution window for the $\tau = 0.1$ ms test (green curve) is 9.7×10^{-4}. The RMS error of the standard $\tau = 0.4$ ms test (blue curve) is a factor of 3.7 smaller at 2.6×10^{-4}. When the closure is then calculated only once every four time steps (red curve), the RMS error increases only by a factor of 1.4 to 3.6×10^{-4}. Finally, when the number of MC packets is then doubled, the RMS error decreases again by a factor of $1.3 = 0.91\sqrt{2}$ to 2.8×10^{-4}. These tests demonstrate accurate and stable evolution, and show that noise decreases linearly with smoothing timescales, but only approximately as the square root of the number of packets simulated. The error introduced in this test from recalculating the closure less often is very sub-linear. These tests are promising for efficient MC closure simulations, but thorough tests are required to assess how far these noise reduction techniques can be pushed before having a significant impact on results.

The central Y_e in the MC tests also closely follows that in the M1 baseline calculation, except for a constant offset of $\sim 2 \times 10^{-5}$ seen after ~ 0.2 ms in the MC test with the shortest temporal smoothing timescale. The origin of such a difference is not obvious from these proof of concept calculations, but will become apparent in future thorough tests.

Figure 3.6 shows the energy-integrated electron neutrino luminosity at the outer boundary of the same tests. There are transient oscillations at the beginning of the evolution, since the shift in the closure treatment of the closure allows neutrinos to diffuse out differently. The oscillations die out on a timescale of 0.3 ms, corresponding to a light distance of ~ 100 km, independent of the temporal smoothing parameter. The test with the shortest smoothing parameter ($\tau = 0.1$ ms, green curve) shows statistical noise-induced oscillations around the smoother $\tau = 0.4$ ms blue curve. The timescale of these oscillations is approximately the temporal smoothing parameter, as one would expect.

Figure 3.7 shows the average electron neutrino energy at the outer boundary of the simulation for the same test calculations. Once again, there are transient oscillations in the MC tests that are independent of the smoothing timescale, but that die out on a longer timescale. Unlike the net luminosity, the average energy settles to a value that is different from the M1 baseline test. Though we expect the MC closure to yield

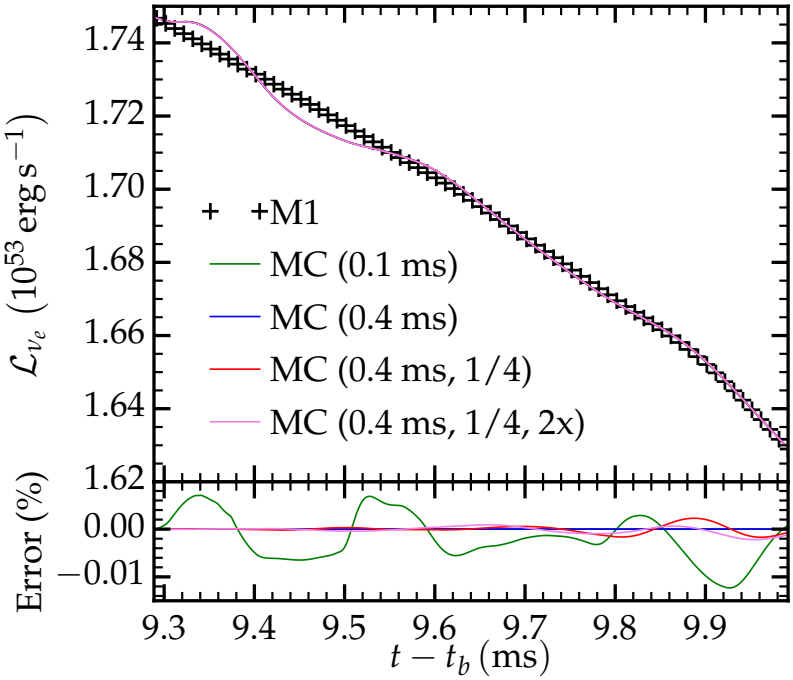

Figure 3.6: **MC closure electron neutrino luminosity:** Electron neutrino luminosity from a 1D 15 $M_\odot$ core collapse simulation in the early post-bounce phase. The crosses are data from the standard M1 evolution. The colored curves show results from simulations where the closure was switched from M1 to a MC closure at 9.3 ms after bounce, all of which use second order binomial spatial filtering. The green curve shows data from a simulation that uses $\tau = 0.1$ ms temporal smoothing. The blue curve uses $\tau = 0.4$ ms temporal smoothing. The red curve uses a setup identical to that of the blue curve, except that the closure is recalculated only once every four time steps. The violet curve uses a setup identical to that of the red curve, except uses twice as many MC packets. The bottom panel shows the error relative to the standard $\tau = 0.4$ ms (blue) curve. Transient oscillations appear in the M1 results over the first ~ 0.3 ms as the radiation field adjusts to the change in transport method, but otherwise the MC results agree well with the M1 results. Small oscillations on the timescale of the smoothing time are visible in the green curve as a byproduct of statistical noise.

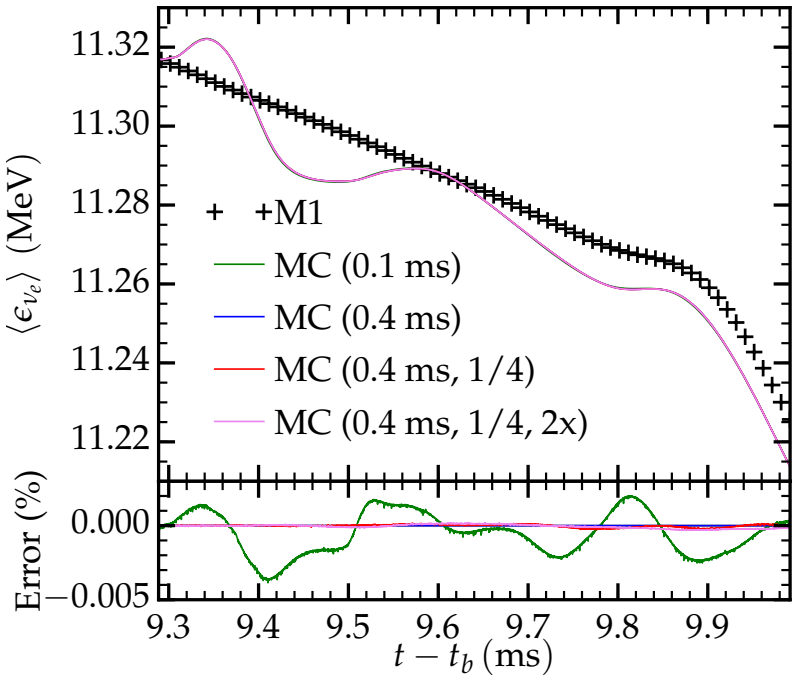

Figure 3.7: **MC closure electron neutrino average energy:** Electron neutrino average escaping energy from a 1D 15 $M_\odot$ core collapse simulation in the early post-bounce phase. The crosses are data from the standard M1 evolution. The colored curves show results from simulations where the closure was switched from M1 to a MC closure at 9.3 ms after bounce, all of which use second order binomial spatial filtering. The green curve shows data from a simulation that uses $\tau = 0.1$ ms temporal smoothing. The blue curve uses $\tau = 0.4$ ms temporal smoothing. The red curve uses a setup identical to that of the blue curve, except that the closure is recalculated only once every four time steps. The violet curve uses a setup identical to that of the red curve, except uses twice as many MC packets. The bottom panel shows the error relative to the standard $\tau = 0.4$ ms (blue) curve. Transient oscillations in the MC results appear over the first ~ 0.5 ms as the radiation field adjusts to the change in transport method, and the average energies settle to a slightly different value than the M1 results do. Small oscillations on the timescale of the smoothing time are visible in the green curve as a byproduct of statistical noise.

a different result than the M1 closure (that is indeed the purpose of the MC closure code), more thorough tests over a longer range in time will reveal the origin of these differences. Once again, the $\tau - 0.1$ ms test (green curve) shows oscillations on the timescale of the temporal smoothing parameter around the standard $\tau = 0.4$ ms test (blue curve), as expected.

These tests are but a taste of the capabilities of a full MC closure method. They prove the possibility of stable evolution in CCSNe, and demonstrate that the noise and errors behave as we expect and decrease with increasing fidelity and smoothing.

Chapter 4

NEUTRINO TRANSPORT IN NEUTRON STAR MERGERS

I apply my Monte Carlo neutrino transport code Sedonu to snapshots from two-dimensional simulations of accretion disks left behind by binary neutron star mergers, varying the input physics and comparing to the results obtained with a leakage scheme for the case of a central black hole and a central hypermassive neutron star. Neutrinos are guided away from the densest regions of the disk and escape preferentially around 45 degrees from the equatorial plane. Neutrino heating is strengthened by MC transport a few scale heights above the disk midplane near the innermost stable circular orbit, potentially leading to a stronger neutrino-driven wind. Neutrino cooling in the dense midplane of the disk is stronger when using MC transport, leading to a globally higher cooling rate by a factor of a few and a larger leptonization rate by an order of magnitude. I calculate neutrino pair annihilation rates and estimate that an energy of 2.8×10^{46} erg is deposited within 45° of the symmetry axis over 300 ms when a central BH is present. Similarly, 1.9×10^{48} erg is deposited over 3 s when an HMNS sits at the center, but neither estimate is likely to be sufficient to drive a GRB jet.

This work was originally published as **[Sherwood Richers, Daniel Kasen, Evan O'Connor, Rodrigo Fernández, and Christian D. Ott (2015). "Monte Carlo Neutrino Transport through Remnant Disks from Neutron Star Mergers".** ***The Astrophysical Journal*** **813,1]**. In this chapter E_ν represents neutrino energy (ϵ in other chapters), ϵ_ν represents neutrino energy density (E in other chapters), and $\mathbf{D}$ represents the neutrino propogation direction ($\mathbf{\Omega}$ in other chapters). Much of the original methods text on Monte Carlo transport has been relegaded to Chapter 3.

I revamped a stripped version of the Sedona Monte Carlo photon transport code from UC Berkeley Professor Daniel Kasen and coupled it to the NuLib neutrino reaction rate library from CITA Postdoc Evan O'Connor to make the specialized neutrino transport code Sedonu. I verified the code performance against several tests, imported simulation data from UC Berkeley postdoc Rodrigo Fernandez, ran the time-independent MC transport calculations, reduced the data, and wrote the text.

4.1 Introduction

Neutron star-neutron star (NS-NS) and neutron star-black hole (NS-BH) mergers are prime candidates for explaining observed short gamma ray bursts (sGRBs) and their afterglows (see, e.g., Berger, Fong, and Chornock 2013 for a recent review). The large amount of extremely neutron-rich matter and available energy make these systems potentially capable of ejecting matter up to $A \sim 200$ through the r-process (e.g., J. M. Lattimer and Schramm 1974; Freiburghaus, Rosswog, and Thielemann 1999; Korobkin et al. 2012; Goriely, Sida, et al. 2013). The thermal and radioactive glow of this ejecta is thought to cause largely isotropic (depeding on the distribution of dynamical ejecta), observable infrared/optical emission lasting on the order of hours to days (L.-X. Li and Paczyński, 1998; Metzger, Martínez-Pinedo, et al., 2010; Berger, Fong, and Chornock, 2013; Barnes and Kasen, 2013). Observation of this so-called kilonova would provide key information about the merger to complement gravitational wave observations (e.g., Metzger and Berger 2012; Nissanke, Kasliwal, and Georgieva 2013; Piran, Nakar, and Rosswog 2013). Some observational evidence of such a kilonova has already been suggested for GRB130603B (Tanvir et al., 2013; Berger, Fong, and Chornock, 2013) and GRB060614 (Yang et al., 2015).

Realistic simulations of merging compact objects need to account for general relativity, a hot nuclear equation of state (EOS), magnetohydrodynamics (MHD), nuclear reactions, spectral and angle-dependent neutrino transport, and possibly neutrino quantum effects (e.g. flavor oscillations). Neutrinos in particular play an important role in determining the dynamics, brightness, and color of predicted ejecta emission. Neutrino emission and absorption modify the electron fraction and specific entropy of the material, which in turn determine which elements form from the cooling ejecta (**korobkin:12**; L. F. Roberts, Kasen, et al., 2011; Wanajo, Y. Sekiguchi, et al., 2014) and the resulting photon opacities (Barnes and Kasen, 2013; Kasen, Badnell, and Barnes, 2013). Neutrino irradiation can also drive a thermal outflow, generally increasing the amount and electron fraction of ejecta (McLaughlin and Surman, 2005; Surman, McLaughlin, and Hix, 2006; Wanajo and H.-T. Janka, 2012; Fernández and Metzger, 2013; Just, Bauswein, et al., 2015; Martin et al., 2015; Goriely, Bauswein, et al., 2015; Foucart, E. O'Connor, L. Roberts, Duez, et al., 2015), especially in the presence of a central hypermassive neutron star (HMNS) (Dessart, Ott, et al., 2009; Perego, Rosswog, et al., 2014; Y. Sekiguchi et al., 2015; Metzger and Fernández, 2014). Neutrino-antineutrino annihilation may generate large amounts of thermal energy in baryon-poor regions and remains a possible engine driving the

GRB jet (D. Eichler et al., 1989; Meszaros and Rees, 1992; Popham, Woosley, and C. Fryer, 1999; Zalamea and Beloborodov, 2011; Leng and Giannios, 2014), though many calculations show that the energy production is at best marginally capable of powering GRBs (e.g. Setiawan, Ruffert, and H.-T. Janka 2006; Dessart, Ott, et al. 2009)

Due to the great complexity of this problem, all current and past simulation efforts make some level of approximation or evolve only for very short times to make the problem computationally tractable (see, e.g., Faber and Rasio 2012; M. Shibata and Taniguchi 2011 for reviews). Neutrinos are ignored altogether in many studies for simplicity or efficiency (e.g., Etienne et al. 2012; Kiuchi, Kyutoku, et al. 2014; Bauswein, Stergioulas, and H.-T. Janka 2014; Bernuzzi, Dietrich, and Nagar 2015; Takami, Rezzolla, and Baiotti 2015). Fernández and Metzger, 2013 approximate self-irradiation from the disk as a gray lightbulb arising from a ring, with optically thin cooling rates corrected for optical depth effects. Various forms of the leakage scheme of Ruffert, H.-T. Janka, and Schaefer, 1996 can be used to more accurately treat cooling, heating, and electron fraction changes from neutrinos whenever the disk becomes optically thick (H.-T. Janka, Eberl, et al. 1999; Ruffert and H. Janka 1999; Rosswog, Ramirez-Ruiz, and Davies 2003; Y. Sekiguchi et al. 2011; Y. Sekiguchi and M. Shibata 2011; Y. Sekiguchi et al. 2012; Kiuchi, Y. Sekiguchi, et al. 2012; Deaton et al. 2013; Galeazzi et al. 2013; Neilsen et al. 2014; Foucart, Deaton, et al. 2014) although ad-hoc assumptions about the angular distribution of radiation are still needed to compute neutrino absorption (Metzger and Fernández, 2014; Perego, Rosswog, et al., 2014; Fernández, 2015; Fernández, Kasen, et al., 2015). Moving from simple approximations to actual neutrino transport, Dessart, Ott, et al., 2009 use Newtonian multi-group flux-limited diffusion (MGFLD) during evolution and multi-group multi-angle transport during post-processing analysis. General relativistic two-moment neutrino transport with an analytic closure (e.g., Thorne 1981; M. Shibata, Kiuchi, et al. 2011; Cardall, Endeve, and Mezzacappa 2013) is the state of the art in multi-dimensional simulations and currently gives the most accurate approximation to full Boltzmann transport of all of the methods employed in time-dependent simulations. Initial studies have employed a gray (energy-integrated) transport scheme with general relativity to simulate a merger and remnant (Masaru Shibata and Y. Sekiguchi, 2012; Y. Sekiguchi et al., 2015; Foucart, E. O'Connor, L. Roberts, Duez, et al., 2015), and Just, Bauswein, et al., 2015 recently simulated an axisymmetric remnant disk with Newtonian multi-group two-moment transport.

Unlike the above transport methods, Monte Carlo (MC) transport is continuous in space, direction, and energy, freeing it from many of the grid effects and distribution function approximations used in other methods. Though it is more accurate, it is more computationally expensive and has seen more limited use in the past. MC transport has been used to study neutrino equilibration in a static isotropic background (Tubbs, 1978) and to study transport through static spherically symmetric fluid in the context of core-collapse supernovae (e.g., H.-T. Janka and Hillebrandt 1989b; H.-T. Janka 1991; Keil, Raffelt, and H.-T. Janka 2003). More recently, E. Abdikamalov, Burrows, et al., 2012 use a time-dependent MC neutrino transport scheme in static spherically symmetric core-collapse simulation snapshots. MC transport has also been used in the context of photon transport in Ia supernova explosions (e.g., Kasen, Thomas, and Nugent 2006; Wollaeger et al. 2013; Roth and Kasen 2015) and accretion disks (e.g., Ryan, Dolence, and Gammie 2015).

In this chapter, I investigate the effect of neutrinos on the rates of change of the composition and thermal energy of the remnant disk and ejecta using time-independent MC neutrino transport calculations. I calculate properties of the neutrino radiation fields to pinpoint the regions of largest error in more approximate schemes and proceed to estimate the effect this would have on dynamical simulations of compact object mergers. I begin by introducing the specifics of the neutrino transport scheme and the background fluid in Section 4.2. I proceed to describe the observed properties and effects of the neutrino radiation field and a comparison to those seen by the leakage scheme in the dynamical calculation with a central black hole in Section 4.3. In Section 4.4, I extend the results to fluid backgrounds with a central hypermassive neutron star (HMNS). I briefly discuss the effects of neutrino pair annihilation for both sets of background data in Section 4.5. In Section 4.6, I discuss the potential implications of these results on the dynamical calculation and the implications for nucleosynthesis and kilonovae. In Section 4.7, I conclude and list the main points that can be drawn from the results.

4.2 Methods

Background Fluid

The background fluid snapshots come from the axisymmetric 2D simulations from Metzger and Fernández, 2014 of remnant disks modeled after those left behind by a binary neutron star merger. The disks have a mass of $0.03 M_\odot$ and circle a $3 M_\odot$ BH or HMNS. Table 4.1 lists the times and global properties of the fluid snapshots I use. Figure 4.1 shows the background density, temperature, electron fraction,

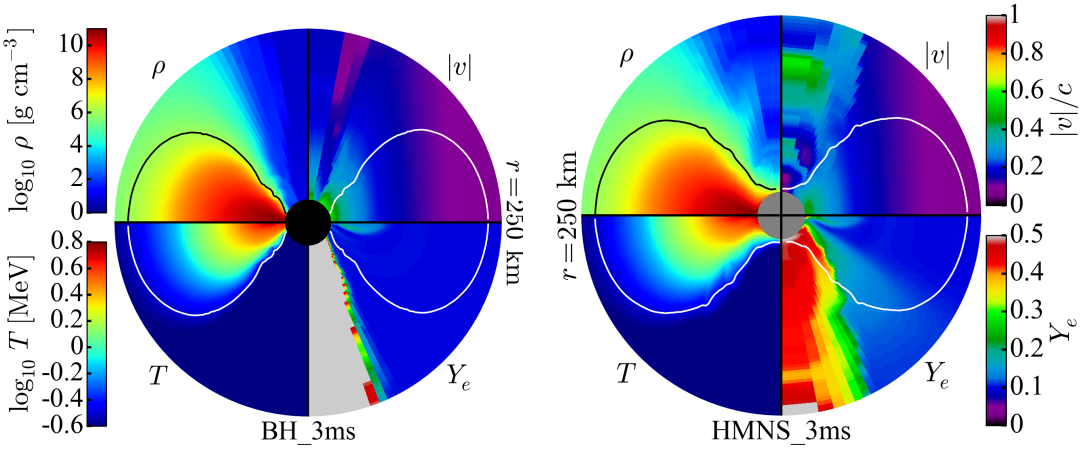

Figure 4.1: **Fluid backgrounds** at $t = 3$ ms from the start of the dynamical simulations of Metzger and Fernández, 2014. *Left*: central BH *Right*: central HMNS. The outer radius on the plot is at 250 km and the inner radius is 30 km. Each quadrant covers half of the simulation domain. On the top left of each plot is the density, which peaks at around 5×10^{10} g cm^{-3}. On the top right is the magnitude of the velocity in units of c. On the bottom right is the electron fraction, where grey colors indicate electron fractions larger than 0.5 due to very low-density hydrogen that is present for numerical reasons. On the bottom left is the temperature, which peaks around 5 MeV. The black/white curve is the $\rho = 10^6$ g cm^{-3} contour, below which Sedonu opacities and emissivities are set to zero (see Section).

and fluid speed at 3 ms after the start of the dynamical simulations. To avoid large inconsistencies in using a relativistic transport code with fluid velocities calculated with a Newtonian code, I cap the fluid speeds at a maximum Lorentz factor of 2.

Though the fluid moves around on an orbital timescale of about 3 ms (at $R = 50$ km), the time required for the disk to significantly change its structure is set by the viscous timescale of about 1 s (Fernández and Metzger, 2013). The diffusion time for the neutrinos can be approximated by $t_{\rm diff} \sim \frac{\tau l}{c} \approx 10^{-3}$ s, where $\tau \sim 3$ is a representative average optical depth, $l \sim 10^7$ cm is an approximate characteristic size of the portion of the disk opaque to neutrinos, and c is the speed of light. The neutrino diffusion time is much shorter than the viscous timescale. Hence, although the fluid orbits faster than neutrinos can escape, we can safely assume that the global disk structure is effectively static on the neutrino propagation timescale.

The $3M_\odot$ central object is well above the maximum mass of current observational and theoretical constraints for the maximum mass of a cold neutron star (e.g., J. M. Lattimer and Prakash 2000; Steiner, Hempel, and Fischer 2013). The central object in these simulations is likely to become a black hole, but the temporary stability

Time (ms)	$M_{\rm disk}$ ($M_\odot$)	$\langle T\rangle$ (MeV)	$\langle Y_e\rangle$	$\mathcal{H}_{\rm visc}$ (B s^{-1})	$\mathcal{L}_{\rm core}$ (B s^{-1}) each $\nu_e, \bar{\nu}_e$	$C_\nu - \mathcal{H}_\nu$ (B s^{-1})	$\left\langle \frac{dY_e}{dt} \right\rangle$ (s^{-1})	M_ν ($M_\odot$)	$\mathcal{L}_{\rm SI}$ (B s^{-1}) ν_e	$\bar{\nu}_e$	$\langle E_{\nu,\rm SI}\rangle$ (MeV)
Central BH											
0	3.01(-2)	2.95	0.102	3.02(1)	–	5.19(1)	2.49(1)	2.24(-6)	1.58(1)	4.01(1)	17.3
3	2.93(-2)	2.81	0.121	2.84(1)	–	3.29(1)	2.47	2.27(-7)	1.54(1)	1.92(1)	15.1
30	1.52(-2)	1.93	0.114	7.95	–	5.77	4.92(-1)	1.35(-8)	2.86	3.19	10.8
300	4.48(-3)	6.29(-1)	0.190	3.63(-1)	–	1.93(-2)	1.47(-1)	0.00	4.93(-2)	1.44(-2)	5.08
Central HMNS											
0	3.01(-2)	2.95	0.102	3.05(1)	1.73(1)	3.58(1)	3.33(1)	2.42(-3)	1.60(1)	3.90(1)	15.4
3	3.01(-2)	2.93	0.137	2.89(1)	1.73(1)	2.77(1)	6.51	2.22(-3)	2.67(1)	2.64(1)	16.0
30	3.01(-2)	2.75	0.177	2.11(1)	1.02(1)	1.87(1)	3.14(-1)	6.46(-3)	2.59(1)	1.84(1)	16.6
300	3.01(-2)	1.09	0.264	5.85	3.22	4.75	2.43(-1)	5.88(-3)	4.99	3.84	13.6
3000	1.32(-2)	4.66(-2)	0.300	1.19(-1)	1.02	-8.41(-4)	1.41(-3)	9.62(-3)	3.98(-7)	2.73(-6)	2.43

Table 4.1: **NS merger input quantities.** Quantities extracted from the dynamical simulations conducted by Metzger and Fernández, 2014. The numbers in parentheses indicate the power of 10 with which the data given must be scaled, e.g., $6.95(-1)$ is 6.95×10^{-1}. $M_{\rm disk}$ is the mass remaining in the disk. $\langle T\rangle$ and $\langle Y_e\rangle$ are mass-weighted averages of the disk temperature and electron fraction, respectively. $\mathcal{H}_{\rm visc}$ is the integrated viscous heating rate. $\mathcal{L}_{\rm core}$ is the luminosity of *each* neutrino species emitted from the core. Each of the previous quantities are taken as input to Sedonu, and the following can be compared to the Sedonu results. $C_\nu - \mathcal{H}_\nu$ is the net rate of energy loss from the fluid by neutrinos and $\langle dY_e/dt\rangle$ is the mass-weighted average of the rate of change of the electron fraction computed by neutrino leakage. M_ν is the mass in which neutrinos are a larger source of heat than viscosity is, i.e. $\mathcal{H}_\nu - C_\nu > \mathcal{H}_{\rm visc}$. $\mathcal{L}_{\rm SI}$ is the luminosity of the disk self-irradiation assumed to be emitted from two rings above and below the equatorial plane. $\langle E_{\nu,\rm SI}\rangle$ is the energy density-weighted average energy of these emitted neutrinos. $1\,\mathrm{B} = 10^{51}$ erg.

depends on rotation, thermal support against collapse (e.g. Kaplan et al. 2014), and magnetic field strength and configuration, though the latter requires magnetic fields on the order of 10^{18} G for the effect to be relevant (e.g., Cardall, Mezzacappa, and Liebendoerfer 2001). As did Metzger and Fernández, 2014, I remain agnostic to how long the mass in the central object is supported against collapse and consider both instant black hole creation and indefinite HMNS stability to bracket the parameter space.

Opacities and Emissivities

Neutrino-fluid interactions depend on the fluid density ρ, temperature T, and electron fraction Y_e, as well as the neutrino energy E_ν and species s_ν. The interactions are taken into account via neutrino opacities and emissivities calculated by NuLib[1] (E. O'Connor, 2015) and are output in tabular form for a range of values of $\{\rho, T, Y_e, E_\nu, s_\nu\}$[2]. I use a table spanning $\rho = 10^{6-15}\,\mathrm{g\,cm^{-3}}$ with 82

[1] open source, available at www.nulib.org

[2] input files available at bitbucket.org/srichers/sedonu

Process	Leakage	Full	Shen	LS220	NoWM	NoScat	NoPair	NoRel	Simple
$\nu_e/\bar{\nu}_e$ Emis/Abs on n, p	✓	✓	✓	✓	✓	✓	✓	✓	✓
Weak Magnetism Correction		✓	✓	✓		✓	✓	✓	
Elastic Scatter on e, n, p, α		✓	✓	✓	✓		✓	✓	
ν_x Emis/Abs/Pair Production		✓	✓	✓	✓	✓		✓	
Special Relativity		✓	✓	✓	✓	✓	✓		
Elastic Scatter on Heavy Nuclei			✓	✓					
Equation of State	Helmholtz	Helmholtz	Shen	LS220	Helmholtz	Helmholtz	Helmholtz	Helmholtz	Helmholtz

Table 4.2: **Included physics** in each class of neutrino transport simulations. The first column represents the physics included in the leakage scheme in the original dynamical simulations by MF14. Full represents the most complete set of physics, while Simple is designed to replicate the physics used in the leakage calculations as closely as possible. The inclusion of the first four processes and the choice of equation of state go into generating the NuLib opacity tables. Special relativistic physics is turned on or off within Sedonu.

logarithmically-spaced points, $T = 0.05 - 200\,\mathrm{MeV}$ with 65 logarithmically-spaced points, $Y_e = 0.035 - 0.55$ with 51 linearly-spaced points, and $E_\nu = 0.5 - 200\,\mathrm{MeV}$ with 48 logarithmically-spaced bins. I demonstrate that this table has sufficient resolution in the microphysics resolution study below. The opacities and emissivities below the table minima in $\{\rho, T, Y_e, E_\nu\}$ are very low or affect a very small amount of mass. They are hence dynamically unimportant, so I assume them to be zero. Heavy lepton neutrinos play a relatively minor role (see Section 4.3 and 4.4) since they deposit energy only via neutral current reactions, so I simulate three effective neutrino species $s_\nu = \{\nu_e, \bar{\nu}_e, \nu_x\}$, where ν_x accounts for ν_μ, $\bar{\nu}_\mu$, ν_τ, and $\bar{\nu}_\tau$.

I experiment with excluding various processes and corrections as listed in Table 4.2 to determine how much each approximation affects the resulting neutrino radiation field and fluid source terms. The Full simulations embody the most complete set of physics which will serve as the standard for comparison. The Simple simulations account only for charged-current interactions on free nucleons in order to match as closely as possible the physics assumed in the leakage scheme used in the dynamical simulations of MF14. The Full simulations include weak magnetism and recoil corrections and the opacity for each neutrino species to scatter elastically on electrons, neutrons, protons, α particles, and heavy nuclei, unlike the Simple and Leakage simulations. Opacities for scattering on heavy nuclei are corrected for ion-ion correlations, the heavy-ion form factor, and electron polarization, though heavy nuclei are ignored when using the Helmholtz equation of state (EOS, see below). Each of these processes is implemented as described in Burrows, Reddy, and Thompson, 2006.

Absorption opacities are converted into emissivities via Kirchhoff's Law and account

for final-state electron and positron blocking. There are additional approximate emissivities calculated for pair processes, namely electron-positron annihilation ($e^- + e^+ \longleftrightarrow \nu_i + \bar{\nu}_i$) and nucleon-nucleon Bremsstrahlung ($n_1 + n_2 \longleftrightarrow n_3 + n_4 + \nu_i + \bar{\nu}_i$ where n_j represents any nucleon). While it is in principle incorrect to apply Kirchhoff's Law to these emissivities to get opacities since the opacities depend on both neutrinos and anti-neutrinos (which are not necessarily in equilibrium), doing so gives correct absorption rates in the optically-thick and trivial neutrino-free limits. In this way, NuLib yields annihilation rates that are correct to an order of magnitude, though it somewhat overestimates the effective opacity. In light of this, I include pair processes only for heavy lepton neutrinos during the transport step (post-processing annihilation calculations are described later in this section).

The opacities are corrected for final-state blocking and in general depend on the chemical potentials of the particles involved in reactions (Burrows, Reddy, and Thompson, 2006). The nucleon and lepton chemical potentials at a given density, temperature, and electron fraction depend on the details of the equation of state (EOS). To compare as directly as possible with the dynamical simulations, I use the Helmholtz EOS (Timmes and Swesty, 2000) including neutrons, protons, and α particles in nuclear statistical equilibrium (NSE). I also use two popular hot nuclear equations of state: those from H. Shen et al., 2011 and the 220-MeV incompressibility version from J. M. Lattimer and Swesty, 1991[3].

Monte Carlo Neutrino Transport

I use the Monte Carlo neutrino transport code Sedonu (Chapter 3) to calculate a steady state radiation field on the fluid snapshots. By their very nature, MC simulations output data with random fluctuations that decrease with the number of MC elements. To keep the fluctuations of global quantities in Table 4.4 below 0.1% I propagate $2 - 4 \times 10^7$ packets in each simulation. Each grid cell has a distribution function consisting of 6144 energy/direction bins composed of (8 latitudinal bins)$\times$ (16 longitudinal bins) $\times$ (48 energy bins). The latitudinal bins have constant size in $\cos(\theta)$, where θ is the angle from the pole, so each bin covers the same solid angle. The energy bins match those of the NuLib table.

Neutrinos are emitted as described in Section 3.1. The energy bin of any given neutrino is chosen by randomly sampling the local neutrino energy-dependent emissivity. Neutrinos are emitted only from the center of a neutrino energy bin $E_{\nu,i}$. This

[3] both available in tabular form at stellarcollapse.org

is to better maintain consistency required by Kirchhoff's Law between the emissivity of a grid cell and the product of the opacity and the neutrino blackbody function, both of which are also evaluated at the bin center. As neutrinos move through fluid cells with different velocities, they are Lorentz transformed away from the bin centers, reducing the level of consistency, but I ignore this minor discrepancy.

Neutrinos are emitted from the central HMNS as described in Section 3.1 assuming zero chemical potential. The temperature and luminosity of electron neutrinos and electron anti-neutrinos emitted from a central HMNS are taken directly from MF14. There, $T_{\nu_e} = 4\,\mathrm{MeV}$ and $T_{\bar{\nu}_e} = 5\,\mathrm{MeV}$, and the luminosity of each species obeys

$$\frac{\mathcal{L}_{\mathrm{core}}}{20\,\mathrm{B\ s^{-1}}} = \begin{cases} \left(\frac{10\,\mathrm{ms}}{30\,\mathrm{ms}}\right)^{-1/2} & t \leq 10\,\mathrm{ms}\ , \\ \left(\frac{t}{30\,\mathrm{ms}}\right)^{-1/2} & t > 10\,\mathrm{ms}\ . \end{cases} \tag{4.1}$$

The values of the HMNS luminosity at each of the snapshots is also listed in Table 4.1. When heavy lepton neutrinos are included, I choose their temperature and luminosity to be the same as those of electron anti-neutrinos. The HMNS emits 2×10^7 packets *in addition* to the 2×10^7 emitted from fluid in the disk, and the energy of each HMNS-emitted neutrino packet is then chosen such that the total HMNS luminosity is equal to $\mathcal{L}_{\mathrm{core}}$.

In this chapter, I use a slightly different method of determining the neutrino step size than was described in Chapter 3, since this work is done with an earlier version of Sedonu. The distance moved along any straight-line segment is the minimum of the following computed distances along the packet's direction of travel: (1) the distance to the simulation outer boundary d_{boundary}, (2) d_{cell}, which is 0.4 times the length of the smallest dimension of the cell currently occupied, and (3) the interaction distance d_{interact}. I use this method of calculating d_{cell} rather than computing a geometric distance to the cell boundary for efficiency, but I demonstrate that the factor of 0.4 is small enough to adequately substitute for a more precise geometric calculation below. I use the *discrete absorption* model described in Section 3.3 to account for neutrino absorption.

It should be noted that the fluid in a moving cell is length contracted, such that its rest-frame volume is larger than its lab-frame volume by a factor of the Lorentz factor. Thus, including special relativity increases the rest mass (by at most 4% in any snapshot), average neutrino energy, and the net luminosity of moving grid cells. When special relativity is included, the grid structure is assumed to be in the lab frame and the fluid properties are given in the rest frame. In a real merger,

general relativity would diminish the energy of outgoing neutrinos and increase the energy of incoming ones. To estimate the magnitude of this effect, we can assume a Schwarzschild metric outside of and sourced only by the $3M_\odot$ central object, which implies that

$$\frac{E_{\nu,1}}{E_{\nu,2}} = \left(\frac{1 - 2GM/r_2c^2}{1 - 2GM/r_1c^2}\right)^{1/2} , \tag{4.2}$$

where M is the mass of the central object and $E_{\nu,1}$ and $E_{\nu,2}$ are the energies of a given neutrino at radii r_1 and r_2, respectively. The strongest redshift effect we could expect is the difference between the neutrino energy at the inner boundary (30 km) and the outer edge of the disk ($\sim$ 250 km), which comes out to be $E_{\nu,250\,\mathrm{km}}/E_{\nu,30\,\mathrm{km}} = 0.86$. The neutrino opacities scale approximately as $\sigma \sim E_\nu^2$ (e.g., Burrows, Reddy, and Thompson 2006), resulting in about a 25% effect on the opacities over this distance. However, most of the neutrino energy is emitted and absorbed over distances of tens of kilometers, so errors from excluding gravitational redshift will be necessarily smaller than this. In general relativity, neutrinos would also follow null geodesics rather than straight lab-frame lines (see Section 4.6 for a discussion).

Annihilation

In each grid cell, Sedonu records the neutrino distribution function by accumulating neutrino energy density in bins of neutrino species, neutrino energy, and direction. In a separate post-processing step that does not feed back into the neutrino distribution, I use this information to calculate an annihilation rate (erg $\mathrm{s}^{-1}\mathrm{cm}^{-3}$) in each cell following Ruffert, H.-T. Janka, Takahashi, et al., 1997. The derivation here assumes that the resulting electrons and positrons are extremely relativistic, i.e., that the incoming neutrino energies are much larger than the sum of the electron and positron rest masses. This assumption is well justified for most of the neutrino energy range we consider.

The general neutrino annihilation rate in vacuum is given by Ruffert, H.-T. Janka, Takahashi, et al., 1997, equation 1, representing the rate of energy deposition from the annihilation of neutrinos and anti-neutrinos. After subtracting out the electron rest mass, we have

$$\begin{aligned} Q^+_{\mathrm{ann}} = {} & \frac{\sigma_0 c}{4(m_e c^2)^2} \int_0^\infty dE_\nu \int_0^\infty d\bar{E}_\nu \oint_{4\pi} d\Omega \oint_{4\pi} d\bar{\Omega} \frac{f E_\nu^3}{(hc)^3} \frac{\bar{f}\bar{E}_\nu^3}{(hc)^3} \\ & \times \left(E_\nu + \bar{E}_\nu - 2m_e c^2\right) \left[\frac{C_1 + C_2}{3}(1 - \cos\theta)^2 + C_3 \frac{(m_e c^2)^2}{E_\nu \bar{E}_\nu}(1 - \cos\theta)\right] . \end{aligned} \tag{4.3}$$

Barred quantities refer to the anti-neutrino species, E_ν is the neutrino energy, m_e is

the electron mass, c is the speed of light, θ is the angle between the two incoming neutrinos, and $\sigma_0 = 1.76 \times 10^{-44}\,\mathrm{cm}^2$ is the fiducial weak interaction cross section. The weak coupling constants depend on the neutrino species that is annihilating. For electron neutrino and electron anti-neutrino (other species) annihilation, $C_1 + C_2 \approx 2.34\,(0.50)$ and $C_3 \approx 1.06\,(-0.16)$. f is the phase space distribution function (values lie between 0 and 1) and $f\nu^3/c^3$ is the neutrino energy density per unit neutrino energy per steradian of direction. The latter quantity only differs by a factor of c from the specific intensity I_ν used in Dessart, Ott, et al., 2009. For simplicity, I perform a first-order numerical integral, and assume the energies and directions are confined to delta functions at the energy/direction bin. Applying this assumption, we arrive at

$$\begin{aligned} Q^{+}_{\mathrm{ann}} =& \frac{\sigma_0 c}{4(m_e c^2)^2} \sum_{E_{\nu,i}} \sum_{\bar{E}_{\nu,k}} \sum_{\Omega_j} \sum_{\bar{\Omega}_l} \epsilon_{\nu,ij} \bar{\epsilon}_{\nu,kl} (E_{\nu,i} + \bar{E}_{\nu,k}) \\ & \times \left[\frac{C_1 + C_2}{3} (1 - \cos\theta_{jl})^2 + C_3 \frac{(m_e c^2)^2}{E_{\nu,i} \bar{E}_{\nu,k}} (1 - \cos\theta_{jl}) \right], \end{aligned} \tag{4.4}$$

where $E_{\nu,i}$ and $\bar{E}_{\nu,k}$ are energy bin centers for the neutrino and anti-neutrino species, respectively. $\epsilon_{\nu,ij}$ and $\bar{\epsilon}_{\nu,kl}$ are the integrated (i.e. total measured in the transport simulation) energy density in the corresponding energy/direction bin. θ_{jl} is the angle between the centers of direction bins j and l. This must then be summed over all three neutrino species–anti-species pairs to get the total energy deposition rate. Since I group all four heavy anti/neutrino species together in the simulations, I set $\epsilon_{\nu_\mu} = \bar{\epsilon}_{\nu_\mu} = \epsilon_{\nu_\tau} = \bar{\epsilon}_{\nu_\tau} = \epsilon_{\nu_x}/4$ before performing the annihilation calculations.

In the derivation above, I subtract the mass energy of the electron-positron pair from the annihilation rate to under-emphasize energy contributed near the minimum-energy limit. Additionally, this causes the annihilation rate to represent only the deposited thermal energy without counting mass energy. To check how large of an effect this has, I calculate the integrated annihilation rate at the 3 ms snapshot for both the BH and HMNS cases within 45° of the axis of symmetry without subtracting the electron rest mass. This caused the energy deposition rate from neutrino annihilation to increase by only 2.5%.

Equilibrium

I use the method described in Section 3.4 to determine what fluid properties are in equilibrium with the radiation field calculated by Sedonu. The true time-independent solution of the NS-NS post-merger disk problem I study here is trivially a zero temperature disk, but to evaluate how strongly the fluid and neutrino radiation fields

are out of equilibrium I stop after a single iteration to arrive at a local rather than global equilibrium.

In this chapter, I include viscous heating in the fluid net heating rates. The lab-frame rate of change of comoving-frame internal energy density ϵ and electron fraction Y_e in a given grid cell is then

$$\begin{aligned} R_\epsilon &\equiv \frac{1}{\epsilon}\frac{d\epsilon}{dt} = \frac{1}{\epsilon V \Delta t}\left(-E_{\rm emit} + \sum_{\rm steps} E_{\rm dep}\right) + \frac{\rho q_{\rm v}}{\gamma \epsilon} \,, \\ R_{Y_e} &\equiv \frac{dY_e}{dt} = \frac{m_n}{\rho V \Delta t}\left(-N_{\rm emit} + \sum_{\rm steps} N_{\rm dep}\right) \,. \end{aligned} \tag{4.5}$$

V is the grid cell's volume in the comoving frame, Δt is the (arbitrary) emission time interval in the lab frame, m_n is the mass of a neutron, and $E_{\rm emit}$ and $N_{\rm emit}$ are the sum of the emitted comoving-frame neutrino energy and lepton number, respectively, from all neutrino species. The sum is over all steps (propagation segments between emission, scattering, absorption, or escape) for all neutrino packets in the cell. The specific heating rate due to viscosity in the comoving frame $q_{\rm v}$ is is taken from the simulations of MF14 and the fluid Lorentz factor γ transforms the time derivative in the viscous heating rate to the lab frame.

Neutrino Leakage

For completeness, I review the neutrino leakage scheme used by Metzger and Fernández, 2014. Throughout the following, only electron neutrino and anti-neutrinos are included.

The central HMNS emits neutrinos with the same temperature and luminosity, and the neutrino flux due to the HMNS at any given location is attenuated by the (grey) optical depth integrated radially from the HMNS.

Metzger and Fernández, 2014 determine the rate of energy loss at any location in the torus by interpolating between the optically thin free-streaming limit and the optically thick diffusion limit, given by the effective luminosity[4]

$$\mathcal{L}^{\rm eff}_{\rm cell} = \sum_i \frac{1}{1 + t_{\rm diff}/t_{\rm loss}} 4\pi V \int_0^\infty \varepsilon_i \, dE_{\nu,i} \,. \tag{4.6}$$

[4]Note the typographical error in Metzger and Fernández, 2014 that reverses the order of the timescales.

Here, ε_i is again the the neutrino emissivity for species i, $t_{\rm loss} = \epsilon V / \mathcal{L}^{\rm eff}_{\rm cell}$ is the characteristic time for the fluid to lose its internal energy via neutrino emission, and $t_{\rm diff} = (\sigma d) \times (d/c)$ is the characteristic time for neutrinos diffusing over a characteristic escape distance. The first term in the expression for $t_{\rm diff}$ represents a typical optical depth through which neutrinos would need to diffuse to escape, where σ is the energy-averaged neutrino absorption coefficient due to charged-current reactions at the given location (see Fernández and Metzger 2013 for details). The second term is the time required for an unimpeded neutrino to cross the same distance. The escape distance is taken to be $d = \min\{r, H_\perp, H_\parallel\}$, where $H_\perp$ and $H_\parallel$ are the vertical and horizontal scaleheights, respectively.

The disk self-irradiation scheme assumes that neutrinos are emitted from two rings, one above and one below the midplane. The location of the ring is at the effective luminosity-weighted average radius and polar angle in each hemisphere, and the luminosity of each ring is half of the volume-integrated effective neutrino luminosity. Neutrinos are emitted from both rings with a zero chemical potential blackbody spectrum, the temperature of which is the effective luminosity-weighted average fluid temperature. The fluxes of each neutrino species at a given location are independently attenuated by an optical depth $\tau_{\rm irr} = \max(\sigma_i d, \sigma_{i,\rm ring} d_{\rm ring})$, where $d_{\rm ring}$ is d evaluated at the ring's location and $\sigma_{i,\rm ring}$ is the absorption coefficient for species i at the ring's location. For details, see Fernández and Metzger, 2013 and Metzger and Fernández, 2014.

Comparing Equation 3.8 (used in computing $\mathcal{L}_{\rm emit}$ in Tables 4.4 and 4.3) with Equation 4.6 (used in computing the self-irradiation luminosity $\mathcal{L}_{\rm SI}$ in Table 4.1), it is clear that $\mathcal{L}_{\rm SI} < \mathcal{L}_{\rm emit}$. The quantities both represent neutrino radiation coming from the disk itself in some capacity, but $\mathcal{L}_{\rm SI}$ is diminished by optical depth effects, preventing direct comparison with $\mathcal{L}_{\rm emit}$.

Microphysics Resolution Study

To ensure that the results are robust against my choices of numerical discretization, I repeat transport simulations for the 3 ms snapshots with different discretizations, all using the Full set of physics, and compare to the original simulations in Table 4.3. The discretization of the NuLib tables was tested by in turn doubling the neutrino energy, matter density, matter temperature, and electron fraction grid resolution. I also in turn double the angular resolution of the neutrino distribution functions in each cell, which only has an effect on the annihilation rates. Finally, I double the

number of steps each neutrino packet must take by changing $d_{\rm cell}$ to be 0.2 rather than 0.4 times the cell's smallest dimension (see Section 4.2 for details).

The differences between simulations with enhanced microphysics resolution in Table 4.3 and the originals in Table 4.4 are all small, indicating that my discretization is sufficiently fine. Increasing the angular resolution of the annihilation kernels causes annihilation rates to drop slightly, supporting the supposition that most of the annihilation is from small incident angles.

Increasing the number of Monte Carlo neutrino packets does not introduce any systematic change, but rather only reduces the size of random fluctuations in results when the same simulation is run multiple times. I use $2 - 4 \times 10^7$ packets in order to keep random fluctuations of the results in Table 4.4 at $\sim 0.1\%$.

4.3 Results (Central BH)

In this section, I present the results for the simulations where it is assumed that a black hole forms immediately upon merger and is present in every snapshot. Table 4.4 lists the times at which I simulate MC neutrino transport and the corresponding global fluid and neutrino radiation properties. In what follows, I will probe the neutrino radiation field and its interaction with the fluid, and try to explain differences between the Full MC simulations, the Simple MC simulations, and the leakage data of Metzger and Fernández, 2014. I do most of the comparisons with snapshots from a time of 3 ms after the start of the dynamical simulation as differences between the methods are most striking then, though the composition and amount of ejecta are determined by the long-term evolution.

Mentioning one caveat is in order. The fluid snapshots were evolved in the dynamical simulations using the leakage neutrino treatment of Metzger and Fernández, 2014, and I simply perform MC transport on snapshots of the evolved fluid. Though the Simple MC transport employs the same set of neutrino interactions, the geometry and spectral shape of the neutrino radiation field are different from what is assumed in the leakage scheme. Fluid may be near thermal and weak equilibrium with neutrinos in the leakage scheme, but this is not necessarily true after switching to MC transport. This potential discrepancy can easily cause artificially large or small heating and leptonization rates. If the fluid were evolved with a MC treatment instead, it would likely be much closer to equilibrium with the MC neutrinos, and the rates might not be as high. Because of this, the comparisons between leakage and MC results indicate the qualitative effects, such as faster cooling and leptonization rates, but the

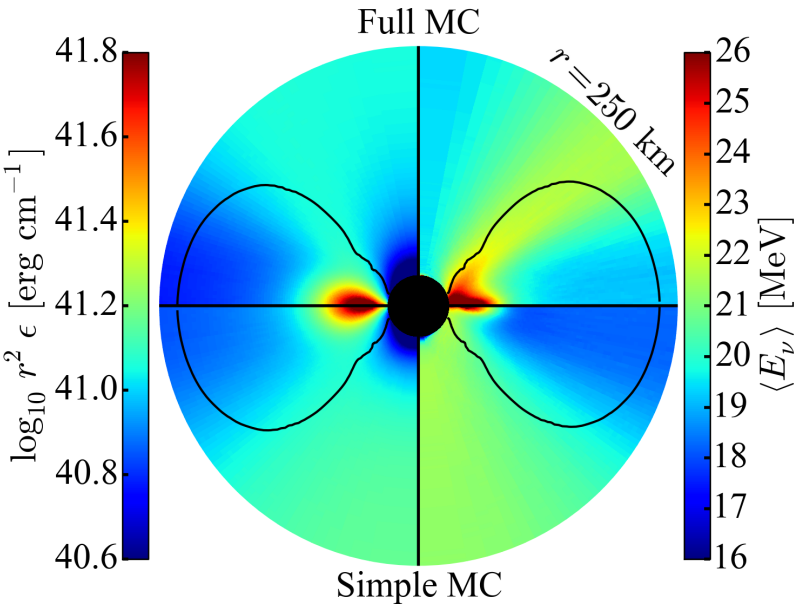

Figure 4.2: **Neutrino energy density and average energy (central BH)** at $t = 3$ ms. *Left hemisphere*: Neutrino energy density, summed over all species and multiplied by r^2 to remove effects of distance from the center. *Right hemisphere*: energy density-weighted average neutrino energy, averaged over all species. *Bottom hemisphere*: Simple MC results. *Top hemisphere*: Full MC results. The black curve is the $\rho = 10^6$ g cm^{-3} contour, below which Sedonu opacities and emissivities are set to zero. The outer radius on the plot is at 250 km and the inner radius is 30 km. The neutrino radiation field is very asymmetric and sensitive to the included physics. The disk casts a shadow as higher-energy neutrinos are preferentially absorbed. Much more asymmetry is present when the Full suite of physics is included.

magnitudes of the differences are likely not reliable. The effects of MC transport on the end results of dynamical simulations are thus difficult to determine. The dynamical simulations also begin with a disk of uniform electron fraction $Y_e = 0.1$, which is not initially in equilibrium with either leakage or MC neutrinos. Addressing this out-of-equilibrium issue requires the dynamical simulations to begin before the merger and to be coupled to MC neutrino transport, which I leave to future work.

Neutrino Radiation Field (Central BH)

In Figure 4.2 I show the spatial distribution of the neutrino radiation field at $t = 3$ ms for both Simple and Full neutrino physics. Though the plot includes all neutrino species, the radiation is dominated by electron anti-neutrinos. Most of the neutrino energy comes from the inner regions of the disk close to the central object, and the dense disk casts a shadow that reduces the neutrino luminosity and energy density at large radii near the equator. The inner boundary also blocks neutrinos from

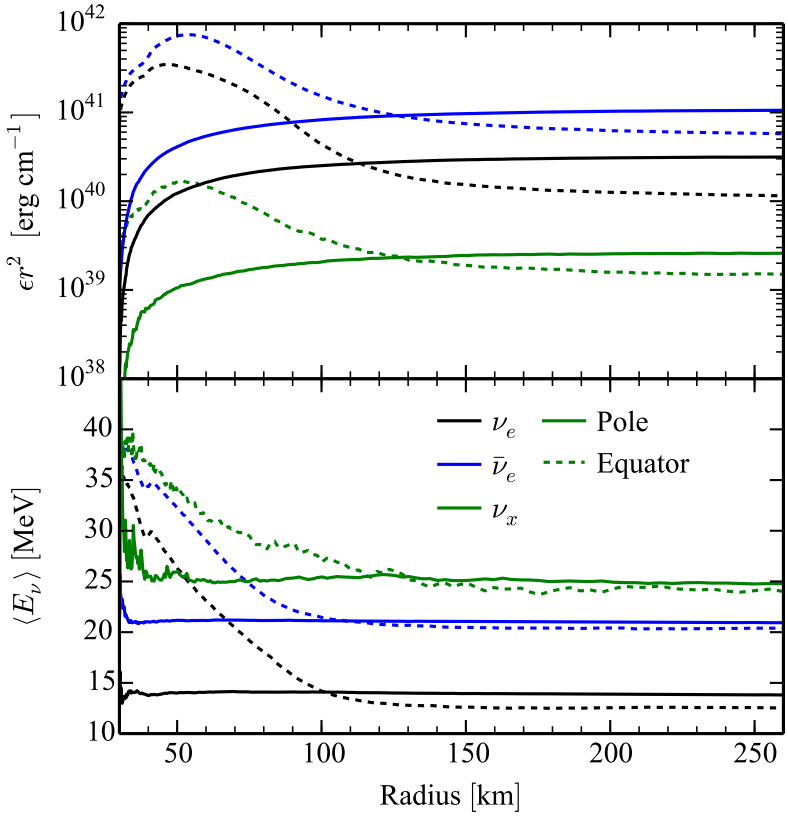

Figure 4.3: **Neutrino radiation profile (central BH)** from the Full MC simulation at $t = 3$ ms for all three simulated neutrino species. The neutrino radiation field is asymmetric and dominated by electron anti-neutrinos. *Top*: neutrino energy density along the pole (solid lines) and the equator (dashed lines), multiplied by r^2 to remove effects of distance from the center. *Bottom*: energy density-weighted average neutrino energy along radial lines. The green ν_x curves represent the sum of all four heavy lepton neutrino species.

moving to the other side of the disk and creates a polar shadow. The elastic electron scattering in the Full simulations results in higher opacities, which in turn deepens the equatorial and polar shadows. The Lorentz transformation of neutrinos in fluid moving at around $0.6c$ near the inner boundary increases the average energy of neutrinos emitted from the hot inner disk by $\sim 30\%$. Additionally, the neutrinos are beamed in the azimuthal direction, causing fewer of the higher-energy neutrinos coming from the inner parts of the disk to be present in the polar regions and more to be present along the 45° radial. With either set of physics, this is different from the neutrino radiation field described by Fernández and Metzger, 2013, which becomes spherical at large distances.

Profiles of the neutrino radiation field split into the different neutrino species are

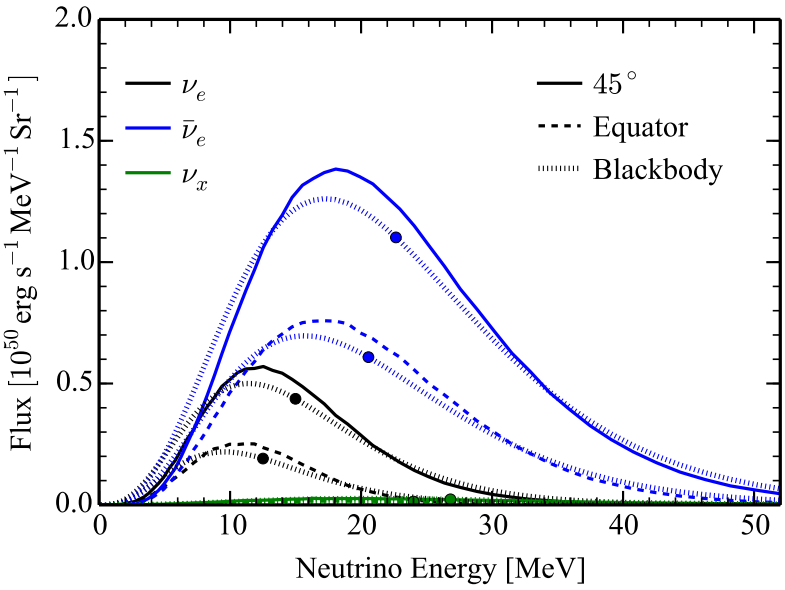

Figure 4.4: **Neutrino spectra (central BH)** from the Full MC simulation at $t = 3$ ms. Dashed lines are spectra of each neutrino species escaping from within 10° of the equator, while the solid lines are those from within 10° of the 45° cones, normalized by the solid angle covered by the respective regions. Overplotted for both directions (distinguished by proximity to the data curves) are dotted zero-chemical potential blackbody curves with the same total flux and average energy as the measured spectrum. The large dot on the blackbody curve indicates this average energy. For smoothness, the spectra are taken from the 2xEnergy run in Section 4.2. The escaping neutrino radiation is somewhat nonthermal and asymmetric.

shown in Figure 4.3. There is some noise at small radii due to a relatively small number of simulated neutrino packets present there. Along the equator, normalized neutrino energy density and average energy are much higher close to the black hole than farther out in the disk, since the higher-energy neutrinos are preferentially absorbed by the disk. Moving radially along the pole, the energy density increases quickly as more of the disk becomes visible. However, the average energy is always close to the average energy escaping from the disk listed in Table 4.4. In all directions, the neutrino species follow the same hierarchy, such that electron anti-neutrinos everywhere contribute most to the energy density and heavy lepton neutrinos everywhere have the highest average energy.

$\mathcal{L}_{\rm emit}$, $\mathcal{L}_{\rm escape}$, $\langle E_{\nu,{\rm emit}}\rangle$, and $\langle E_{\nu,{\rm escape}}\rangle$ in Table 4.4 describe the global lab-frame properties of the neutrinos that are emitted and of those that escape through the outer boundary. In the snapshot at 3 ms, there is more energy emitted as electron neutrinos than as electron anti-neutrinos, but this is before the initial data in the simulations

of Metzger and Fernández, 2014 has had any time to come into a quasi-equilibrium with the viscous heating and neutrino interactions. At all other times, electron anti-neutrino emission is stronger, reflecting a tendency of the fluid to relax to a higher electron fraction. The subsequent emission rates of all species decrease with time as the disk loses mass and cools. Heavy lepton neutrinos interact much more weakly with the fluid than do electron neutrinos and anti-neutrinos both in absorption and emission since they participate only in neutral-current reactions. This, combined with the low optical depths that prevent a blackbody distribution from building up, causes the heavy lepton neutrinos to always be subordinate to electron neutrinos and anti-neutrinos in energy density and in fluid heating and cooling.

If we assume the neutrinos form a zero-chemical potential blackbody distribution as is done in Metzger and Fernández, 2014, we can relate temperature to average energy through

$$\langle E_\nu \rangle = \frac{\int_0^\infty E_\nu B_{E_\nu}(0,T)\, dE_\nu}{\int_0^\infty B_{E_\nu}(0,T)\, dE_\nu} = 4.11 k_b T \ , \tag{4.7}$$

where E_ν is the neutrino energy, k_b is the Boltzmann constant, and $B_{E_\nu}(\mu, T)$ is the neutrino blackbody function at temperature T and chemical potential μ (Equation 3.36). While the density-weighted average fluid temperature at $t = 3\,\mathrm{ms}$ is around 3 MeV, the average emitted neutrino energy is between 26 and 29 MeV for all species. Thus, most of the neutrinos are created in the hottest regions of the disk very close to the black hole. The opacity to neutrinos scales approximately like E_ν^2 (e.g., Burrows, Reddy, and Thompson 2006) causing more higher-energy neutrinos to be absorbed and the average energy of escaping neutrinos to be much smaller than that of the emitted neutrinos. The heavy lepton neutrinos have the coolest emission temperature but the hottest escape temperature, since electron neutrinos and anti-neutrinos have much larger opacities and higher-energy neutrinos are preferentially absorbed.

The disk's self-irradiation in the leakage scheme is calculated as in Metzger and Fernández, 2014, and the global properties are summarized in Table 4.1. The temperature of the radiation in the leakage scheme is determined by an emissivity-weighted average and is the same for both electron neutrinos and anti-neutrinos. The average energy in Table 4.1 is computed from a zero-chemical potential blackbody of this temperature using Equation 4.7. Both the average energy and volume-integrated emission luminosities from the leakage data are much lower than those

computed by Sedonu, since the "emission" in the leakage scheme approximately accounts for immediate re-absorption in the same grid cell. The leakage and MC emission quantities then do not represent the same physics, but the difference further illustrates that the higher-energy neutrinos are re-absorbed locally while the lower-energy neutrinos are able to escape.

Using instead the Simple set of physics described in Table 4.2 does little to bring the leakage (Table 4.1) and Sedonu (Table 4.4) results closer together. However, it does result in significant deviations from the Full set of physics. In the following, I exclude individual pieces of physics to pinpoint the origin of the differences in the $t = 3$ ms snapshot. The exclusion of scattering predictably does nothing to the properties of the created neutrinos in the disk, but by decreasing the optical depth, allows more of the higher-energy neutrinos to escape. Ignoring special relativity results in a decrease of the emission luminosity and average energy of all species. Neglecting to correct for weak magnetism and recoil effects causes the electron anti-neutrino emission rate to increase by about 20%, but since most of the opacity is also increased by a similar amount, the escaping luminosity increases by only about 3%. The other species are minimally affected.

The low electron fraction throughout the disk causes electron neutrinos to be very likely to absorb onto neutrons, allowing few of them to escape. Their escape luminosity in Table 4.4 is around an order of magnitude lower than their emitted luminosity, indicating an average optical depth of $\tau \sim 3$ for electron neutrinos, $\tau \sim 1$ for electron anti-neutrinos, and $\tau \ll 1$ for heavy lepton species. Figure 4.4 shows neutrino spectra that further demonstrate the asymmetry of the escaping neutrino radiation. The leakage scheme does not yield data with which we can directly compare the escape spectra. However, I show that the spectra appear qualitatively similar in shape to zero-chemical potential blackbody spectra with the same average energy and total flux (dotted lines in Figure 4.4), though the MC spectra are somewhat pinched with peak energies higher by a few MeV.

Neutrino-Fluid Interaction (Central BH)

Different treatments of neutrino effects can have a significant impact on the fluid evolution. Panel A of Figure 4.5 shows rapid cooling in the densest parts of the disk and net heating above and below the equatorial plane in both the MC and leakage results at $t = 3$ ms. However, MC transport results in faster heating directly above the disk by more than an order of magnitude, a smaller cooling region,

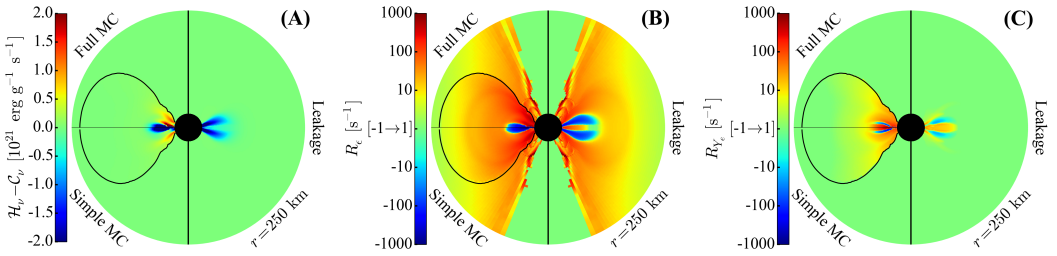

Figure 4.5: **Neutrino-fluid interaction (central BH)** at $t = 3$ ms. In each plot, the right half shows results calculated with neutrino leakage in the dynamical simulations of Metzger and Fernández, 2014, while the left half is calculated by Sedonu. Each quadrant of Sedonu results depicts only half of the simulation domain. The top left quadrant uses the Full set of physics, while the bottom left uses the Simple set of physics. Panel A shows the difference between absorptive heating and emissive cooling. Panels B and C depict the relative rate of change of internal energy (including viscous heating) divided by internal energy and of electron fraction, respectively. Red represents a large positive rate of change while blue represents a large negative rate of change. Any rate of change whose magnitude is smaller than 1 s^{-1} is plotted as 0. The outer radius on each plot is at 250 km and the inner radius is 30 km. The black curve is the $\rho = 10^6$ g cm^{-3} contour, below which Sedonu opacities and emissivities are set to zero. Using MC neutrino transport would likely significantly affect the thermal and compositional evolution of the disk.

and much faster cooling on the equator than leakage, making the leakage heating nearly invisible in Panel A of Figure 4.5. The differences are largely due to the approximate nature of the disk self-irradiation and leakage scheme of Metzger and Fernández, 2014, the accuracy of which suffers especially at the midplane of the disk. For efficiency, the leakage scheme calculates the optical depth at a given point to be $\tau = \sigma \min\{r, H_\perp, H_\parallel\}$, where σ is the opacity, r is the radius, and $H_\perp$ and $H_\parallel$ are the vertical and horizontal pressure scale heights, respectively. This optical depth calculation is only accurate to within a factor of a few. MC transport allows neutrinos to escape in any direction rather than just vertically and radially, increasing the amount of escaping neutrinos. Using Full neutrino physics dramatically increases the heating rate just above the hottest part of the disk due to special relativistic effects boosting the luminosity and average energy of neutrinos, and the larger global heating rate is also reflected in a smaller value of $C_\nu - \mathcal{H}_\nu$ in Table 4.4.

Viscosity, neutrino heating, and neutrino cooling all affect the thermal evolution of the disk. The relative importance of neutrinos and viscosity can be seen in the amount of mass for which neutrino heating is larger than viscous heating in Table 4.4.

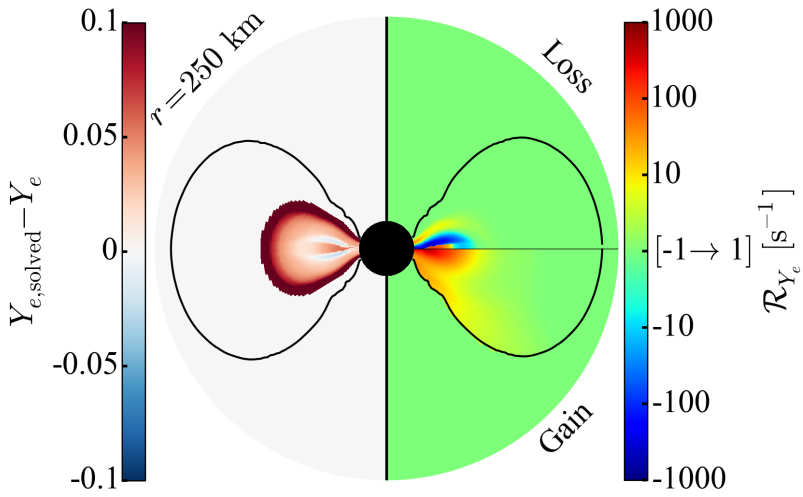

Figure 4.6: **Equilibrium electron fraction (central BH)** at $t = 3$ ms. *Left Hemisphere:* equilibrium electron fraction at which the net lepton number absorption rate is equal to the net lepton number emission rate. The equilibrium solver is unreliable below ~ 1.5 MeV as the energy grid ceases to be able to resolve the neutrino distributions, so $Y_{e,\mathrm{solved}} - Y_e$ at locations with a temperature less than this is plotted as zero. *Right Hemisphere:* rate of change of electron fraction, as in Figure 4.5, but separately depicting that caused by emission (top) and absorption (bottom). The black curve is the $\rho = 10^6$ g cm^{-3} contour, below which Sedonu opacities and emissivities are set to zero. The outer radius on the plot is at 250 km and the inner radius is 30 km.

At the 3 ms Full MC snapshot, $3.15 \times 10^{-3} M_\odot$ is heated more strongly by neutrinos than viscosity, though after this time the number drops very quickly. Simple neutrino physics causes this mass to be 60% smaller, and in the Leakage simulation this mass is almost zero. In Panel B of Figure 4.5 I show $R_\epsilon = (1/\epsilon) d\epsilon/dt$, the relative rate of change of internal energy including the viscous heating rate used in the dynamical simulations of Metzger and Fernández, 2014, scaled by each point's current energy density. The extra heated wings above the disk in the MC simulation cause the internal energy to change several times faster than leakage would suggest. More dramatically, the MC simulations show neutrino cooling dominating viscous heating along the equator, while the opposite is true in the leakage results. From this I would expect a stronger neutrino-driven wind, a thinner disk, and much faster disk cooling, though dynamical simulations would be required to investigate this quantitatively.

In a similar manner, I show $R_{Y_e} = dY_e/dt$ in Panel C of Figure 4.5. There is very little difference between the Simple and Full MC simulations, though both represent a significant departure from the leakage data. In all cases, electron fraction is

increasing near the equator as the low-electron fraction fluid is emitting primarily electron anti-neutrinos. Above the equator, there is a pattern of regions of both increasing and decreasing electron fraction. The right half of Figure 4.6 shows that this pattern of increasing and decreasing electron fraction is caused by neutrino emission rather than absorption, indicating that variations in density and temperature cause the equilibrium electron fraction to vary. In the left half of Figure 4.6, I show the difference between the current electron fraction and the equilibrium electron fraction (including neutrino interactions, see Section 4.2). The initial conditions of the dynamical simulation began with an electron fraction of $Y_e = 0.1$, leaving the center of the disk far from equilibrium, and the slower rates in the leakage scheme prevent it from coming into equilibrium more quickly.

As the disk spreads, cools, and accretes onto the central BH, neutrinos affect the evolution of the disk and outflow more slowly. However, MC transport differs significantly from leakage for at least several tens of milliseconds. The volume-integrated neutrino cooling minus heating through the 3 ms snapshot is up to $\sim 38\%$ larger in the Full MC simulations than in the Leakage ones. At all later times, though, the Leakage simulations cool faster by up to 22%. Throughout the disk's evolution MC results in a higher leptonization rate, up to 7.7 times that of the Leakage simulation at 3 ms. This is due to the way the leakage scheme treats optical depths, as discussed in Section 4.6.

In Figure 4.7, I show the difference between the rates of change of internal energy due only to neutrinos ($\mathcal{R}'_\epsilon$) and electron fraction ($\mathcal{R}_{Y_e}$) calculated using leakage and using MC transport. Though the differences are most striking at 3 ms, we still see a significantly larger $\mathcal{R}'_\epsilon$ near the 45° radials and a larger $\mathcal{R}_{Y_e}$ near the midplane in the MC results at 30 ms. In these simulations, Sedonu takes the opacity at densities lower than 10^6 g cm^{-3} to be zero, so the leakage scheme shows more neutrino heating for a very small amount of mass outside the disk. However, the left and right halves of Panel B of Figure 4.5 outside of the region covered by Sedonu appear almost identical because in this region viscous heating is completely dominant. Comoving frame viscous heating is identical in all cases, but time dilation slightly modifies the heating rates in all but the Simple and NoRel cases. At 300 ms neutrino cooling by leakage is more efficient than Monte Carlo cooling, though the differences are only apparent at the densest part of the disk and are anyway dominated by viscous heating.

For calculating opacities and interaction rates, NuLib requires as input an EOS

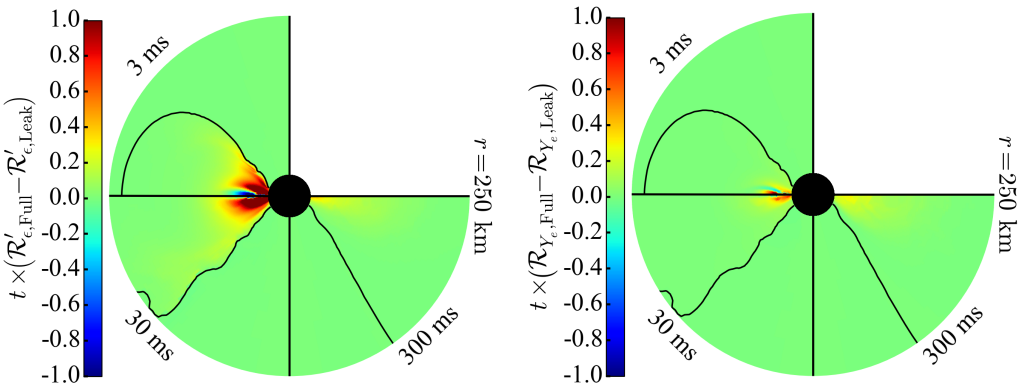

Figure 4.7: **Leakage-MC difference (central BH)**. Full MC transport results differ significantly from leakage results for at least several tens of milliseconds. Difference between the Full and Leakage relative rate of change of internal energy ignoring viscosity (top panel) and electron fraction (bottom panel), multiplied by the snapshot time in order to estimate the potential impact of improved neutrino transport on dynamical simulations. The black curve is the $\rho = 10^6\,\mathrm{g\,cm^{-3}}$ contour, below which Sedonu opacities and emissivities are set to zero. The outer radius on the plot is at 250 km and the inner radius is 30 km. In both plots, values larger than unity imply that if such rates continued for a time equal to the snapshot time, the difference between MC and leakage would be dynamically important. For this plot, data is taken from the 2xEnergy run in Section 4.2 for increased solution accuracy.

to determine the chemical potentials of the particles involved in each interaction. Thus, different EOS result in different interaction rates. In addition to the fiducial Helmholtz EOS (Timmes and Swesty, 2000), I repeat the calculations using the LS220 (J. M. Lattimer and Swesty, 1991) and the H. Shen (H. Shen et al., 2011) EOS. I find that the choice of EOS has no significant effect, as is demonstrated by the results summarized in Table 4.4. This is reassuring, since all of the neutrino emission and absorption occurs at sub-nuclear densities where the details of the treatment of the strong force are less significant.

4.4 Results (Central HMNS)

Following the merger of two neutron stars, the central object that forms may be a black hole, a stable neutron star, or an only temporarily-stable hypermassive neutron star (HMNS), depending on details of the equation of state and the object's mass (e.g., Kaplan et al. 2014). In this section, I bracket the parameter space by repeating the analysis of the previous section, but with simulations including an HMNS assumed to be permanently stable. The inner boundary, which models an HMNS by reflecting matter, prevents mass from accreting through it and leads to a disk that stays hot and

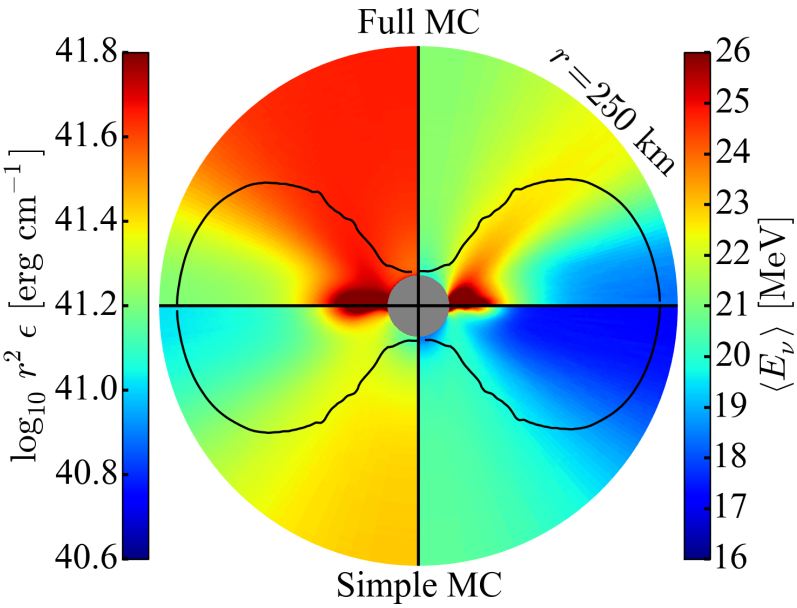

Figure 4.8: **Neutrino energy density and average energy (central HMNS)** at $t = 3$ ms. The quantities shown are the same as in Figure 4.2, but using the HMNS snapshot. *Left hemisphere*: Neutrino energy density, summed over all species and multiplied by r^2 to remove effects of distance from the center. *Right hemisphere*: Neutrino energy density-weighted average energy, averaged over all species. *Bottom hemisphere*: Simple MC results. *Top hemisphere*: Full MC results. The black curve is the $\rho = 10^6$ g cm^{-3} contour, below which Sedonu opacities and emissivities are set to zero. The outer radius on the plot is at 250 km and the inner radius is 30 km. The neutrino radiation field is very asymmetric and sensitive to the included physics. The disk casts a shadow as higher-energy neutrinos are preferentially absorbed. Much more asymmetry is present when the Full suite of physics is included. Both the energy density and average neutrino energy are higher than in the BH case. At this point in time, the luminosities and average energies of $\{\nu_e, \bar{\nu}_e, \nu_x\}$ from the central HMNS are set to $\{10.2, 10.2, 40.8\}$ B s^{-1} and $\{16.4, 20.5, 20.5\}$ MeV, respectively.

massive for a much longer time. As did Metzger and Fernández, 2014, I assume the HMNS emits neutrinos with a zero-chemical potential blackbody distribution and the average energies listed in Table 4.1. Heavy lepton neutrinos, when present, have the same luminosity and average energy as electron anti-neutrinos. Table 4.4 lists the simulations I run and the corresponding global properties of the fluid and radiation field.

Neutrino Radiation Field (Central HMNS)

As seen in Figure 4.8, in the presence of an HMNS the neutrino radiation field at $t = 3$ ms shows the same disk and polar shadows and relativistic beaming as

when a BH is present, though the neutrino energy densities and average energies are somewhat higher due to the hotter fluid and extra irradiation from the HMNS. The Full physics neutrino radiation field shows higher energy densities by a factor of ~ 1.5 in the free streaming regions outside the disk than the Simple physics neutrino radiation field. This is due mostly to the production of copious amounts of heavy lepton neutrinos in the HMNS, which have comparatively small cross sections and so are able to pass much more easily through the disk. As in the BH case, special relativity increases the average neutrino energy by up to $\sim$ 30%, especially 45 degrees from the pole.

$\mathcal{L}_{\rm emit}$, $\mathcal{L}_{\rm escape}$, $\langle E_{\nu,\rm emit}\rangle$, and $\langle E_{\nu,\rm escape}\rangle$ in Table 4.4 describe the global lab-frame properties of the neutrinos in the simulations with an HMNS. Since the initial disk conditions are the same for both dynamical simulations, the properties of the neutrinos emitted from the disk at $t = 0$ ms are also identical. The extra irradiation from the HMNS results in a slower net cooling rate of the disk at early times. After the first 3 ms, the large disk mass around the HMNS causes the net cooling rate to be much larger, though the higher temperatures and amount of irradiation by nearly equal numbers of electron neutrinos and anti-neutrinos imposed from the HMNS boundary condition (see Section 4.2) cause a slower change in electron fraction than in the BH case. The high densities and viscously-amplified temperatures near the HMNS cause 1.9 times as much neutrino energy to be emitted from the disk, though the vast majority is immediately re-absorbed. A combination of the HMNS's extra radiation and the higher disk luminosity causes the escaping neutrino luminosity to be larger by factors of 2.8, 1.5, and 90 for ν_e, $\bar{\nu}_e$, and ν_x, respectively. The energies of the escaping neutrinos are similar to those in the BH case, but the ν_x average energy is decreased due to dilution from the HMNS. Note that in simulations that include the HMNS, the HMNS is much hotter than the disk (e.g., Dessart, Ott, et al. 2009), but I parameterize the neutrinos being emitted from the HMNS for consistency with the dynamical simulations of Metzger and Fernández, 2014.

Figure 4.9 shows a complicated interaction between radiation from the HMNS and that from the disk. Along the poles there is an initial dip in intensity as neutrinos are absorbed by a layer of matter just outside of the HMNS. Moving outward along the pole, as the disk comes into view, the electron neutrinos and anti-neutrinos emitted from the disk bump their respective intensities up again. Though they interact more weakly than electron neutrinos and anti-neutrinos, heavy lepton neutrinos are scattered by the disk, as seen in the divergence of the pole and equatorial energy

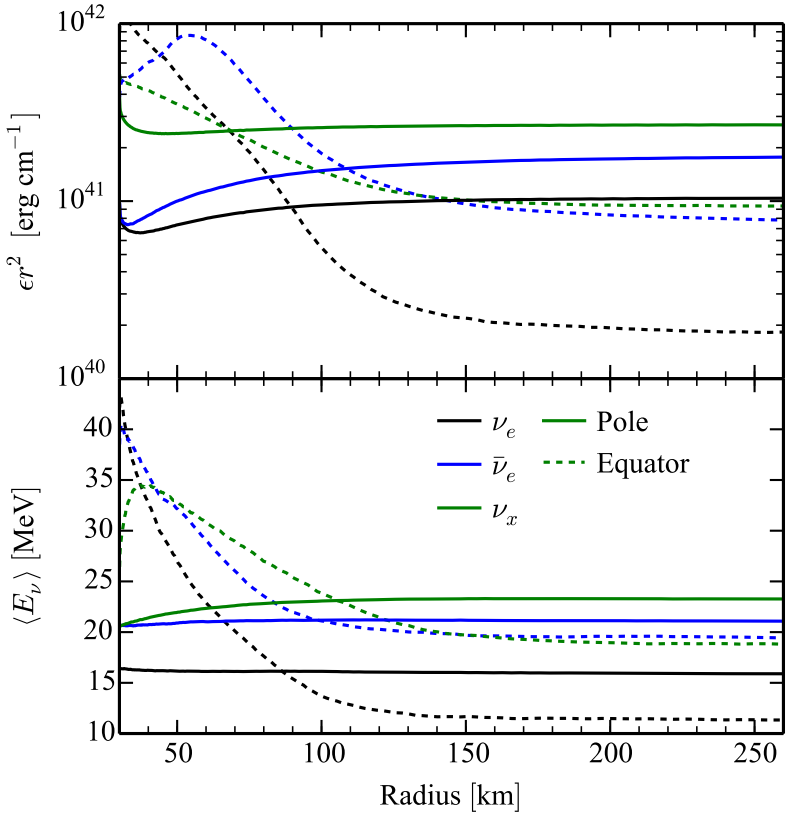

Figure 4.9: **Neutrino radiation profile (central HMNS)** from the Full MC simulation at $t = 3$ ms for all three simulated neutrino species. The quantities shown are the same as in Figure 4.3. The neutrino radiation field is asymmetric and dominated by electron anti-neutrinos. *Top*: neutrino energy density along the pole (solid lines) and the equator (dashed lines), multiplied by r^2 to remove effects of distance from the center. *Bottom*: energy density-weighted average neutrino energy along radial lines. The green ν_x curves represent the sum of all four heavy lepton neutrino species. Note the difference in the y-axis scale compared with Figure 4.3. The hierarchy between neutrino species is shuffled at small radii due to competing emission from the HMNS and the disk, and from disk absorption.

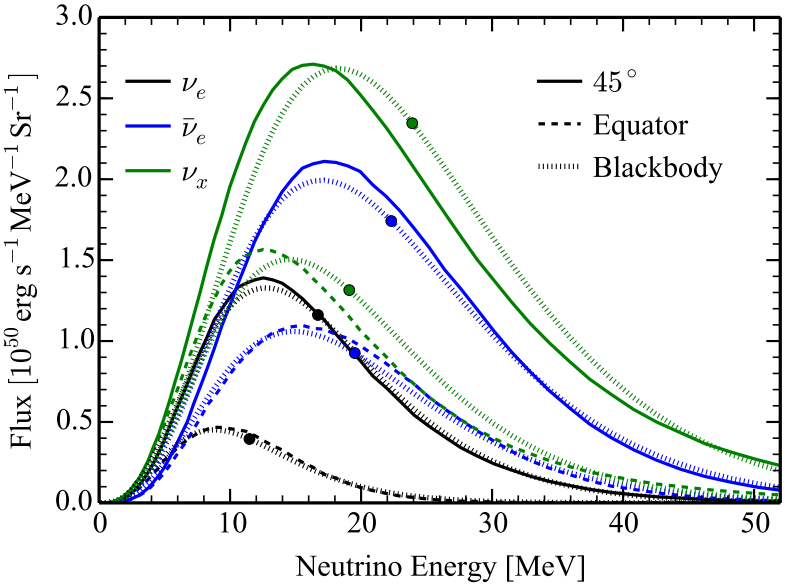

Figure 4.10: **Neutrino spectra (central HMNS)** from the Full MC simulation at $t = 3$ ms. The quantities shown are the same as in Figure 4.4, though note that the vertical axis differs. The escaping neutrino radiation is somewhat nonthermal and asymmetric. Dashed lines are spectra of each neutrino species escaping from within 10° of the equator, while the solid lines are those from within 10° of the 45° cones, normalized by the solid angle covered by the respective regions. Overplotted for both directions (distinguished by proximity to the data curves) are dotted zero-chemical potential blackbody curves with the same total flux and average energy as the measured spectrum. The large dot on the blackbody curve indicates this average energy. For smoothness, the spectra are taken from the 2xEnergy run in Section 4.2. The heavy lepton neutrinos are near blackbodies since most come from the central HMNS.

density. In fact, the scattering combined with Doppler boosting in the Full simulation cause the average heavy lepton neutrino energy peak in the inner regions of the disk, and the scattered neutrinos even cause radially increasing average neutrino energy along the poles. Below 150 km along the equator, electron and heavy lepton neutrino intensities decline as their emission from the HMNS is absorbed by the disk. The dense part of the disk below 60 km is such a strong emitter of electron anti-neutrinos, however, that the intensity rises before falling again farther out. In all cases, the neutrino radiation field becomes free-streaming after a radius of $\sim$ 150 km, indicated by horizontal lines in Figure 4.9.

Figure 4.10 demonstrates the asymmetry of the neutrino radiation field and its departure from a zero-chemical potential blackbody. At all times, the irradiation from the HMNS makes the net escaping flux from heavy lepton neutrinos comparable

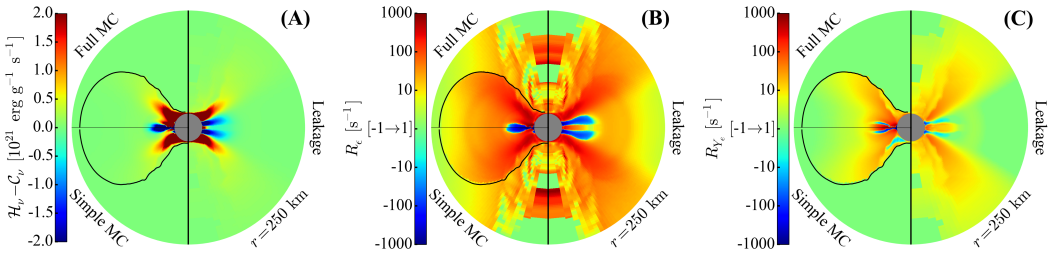

Figure 4.11: **Neutrino-fluid interaction (central HMNS)** at $t = 3$ ms. The quantities shown are the same as in Figure 4.5. In each plot, the right half shows results calculated with neutrino leakage in the dynamical simulations of Metzger and Fernández, 2014, while the left half is calculated by Sedonu. Each quadrant of Sedonu results depicts only half of the simulation domain. The top left quadrant uses the Full set of physics, while the bottom left uses the Simple set of physics. Panel A shows the difference between absorptive heating and emissive cooling. Panels B and C depict the relative rate of change of internal energy (including viscous heating) divided by internal energy and of electron fraction, respectively. Red represents a large positive rate of change while blue represents a large negative rate of change. Any rate of change whose magnitude is smaller than 1 s^{-1} is plotted as 0. The outer radius on each plot is at 250 km and the inner radius is 30 km. The black curve is the $\rho = 10^6$ g cm^{-3} contour, below which Sedonu opacities and emissivities are set to zero. Using MC neutrino transport would likely significantly affect the thermal and compositional evolution of the disk.

to that from electron anti-neutrinos, in contrast to the BH case.

Just as with the BH snapshots, using Full physics adds a scattering opacity which prevents neutrinos from escaping as easily as with Simple physics, causing Simple physics to allow for a larger cooling and leptonization rate, as well as naturally larger escape luminosities. Full physics also increases the neutrino creation rate through weak magnetism corrections and Lorentz transformations. Even though a large number of heavy lepton neutrinos are produced by the HMNS, Figure 4.9 shows that they contribute much less to disk heating than electron anti-neutrinos do. This is because they deposit energy into the fluid only through NuLib's approximate treatment of inverse Bremsstrahlung and neutrino pair annihilation. Excluding heavy lepton neutrinos only results in the disk cooling 3% more quickly. Otherwise, the exclusion of various elements of physics has the same effect as in the BH snapshots.

Neutrino-Fluid Interaction (Central HMNS)

Figure 4.11 describes the interaction of neutrinos with the background fluid. Near the equator, the structures of the heating rates, R_ϵ, and R_{Y_e} are very similar to the

BH case. Panel A shows the local neutrino heating rates, the volume integrals of which are displayed in Table 4.4. Full MC, as in the BH case, shows slower integrated neutrino cooling than the Simple MC simulation (factor of ~ 0.91) but much faster cooling than the Leakage simulation (factor of ~ 2.2). The relative effects of neutrinos and viscosity can be seen in the amount of mass for which neutrino heating is larger than viscous heating. This mass is $\sim 26\%$ larger in the Full MC simulations than in the Simple MC simulation and ~ 5.6 times larger than in the Leakage simulation. This is visible in the relative sizes of the neutrino-heated regions above and below the disk.

The rates of change of internal energy in Panel B of Figure 4.11 demonstrate that both Full and Simple MC neutrinos escape from and pass through the densest regions of the disk more easily than leakage allows, causing visibly faster heating near the equator beyond the disk. Similar to the heating rates, the volume-integrated leptonization rate indicated by the Full MC simulation is faster than that predicted by the Leakage simulation. The slight difference between the Simple and Full MC simulations is also reflected in Table 4.4. Simple physics decreases opacities and results in a faster increase in electron fraction, mostly near the HMNS above the disk. Monte Carlo allows neutrinos to escape easier than they could in the Leakage simulation and hence has higher cooling and leptonization rates.

Although the differences stem from the same effects, the Full MC net neutrino cooling rate is at times a factor of 8 higher than the leakage net neutrino cooling rate (at $t = 30\,\mathrm{ms}$), though this is likely artificially high due to the out-of-equilibrium effects discussed in Section 4.3. Unlike in the BH case, MC net neutrino cooling minus heating is larger than that from leakage calculations through 300 ms since the disk retains its mass, and the greater ease of escape for MC neutrinos allows the disk to absorb less energy from the HMNS neutrinos and to cool more quickly. In addition, the HMNS emits nearly equal numbers of electron neutrinos and anti-neutrinos, but the easier escape allowed to MC neutrinos means the HMNS neutrinos are not as effective at bringing the electron fraction up. At $t = 3\,\mathrm{ms}$, MC leads to faster cooling than leakage does by a factor of ~ 2.2 and leptonization by a factor of ~ 2.7. However, unlike the BH case, after the 3 ms snapshot MC leptonization is slower than leakage. By the 3 s snapshot, the dynamical simulation has overshot MC's equilibrium and so the MC disk is slowly heating rather than cooling.

The disk mass remains in the HMNS simulation for almost a hundred times as long as it does in the BH snapshots, and neutrinos from both disk and HMNS

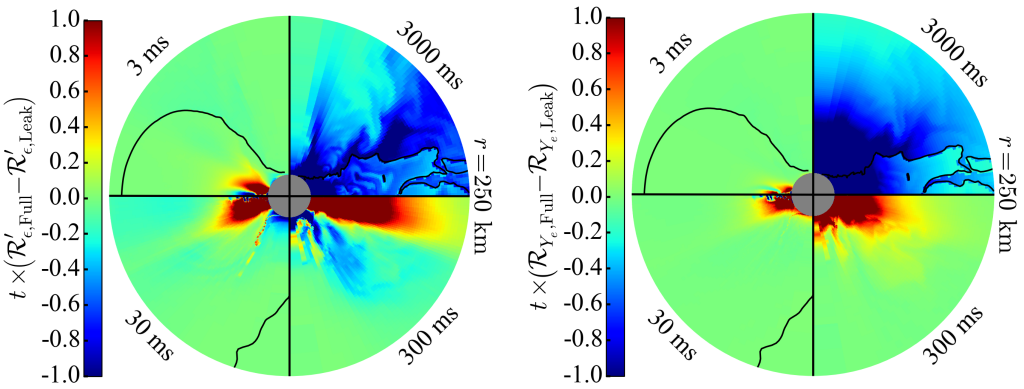

Figure 4.12: **Leakage-MC difference (central HMNS)**. The quantities shown are the same as in Figure 4.7. Difference between the Full and Leakage relative rate of change of internal energy ignoring viscosity (top panel) and electron fraction (bottom panel), multiplied by the snapshot time in order to estimate the potential impact of improved neutrino transport on dynamical simulations. The black curve is the $\rho = 10^6$ g cm^{-3} contour, below which Sedonu opacities and emissivities are set to zero. At 300 ms everything in the image is above the density cutoff. The outer radius on the plot is at 250 km and the inner radius is 30 km. In both plots, values larger than unity imply that if such rates continued for a time equal to the snapshot time, the difference between MC and leakage would be dynamically important. Full MC transport results differ significantly from leakage results at all times. For this plot, data is taken from the 2xEnergy run in Section 4.2 for increased solution accuracy.

emission play an important role for at least ten times as long as in the BH snapshots. Figure 4.12 compares the leptonization rates and the difference between cooling and heating rates due only to neutrinos through the 3 s snapshot. The data in the 3 ms quadrants effectively replicates information conveyed in Figure 4.11 by showing that MC transport allows the disk to cool faster, heats the regions above the disk faster, and allows the disk Y_e to change more quickly. In the 30 and 300 ms quadrants, leakage predicts that neutrinos are unable to cool the matter in the equatorial plane, but are able to cool the disk above and below the equator. MC transport, on the other hand, predicts some cooling in isolated domains on the equator and next to the HMNS at high latitudes, but neutrino heating balances neutrino cooling in the mid-latitude disk regions. In addition, leakage predicts much stronger heating of the low-density polar regions, a trend which continues to be evident at later times. In the 3 s quadrants, very little mass remains in the disk and the predicted leakage rates are far in excess of the MC ones, just as they were in the low-density regions in previous snapshots. This is all consistent with the above statement that MC allows

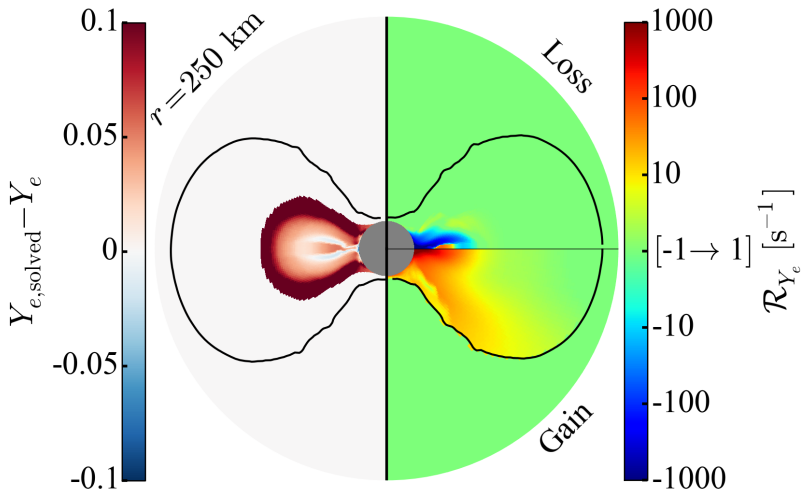

Figure 4.13: **Equilibrium electron fraction (central HMNS)** at $t = 3$ ms. The dense region of the disk is far from equilibrium, as is the fluid in contact with the HMNS at high latitudes. The quantities shown are the same as in Figure 4.6. *Left Hemisphere:* equilibrium electron fraction at which the net lepton number absorption rate is equal to the net lepton number emission rate. The equilibrium solver is unreliable below 1 MeV as the energy grid ceases to be able to resolve the neutrino distributions, so $Y_{e,\mathrm{solved}} - Y_e$ at locations with a temperature less than this is plotted as zero. *Right Hemisphere:* rate of change of electron fraction, as in Figure 4.5, but separately depicting that caused by emission (top) and absorption (bottom). The black curve is the $\rho = 10^6$ g cm^{-3} contour, below which Sedonu opacities and emissivities are set to zero. The outer radius on the plot is at 250 km and the inner radius is 30 km.

neutrinos to escape more easily than leakage does.

I solve for the equilibrium electron fraction in Figure 4.13. The results are very similar to the BH case. The leakage neutrinos effectively interact more strongly than MC neutrinos do, which causes the fluid in the low-density polar regions to an increase in electron fraction through absorption of electron neutrinos from the HMNS in the dynamical simulation, bringing it closer to equilibrium. In the main region of the disk, the fluid is below the equilibrium electron fraction since there is a sufficiently large amount of mass that neutrinos have not yet been able to significantly raise the electron fraction. If significant neutrino processing occurs before the disk is formed (i.e., before the initial conditions of the dynamical simulations of Metzger and Fernández, 2014), the electron fraction would be higher and not as far from equilibrium.

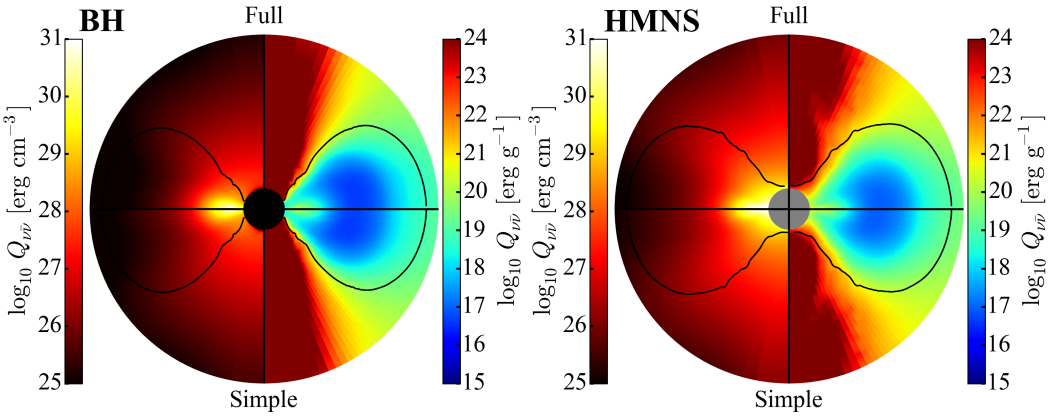

Figure 4.14: **Neutrino annihilation rates** at $t = 3$ ms for the BH case (top panel) and the HMNS case (bottom panel). *Left hemisphere*: annihilation rate per unit volume. *Right hemisphere*: the same annihilation rate per unit mass. *Top hemisphere*: Full MC simulations. *Bottom hemisphere*: Simple MC simulations. The outer curve is the $\rho = 10^6$ g cm^{-3} contour, below which Sedonu opacities and emissivities are set to zero. The outer radius on the plot is at 250 km and the inner radius is 30 km. Most annihilation occurs in the dense disk, but is most significant per unit mass along the poles.

4.5 Neutrino Pair Annihilation

I calculate neutrino pair annihilation rates in a post-processing step after neutrinos have finished propagating through the disk. The resulting rates are plotted in Figure 4.14 for the 3 ms snapshots with both BH and HMNS backgrounds, and volume-integrated rates are given for every snapshot in Table 4.4. The NoPair simulations do not include pair processes in the NuLib tables, but the annihilation post-processing requires only neutrino distribution functions and does not rely on the NuLib tables. In the sparse polar regions, the density is low enough that annihilation would rapidly increase the temperature and entropy, which has the potential to generate a rapid outflow. However, annihilation accounts for at most $\sim 4\%$ of the global energy gain/loss rate in any snapshot with either central object, and so will not dramatically affect the dynamics of most of the disk mass. In order to better estimate the role annihilation would have in driving a relativistic jet, I integrate only over regions less than 45° from the poles. This excludes annihilation in the bulk of the disk and in regions far from the poles, which are either too dense or too far from the pole to contribute to acceleration along the poles. The ratio of the total annihilation to that just within 45° of the poles can be as high as 120 in the BH snapshots (at 3 ms) and 220 in the HMNS snapshots (at 30 ms). Determining how much mass and energy is driven by annihilation, and whether this can actually

produce a jet, would require including annihilation rates in the dynamical simulation.

An order-of-magnitude estimate of the total energy deposited in polar regions from neutrino pair annihilation can be found by time interpolating the volume-integrated values of annihilation rate given in Table 4.4 and integrating assuming that $\mathcal{H}_{\nu\bar{\nu}} = Ct^k$, where k and C are parameters set to create a piecewise-continuous interpolation. Integrating this interpolation for the Full physics simulations, I find that the total amount of energy deposited is $E_{\nu\bar{\nu},\mathrm{net}} = 2.2 \times 10^{48}$ erg after 300 ms for the BH case and $E_{\nu\bar{\nu},\mathrm{net}} = 1.8 \times 10^{50}$ erg after 3 s for the HMNS case. If for the reasons above I include only the volume within 45° of the poles as in Table 4.4, the integrated deposited energy becomes $E_{\nu\bar{\nu},\mathrm{net}} = 2.8 \times 10^{46}$ erg for the BH case and $E_{\nu\bar{\nu},\mathrm{net}} = 1.9 \times 10^{48}$ erg for the HMNS case. However, $10^{48} - 10^{50}$ erg s^{-1} is required to launch a GRB jet (e.g., Lee and Ramirez-Ruiz 2007). Given the assumptions used in both the MC neutrino transport and the dynamical simulations of Metzger and Fernández, 2014, this calculation is certainly not accurate enough to definitively rule out the possibility of an annihilation-driven $e^+ - e^-$ jet, but it is on the lower end of this energy requirement.

The effects of various approximations on the annihilation rate at 3 ms for both the BH and HMNS cases are also summarized in Table 4.4. Though special relativity increases the average neutrino energy, it also beams the neutrinos along similar trajectories in the azimuthal direction, which decreases the relative angle between neutrinos and causes the NoRel annihilation rate to be higher than the Full rate by $\sim 44\%$ in the BH snapshot and $\sim 13\%$ in the HMNS snapshot. Scattering off of rapidly moving fluid boosts neutrino energies and so the annihilation rate in the NoScat simulation of the BH snapshot is $\sim 5\%$ lower than in the Full simulation. Additionally, scattering causes neutrinos that would otherwise have passed straight through the disk to be deflected up toward the polar regions, and together with the increased neutrino energy this results in a $\sim 18\%$ increase in the annihilation rate in the HMNS snapshot. The weak magnetism correction results in a smaller escape luminosity of electron anti-neutrinos, which decreases the annihilation rate by $\sim 5\%$ in the BH snapshot and $\sim 2\%$ in the HMNS snapshot. In the BH snapshots, so few heavy lepton neutrinos are produced that they provide essentially no additional contribution to pair annihilation rates, but the heavy lepton neutrinos emitted from an HMNS can increase the global annihilation rate by $\sim 20\%$. These numbers apply only to the 3 ms snapshots, but indicate the direction and approximate relative magnitude of the effect each piece of physics has on the instantaneous annihilation

rate.

4.6 Discussion

Alhough MC neutrino transport is a less approximate treatment of neutrinos than leakage, it should be noted that there are still many approximations being made. The largest is the neglect of general relativity, which would red/blueshift neutrinos moving outward/inward, respectively, and would bend the neutrino trajectories along geodesics. Previous works have indicated that this following of geodesics causes neutrino trajectories to intersect at higher angles, increasing the annihilation rates by at most a factor of two (Asano and Fukuyama, 2000; Asano and Fukuyama, 2001; W. A. Miller et al., 2003; Birkl et al., 2007; Harikae et al., 2010). Moreover, the step between depositing neutrino energy and building a jet cannot be determined by stationary simulations. Neutrino annihilation in the very sparse regions would also result in a very large entropy per baryon and thus a very efficient r-process even in matter that is barely neutron-rich, but the amount of mass in the polar regions is so small that the amount of r-process elements would be insignificant (Fernández, Quataert, et al., 2015).

Second, the annihilation kernels I use do not account for final-state electron and positron blocking, and are valid only for neutrinos with energies much larger than the electron rest mass (see Section 4.2). Third, neutrinos are fermions, and Pauli exclusion in regions where neutrinos are degenerate should affect their trajectories (e.g., H.-T. Janka, Dgani, and van den Horn 1992). I account for the fermionic nature of neutrinos only in their interactions with matter and not in their propagation, but the very low degeneracy of the neutrinos makes this a good approximation. Fourth, scattering kernels are actually inelastic and anisotropic, but I treat them as elastic and isotropic, and include a correction factor to approximate "effective" anisotropic scattering (e.g., Burrows, Reddy, and Thompson 2006), and I ignore inelasticity for the sake of simplicity. Since scattering opacities can have a significant impact on the neutrino radiation field, proper treatment of inelastic and anisotropic scattering could become an important source of energy deposition as, e.g., in the context of core-collapse supernovae (Lentz, Mezzacappa, Messer, Liebendörfer, et al., 2012). Finally, the opacities in the outskirts of the disk where $T <\sim 0.5$ MeV depend on the composition, which is likely not in NSE. However, addressing these approximations is beyond the current capabilities of Sedonu and I defer to future work to evaluate their importance more carefully.

We see very significant differences in the cooling and leptonization rates between MC transport and leakage. The rate of energy loss predicted by MC transport is consistently larger than that predicted by leakage, but some systematic error is not unexpected from such an approximation and I expect the MC neutrinos to be out of equilibrium with the fluid evolved with the leakage scheme. In the BH snapshots, the global leptonization rates calculated by MC transport are ~ 7 times larger than those calculated by leakage through the 30 ms snapshot. Since neutrino opacities scale roughly with the square of the neutrino energy (e.g., Burrows, Reddy, and Thompson 2006), the leakage scheme used by Metzger and Fernández, 2014 attempts to account for the energy loss rate by calculating the optical depth based on the opacity of the fluid at the neutrino energy

$$\begin{aligned} \langle E_\nu \rangle &= \sqrt{\frac{\int_0^\infty E_\nu^2 B_\nu(0,T)\, dE_\nu}{\int_0^\infty B_\nu(0,T)\, dE_\nu}} \\ &= \sqrt{\mathcal{F}_5(0)/\mathcal{F}_3(0)} = 4.56\, k_B T \ , \end{aligned} \tag{4.8}$$

where $\mathcal{F}_n(\mu)$ are Fermi integrals of order n Equation 3.38). Note that here I assume the chemical potential is zero, as do Metzger and Fernández, 2014. When applied to energy escape, this accounts for the fact that low-energy neutrinos are able to escape more easily than higher-energy neutrinos due to the scaling of the opacity with neutrino energy. However, this choice of energy is designed to properly account for energy loss, not lepton number change. If we repeat the same exercise, but replace $B_\nu(T)$ with $B_\nu(T)/E_\nu$ to represent number escape rather than energy escape, we get

$$\begin{aligned} \langle E_\nu \rangle &= \sqrt{\frac{\int_0^\infty E_\nu^2 B_\nu(0,T)\, dE_\nu/E_\nu}{\int_0^\infty B_\nu(0,T)\, dE_\nu/E_\nu}} \\ &= \sqrt{\mathcal{F}_4(0)/\mathcal{F}_2(0)} = 3.59\, k_B T \ . \end{aligned} \tag{4.9}$$

Thus, the average energy to use when calculating opacities to account for lepton number loss is about 11% smaller than that used when accounting for energy loss rate. Since the opacity for lower energy neutrinos is lower, using the same mean opacity for number and energy escape causes the leakage scheme to underestimate the number of escaping leptons. The leakage scheme could be made more consistent by calculating separate optical depths for neutrino energy and number escape (Ruffert, H.-T. Janka, and Schaefer, 1996) or by calculating separate optical depths for each energy bin (e.g., Perego, Rosswog, et al. 2014 in the context of the isotropic diffusion source approximation). Additionally, since this issue is a spectral effect rather than

a geometric one, it could be accounted for in many of the more sophisticated energy-dependent transport schemes, such as spectral two-moment transport (e.g., M. Shibata, Kiuchi, et al. 2011; Cardall, Endeve, and Mezzacappa 2013; Just, Bauswein, et al. 2015).

One of the main differences between the effects of neutrinos calculated by leakage versus those calculated by MC transport is the amount of heating above the disk where densities are relatively low. Metzger and Fernández, 2014 argued that neutrinos are unable to drive a significant wind, but can affect the composition, especially above the disk, which increases the electron fraction of the viscously driven ejecta. To estimate the potential impact of the increased heating in the MC simulations, we look at the amount of mass M_ν for which neutrino heating dominates over viscous heating. M_ν is listed in Tables 4.1 and 4.4. In the BH snapshots, the leakage results indicate that essentially no mass is heated more strongly by neutrinos than by viscosity. However, for the first several tens of milliseconds, MC transport shows neutrinos being dynamically important in 11-50% of the mass in same snapshots (though quickly approaching zero after that). In the HMNS snapshots, M_ν increases with time according to leakage ($\sim$ 8% of the disk mass at 0 ms to $\sim$ 73% at 3 s), but decreases according to MC transport ($\sim$ 42% at 3 ms to essentially none at 3 s). This is largely due to the disk spreading out in the HMNS simulations such that much of the disk mass is below the minimum density for which neutrino interactions are accounted for in Sedonu. Though essentially all of the mass is still above the minimum density at 30 ms, by 300 ms 75% of the disk mass is above the minimum density (average density is 10^{10} g cm^{-3}), and by 3 s only 0.09% is above the minimum density (average density is 10^4 g cm^{-3}).

There is still much to be done before predictive simulated kilonova light curves become available, but the differences we see between the leakage and MC results could have dramatic implications for the elements formed in the ejecta and the resulting light curve. Previous studies indicate that the production of heavy r-process elements requires electron fractions below $Y_e \sim 0.2 - 0.3$ (e.g., Wanajo, Y. Sekiguchi, et al. 2014; Kasen, Fernández, and Metzger 2015). Figures 4.7 and 4.12 suggest that significant increases to the electron fraction of the disk ejecta are possible with Monte Carlo neutrino transport, since it results in the matter outside of the disk being more strongly neutrino processed. A weak r-process would still make elements up to $A \sim 90$ in electron fractions up to $Y_e \sim 0.4$ if the entropy is sufficiently high (Wanajo, Y. Sekiguchi, et al., 2014). However, the lack of a strong

r-process in the disk wind would imply a stronger early blue peak in the kilonova light curve if the merger is observed from a polar direction where the disk is not obscured by the lanthanide-rich dynamical ejecta (Metzger and Fernández, 2014; Kasen, Fernández, and Metzger, 2015).

We can apply the interpolation and integration scheme we used in Section 4.5 to the annihilation rates listed in Table 1 of Dessart, Ott, et al., 2009 (assuming no BH spin) to estimate the total annihilation energy deposited for the 100 ms simulation to be 5.1×10^{48} erg. This is about two orders of magnitude smaller than my estimate in Section 4.5 using the entire domain in the HMNS case, but is very similar to the estimate using only the regions within 45° of the poles. However, a direct comparison is somewhat difficult for the following reasons. (1) Dessart, Ott, et al., 2009 do not have an inner boundary condition, (2) their HMNS is $\sim 0.5 M_\odot$ less massive than the one I assume, (3) the HMNS luminosity is an order of magnitude more luminous at 30 ms, (4) the disk is $\sim$ 7 times more massive (with correspondingly higher densities), (5) they neglect viscous heating, and (6) they use a density cutoff of $\rho = 10^{11}\,\mathrm{g\,cm^{-3}}$ for calculating annihilation rates rather than an angle from the poles. This cutoff serves to exclude the HMNS and dense inner disk from the annihilation calculations, since energy deposited there is effectively trapped and unable to contribute to outflows. Since the disk is so much less massive, all of the disk mass has density $\rho < 10^{11}\,\mathrm{g\,cm^{-3}}$. Given the vast differences in the background fluid with which the annihilation calculations were performed, the differences in the annihilation rates are reasonable and to be expected.

The annihilation rate, however, depends on the product of the neutrino and anti-neutrino intensities, and so is sensitive to changes in the neutrino luminosity. Though Dessart, Ott, et al., 2009 see neutrino luminosities similar to ours, other studies show somewhat higher luminosities of all species. Foucart, E. O'Connor, L. Roberts, Duez, et al., 2015 simulate a NS-BH merger and find electron neutrino luminosities of $\lesssim 100\,\mathrm{B\,s^{-1}}$, electron anti-neutrino luminosities of $\lesssim 300\,\mathrm{B\,s^{-1}}$ and collective heavy-lepton neutrino luminosities of $\lesssim 100\,\mathrm{B\,s^{-1}}$ for a few tens of milliseconds. Y. Sekiguchi et al., 2015 simulate a NS merger including the HMNS and see see similar luminosities over a similar time. In both cases, the luminosities are larger than ours by a factor of a few, which has the potential to increase the annihilation rate by an order of magnitude. If these luminosities are closer to those in nature than those computed by us and Dessart, Ott, et al., 2009 and the geometry of the emission favors increased annihilation rates, there may yet be hope for the neutrino

annihilation-powered GRB model.

Dynamical simulations with MC neutrino transport (or other methods more sophisticated than leakage) are required to determine the true long-term effects of the increased cooling and leptonization rates. For instance, although the results show that MC results in faster global cooling at all times, what may happen in a full simulation is faster cooling at early times and slower cooling at late times, since the disk will have become cold much faster. However, MC transport is currently too computationally expensive to be used at every timestep in a three-dimensional dynamical calculation. Other transport methods like energy-dependent two-moment transport (e.g., Thorne 1981; M. Shibata, Kiuchi, et al. 2011; Just, Obergaulinger, and H.-T. Janka 2015) will be able to account for the spectral effects and many of the geometric ones, but in this approximation one must choose an otherwise undetermined closure relation to close the system of equations. Several physically-motivated analytic closures and variable Eddington factor methods (e.g., Cardall, Endeve, and Mezzacappa 2013) have been proposed, but any method with a local closure (i.e., one that is determined only by the radiation in the current grid cell) introduces a nonlinearity into the transport equation that leads to unphysical radiation shocks (e.g., Olson, Auer, and Hall 2000). In the future, it may be possible to find a closure treatment that maintains the efficiency of the two-moment transport scheme while accurately reproducing Monte Carlo results.

4.7 Conclusions

I have simulated neutrino transport through snapshots of post-merger disks using Monte Carlo (MC) techniques with various elements of physics. I compare the results to the leakage scheme used in the original dynamical simulations by Metzger and Fernández, 2014. Since the Monte Carlo neutrinos are out of equilibrium with the fluid evolved with the leakage scheme in the dynamical calculations, I believe that the qualitative trends I indicate are robust. However, determining the magnitudes of the differences between the two methods would require MC transport to be coupled to the fluid evolution. In light of this, I summarize my findings below.

1. Compared with leakage, MC transport results in global cooling and leptonization rates that are higher than those predicted by leakage during the optically-thick disk stage. If the disk is optically thin with a central BH, MC cooling is slower and leptonization is faster than leakage. If the disk is optically thin with a central HMNS, MC cooling is faster and leptonization is

slower than leakage. This suggests a stronger blue component of the kilonova light curve if viewed from polar angles.

2. MC exhibits up to an order of magnitude stronger neutrino heating above the disk that could increase the strength of a neutrino-driven wind.

3. In the disk midplane, cooling via MC neutrinos dominates viscous heating through the 30 ms snapshot with either central object, in constrast to the leakage results.

4. The neutrino radiation field at large radii is very asymmetric, with most of the radiation escaping around 45° from the equator.

5. The peak energies of the neutrino distribution functions can be shifted by a few MeV higher ($\nu_e, \bar{\nu}_e$) or lower (ν_x) from the peak of a zero-chemical potential blackbody with the same average energy and flux.

6. Neutrino pair annihilation deposits an order of magnitude more energy with a central HMNS ($\sim 1.9 \times 10^{48}$ erg) than with a central BH ($\sim 2.8 \times 10^{46}$ erg), though this is still unlikely to be sufficient to drive a jet, though higher neutrino luminosities could make it plausible.

7. Special relativity increases the average energies of escaping neutrinos by around $1 - 3$ MeV and beams higher-energy neutrinos away from the poles. The inclusion of heavy lepton neutrinos, pair processes, scattering, weak magnetism, and variations in the equation of state have together at most a 10% effect on the integrated cooling and leptonization rates.

Physics	$C_\nu - \mathcal{H}_\nu$ (B s^{-1})	$\left\langle \frac{dY_e}{dt} \right\rangle$ (s^{-1})	M_ν ($10^{-3} M_\odot$)	$\mathcal{L}_{\rm emit}$ (B s^{-1})			$\mathcal{L}_{\rm escape}$ (B s^{-1})			$\langle E_{\nu,\rm emit} \rangle$ (MeV)			$\left\langle E_{\nu,\rm escape} \right\rangle$ (MeV)			$\mathcal{H}_{\nu\bar{\nu}}$ (B s^{-1})
				ν_e	$\bar{\nu}_e$	ν_x	ν_e	$\bar{\nu}_e$	ν_x	ν_e	$\bar{\nu}_e$	ν_x	ν_e	$\bar{\nu}_e$	ν_x	
BH Disk Global Quantities																
2xEnergy	45.4	18.9	3.16	111	71.5	0.874	7.63	31.3	0.776	29.1	29.0	26.1	14.2	21.9	25.9	3.86(-3)
2xρ	45.5	19.0	3.12	110	71.7	0.870	7.62	31.3	0.772	29.1	29.0	26.1	14.2	21.9	25.9	3.86(-3)
2xT	45.7	19.2	3.22	111	72.3	0.879	7.63	31.5	0.779	29.1	29.1	26.2	14.2	21.9	26.0	3.90(-3)
2xY_e	45.4	18.9	3.16	110	71.5	0.867	7.63	31.2	0.769	29.1	29.0	26.2	14.2	21.9	26.0	3.85(-3)
2xϕ	45.4	18.9	3.12	110	71.5	0.872	7.63	31.2	0.775	29.1	29.0	26.2	14.2	21.9	26.0	3.79(-3)
2xμ	45.4	18.9	3.14	110	71.5	0.873	7.62	31.2	0.773	29.1	29.0	26.1	14.2	21.9	25.9	2.55(-3)
2xSteps	45.5	18.9	3.13	110	71.5	0.871	7.66	31.3	0.773	29.1	29.0	26.2	14.2	21.9	25.9	3.86(-3)
HMNS Disk Global Quantities																
2xEnergy	61.5	17.8	12.5	250	102	2.11	21.2	48.0	69.3	36.0	32.4	32.5	15.6	21.4	22.7	4.64(-2)
2xρ	61.5	17.9	12.5	249	102	2.11	21.2	48.1	69.3	36.0	32.4	32.6	15.6	21.4	22.7	4.65(-2)
2xT	61.8	18.0	12.7	250	103	2.12	21.2	48.3	69.3	36.1	32.5	32.7	15.6	21.5	22.7	4.67(-2)
2xY_e	61.4	17.8	12.5	250	102	2.11	21.2	48.0	69.3	36.0	32.4	32.6	15.6	21.4	22.7	4.64(-2)
2xϕ	61.4	17.8	12.5	250	102	2.11	21.2	48.0	69.3	36.0	32.4	32.6	15.6	21.4	22.7	4.61(-2)
2xμ	61.4	17.8	12.5	250	102	2.10	21.2	48.0	69.3	36.0	32.4	32.6	15.6	21.4	22.7	3.17(-2)
2xSteps	61.6	17.8	12.5	250	102	2.11	21.3	48.1	69.3	36.0	32.4	32.6	15.6	21.5	22.7	4.64(-2)

Table 4.3: **NuLib Resolution Test.** Volume-integrated quantities from the neutrino transport calculated by Sedonu. Each listed run doubles the number of points used in the indicated direction. E_ν, ρ, T, Y_e resolutions are properties of the NuLib opacity tables. ϕ and μ are the dimensions of the distribution function in each grid cell. In the 2xSteps run, the distance a neutrino moves in a single step is changed from 0.4 to 0.2 times the smallest dimension of the occupied grid cell. The numbers in parentheses indicate the power of 10 with which the data given must be scaled, e.g., 6.95(−1) is 6.95×10^{-1}. The table quantities are the same as in Table 4.4: $\mathcal{L}_{\rm escape}$ and $\left\langle E_{\nu,\rm escape} \right\rangle$ are the integrated luminosity and average energy of neutrinos that escape to infinity. $\mathcal{H}_{\nu\bar{\nu}}$ is the integrated annihilation rate within 45° from the axis of symmetry. $C_\nu - \mathcal{H}_\nu$ is the net rate of energy loss from the fluid by neutrinos. $\langle dY_e/dt \rangle$ is the mass-weighted average of the rate of change of the electron fraction. M_ν is the mass in which neutrinos are a larger source of heat than viscosity, i.e. $\mathcal{H}_\nu - C_\nu > \mathcal{H}_{\rm visc}$. $\mathcal{L}_{\rm emit}$ is the rate at which neutrino energy is emitted in the disk. $\langle E_{\nu,\rm emit} \rangle$ is the energy density-weighted average energy of these emitted neutrinos. ν_x represents the sum of all four heavy lepton neutrino species. 1 B = 10^{51} erg.

Physics	Time	$C_\nu - \mathcal{H}_\nu$	$\left\langle \frac{dY_e}{dt} \right\rangle$	M_ν	$\mathcal{L}_{\rm emit}$ (B s^{-1})			$\mathcal{L}_{\rm escape}$ (B s^{-1})			$\langle E_{\nu,\rm emit} \rangle$ (MeV)			$\left\langle E_{\nu,\rm escape} \right\rangle$ (MeV)			$\mathcal{H}_{\nu\bar{\nu}}$
	(ms)	(B s^{-1})	(s^{-1})	($M_\odot$)	ν_e	$\bar{\nu}_e$	ν_x	ν_e	$\bar{\nu}_e$	ν_x	ν_e	$\bar{\nu}_e$	ν_x	ν_e	$\bar{\nu}_e$	ν_x	(B s^{-1})
BH Disk Global Quantities																	
Full	0	8.39(1)	5.66(1)	7.56(-3)	5.46(1)	1.32(2)	1.06	4.96	7.13(1)	9.76(-1)	27.3	27.6	23.8	14.5	22.8	23.8	6.28(-3)
	3	4.54(1)	1.89(1)	3.15(-3)	1.10(2)	7.15(1)	8.70(-1)	7.63	3.12(1)	7.74(-1)	29.1	29.0	26.1	14.2	21.9	26.0	3.85(-3)
	30	4.50	3.27	2.17(-8)	3.33	3.54	2.34(-2)	1.16	2.81	2.08(-2)	19.0	18.8	16.0	13.9	17.6	15.9	2.82(-5)
	300	1.70(-2)	1.90(-1)	0.00	2.16(-3)	1.44(-2)	5.46(-4)	2.03(-3)	1.38(-2)	5.15(-4)	9.22	9.13	8.03	9.13	9.07	7.98	7.85(-11)
Simple	0	9.62(1)	6.93(1)	8.07(-3)	5.06(1)	1.51(2)	–	5.25	8.23(1)	–	24.8	26.0	–	14.2	22.1	–	8.93(-3)
	3	5.12(1)	2.40(1)	1.17(-3)	1.01(2)	8.16(1)	–	8.35	3.63(1)	–	25.7	26.9	–	13.9	21.1	–	6.06(-3)
	30	4.65	3.98	0.00	3.05	3.74	–	1.15	2.94	–	16.7	17.0	–	13.0	16.0	–	3.77(-5)
	300	1.69(-2)	2.04(-1)	0.00	2.05(-3)	1.48(-2)	–	1.92(-3)	1.42(-2)	–	8.49	8.66	–	8.40	8.58	–	9.90(-11)
NoPair	3	4.45(1)	1.89(1)	3.15(-3)	1.10(2)	7.15(1)	–	7.62	3.12(1)	–	29.1	29.0	–	14.2	21.9	–	3.85(-3)
NoScat	3	5.03(1)	2.07(1)	6.13(-3)	1.10(2)	7.15(1)	8.71(-1)	8.27	3.54(1)	7.90(-1)	29.1	29.1	26.2	14.6	23.3	26.3	3.65(-3)
NoRel	3	4.47(1)	1.96(1)	5.30(-4)	1.03(2)	6.70(1)	8.16(-1)	7.66	3.01(1)	7.06(-1)	25.8	26.0	23.3	13.5	20.3	22.9	5.54(-3)
NoWM	3	4.68(1)	2.05(1)	3.83(-3)	1.08(2)	8.71(1)	8.68(-1)	7.65	3.23(1)	7.69(-1)	28.9	30.1	26.1	14.3	21.2	25.8	4.04(-3)
Shen	3	4.53(1)	1.89(1)	2.98(-3)	1.08(2)	7.07(1)	8.71(-1)	7.58	3.12(1)	7.75(-1)	29.1	29.0	26.1	14.2	22.0	25.9	3.82(-3)
LS220	3	4.52(1)	1.88(1)	3.50(-3)	1.09(2)	7.07(1)	8.71(-1)	7.58	3.11(1)	7.73(-1)	29.1	29.0	26.2	14.2	21.9	25.9	3.84(-3)
HMNS Disk Global Quantities																	
Full	0	7.28(1)	5.78(1)	1.06(-2)	5.45(1)	1.32(2)	1.06	1.49(1)	8.57(1)	7.08(1)	27.3	27.6	23.9	15.0	22.4	22.5	5.94(-2)
	3	6.14(1)	1.78(1)	1.25(-2)	2.50(2)	1.02(2)	2.10	2.12(1)	4.80(1)	6.93(1)	36.0	32.4	32.6	15.6	21.4	22.7	4.65(-2)
	30	1.37(2)	3.83(-1)	9.48(-3)	1.55(3)	1.22(2)	2.33	1.65(1)	2.25(1)	3.73(1)	49.8	43.1	40.6	15.4	20.8	22.1	1.38(-2)
	300	2.15(1)	-1.40(-1)	2.19(-3)	1.31(2)	7.81	1.01(-1)	4.56	5.67	1.21(1)	38.3	30.3	26.3	15.5	20.2	21.6	7.59(-4)
	3000	-2.36(-4)	-6.40(-1)	2.53(-9)	1.05(-7)	1.69(-6)	4.40(-7)	1.02	1.02	4.07	5.92	5.43	4.48	16.4	20.5	20.5	4.04(-5)
Simple	0	8.62(1)	7.05(1)	1.06(-2)	5.04(1)	1.51(2)	–	1.54(1)	9.68(1)	–	24.8	26.0	–	14.8	21.6	–	5.41(-2)
	3	6.78(1)	2.26(1)	9.91(-3)	2.23(2)	1.18(2)	–	2.30(1)	5.41(1)	–	30.9	29.8	–	15.3	20.7	–	4.45(-2)
	30	1.34(2)	1.72	5.56(-3)	1.36(3)	1.47(2)	–	1.79(1)	2.56(1)	–	42.5	39.2	–	14.8	19.8	–	1.33(-2)
	300	2.07(1)	5.87(-2)	1.27(-3)	1.15(2)	8.71	–	4.73	6.07	–	32.7	27.3	–	14.7	18.9	–	6.29(-4)
	3000	-1.86(-4)	-6.40(-1)	2.04(-9)	9.73(-7)	1.68(-6)	–	1.02	1.02	–	5.21	4.98	–	16.4	20.5	–	2.74(-5)
NoPair	3	5.96(1)	1.78(1)	1.25(-2)	2.50(2)	1.02(2)	–	2.12(1)	4.80(1)	–	36.0	32.4	–	15.6	21.4	–	3.86(-2)
NoScat	3	6.80(1)	2.02(1)	1.53(-2)	2.50(2)	1.02(2)	2.11	2.23(1)	5.36(1)	7.08(1)	36.0	32.4	32.5	15.9	22.5	20.8	3.81(-2)
NoRel	3	6.17(1)	1.81(1)	5.76(-3)	2.29(2)	9.49(1)	1.93	2.17(1)	4.70(1)	6.60(1)	31.0	28.5	28.1	15.0	20.0	20.2	5.26(-2)
NoWM	3	6.27(1)	1.89(1)	1.34(-2)	2.43(2)	1.27(2)	2.11	2.13(1)	4.84(1)	6.89(1)	35.8	33.9	32.6	15.7	20.8	22.7	4.76(-2)
Shen	3	6.11(1)	1.78(1)	1.23(-2)	2.45(2)	1.01(2)	2.10	2.12(1)	4.80(1)	6.93(1)	36.0	32.4	32.5	15.6	21.5	22.7	4.63(-2)
LS220	3	6.10(1)	1.77(1)	1.27(-2)	2.45(2)	1.01(2)	2.11	2.11(1)	4.79(1)	6.93(1)	36.0	32.4	32.6	15.6	21.5	22.7	4.64(-2)

Table 4.4: **Merger disk results.** Volume-integrated quantities from the neutrino transport calculated by Sedonu. Compare with Table 4.1. The numbers in parentheses indicate the power of 10 with which the data given must be scaled, e.g., 6.95(−1) is 6.95×10^{-1}. $\mathcal{L}_{\rm escape}$ and $\left\langle E_{\nu,\rm escape} \right\rangle$ are the integrated luminosity and average energy of neutrinos that escape to infinity. $\mathcal{H}_{\nu\bar{\nu}}$ is the integrated annihilation rate within 45° from the axis of symmetry. All other quantities are the same as in Table 4.1: $C_\nu - \mathcal{H}_\nu$ is the net rate of energy loss from the fluid by neutrinos. $\langle dY_e/dt \rangle$ is the mass-weighted average of the rate of change of the electron fraction. M_ν is the mass in which neutrinos are a larger source of heat than viscosity, i.e. $\mathcal{H}_\nu - C_\nu > \mathcal{H}_{\rm visc}$. $\mathcal{L}_{\rm emit}$ is the rate at which neutrino energy is emitted in the disk. $\langle E_{\nu,\rm emit} \rangle$ is the energy density-weighted average energy of these emitted neutrinos. ν_x represents the sum of all four heavy lepton neutrino species. 1 B = 10^{51} erg.

Chapter 5

NEUTRINO TRANSPORT IN CORE-COLLAPSE SUPERNOVAE

The mechanism driving core-collapse supernovae is sensitive to the interplay between matter and neutrino radiation. However, neutrino radiation transport is very difficult to simulate, and several radiation transport methods of varying levels of approximation are available. We carefully compare for the first time in multiple spatial dimensions the discrete ordinates (DO) code of Nagakura, Yamada, and Sumiyoshi and the Monte Carlo (MC) code Sedonu, under the assumptions of a static fluid background, flat spacetime, elastic scattering, and full special relativity. We find remarkably good agreement in all spectral, angular, and fluid interaction quantities, lending confidence to both methods. The DO method excels in determining the heating and cooling rates in the optically thick region. The MC method predicts sharper angular features due to the effectively infinite angular resolution, but struggles to drive down noise in quantities where subtractive cancellation is prevalent, such as the net gain in the protoneutron star and off-diagonal components of the Eddington tensor. We also find that errors in the angular moments of the distribution functions induced by neglecting velocity dependence are sub-dominant to those from limited momentum-space resolution. We briefly compare directly computed second angular moments to those predicted by popular algebraic two-moment closures, and find that the errors from the approximate closures are comparable to the difference between the DO and MC methods. Included in this work is an improved Sedonu code, which now implements a fully special relativistic, time-independent version of the grid-agnostic Monte Carlo random walk approximation.

This work is being submitted as **[Sherwood Richers, Hiroki Nagakura, Christian Ott, Joshua Dolence, Kohsuke Sumiyoshi, and Shoichi Yamada (2017). "A Detailed Comparison of Multi-Dimensional Boltzmann Neutrino Transport Methods in Core-Collapse Supernovae". Submiting to *The Astrophysical Journal Supplement Series*.]** Much of the discussions on transport methods has been relegaded to Chapter 2.

I derived and implemented the time-independent relativistic version of the random walk approximation, ran all Monte Carlo simulations, performed all data analysis on the Monte Carlo simulations, unified the data from the two different codes for plotting and analysis, and wrote the text.

5.1 Introduction

Most massive stars ($M \gtrsim 10M_\odot$) end their lives in a cataclysmic core-collapse supernova (CCSN) explosion that releases around 10^{51} erg of kinetic energy and around 10^{53} erg of neutrino energy. The iron core begins to collapse when it exceeds

its effective Chandrasekhar mass as degenerate electrons capture onto nuclei and photodissociation breaks apart nuclei (e.g., Bethe 1990). Within a few tenths of a second after the onset of collapse, the inner core becomes very neutron-rich ($Y_e \sim 0.3$) and exceeds nuclear densities ($\sim 2.7 \times 10^{14}\,\mathrm{g\,cm^{-3}}$). At this point, the strong nuclear force kicks in, dramatically stiffening the equation of state (EOS) and abruptly stopping the collapse of the inner core within a few milliseconds. The inner core then rebounds, sending a shock wave through the supersonically infalling outer core. Neutrino cooling removes energy from the matter under the shock and photodissociation of heavy nuclei weakens the shock. The shock subsequently stalls at around 150 km as it is lacks pressure support from below to overcome the ram pressure of the accreting outer stellar core.

Understanding the mechanism that revives the shock's outward progress and results in a CCSN is presently the main target of CCSN theory. The canonical theory is the neutrino mechanism (Bethe and Wilson, 1985), whereby neutrinos emitted from the dense inner core pass through the matter below the shock, depositing enough thermal energy to revive the shock via thermal support and by driving turbulence (e.g., H.-T. Janka 2001; Burrows 2013; B. Müller 2016). However, the strongly nonlinear dynamics in this stage is inexorably coupled to a variety of microphysical processes. In particular, it is very sensitive to properties of the neutrino field passing through the matter. During the stalled shock phase, the star delicately straddles the line between explosion and total collapse, so small differences in how the neutrinos interact with the matter can be the difference between an explosion and a dud (e.g., H.-T. Janka 2001; Murphy and Burrows 2008; E. O'Connor and Ott 2011; Melson, H.-T. Janka, Bollig, et al. 2015; Couch and Ott 2015; Burrows, Vartanyan, et al. 2016).

Computation has become the primary tool for studying these nonlinear processes, as it allows us to see detailed dynamics and make observable predictions (electromagnetic radiation, neutrinos, gravitational waves) under the assumptions imposed by the model. However, computational techniques and resources are still too primitive to allow for simulations complete with all of the required fidelity and involved physics. In general, simulations of CCSNe require a three-dimensional general-relativistic (GR) treatment of magnetohydrodynamics, neutrino radiation transport, and a microphysical equation of state (EOS) (e.g., Kotake, Sumiyoshi, et al. 2012; H.-T. Janka 2012; Ott 2016). The simulations also require sufficient resolution or sub-grid modeling to capture everything from global dynamics to 100 meter-scale

or smaller turbulence (Radice, Ott, et al., 2016; Ott, 2016).

Deep in the inner core, neutrinos are trapped and form an isotropic thermal distribution that slowly diffuses out. Outside the shock, the neutrinos are free-streaming and move only radially outward. Though radiation transport methods are constructed to simulate these limits well, the intermediate semi-transparent region is challenging to accurately simulate. This region is responsible for most of the dynamics that support the shock's progress due to neutrino heating. In addition, the neutrino opacity scales approximately as the square of the neutrino energy, causing the energy deposition rate and the location of the transition from trapped to free-streaming to depend sensitively on neutrino energy. Hence, we require a means of simulating neutrinos of many energies in all regions of a CCSN.

A full treatment of classical neutrino radiation requires evolving the neutrino distribution function of each neutrino species according to the seven-dimensional Boltzmann equation (e.g., Mihalas and Weibel-Mihalas 1999) (three spatial dimensions, three momentum dimensions, time), which presents a significant computational challenge. A wide variety of methods have been used to capture the most important aspects of neutrino transport through the supernova that can be broadly categorized as either phenomenological, deterministic, or probabilistic methods. Though some methods are definitively more accurate than others, there is always a trade-off between efficiency and accuracy.

Phenomenological approaches include the light bulb scheme and neutrino leakage and only very approximately account for neutrino effects. These schemes are very efficient, making them very conducive to parameter studies. In the light bulb scheme (e.g., Bethe and Wilson 1985; H.-T. Janka and E. Müller 1996; Ohnishi, Kotake, and Yamada 2006; Murphy and Burrows 2008) the luminosity and temperature of each neutrino species are simply input parameters. All heating rates are based on this parameter and cooling rates are estimated based on an approximate optical depth. The inner light bulb boundaries have also been combined with gray transport schemes in the semi-transparent and transparent regimes (Scheck et al., 2006). In the leakage scheme, an approximate neutrino optical depth at each point is calculated, and this is used to set the cooling rate at each point (Ruffert, H.-T. Janka, and Schaefer, 1996; Rosswog and Liebendörfer, 2003). Neutrino heating can be included approximately by assuming that the neutrino luminosity through a given point is determined by the energy leaking radially outward from below (E. O'Connor and Ott, 2010; Fernández and Metzger, 2013; Perego, Cabezón, and Käppeli, 2016).

Approximate deterministic methods solve a simplified version of the Boltzmann equation in order to make a more tractable problem. The isotropic diffusion source approximation (IDSA) method evolves an isotropic trapped component and a free-streaming component of the distribution function (Liebendörfer, Whitehouse, and Fischer, 2009). In truncated moment methods, the distribution function is discretized into an infinite list of angular moments, only the first few of which are directly evolved. Flux-limited diffusion (FLD, Levermore and G. C. Pomraning 1981; Mihalas and Klein 1982; G. C. Pomraning 1983; Castor 2004; Krumholz et al. 2007) is a one moment method that evolves only the zeroth moment of the distribution function (energy density) and requires a closure relation to estimate the first moment (flux). However, FLD is numerically diffusive and fails to capture angular information about the distribution function (e.g., H.-T. Janka 1992; Burrows, Young, et al. 2000; Liebendörfer, Messer, et al. 2004; Ott, Burrows, Dessart, et al. 2008; W. Zhang et al. 2013). In the two-moment method (G. C. Pomraning, 1969; J. L. Anderson and Spiegel, 1972; Thorne, 1981; Dubroca and Feugeas, 1999; Audit et al., 2002; M. Shibata, Kiuchi, et al., 2011; Vaytet et al., 2011; Cardall, Endeve, and Mezzacappa, 2013), the zeroth and first moments are evolved, and a closure relation is required to estimate the second moment (pressure tensor) and complete the system of equations. The closure can be provided by some ad-hoc analytical function (e.g., Smit, van den Horn, and Bludman 2000; Murchikova, E. Abdikamalov, and Urbatsch 2017 and references therein). This is also known as the M1 method, though M1 confusingly refers to a specific closure as well (Levermore, 1984; Dubroca and Feugeas, 1999). The closure can also be more accurately determined using a direct solution of the Boltzmann equation, reffered to as a variable Eddington tensor (VET) method (e.g., Stone, Mihalas, and M. L. Norman 1992; J. C. Hayes and M. L. Norman 2003).

In discrete ordinates (DO or S_n) methods, the distribution function is discretized into angular bins, each of which is directly evolved (e.g., G. C. Pomraning 1969; Mihalas and Weibel-Mihalas 1999 and references therein). In spherical harmonic (P_n) methods, the distribution function is decomposed in terms of spherical harmonics, and a small number of these are evolved (e.g., G. Pomraning 1973; Radice, E. Abdikamalov, et al. 2013). Finally, fully spectral methods in all six space-momentum dimensions have been applied to stationary neutrino transport calculations (Peres et al., 2014).

Monte Carlo (MC) radiation transport (J.A. Fleck, Jr., and Cummings, 1971; J.A

Fleck and Canfield, 1984; Densmore et al., 2007; E. Abdikamalov, Burrows, et al., 2012) is a probabilistic method that samples the trajectories of a finite number of individual neutrinos and assumes their behavior is representative of the rest of the bulk neutrino behavior. Tubbs, 1978 applied MC methods to neutrino transport for the first time to study neutrino-matter equilibration in an infinite uniform medium. MC transport has been long used in 1D steady-state transport calculations (H.-T. Janka and Hillebrandt, 1989a; H.-T. Janka, 1991; H.-T. Janka, 1992; Yamada, H.-T. Janka, and Suzuki, 1999; Keil, Raffelt, and H.-T. Janka, 2003; E. Abdikamalov, Burrows, et al., 2012), though the code of E. Abdikamalov, Burrows, et al., 2012 was also designed to perform time-dependent calculations. Richers et al., 2015 performed steady-state MC transport calculations on 2D snapshots of accretion disks from neutron star mergers, though the optical depths were much lower than in the CCSN context.

There is much more to a radiation transport code than the broad classes of methods mentioned above. Detailed Boltzmann transport using either DO or VET methods in dynamical simulations has been achieved in one (Mezzacappa and Bruenn, 1993; Yamada, H.-T. Janka, and Suzuki, 1999; Burrows, Young, et al., 2000; Rampp and H.-T. Janka, 2002; L. F. Roberts, 2012) and two (Livne et al., 2004; Ott, Burrows, Dessart, et al., 2008; Nagakura, Iwakami, Furusawa, Sumiyoshi, et al., 2017) spatial dimensions, but three dimensional calculations are presently only possible when the fluid is assumed to be stationary (Sumiyoshi and Yamada, 2012; Sumiyoshi, Takiwaki, et al., 2015). The local two-moment method is used in 1D (E. O'Connor, 2015), 2D (E. O'Connor and Couch, 2015; Just, Bauswein, et al., 2015), and 3D (Y. Sekiguchi et al. 2015; L. F. Roberts, Ott, et al. 2016; Foucart, Haas, et al. 2016; Kuroda, Takiwaki, and Kotake 2016, see also B. Müller and H.-T. Janka 2015) core collapse and neutron star merger simulations. FLD is also popular in 2D simulations (Dessart et al., 2006; Swesty and Myra, 2009; W. Zhang et al., 2013). Various versions of the ray-by-ray (RbR) approximation can also be used to extend a 1D transport method to two (Burrows, J. Hayes, and Fryxell, 1995; Buras et al., 2006; B. Müller, H.-T. Janka, and Dimmelmeier, 2010; Suwa, Kotake, Takiwaki, Whitehouse, et al., 2010; Pan et al., 2016) or three (Hanke et al., 2013; Takiwaki, Kotake, and Suwa, 2012; Lentz, Bruenn, et al., 2015; Melson, H.-T. Janka, and Marek, 2015) spatial dimensions in an efficient manner by making transport along individual radial rays nearly independent of other rays and/or by solving a single spherically averaged 1D transport problem. Fully general relativistic neutrino radiation hydrodynamics simulations are now possible (H.-T. Janka, 1991; Yamada, H.-T. Janka, and Suzuki,

1999; Liebendörfer, Mezzacappa, and Thielemann, 2001; Sumiyoshi, Yamada, et al., 2005; B. Müller, H.-T. Janka, and Dimmelmeier, 2010; Masaru Shibata and Y. Sekiguchi, 2012; Kuroda, Kotake, and Takiwaki, 2012; E. O'Connor, 2015; Foucart, Haas, et al., 2016; L. F. Roberts, Ott, et al., 2016; Kuroda, Takiwaki, and Kotake, 2016) and many codes incorporate general relativistic effects with various levels of approximation (e.g., B. Müller, H.-T. Janka, and Dimmelmeier 2010; E. O'Connor and Couch 2015; Skinner, Burrows, and Dolence 2016). Special-relativistic effects can be accounted for in full generality (Masaru Shibata and Y. Sekiguchi, 2012; Richers et al., 2015; Foucart, Haas, et al., 2016; Nagakura, Iwakami, Furusawa, Sumiyoshi, et al., 2017) or by using only up to $O(v/c)$ terms (e.g., Rampp and H.-T. Janka 2002; Lentz, Bruenn, et al. 2015; Just, Bauswein, et al. 2015; Dolence, Burrows, and W. Zhang 2015; Skinner, Burrows, and Dolence 2016; B. Müller, H.-T. Janka, and Dimmelmeier 2010). Even if the transport method is equivalent, simulations differ in how neutrino-matter and neutrino-neutrino interactions are treated (e.g., Lentz, Mezzacappa, Messer, Hix, et al. 2012). In short, each piece of relevant physics can be simulated accurately, but 3D simulations containing all pieces remain a goal that hs not yet been achieved.

Any computational method is an approximation of reality, and every method has strengths and weaknesses. It is therefore expected that computations performed by different codes should arrive at different solutions, though they should converge to the physical answer with increasing simulation fidelity. Understanding the weaknesses of a given method is a prerequisite to interpreting the physical meaning of simulation results. It is standard practice to test that codes produce known solutions to simple problems and to perform self-convergence tests to ensure that results are not mistakes or numerical artifacts. However, even with these practices in place, different codes produce different results and independent verification is required to help determine which features of each are realistic (Calder et al., 2002).

Several works in the past have evaluated the accuracy of a low-order method like FLD or two moment transport by comparing with a high-order DO, MC, or VET method (e.g., H.-T. Janka 1992; Mezzacappa and Bruenn 1993; Messer et al. 1998; Burrows, Young, et al. 2000; Liebendörfer, Messer, et al. 2004; Ott, Burrows, Dessart, et al. 2008). However, in these comparisons, the low-order method is not expected to converge to the same result as the high-order method, which does not help to verify the high-order method. There have been few detailed comparisons between high-order methods that solve the same full Boltzmann equation (i.e., VET,

DO, and MC methods), and none in more than one spatial dimension. Yamada, H.-T. Janka, and Suzuki, 1999 compared the results of a new DO implementation to the MC code of H.-T. Janka, 1991 in 1D GR snapshots of CCSN simulations, but ignored fluid motion. Liebendörfer, Rampp, et al., 2005 performed a comparison of dynamical 1D CCSN simulations using the GR DO code Agile-BOLTZTRAN (Liebendörfer, Messer, et al., 2004) with the Newtonian VET code VERTEX-PROMETHEUS (Rampp and H.-T. Janka, 2002). They found very good agreement once an effective potential was introduced to VERTEX-PROMETHEUS to account for GR effects (Marek, Dimmelmeier, et al., 2006). Several groups have since used the results of Liebendörfer, Rampp, et al., 2005 as a standard for comparison (e.g., Sumiyoshi, Yamada, et al. 2005; B. Müller, H.-T. Janka, and Dimmelmeier 2010; Suwa, Kotake, Takiwaki, Liebendörfer, et al. 2011; Lentz, Mezzacappa, Messer, Liebendörfer, et al. 2012; Lentz, Mezzacappa, Messer, Hix, et al. 2012; E. O'Connor and Ott 2013; E. O'Connor 2015; Just, Obergaulinger, and H.-T. Janka 2015; Suwa, Yamada, et al. 2016). With the recent arrival of the many advanced multi-dimensional neutrino radiation hydrodynamics codes mentioned previously, continued independent verification is essential to interpreting simulation results.

In this chapter, we perform the first detailed multi-dimensional comparison between fully special relativistic Boltzmann neutrino transport codes using a DO neutrino radiation hydrodynamics code (Nagakura, Iwakami, Furusawa, Sumiyoshi, et al., 2017) (hereafter NSY) and the Monte Carlo radiation transport code `Sedonu` (Richers et al., 2015). We make the time-independent comparisons on spherically symmetric (1D) and in axisymmetric (2D) snapshots from CCSN simulations at around 100 ms after core bounce. Both codes are carefully configured to calculate the full steady-state neutrino distribution function from first principles in as similar a manner as possible. We find remarkably good agreement in all spectral, angular, and fluid interaction quantities, lending confidence to both methods. The MC method predicts sharper angular features due to the effectively infinite angular resolution, but struggles to drive down noise in quantities where subtractive cancellation is prevalent (e.g., net gain within the protoneutron star and off-diagonal components of the Eddington tensor). We test the importance of accounting for fluid velocities by setting all velocities to zero and find that the differences induced are much smaller than the errors due to finite momentum-space resolution. We compare directly computed second angular moments to those predicted by popular two-moment closures, and find that the error from the approximate closure is comparable to the difference between the DO and MC methods.

This chapter is organized as follows. In Section 5.2, we review the discrete ordinates, Monte Carlo, and two moment methods. We present the results of the transport method comparisons in spherical symmetry in Section 5.4 and in axial symmetry in Section 5.5. We summarize our conclusions in Section 5.6. The MC transport code Sedonu is publicly available at `https://bitbucket.org/srichers/sedonu` and the results obtained in this study from both transport codes are available at `https://stellarcollapse.org/MCvsDO`.

5.2 Numerical Methods of Neutrino Transport

The transport of classical neutrinos is described in general by the Boltzmann equation (Equation 2.45). The neutrino propagation is generally calculated in reference to coordinates defined in the lab frame, but interactions between matter and neutrinos are formulated in the fluid rest frame (a.k.a. the comoving frame). It is thus important to very carefully keep track of the frame in which various quantities are defined. This is consistent with widely used conventions in the relativistic neutrino transport community (e.g., M. Shibata, Kiuchi, et al. 2011; Cardall, Endeve, and Mezzacappa 2013). We simulate ν_e and $\bar{\nu}_e$ individually, but group all of the heavy-lepton neutrinos into a single simulated species ν_x for computational efficiency.

Neutrino interaction rates depend on the properties of the fluid through which they traverse. In this study, we use the non-hyperonic equation of state (EOS) of H. Shen et al., 2011 to determine the abundances and chemical potentials of each constituent (i.e., leptons, nucleons, and nuclei) given the fluid density, temperature, and electron fraction. We consider the following minimum but essential sets of neutrino-matter interactions in the postbounce phase of CCSNe:

$$\begin{aligned}
e^- + p &\longleftrightarrow \nu_e + n \,, \\
e^+ + n &\longleftrightarrow \bar{\nu}_e + p \,, \\
\nu(\bar{\nu}) + N &\longleftrightarrow \nu(\bar{\nu}) + N \,, \\
e^- + e^+ &\longleftrightarrow \nu + \bar{\nu} \,, \\
N + N &\longleftrightarrow N + N + \nu + \bar{\nu} \,,
\end{aligned}$$

where $N \in \{n, p\}$. From top to bottom, these processes are electron capture by free protons, positron capture by free neutrons, isoenergetic scattering with nucleons, electron-positron pair annihilation, and nucleon-nucleon bremsstrahlung, along with each of their inverse reactions.

The three source terms on the right hand side of Equation 2.45 each encapsulate multiple processes, and are grouped into the mathematical nature of each term.

In both Sedonu and the NSY code, all of these source terms are evaluated in the comoving frame. Details of how the NSY code computes reaction rates are explained by Bruenn, 1985 and Sumiyoshi, Yamada, et al., 2005.

The emission and absorption term takes the form of Equation 2.46. Sedonu takes advantage of the concept of stimulated absorption to account for final-state neutrino blocking (Burrows, Reddy, and Thompson, 2006), in which the effective absorption reaction rate is $\widetilde{R}_{\rm abs} = R_{\rm abs} + R_{\rm emis}$. This removes the need to treat final-state blocking explicitly in the neutrino emission process.

The scattering term accounts for neutrinos scattering into and out of a given direction according to Equation 2.47. Both Sedonu and the NSY code assume isoenergetic scattering, so the scattering reaction rate becomes $R_{\rm scat}(\epsilon', \epsilon, \mathbf{\Omega}' \cdot \mathbf{\Omega}) = \delta(\epsilon, \epsilon')\widetilde{R}_{\rm scat}(\epsilon, \mathbf{\Omega} \cdot \mathbf{\Omega}')$. Under this assumption, the scattering source term reduces to

$$\left[\frac{\partial f}{c\partial t}\right]_{\rm scat} = \int d\mathbf{\Omega}' \widetilde{R}_{\rm scat}(\epsilon, \mathbf{\Omega} \cdot \mathbf{\Omega}')(f' - f) \ . \tag{5.1}$$

Sedonu uses $\int d\mu \widetilde{R}_{\rm scat}(\epsilon, \mu)$, where $\mu = \mathbf{\Omega} \cdot \mathbf{\Omega}'$, as the scattering opacity directly.

Finally, pair annihilation and neutrino bremsstrahlung source terms take the form of Equation 2.49. In order to ensure the same assumptions go into both radiation transport schemes, the NSY code calculates these reactions assuming the anti-species is isotropic, i.e.,

$$\begin{aligned} \bar{f}_{\rm iso} &= \frac{1}{4\pi} \int d\bar{\mathbf{\Omega}} \bar{f} \ , \\ R_{\rm PB,iso}(\epsilon, \bar{\epsilon}) &= \int d\bar{\mathbf{\Omega}} R_{\rm PB}(\epsilon, \bar{\epsilon}, \mathbf{\Omega} \cdot \bar{\mathbf{\Omega}}) \ , \end{aligned} \tag{5.2}$$

where $\bar{f}_{\rm iso}$ depends only on energy and not on direction. Under this assumption, the source term can be written as

$$\begin{aligned} \left[\frac{\partial f}{c\partial t}\right]_{\rm PB} = & \overbrace{\int d\left(\frac{\bar{\epsilon}^3}{3}\right) R_{\rm PB,emis,iso}(\epsilon, \bar{\epsilon})(1 - \bar{f}_{\rm iso})}^{\widetilde{R}_{\rm PB,emis}} \\ & - f \underbrace{\int d\left(\frac{\bar{\epsilon}^3}{3}\right) \left[R_{\rm PB,emis,iso}(\epsilon, \bar{\epsilon})(1 - \bar{f}_{\rm iso}) + R_{\rm PB,abs,iso}(\epsilon, \bar{\epsilon})\bar{f}_{\rm iso}\right]}_{\widetilde{R}_{\rm PB,abs}} \ . \end{aligned} \tag{5.3}$$

Sedonu uses $\widetilde{R}_{\rm PB,abs/emis}$ in the same way as $\widetilde{R}_{\rm abs/emis}$.

Since the NSY code evolves f, they use the reaction rates (units of $\rm cm^{-1}$) directly, but Sedonu needs to convert the emission reaction rates to physical emissivities. For

an emissivity η with units of (erg cm^{-3} s^{-1}),

$$\eta = \widetilde{R}_{\text{emis}} \frac{\epsilon_i}{c^2 h^3} \Delta \left(\frac{\epsilon^3}{3} \right)_i \quad . \tag{5.4}$$

Here, $\Delta \left(\epsilon^3/3 \right)_i$ and ϵ_i are the momentum-space volume (normalized by 4π) and center of energy bin i, respectively. The absorption and scattering reaction rates with tildes ($\widetilde{R}$) are already equivalent to absorption and scattering opacities.

Though a multitude of phenomenological, approximate, and exact transport methods exist in the literature, we will focus on three of them. The discrete ordinates method (DO) and the Monte Carlo (MC) methods both solve the Boltzmann equation directly in all three momentum dimensions and multiple spatial dimensions, and so should converge to the same physical result. We also investigate how well approximate closure relations in the two-moment method compare to the solutions computed by DO and MC calculations.

Discrete Ordinates

The DO Boltzmann code of Nagakura, Sumiyoshi, and Yamada (hereafter NSY) is a grid-based multi-dimensional neutrino radiation hydrodynamics code that solves the conservative form of Equation 2.45 in the language of the 3+1 formulation of general relativity (GR). The numerical method is essentially the same as described by Sumiyoshi and Yamada, 2012, though it has since been extended to account for special relativistic effects as has been coupled with Newtonian hydrodynamics (Nagakura, Sumiyoshi, and Yamada, 2014; Nagakura, Iwakami, Furusawa, Sumiyoshi, et al., 2017). The newest version of this code was recently applied to axisymmetric CCSN simulations in Nagakura, Iwakami, Furusawa, Okawa, et al., 2017.

The neutrino distribution function f is discretized onto a spherical-polar spatial grid described by radius r, polar angle θ, and azimuthal angle ϕ. The radial grid is constructed so as to provide good resolution where the density gradient is large. The radial mesh spacing is set to $\Delta r = 300\,\text{m}$ at the center and decreases with increasing radius up to the location of the steepest density gradient at $r = 10\,\text{km}$, where $\Delta r = 104\,\text{m}$. For $r \geq 10\,\text{km}$, the spacing increases by 1.7% per zone up to $r = 500\,\text{km}$. For $r \geq 500\,\text{km}$, the spacing increases by 3.8% per zone up to the outer boundary of $r = 5000\,\text{km}$. This results in 384 radial grid zones over the entire domain. The spatial angular grid is set to 128 Gaussian quadrature points from $0 \leq \theta \leq \pi$. At each spatial location, f is discretized onto a spherical-polar momentum space grid described by neutrino energy ϵ, neutrino polar angle $\bar{\theta}$ (where

$\bar{\theta} = 0$ is in the radial direction), and neutrino azimuthal angle $\bar{\phi}$. The first bin of the neutrino energy grid extends over $0 - 2$ MeV in the 1D_1x and 2D calculations, $0 - 1$ MeV in the 1D_2x calculations, and $0 - 0.5$ Mev in the 1D_4x calculations. The rest of the energy bins are logarithmically spaced from 2 MeV to 300 MeV. The number of energy and direction bins used in each simulation is listed in Table 5.1.

The NSY code treats the advection terms in the GR Boltzmann equation semi-implicitly. Both advection and collision terms are implemented self-consistently by using a mixed-frame approach with separate momentum-space grids in the lab and comoving frames. See Nagakura, Iwakami, Furusawa, Sumiyoshi, et al., 2017 for implementation details.

Though the NSY code is capable of evolving coupled neutrino radiation hydrodynamics, we restrict the capability of the code in this study to evolve only the radiation field on top of a fixed fluid background with a flat spacetime metric until a nearly steady-state solution is reached. As we list in Table 5.1, the maximum time variability in the energy density at any spatial location relative to the value averaged over 1 ms is less than 0.1%, which is significantly smaller than difference between DO and MC results.

Monte Carlo

I describe the MC transport code Sedonu in Chapter 3. We employ the Sedonu MC neutrino transport code (Richers et al., 2015) to solve for equilibrium neutrino radiation fields and neutrino-matter interaction rates. We use the *exponential decay* model of neutrino energy deposition in this study. If the cell is optically thick to neutrinos, we use a time-independent relativistic version of the Monte Carlo random walk approximation to allow the neutrino to make a large step through many effective isotropic elastic scatters (see Section 3.3).

In this study, we perform the transport on 1D and 2D fluid grids in spherical-polar coordinates that are identical to those employed by the NSY code. We tally the radiation field in two different ways. In the first, we use energy and direction bins identical to those used by the NSY code. The data output is thus discretized, even though the neutrinos themselves are always transported through continuous space and are not influenced by any grid structure except in evaluating the opacities. In the second way ("native"), we accumulate neutrino energy directly into angular moments without any reference to a discrete direction grid, though we still use the same energy bins. The version of Sedonu used in this chapter is fundamentally the

same as that used in Richers et al., 2015, except that it includes the Monte Carlo random walk approximation for regions of large optical depth, the native moment prescription, and various performance and usability upgrades. Sedonu is open source and available at `https://bitbucket.org/srichers/sedonu`.

5.3 Two-Moment Analysis

In this study, we do not perform two-moment radiation transport, but rather compare the radiation pressure tensor predicted by approximate closures to the actual radiation pressure tensor output from the MC and DO calculations. In our analysis, we ignore the $O(v/c)$ term in Equation 2.56 for simplicity.

The DO and MC methods are very different, so care is required to make meaningful comparisons between angular moments using the two codes. The NSY code evolves the distribution function f, while Sedonu calculates the amount of neutrino energy in each spatial-energy-direction cell in non-native calculations. The Sedonu distribution function value at the bin center $(r_a, \theta_b, \epsilon_k, \bar{\theta}_m, \bar{\phi}_n)$ is calculated using

$$f_{\text{Sedonu},abkmn} = \frac{\varepsilon_{akmn}}{V_{ab}\Delta(\frac{\epsilon^3}{3})_k \Delta\cos(\bar{\theta})_m \Delta\bar{\phi}_n} , \tag{5.5}$$

where ε_{akmn} is the total neutrino energy content (units of ergs) in spatial-direction-energy bin $\{akmn\}$, V_a is the spatial volume of the grid cell in the lab frame, $\bar{\theta}$ and $\bar{\phi}$ are the neutrino direction angles in the lab frame, and ϵ is the neutrino energy in the comoving frame.

In the 1D simulations where Sedonu collects radiation information on angular bins rather than native moments, we take care to ensure that the post-processing for the two codes are equivalent. For both Sedonu and the NSY code, the distribution function is linearly interpolated to $\widetilde{f}$ on identical fine angular grids in $\{\cos(\bar{\theta}), \bar{\phi}\}$ of $\{80, 40\}$ zones, respectively. Throughout this section, the subscript (a) refers to the spatial mesh index, the subscript (k) refers to the neutrino energy bin index, the subscripts (mn) refer to the direction indices on the coarse direction grid used in the transport calculation, the subscripts (pq) refer to the direction indices on the high-resolution post-processing angular grid, and the superscripts (ij) refer to directions (i.e., r, θ, or ϕ) in the lab frame.

The specific energy density (lab frame energy density per comoving-frame neutrino energy) is computed as a sum over the coarse grid for Sedonu and over the fine grid in the NSY code. This takes advantage of the fact that Sedonu computes energy

content directly and does not introduce interpolation error into the Sedonu results:

$$\begin{aligned} E_{\epsilon,ak,\text{Sedonu}} &= \frac{1}{V_a \Delta\left(\frac{\epsilon^3}{3}\right)_k} \sum_m \sum_n \varepsilon_{akmn} \ , \\ E_{\epsilon,ak,\text{DO}} &= \epsilon_k \sum_p \sum_q \widetilde{f}_{akpq} \Delta\cos(\bar{\theta}_\nu)_p \Delta(\bar{\phi}_\nu)_q \ . \end{aligned} \tag{5.6}$$

For both Sedonu and the NSY code, the higher-order moments are evaluated as

$$\begin{aligned} F^i_{\epsilon,ak} &= \epsilon_k \sum_p \sum_q \widetilde{f}_{akpq} (\mathbf{\Omega}_{pq} \cdot \mathbf{e}_{(i)}) \Delta\cos(\bar{\theta})_p \Delta(\bar{\phi})_q \ , \\ P^{ij}_{\epsilon,ak} &= \epsilon_k \sum_p \sum_q \widetilde{f}_{akpq} (\mathbf{\Omega}_{pq} \cdot \mathbf{e}_{(i)}) (\mathbf{\Omega}_{pq} \cdot \mathbf{e}_{(j)}) \Delta\cos(\bar{\theta})_p \Delta(\bar{\phi})_q \ . \end{aligned} \tag{5.7}$$

The energy-integrated moments $M = \{E, F^i, P^{ij}\}$ are computed using

$$M_a = \sum_k \Delta\left(\frac{\epsilon^3}{3}\right)_k M_{\epsilon,ak} \ . \tag{5.8}$$

Finally, the average neutrino energy is computed using

$$\bar{\epsilon}_a = \frac{E_a}{N_a} \ . \tag{5.9}$$

5.4 Transport Comparison in Spherical Symmetry

We perform several spherically symmetric (1D) steady-state neutrino transport calculations using different momentum-space treatments listed in Table 5.1. In the 1D_1x, 1D_2x, and 1D_4x simulations, the neutrino radiation field is discretized into the number of angular and energy bins described in the "Spatial Resolution" and "Angular Resolution" columns. They differ only by the number of spatial and energy bins, and are all run in each the NSY code and Sedonu. The 1D_4x_nonrel calculation (performed only by the NSY code) is identical to the 1D_4x calculation, except with all velocities set to zero. In the 1D_4x_native calculation performed only by Sedonu, MC packets are accumulated directly into angular moments rather into angular bins. The 1D_4x_native_nonrel calculation is identical to the 1D_native calculation, but with all velocities set to zero. Note that length contraction causes the simulations that include relativistic effects to have a slightly larger total rest mass, but only by $2 \times 10^{-5}\ M_\odot$. Throughout this section, we primarily compare the highest-resolution DO calculation (1D_4x) to the highest-resolution native-moment MC calculation (1D_4x_native). We use the lower resolution calculations (1D_1x and 1D_2x) in resolution comparisons.

Problem Name	Special Relativity	Spatial Resolution $r \times \theta \times \epsilon$	Angular Resolution $\bar{\theta} \times \bar{\phi}$	MC Packets ($\times 10^9$)	DO $\delta E_{\rm max}$
1D Calculations					
1D_1x	yes	$384 \times 1 \times 20$	10×1	1.82	2.40×10^{-4}
1D_2x	yes	$384 \times 1 \times 40$	20×1	2.33	5.50×10^{-8}
1D_4x	yes	$384 \times 1 \times 80$	40×1	2.67	7.40×10^{-8}
1D_4x_nonrel	no	$384 \times 1 \times 80$	40×1	–	9.80×10^{-8}
1D_4x_native	yes	$384 \times 1 \times 80$	–	2.96	–
1D_4x_native_nonrel	no	$384 \times 1 \times 80$	–	3.25	–
2D Calculations					
2D_LR	yes	$270 \times 128 \times 20$	10×6	–	7.00×10^{-4}
2D_LR_nonrel	no	$270 \times 128 \times 20$	10×6	–	5.84×10^{-4}
2D_HR	yes	$270 \times 128 \times 28$	14×10	–	4.84×10^{-4}
2D_HR_native	yes	$270 \times 128 \times 28$	–	63.4	–

Table 5.1: **List of calculations:** We list the numerical details of each calculation presented in this chapter. The leftmost column gives the name of each steady-state problem that is solved by one or both of Sedonu and the NSY code. The Special Relativity column indicates whether special relativistic effects are taken into account. The Resolution column describes the spatial resolution of the fluid data and the number of neutrino energy bins. The Angular Resolution column describes the number of discrete angular bins in the neutrino momentum space angular discretization of the distribution function. In the "native" MC calculations, neutrinos are accumulated directly into angular moments (E_ϵ, F^r_ϵ, F^θ_ϵ, P^{rr}_ϵ, $P^{r\theta}_\epsilon$, $P^{\theta\theta}_\epsilon$, $P^{\phi\phi}_\epsilon$) without making reference to any discrete angular representation of the distribution function. The final two columns are indicative of the fidelity of the simulation. The MC Packets column shows the number of MC neutrino packets that we simulate. The DO $\delta E_{\rm max}$ measures the time variability in the steady state solution in DO calculations. $\delta E_{\rm max}$ is defined as the maximum difference from time-average energy density during the final 1 ms of the simulation in $r < 500$km.

In Figure 5.1, we show the static fluid background that comes from a spherically symmetric neutrino radiation hydrodynamics simulation of the collapse of a $11.2 M_\odot$ star (Woosley, Heger, and Weaver, 2002) at 100 ms after core bounce using the NSY code (Nagakura, Iwakami, Furusawa, Sumiyoshi, et al., 2017). For the calculations in this chapter, the NSY code is again used to calculate a steady-state solution of the neutrino radiation field on this background using the DO method. The opacities and emissivities are then exported to Sedonu, which computes a steady-state radiation field on the same background.

In Figure 5.2 we show radial profiles of the total energy density of each neutrino species using both the 1D_4x DO calculation and the 1D_4x_native MC calculation. For each species, the energy density is approximately constant in the inner core ($r \lesssim 10$ km) as neutrinos are trapped and in equilibrium with the fluid. In this region, the neutrinos have a Fermi-Dirac distribution function, and so the energy density is determined entirely by the fluid temperature and the electron and nucleon

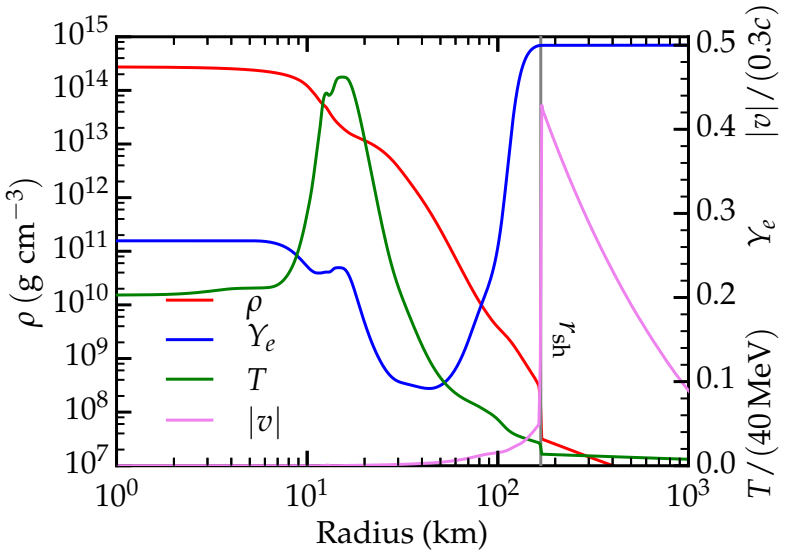

Figure 5.1: **1D fluid properties.** This fluid snapshot from a 1D dynamical simulation in the NSY code at 100 ms after bounce is the background on which we solve the 1D steady-state radiation transport problem. The background fluid density ρ (red graph), electron fraction Y_e (blue graph), temperature T (green graph), and velocity magnitude (magenta graph) are shown as a function of radius. The shock front (gray line labeled with r_{sh}) can be seen in the discontinuities in density, temperature, and velocities at $r = 168$ km.

chemical potentials. In the outer (i.e., shock-processed) core at $r \gtrsim 10$ km, the temperature is very high ($T \approx 20$ MeV), and many more electron anti-neutrinos and heavy lepton neutrinos are emitted than in the cooler inner core. Beyond the energy-averaged neutrinospheres (30 km $\lesssim r \lesssim$ 60 km, depending on the neutrino species), the neutrinos are only weakly coupled to the fluid and the energy density decreases as $E \propto r^{-2}$.

Both codes produce remarkably similar results, with differences in the energy density (Figure 5.2) smaller than 2% everywhere within the shock. The remaining differences near the energy-averaged neutrinospheres (30 km $\lesssim r \lesssim$ 60 km, depending on species) are due to the MC random walk approximation, and decrease when the critical optical depth is increased (see Section 3.3). The differences outside of the decoupling region ($r \gtrsim 40 - 80$ km, depending on species) decreases with increasing DO directional angular resolution. Outside of the shock, the difference in the energy density grows as the NSY code experiences a small departure from r^{-2} scaling of the energy density. This is an artifact of the finite spatial resolution. The size of the error visibly increases at 500 km, where the radial resolution coarsens.

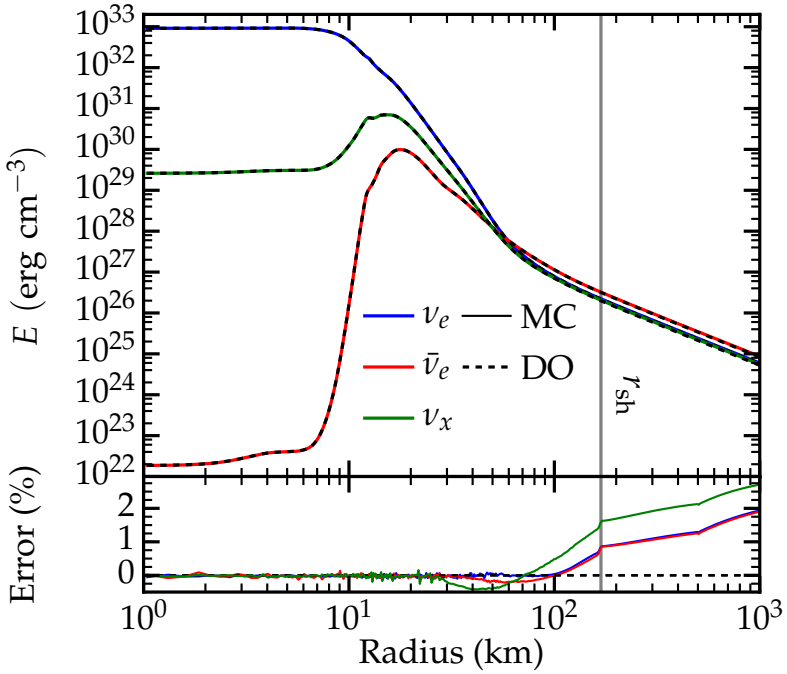

Figure 5.2: **1D neutrino energy density.** The total lab-frame neutrino energy density as a function of radius using the 1D_4x DO calculation and the 1D_4x_native MC calculation. The error is defined as $(E_{\rm MC} - E_{\rm DO})/(E_{\rm MC} + E_{\rm DO})$. There is excellent agreement between MC and DO inside the shock. The small differences between 30 km $\lesssim r \lesssim$ 60 km are due to the error from the MC random walk approximation and decreases with MC random walk sphere size (see Section 3.3). The differences between 70 km $\lesssim r \leq r_{\rm sh}$ results from momentum-space diffusivity in the NSY code in strongly forward-peaked regions and improves with angular resolution. The differences outside of the shock come from slight non-conservation experienced in the NSY code due to finite spatial resolution.

Figure 5.3 shows a quantity akin to the comoving-frame average neutrino energy[1], defined as

$$\bar{\epsilon} = \frac{\sum E_i}{\sum E_i/\epsilon_i} \,, \tag{5.10}$$

where E_i is the lab-frame energy density in bin i and ϵ_i is the comoving-frame bin central energy. Because neutrinos are in equilibrium with the fluid below the decoupling region ($r = 30 - 70$ km, depending on species), they have a Fermi-Dirac distribution function that depends only on the fluid temperature and electron and nucleon chemical potentials. The neutrino absorption opacity scales approximately as $\sigma_a \sim \epsilon^2$, so high-energy neutrinos are preferentially absorbed, causing the average

[1]Recall that we used mixe frame quantities, since many GR transport schemes are formulated in terms of lab-frame energy density and comoving-frame neutrino energy (e.g., M. Shibata, Kiuchi, et al. 2011).

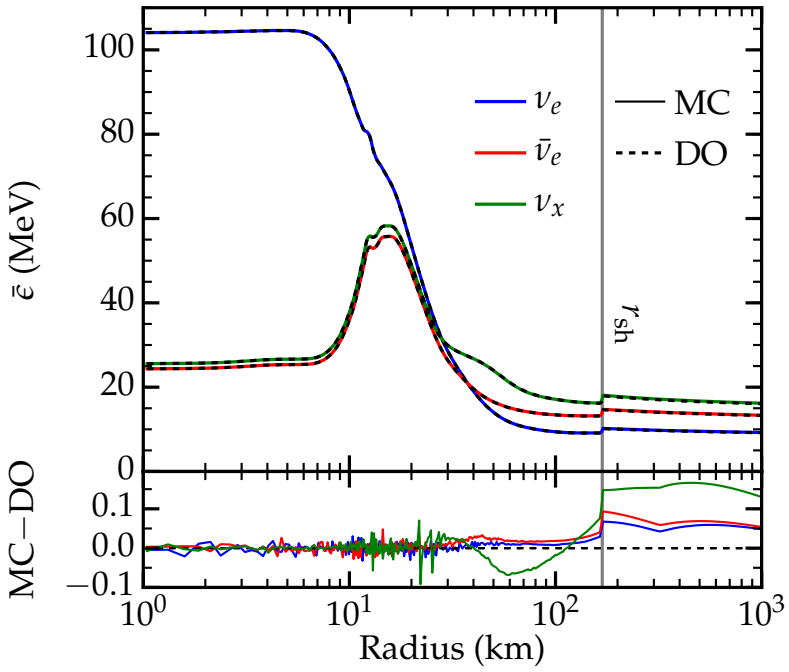

Figure 5.3: **1D neutrino average energy.** The average comoving-frame neutrino energy weighted by the lab-frame energy density (Equation 5.10) for all three neutrino species using the 1D_4x DO calculation and the 1D_4x_native MC calculation. There is good agreement between MC and DO. Resolution tests show that the error improves with momentum-space resolution and MC packet random walk sphere size (see Section 3.3). The average energy jumps at the shock, since the neutrino energy is blueshifted in the comoving frame in the supersonically infalling material outside the shock.

neutrino energy to continuously decrease with radius. The average energy jumps at the shock front, since after passing the shock front, neutrinos are moving through matter falling with speeds of $|v| \sim 0.1c$. The comoving-frame neutrino energy is thus Doppler boosted even though the lab-frame energy density is constant across the shock.

The differences in the average neutrino energy between the 1D_4x DO calculation and the 1D_4x_native MC calculation are smaller than about 0.1 MeV within the shock. Analyzing the various potential sources of errors, the differences at $r \lesssim 30$ km are simply statistical noise that decreases with the square root of the number of MC neutrino packets simulated. The differences below the shock are primarily due to the MC random walk approximation error, and decreases with an increased critical optical depth (see Section 3.3) independent of the momentum-space resolution. The differences near and outside the shock are a result of finite energy resolution, which

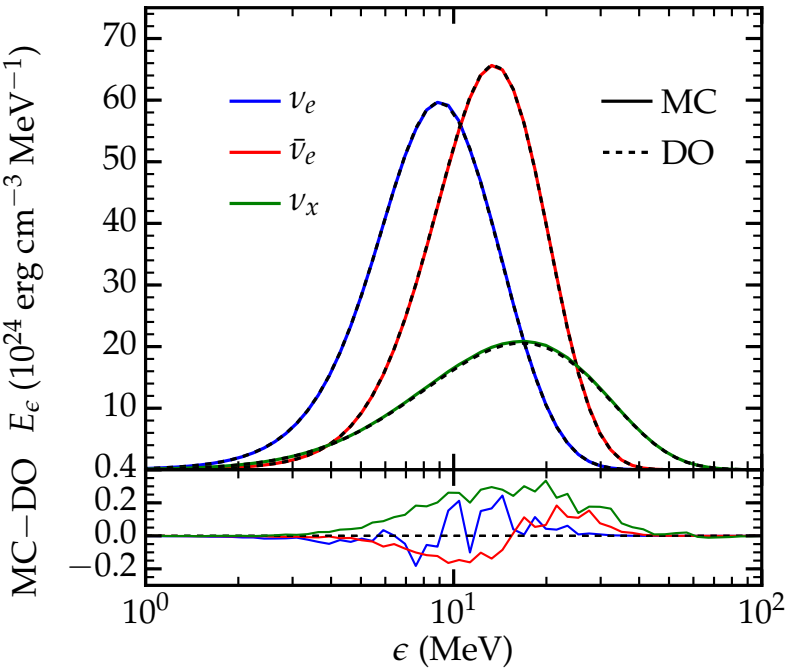

Figure 5.4: **1D spectrum**. The lab-frame direction-integrated spectral energy density based on the comoving-frame neutrino energy density ($E_\epsilon = dE_{\rm lab}/d\epsilon_{\rm com}$) at $r = 105$ km for each species in the 1D_4x DO calculation and the 1D_4x_native MC calculation. This point is inside the shock in the semi-transparent region. In the bottom panel are the differences between the MC and DO results, in the same units. There is good agreement between MC and DO that improves with DO and MC energy resolution. The error below 2 MeV is due to the large width (2 MeV) of the first energy bin. The oscillating errors above 10 MeV are artifacts from the two-grid DO method used in the NSY code (Nagakura, Sumiyoshi, and Yamada, 2014). Resolution tests show that the agreement improves with DO and MC momentum-space resolution. Both sources of error disappear in nonrelativistic calculations.

results in interpolation error when the NSY code transforms energy and direction bins between the comoving and lab frames.

We plot the direction-integrated neutrino energy density spectra at $r = 105$ km for each neutrino species in Figure 5.4. This point is below the shock in the semi-transparent region. The results of the 1D_4x DO calculation and the 1D_4x_native MC calculations agree in every bin with at most $\approx 1.5\%$ of the peak value. In energy bins with little energy density, the relative errors become quite large, but bins with such small energy density have much less dynamical effect in CCSN simulations. Some statistical noise from the MC calculation can be seen in the range of $5 - 20$ MeV, but the small overall offsets are due to the finite neutrino

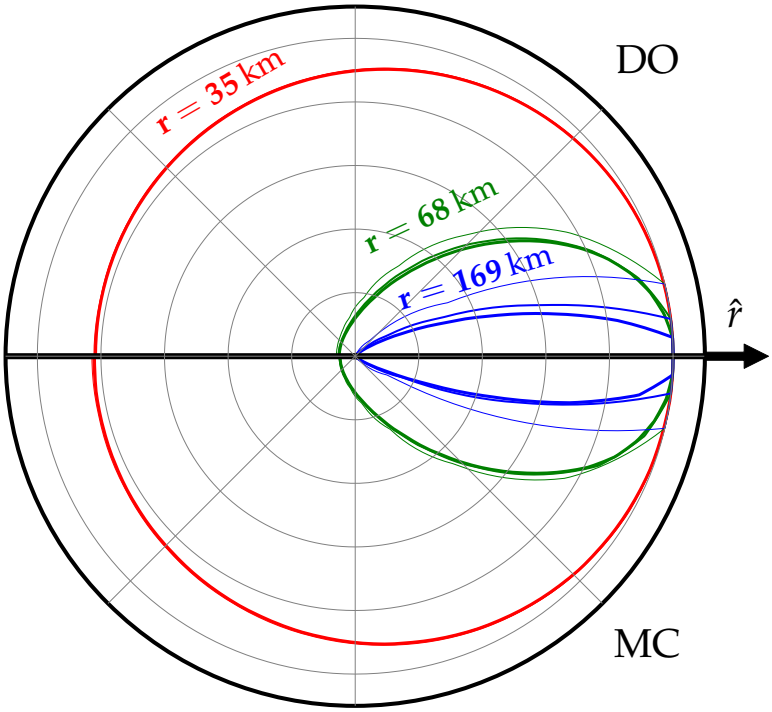

Figure 5.5: **1D distribution function shape**. Normalized lab-frame distribution functions as a function of propagation angle for heavy lepton neutrinos at three radii using both the DO (top) and MC (bottom) calculations. A circular shape indicates isotropic radiation, while sharper shapes indicate radiation moving primarily in one direction. The outward radial direction is to the right in the plot. The distribution functions at three locations are shown: just inside the the shock (169 km – blue), at 68 km (green), and at $\rho = 2 \times 10^{12}$ g cm^{-3} (35 km). Line thickness corresponds to resolution. The thickest lines are from the 1D_4x MC and DO calculations, the medium lines are from 1D_2x MC and DO calculations, and the thinnest lines are from the 1D_1x MC and DO calculations. The 1D_4x_native calculation does not use an angular grid and so cannot be plotted here. The MC and DO results are nearly indistinguishable. The resolution does not affect nearly isotropic radiation fields, but low resolution artificially broadens free-streaming neutrino distributions.

energy and angular resolution.

Figure 5.5 shows the lab-frame energy-integrated heavy lepton neutrino distribution function at three separate radii. The red curves are from the radius where $\rho = 2\times10^{12}$ g cm^{-3} and show that the neutrinos are nearly isotropic. The blue curves are from near the shock front and are nearly free-streaming and very forward-peaked, as almost no neutrinos are moving inward. The green lines show the distribution function at an intermediate location of $r = 68$ km ($\rho = 4.7 \times 10^{10}$ g cm^{-3}) between the trapped and free-streaming limits. In the plot, the distribution function is

normalized by the largest value so the shapes can be easily compared. We assume a constant value for the distribution within the directional bin in the forward direction and linearly interpolate the distribution function for all other directions. This is done to ensure that in post-processing the value of the distribution function never exceeds one. However, this gives rise to the artificially flattened nose of the distribution functions most apparent in the blue curves.

The thickest lines in Figure 5.5 are from high-resolution 1D_4x MC and DO simulations, while thinner lines indicate lower resolution. The 1D_4x_native MC simulation does not collect data on a grid of discrete angular bins, so its results cannot be used to make such a plot. The importance of the angular resolution is very apparent for the blue curves at the shock front, since most of the neutrino energy is in a single angular bin. The MC results look remarkably similar to the DO results, though a lack of numerical diffusion in the MC calculations allows for slightly more sharply forward-peaked distribution functions for a given angular resolution. This angular dependence is reflected in all angular moments of the distribution function.

In Figure 5.6, we show the energy-integrated lab-frame radial flux factor (F^r/E, see Equation 2.51) of the distribution function of all three neutrino species using the 1D_4x DO calculation and the 1D_4x_native MC calculation. Below around 30 km the neutrinos are trapped and the distribution function is nearly isotropic, resulting in a minuscule flux relative to the energy density (corresponding to the red curves in Figure 5.5). In the transition region (corresponding to the green curves in Figure 5.5), an increasing fraction of the neutrino radiation energy is moving radially outward, causing the flux factor to approach 1 at large radii (corresponding to the blue curves in Figure 5.5). F^θ and F^ϕ are identically zero due to spherical symmetry.

The angular moments of the radiation field are naturally sensitive to the angular grid resolution. We see small differences of at most around 0.02 in the flux factor, but the size of this difference scales approximately linearly with the angular grid size for calculations with a coarser angular grid (not plotted). Sedonu consistently predicts a more rapid transition to free streaming than does the NSY code. Here the MC method shows a significant advantage in that by computing moments directly rather than post-processing from an angular grid, we get angular moments with effectively infinite angular resolution. The NSY code comes very close to this solution, but suffers from some angular diffusion. This causes the NSY code to predict distribution functions that are slightly, though artificially, more isotropic.

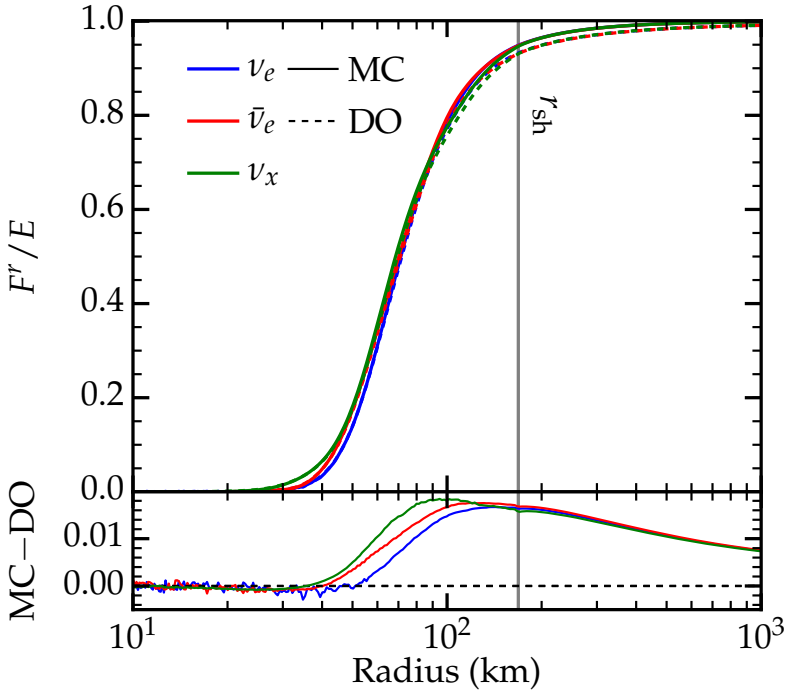

Figure 5.6: **1D flux factor**. The energy-integrated flux factor (F^r/E) for all three neutrino species in the lab frame using the 1D_4x DO calculation and the 1D_4x_native MC calculation. The bottom panel contains the differences between the MC and DO results in the same units. There is good agreement between the MC and DO results that improves with DO directional angular resolution. The largest differences are in the semi-transparent region, where momentum-space diffusivity in the DO method broadens the distribution function angular shape.

The difference approaches a small but constant value at large radii, where almost all of the energy in the DO calculations is contained in the single outward-pointing angular bin. The Sedonu results are, however, visibly noisy in the difference plot, since subtractive cancellation tends to amplify statistical noise. There is a small hump visible in the heavy lepton neutrino difference plot just below $r = 100$ km that is a result of the MC random walk approximation. The size of this hump decreases when the critical optical depth is increased (see Section 3.3), bringing it closer to the electron neutrino and electron anti-neutrino difference curves.

In Figure 5.7, we show the rr component of the energy-integrated lab-frame Eddington tensor (P^{ij}/E, see Equation 2.51) of the distribution function of all three neutrino species. Only the diagonal components of the Eddington tensor (P^{rr}/E,$P^{\theta\theta}/E$, and $P^{\phi\phi}/E$) are nonzero in spherical symmetry. At $r \lesssim 30$ km, all diagonal components of the Eddington tensor are $1/3$ because the radiation is nearly isotropic. After

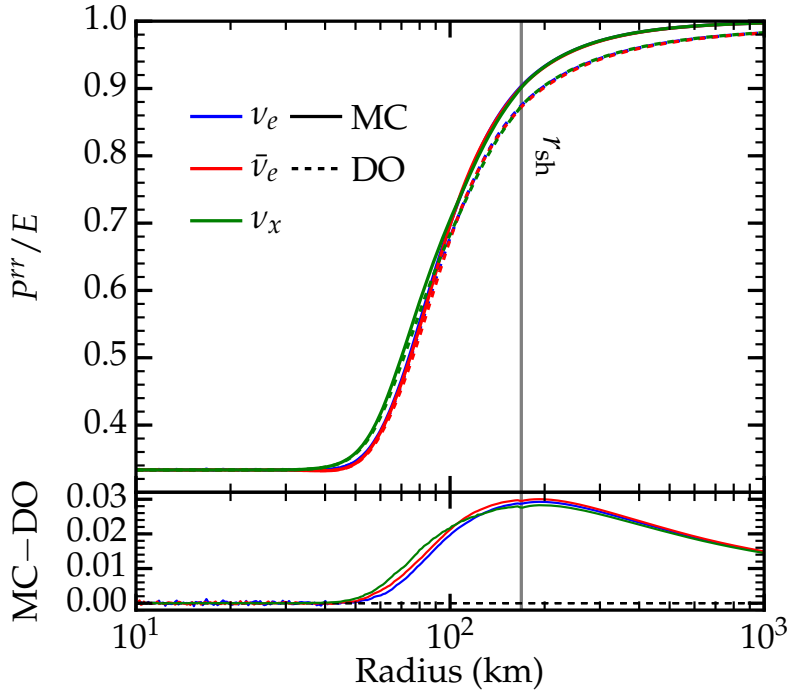

Figure 5.7: **1D Eddington factor**. The energy-integrated rr component of the Eddington tensor (P^{rr}/E) in the lab frame for all three neutrino species using the 1D_4x DO calculation and the 1D_4x_native MC calculation. The bottom panel shows the differences between the MC and DO results in the same units. There is good agreement between MC and DO that improves with DO directional angular resolution (see also Figure 5.8). MC predicts a faster transition to free streaming.

decoupling, the rr component approaches unity as all radiation is moving radially outward, while the $\theta\theta$ and $\phi\phi$ components (not plotted) approach zero.

Once again, the differences between Sedonu and the NSY code scale approximately linearly with the neutrino direction angular zone sizes. However, the maximum difference of 0.03 is larger than the maximum flux factor difference of 0.02. Unlike with previously discussed radiation quantities, the random walk approximation does not add significant error to P^{rr}. Though we do not plot $P^{\theta\theta}$ or $P^{\phi\phi}$, the differences between MC and DO results are similar to those of P^{rr}. Since the integral in Equation 2.51 contains a factor of $(\mathbf{\Omega}\cdot\hat{r})^2$, the results do not suffer from subtractive cancellation and the amount of statistical noise is significantly lower than that of the flux factor.

The dependence of the angular moments on angular resolution can be clearly seen in Figure 5.8, where we plot the rr component of the Eddington tensor for four MC calculations (solid lines) and three DO calculations (dashed lines). We first direct

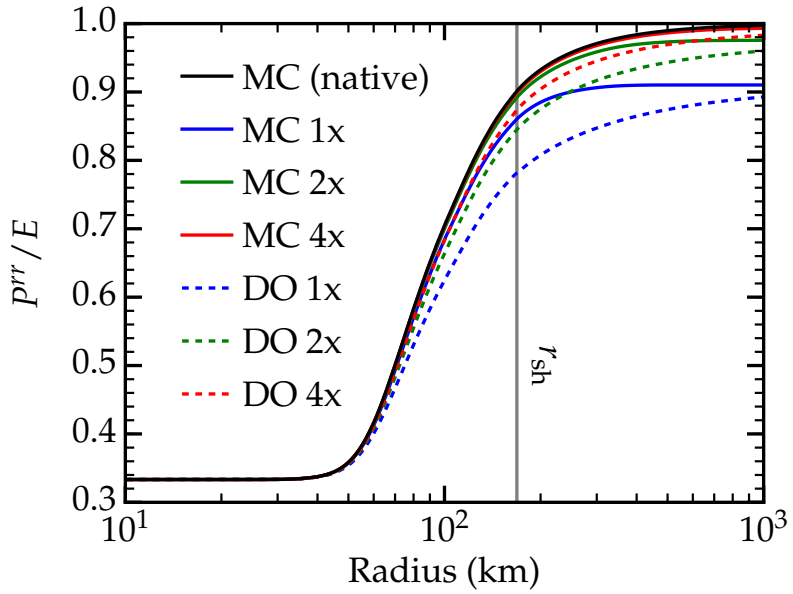

Figure 5.8: **1D resolution**. The rr component of the lab-frame energy-integrated Eddington tensor as calculated using the DO transport method (dashed lines) and the MC method (solid lines). The black solid line shows the results from the 1D_4x_native calculation (MC packets accumulate into moments directly). The colored solid lines show results from MC calculations where MC packets collect into angular bins (1D_1x, 1D_2x, and 1D_3x for blue, green, and red curves, respectively), which are post-processed in the same manner as the DO results. Very high directional angular resolution is required for accurate angular moment results.

our attention to the blue lines, corresponding to the low resolution 1D_1x DO and MC calculations. Even though both are post-processed in the same way from the same angular grid, the MC results transition to large values of P^{rr} faster than do the DO results. At $r \approx 300\,\mathrm{km}$, P^{rr}/E saturates at the maximum value possible given the angular resolution, which the DO results approach at large radii. The same is true for the higher resolution green and red curves, but the saturation occurs at a larger radius and is not so visibly obvious.

Due to the effectively infinite angular resolution of the 1D_4x_native MC calculation, the corresponding black line in Figure 5.8 can be thought of as exact, modulo a small amount of MC noise. Going from coarsest to finest resolution, the maximum difference between the DO results and the black curve are 0.125, 0.057, and 0.028. This corresponds to a factor of 2.2 improvement when going from 1x to 2x resolution, and a factor of 2.0 when going from 2x to 4x resolution. Similarly, the maximum difference between the gridded MC and the native MC results are, in order of increasing resolution, 0.0896, 0.0243, and 0.0062. The accuracy improves

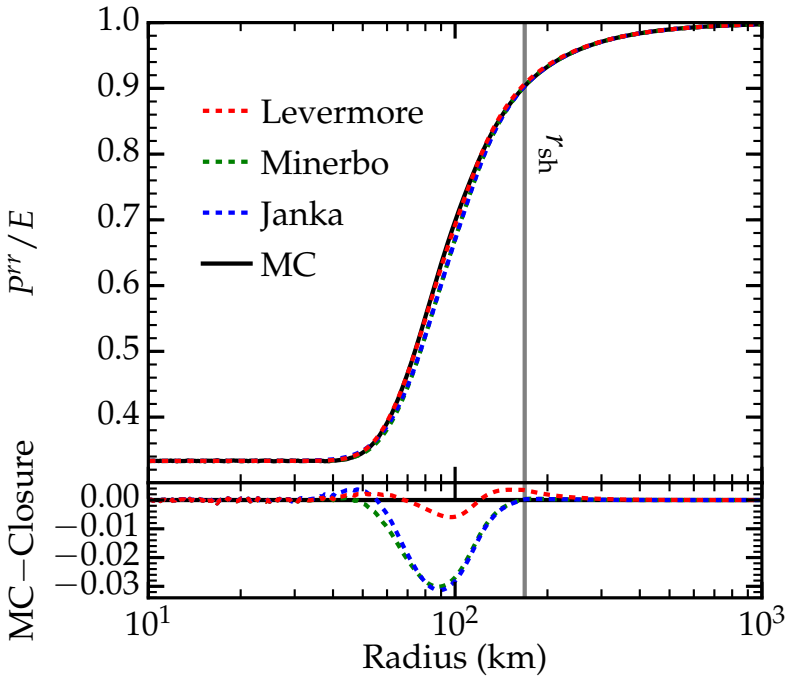

Figure 5.9: **1D approximate closures**. The lab-frame rr components of the energy-integrated Eddington tensor as calculated in the 1D_4x_native MC calculation (black solid line), the Levermore closure (red dashed lines), the Minerbo closure (green dot-dashed lines), and the Janka closure (blue dotted lines). The approximate closure values are calculated using the energy density and flux from the 1D_4x_native MC calculation. The bottom panel shows the difference between the MC results and the closure estimate in the same units. The Levermore closure appears to have the closest agreement with the MC results in this scenario. The differences between the approximate closures and highest resolution DO results (not plotted) are nearly identical to the differences between the approximate closures and MC results. The errors in the $\theta\theta$ component of the Eddington tensor (not plotted) behave in the same way.

by a factor of 3.7 when going from 1x to 2x resolution, and by a factor of 3.9 when going from 2x to 4x resolution. This trend, where DO results are near first order convergence and gridded MC results are near second order convergence, is apparent in the flux factor results as well. This is because the post-processing angular integration scheme is second order (except in the forward-most bin, where it is first order), but the evolution scheme in the NSY code is only first order.

The use of an approximate analytic closure in two-moment radiation transport schemes is significantly faster than either the DO or MC methods. However, since there are many reasonable closures available, it is of great interest to evaluate how well these closures perform against our full Boltzmann results. We re-plot the

electron neutrino P^{rr} curve (black line in Figure 5.8) from the 1D_4x_native MC calculation as a solid black line in Figure 5.9. We then use E and F^r from the same MC calculation to estimate P^{rr} using the three analytic closures given in Equation 2.57. The Janka and Minerbo closures perform similarly and have a maximum difference with MC of ~ 0.03, which is comparable to the differences between the 1D_4x DO calculation and the 1D_4x_native MC calculation. The Levermore closure, however, performs better, with a maximum difference of ~ 0.006. This is significantly better than the accuracy of any DO result and is comparable to the accuracy of the 1D_4x MC calculation. These results are also replicated in a similar analysis of $P^{\theta\theta}$ and $P^{\phi\phi}$ (not plotted). In short, analytic closures perform remarkably well in this particular steady-state spherically-symmetric transport calculation.

The primary role of neutrinos in the explosion mechanism of CCSNe is redistributing thermal energy from the protoneutron star region to the gain region that drives turbulence and pushes the shock outward. The relevance of these detailed transport calculations comes down to how the differences between the methods affect the heating and cooling of matter in the supernova. In Figure 5.10, we show the comoving-frame net gain, i.e., the heating rate less the cooling rate due to neutrinos. We show results from the 1D_4x MC and DO calculations (red line), the 1D_4x_nonrel MC and DO calculations (green line), and the 1D_1x MC and DO calculations (blue line). Below about 90 km the fluid is overall cooling, and the emitted neutrinos pass through the gain region from 90 km to 170 km and deposit energy. Below the shock, the net gain from the 1D_4x MC and DO calculations are very similar, with differences of $\lesssim 1\%$ of the peaks in the gain curve.

Just outside the shock, the fluid densities are low and most nucleons are bound in nuclei. Because of this, the heating is due primarily to neutrino pair annihilation. The pair annihilation rates are underresolved in neutrino energy space even with 80 energy bins, resulting in significant differences between heating rates of different resolutions. However, test results show only a 20% difference between the 1D_4x results and a test with an energy-space resolution of 160 bins. We can use the radial profiles of heating rate, density, and velocity to estimate the amount of energy per nucleon the fluid is heated before passing through the shock as

$$\Delta E \approx \int \frac{m_n \mathcal{H}(r)}{\rho(r)|v(r)|} dr \ , \tag{5.11}$$

where $\mathcal{H}$ is the heating rate. Using the heating rate from the highest-resolution simulations, this predicts a total heating of ~ 0.1 MeV nucleon^{-1}. Compared to the

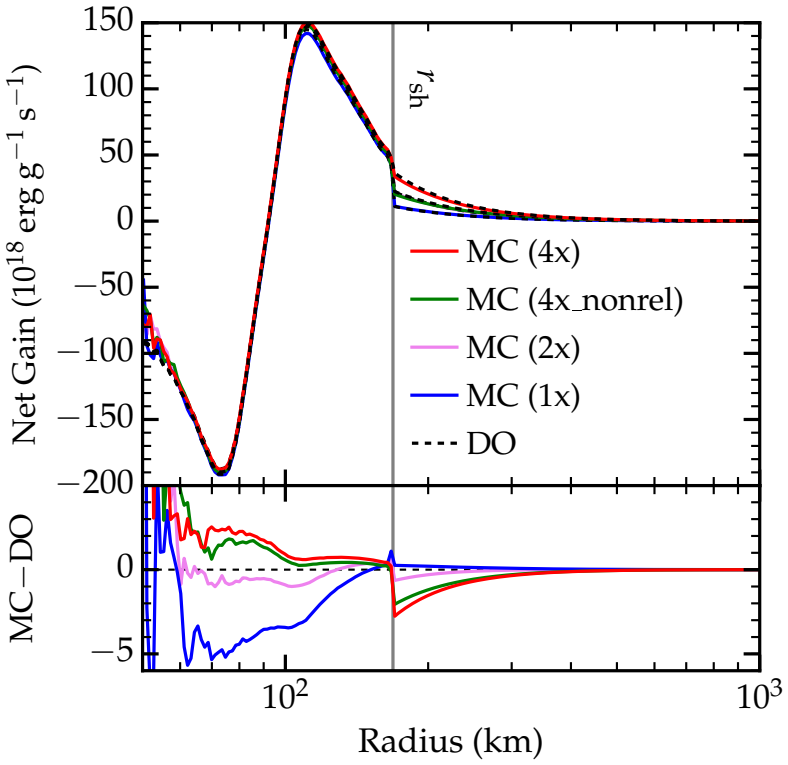

Figure 5.10: **1D net gain**. The net gain (heating − cooling) using the 1D_4x DO calculation and the 1D_4x_native MC calculation. The transition from net cooling to net heating lies at ∼ 90 km. The MC results are very noisy below ∼ 60 km, but otherwise the highest resolution MC and DO results agree within the shock to ∼ 1%. Neutrino pair annihilation is the dominant heating mechanism outside the shock. This process is under-resolved in neutrino energy space, but tests show this heating rate to converge with ≥ 160 energy bins. The jump in the difference at the shock is due to the large jump in density combined with an over-estimate of the heating rate from our neutrino pair annihilation treatment.

post-shock temperatures of $T \lesssim 20$ MeV and the iron-56 binding energy of 8.8 MeV, this pre-shock heating is insignificant.

The differences between MC and DO are amplified outside the shock, where we must divide a volumetric heating rate (in erg cm^{-3} s^{-1}) by the low density to get a specific heating rate. Also, recall that in our calculation of pair annihilation rates, we assume that the neutrino distribution functions are isotropic (see Section 5.2 for details). At large radii relative to the neutrinospheres and to leading order, however, the angular dependence actual reaction rates is (e.g., Bruenn 1985)

$$R_{\text{pair,abs}}(\epsilon, \bar{\epsilon}, \mathbf{\Omega} \cdot \bar{\mathbf{\Omega}}) \propto 1 - \mathbf{\Omega} \cdot \bar{\mathbf{\Omega}} \sim \left(\frac{r}{r_\nu}\right)^{-2}, \tag{5.12}$$

where r_ν is the neutrinosphere radius. The location of the neutrinosphere depends on the neutrino species and energy, but for a typical radius of $r_\nu = 50\,\mathrm{km}$ this angular term scales the reaction rate by a factor of ~ 0.1 at the shock. Thus, we expect the heating rates (and hence the heating rate differences) to be over-estimated by a factor of ~ 10 at the shock.

Including velocity-dependence in neutrino transport algorithms is a complication that can significantly increase the complexity and cost of the transport calculation. It is natural to attempt to quantify the size of the error made in codes that neglect velocity dependence. We repeat the high-resolution calculations with the same rest-frame fluid profile shown in Figure 5.1, but set all velocities to zero. Velocity dependence changes the comoving frame neutrino energies and directions, modifying the rates at which neutrinos interact with the fluid. This has a very minor effect below the shock, but significantly changes the heating rate outside the shock where velocities are $\sim 0.1c$. However, the density drops by a factor of 10 across the shock and the pre-shock fluid moves so quickly that the overall heating is negligible. These small errors outside the shock are unlikely to have a significant impact on simulation results. The volume-integrated net gain in the gain region (where there is net heating under the shock) is $2.16 \times 10^{51}\,\mathrm{erg\,s^{-1}}$ in the 1D_4x DO calculation and $2.18 \times 10^{51}\,\mathrm{erg\,s^{-1}}$ in the 1D_4x_native MC calculation, a difference of only 0.34%. Compare this to the difference of the same quantity between the 1D_4x and 1D_1x DO calculations of 2.0% and between the 1D_4x and 1D_4x_nonrel DO calculations of 1.2%. Though including velocity dependence impacts the heating rates more than the differences between the codes in the highest resolution case, low resolution can cause significantly larger inaccuracies.

5.5 Transport Comparison in Axisymmetry

In this section, we describe results from the first multi-dimensional comparison of Boltzmann-level neutrino transport codes. We present a set of four axisymmetric time-independent neutrino transport calculations as listed in Table 5.1. Once again, the NSY code is used to calculate an approximately steady-state solution and the opacities and emissivities are exported from the completed NSY calculations to Sedonu for the MC calculation. Due to computational cost, we only consider two resolutions in the DO code. The low-resolution (2D_LR) calculations have momentum-space resolution equivalent to the 1D_1x calculations, and the high-resolution (2D_HR) calculations have momentum-space resolution between that of the 1D_1x and 1D_2x calculations.

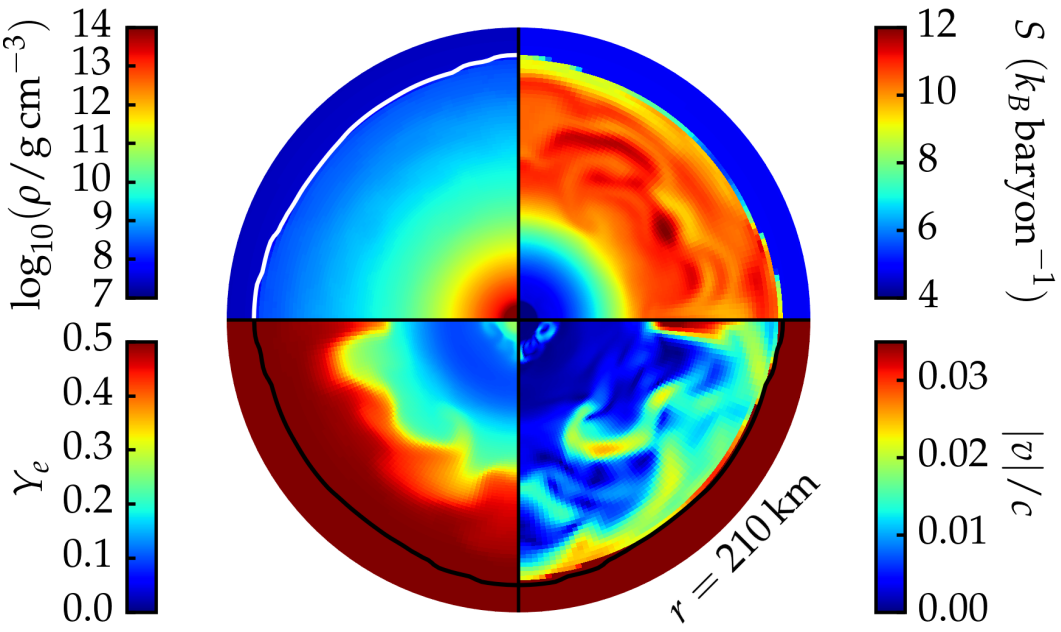

Figure 5.11: **2D fluid background.** The rest frame fluid density (top left), specific entropy (top right), electron fraction (bottom left), and speed (bottom right) from 2D core collapse simulations using the NSY code (Nagakura, Iwakami, Furusawa, Sumiyoshi, et al., 2017) at 100 ms after bounce. The shock front is drawn as a contour at $s = 7\,k_B$ baryon^{-1} and is colored for clarity. The polar axis is vertical and the equatorial plane is horizontal. The gain region hosts neutrino-driven convection and protoneutron star convection is visible in the velocity and electron fraction quadrants. All quadrants in the plot show data from the northern hemisphere, though the computational domain includes both hemispheres. This fluid background is used for all axisymmetric simulations in this study.

The rest-frame fluid profile used in all simulations shown in Figure 5.11 comes from a 2D simulation of the collapse of the same $11.2 M_\odot$ star (Woosley, Heger, and Weaver, 2002) used in Section 5.4 (Nagakura, Iwakami, Furusawa, Sumiyoshi, et al., 2017). In Figure 5.11 and in all other colormap plots in this section, data separated into quadrants shows data from the northern hemisphere of the calculation only to ease visual comparison of datasets. Data on half-circles show the full simulation domain out to $r = 210$ km. In Figure 5.11, multi-dimensional structure in all fluid quantities is apparent and is due to neutrino-driven turbulent convection. The postshock velocity field in particular shows fluid speeds up to $0.037\,c$, compared to the maximum radial velocity of $0.015\,c$ in the 1D calculations. This multi-dimensional structure provides a challenge for any radiation transport method.

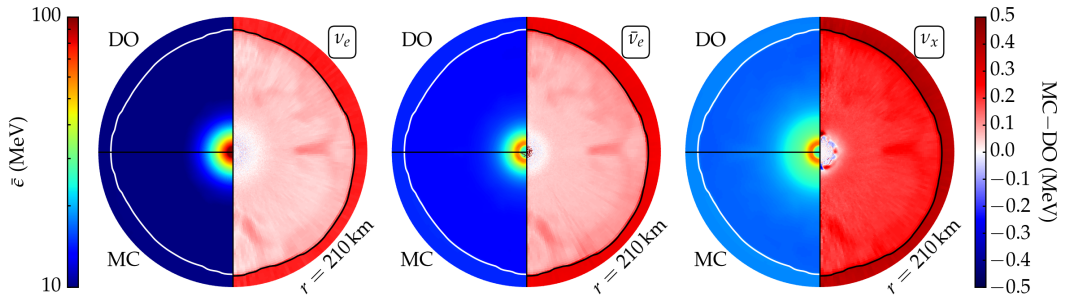

Figure 5.12: **2D neutrino average energy.** All plots show the mixed-frame average neutrino energy (Equation 5.10). In each plot, we show results from the 1D_HR DO calculation (top left quadrant, northern hemisphere data) and the 1D_HR_native MC calculation (bottom left quadrant, northern hemisphere data). The difference between them in MeV is shown in the right half of each plot, which contains data from both hemispheres. The left plot shows results from electron neutrinos, the center plot shows results from electron anti-neutrinos, and the right plot shows results from heavy lepton neutrinos. The shock front is drawn as a contour at entropy $s = 7\,k_B$ baryon^{-1} and is colored for clarity. The results agree well, though the error jumps across the shock due to diffusivity in the two-grid DO method with limited neutrino energy resolution.

We begin with a comparison of the spectral properties of the results from Sedonu and the NSY code. Figure 5.12 shows the comoving-frame average energy of each of the three simulated neutrino species for the 2D_HR DO calculation and the 2D_HR_native MC calculation. Just as in the 1D calculations, the electron neutrinos have the highest energy in the inner core due to the high electron chemical potential, and the lowest energy at large radii since they decouple at the largest radius and the lowest matter temperature. The DO and MC results are nearly identical, so differences can only be seen in the right half of each plot, where we subtract the DO results from the MC results. The average energies differ between the MC and DO results by at most 0.5 MeV, which is larger than in the 1D results in Figure 5.3 due to the lower energy resolution. When electron neutrinos and anti-neutrinos decouple from matter, the opacity is dominated by absorption. Because of this, MC packets that use the random walk approximation quickly lose energy, preventing errors from the random walk approximation from propagating outward through the rest of the domain. However, the heavy lepton neutrino opacity is dominated by scattering, so MC packets carrying errors from the random walk approximation retain their energy when traveling through the rest of the domain, causing errors to be slightly higher. Just as in the 1D results, the differences between the MC and DO average

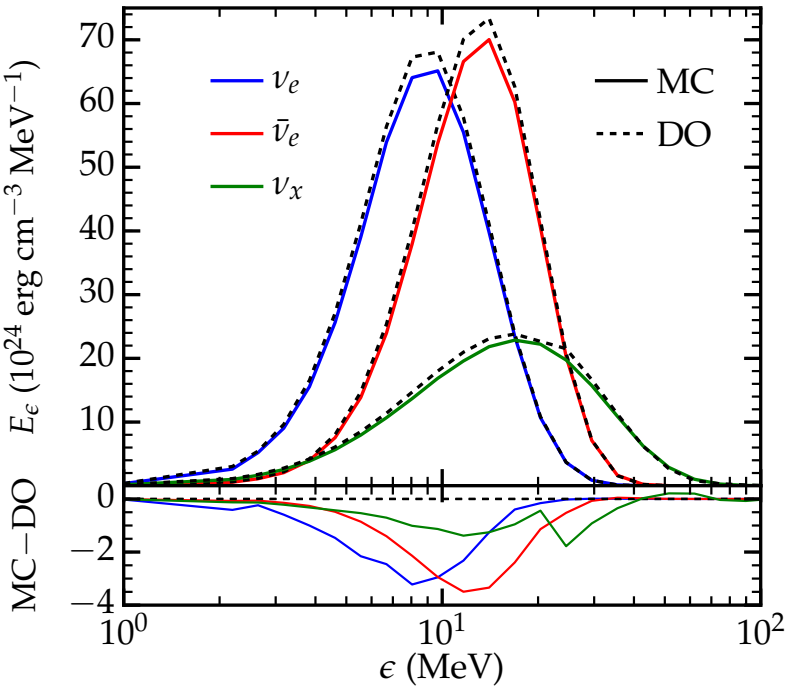

Figure 5.13: **2D spectrum**. The lab-frame direction-integrated spectral energy density based on the comoving-frame neutrino energy density ($E_\epsilon = dE_{\rm lab}/d\epsilon_{\rm com}$) for each species at $r = 105$ km and $\theta = 36°$ (from the north pole). Dashed lines are results from the 2D_HR DO calculation and solid lines are from the 2D_HR_native MC calculation. There is good agreement between the MC and DO results, though the DO results have lower peaks due to low angular resolution. The differences in the amplitudes reflects differences in overall energy density decrease with momentum-space resolution.

energies error jump across the shock, since the NSY code suffers from numerical diffusion when transforming between grids in the two grid approach (Nagakura, Sumiyoshi, and Yamada, 2014). There are also a number of hot spots in the average energy differences within the shock, which correspond to regions of high velocity in Figure 5.11. These differences are also because of some numerical diffusion in the two-grid approach. Heavy lepton neutrinos are more strongly impacted by the protoneutron star convection, since they decouple at a smaller radius. The features visible in the heavy lepton neutrino average energy difference plot (rightmost panel of Figure 5.12) at small radii are diminished by reducing the MC random walk critical optical depth, independent of momentum space resolution.

Though the energy resolution is coarser than in the 1D calculations, we are able to compare the full spectra at a given location. For Figure 5.13, we choose the same radius of 105 km used for Figure 5.4 and an angle of 36° from the north

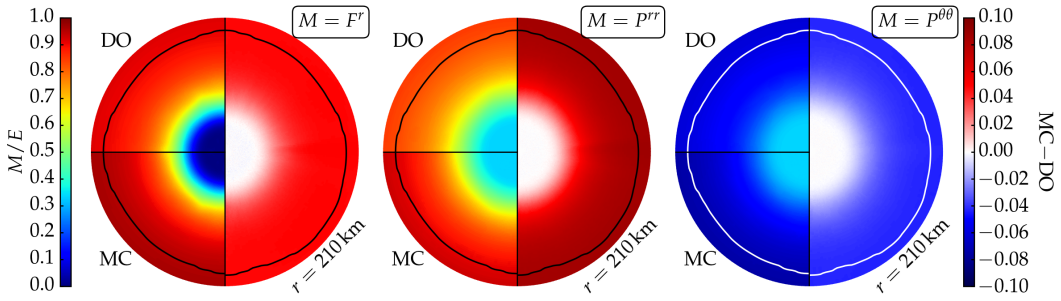

Figure 5.14: **2D flux factor and Eddington tensor (diagonal).** The leftmost plot shows the electron neutrino energy-integrated lab-frame radial flux factor, the center plot shows the rr component of the Eddington tensor, and the right plot shows the $\theta\theta$ component of the Eddington tensor. In each plot, we show the radiation moment computed using the 2D_HR DO calculation (top left quadrant, northern hemisphere data) and the 2D_HR_native MC calculation (bottom left quadrant, northern hemisphere data). The difference between them is shown in the right half of each plot, which shows data from both hemispheres. The shock front is drawn as a contour at entropy $s = 7\,k_B$ baryon^{-1} and is colored for clarity. The results from other neutrino species behave nearly identically. These plots effectively replicate the 1D results in Figures 5.6 and 5.7, but with a DO angular resolution between the 1D_1x and 1D_2x resolutions. MC results show a faster transition to forward-peaked distribution functions due to the limited angular resolution in the DO calculation.

pole. We plot the direction-integrated spectra of all three neutrino species using the 2D_HR DO calculation and the 2D_HR_native MC calculation. The neutrino energy density within each comoving frame energy bin is measured in the lab frame and the individual neutrino energy in the comoving frame, resulting in a mixed-frame quantity. The results are remarkably similar, and effectively reproduce the 1D results. The heights of the peaks differ by $\sim$ 5%, which is comparable to the differences between MC and DO results in the energy density in the lower-resolution 1D results.

In Figure 5.14, we plot the energy-integrated lab-frame electron neutrino flux factor and Eddington tensor using the 2D_HR DO calculation and the 2D_HR_native MC calculation. These plots effectively reproduce the 1D angular moment results in Figures 5.6 and 5.7. We again see that MC results exhibit a quicker transition to a forward-peaked distribution, that the errors in the second moment (P^{rr}/E) are larger than in the first (F^r/E), and that the MC noise in the second moment is smaller than in the first. The magnitude of the differences in P^{rr}/E of $\sim$ 0.1 at the shock can be compared to the 1D results in Figure 5.8. The 2D_HR differences are between the

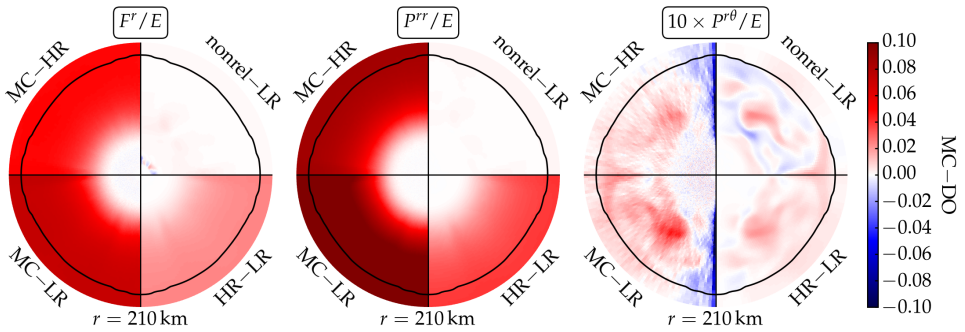

Figure 5.15: **2D resolution and relativity**. All plots show differences between angular moments of the energy-integrated electron neutrino radiation field using different calculations. In each plot, we show a comparison between the 2D_HR_native MC calculation and the 2D_HR DO calculation (top left), between the 2D_HR_native MC calculation and the 2D_LR DO calculation (bottom left), between the 2D_HR DO calculation and the 2D_LR DO calculation (bottom right), and between the 2D_LR_nonrel DO calculation and the 2D_LR DO calculation (top right). The left plot shows the radial component of the flux flux factor, the center plot shows the rr component of the Eddington tensor, and the right plot shows the $r\theta$ component of the Eddington tensor. The shock front is drawn as a contour at entropy $s = 7\,k_B\,\mathrm{baryon}^{-1}$. The left quadrants of each plot show that the DO error decreases with increasing angular resolution. The top right quadrants show that special relativistic effects have a relatively small impact on the moments.

1D_1x and 1D_2x differences, reflecting the fact that the 2D_HR angular resolution is between that of the 1D_1x and 1D_2x calculations. We also demonstrate this resolution dependence in the leftmost (for F^r/E) and center (for P^{rr}/E) plots of Figure 5.15. The top left quadrant of each shows the difference between the moments calculated using the 2D_HR DO calculation and the 2D_HR_native MC calculation. The bottom left quadrant shows the difference between the 2D_LR DO calculation and the same MC calculation. The differences are significantly smaller for the higher resolution DO calculation, indicating that the DO results are converging to the MC results with increasing resolution.

Unlike in spherical symmetry, $P^{r\theta}$ is not identically zero in axisymmetry and is thus a sensitive probe of multidimensional effects on the radiation field. $P^{r\phi}$ and $P^{\theta\phi}$ are still identically zero, since we do not consider azimuthal fluid velocities. In Figure 5.16, we plot the energy-integrated lab-frame $P^{r\theta}/E$ for all three neutrino species using the 2D_HR DO calculation and the 2D_HR_native MC calculation. Since the dominant neutrino propogation direction is radial, the off-diagonal components of the pressure tensor are strongly correlated with the corresponding flux.

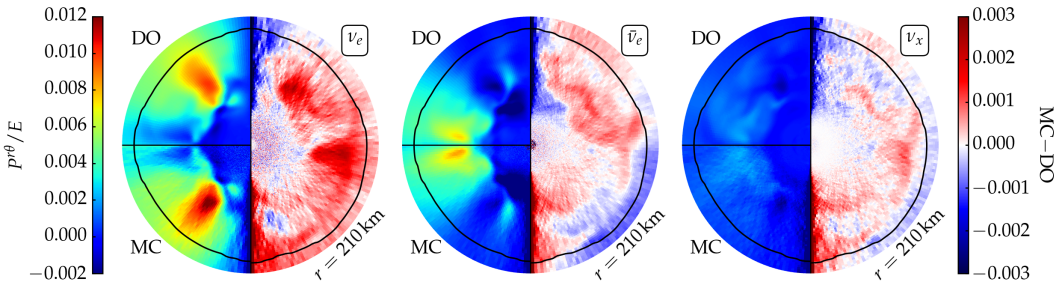

Figure 5.16: **2D Eddington tensor (off-diagonal).** All plots show the energy-integrated lab-frame $r\theta$ component of the Eddington tensor. This is a sensitive probe of multi-dimensional anisotropy, as it is identically zero in 1D calculations. In each plot, we show the radiation moment computed using the 2D_HR DO calculation (top left quadrant, northern hemisphere data) and the 2D_HR_native MC calculation (bottom left quadrant, northern hemisphere data). The left plot shows electron neutrinos, the center shows electron anti-neutrinos, and the right shows heavy lepton neutrinos. The difference between the MC and DO results is shown in the right half of each plot, which shows data from both hemispheres. The shock front is drawn as a contour at entropy $s = 7\,k_B$ baryon^{-1} and is colored for clarity. MC results show larger values of $P^{r\theta}$ due to limited angular resolution in the DO calculation (see right panel of Figure 5.15).

In this particular snapshot, $P^{r\theta}$ happens to be overall mostly positive, and we find the morphology to be indeed very similar to F^{θ} (not shown). Generally, both positive and negative values are to be expected (see Nagakura, Iwakami, Furusawa, Sumiyoshi, et al. 2017). It is interesting to note that the electron neutrino and electron anti-neutrino plots have complementary hot spots. Within the protoneutron star, non-radial neutrino fluxes are present due to turbulent fluid carrying trapped neutrinos. Outside of the convective zone of the protoneutron star but still within the neutrinospheres, electron neutrinos tend to diffuse away from regions of high electron chemical potential while electron anti-neutrinos diffuse toward them. In tests where the inner 105 km is exluded from the calculation, the $P^{r\theta}$ distribution is much more uniform, suggesting that the hot spots are due to a combination of anisotropic neutrinos from the neutrinosphere interacting with multi-dimensional features in the fluid background.

Once again, the MC and DO results for $P^{r\theta}$ look remarkably similar. Unlike for the diagonal moments, much subtractive cancellation occurs when computing $P^{r\theta}$, which in turn requires a large number of MC packets to drive down the noise. Just as is the case with the other moments, the MC calculation tends to show larger values

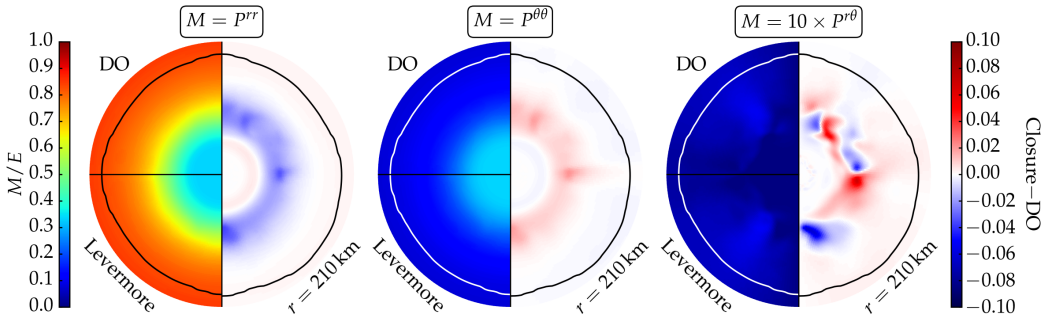

Figure 5.17: **2D approximate closures**. All plots show energy-integrated components of the Eddington tensor of the electron neutrino radiation field in the lab frame. The leftmost plot shows the rr component, the center plot shows the $\theta\theta$ component, and the right plot shows the $r\theta$ component, multiplied by 10 (including the differences) for clarity. In each plot, the top left quadrant shows results from the northern hemisphere of the 2D_HR DO calculation. The bottom left shows results when the energy density and flux from the 2D_HR calculation are used to calculate the Eddington tensor component using the Levermore closure (also northern hemisphere data). The right half shows the difference between the two, and includes data from both hemispheres. The shock front is drawn as a contour at entropy $s = 7\,k_B\,\text{baryon}^{-1}$ and is colored for clarity. As in the 1D calculations, the Levermore closure is a good approximation for diagonal components, but it struggles for off-diagonal components. Other closures show slightly larger errors. Electron anti-neutrino and heavy lepton neutrino results behave similarly, except that the overal magnitude of $P^{r\theta}$ is smaller for heavy lepton neutrinos.

of $P^{r\theta}$, since its effectively infinite angular resolution is able to resolve finer angular structures. We demonstrate this resolution dependence in the rightmost plot of Figure 5.15. The top left quadrant shows the difference between the electron neutrino $P^{r\theta}$ from the 2D_HR DO and 2D_HR_native MC calculations, while the bottom left quadrant compares the 2D_LR DO calculation to the same MC calculation. The differences are significantly larger for the lower-resolution calculation, indicating that the DO calculation is converging to the MC result with increasing angular resolution.

Figure 5.17 compares components of the electron neutrino Eddington tensor computed by the 2D_HR DO calculation to those predicted by the Levermore closure using E and F^i from the same DO calculation. We demonstrated in Section 5.4 that in our spherically symmetric snapshot, the Levermore closure predicts P^{rr}/E and $P^{\theta\theta}/E$ from only the flux factor with an accuracy within 0.01 of the actual Eddington tensor value. This result is reproduced in two dimensions for electron neutrinos in

Figure 5.17. The leftmost and center plots show P^{rr}/E and $P^{\theta\theta}/E$, respectively. The top left quadrant of each shows the moment computed directly from the 2D_HR DO calculation (same data as depicted in Figure 5.14), and the bottom left quadrant shows the same moment predicted by the Levermore closure. They are visually identical, and the error plotted on the right side of each plot shows a maximum error of 0.014 in P^{rr}/E and a maximum error of 0.0089 in $P^{\theta\theta}/E$. Though there is some multi-dimensional structure in how accurately the Levermore closure predicts the diagonal components, this effectively mirrors the results of the 1D calculations. The rightmost plot shows $P^{r\theta}/E$ (same data as in Figure 5.16), multiplied by 10 for visibility on this color scale. The Levermore closure predicts this component of the moment within 0.0077. This is large compared to this component's maximum value of 0.012 and compared to a difference of $\sim$ 0.003 between DO and MC results. Thus, though this analytic closure has small errors for the diagonal components of the Eddington tensor, it has difficulty accurately predicting the small off-diagonal components in this CCSN snapshot. The Minerbo and Janka closures show errors at smaller radii, but the extrema of these errors are only slightly larger than those of the Levermore closure. Other neutrino species behave very similarly, except that the heavy lepton neutrino values for $P^{r\theta}$ (and hence errors) are significantly smaller.

Ignoring special relativistic effects in radiation transport calculations greatly simplifies the problem. Fluid velocities are also generally only a few percent of the speed of light below the shock, but are larger in 2D ($\sim 0.037c$) than in 1D ($\leq 0.015c$). We test the effects of ignoring fluid velocities in Figure 5.15, where we plot the difference between the 2D_LR_nonrel and 2D_LR DO calculations. The error in F^r/E and P^{rr}/E from ignoring velocities is much smaller than the difference between MC and DO calculations or the difference between resolutions. The only exception is in the convective region of the protoneutron star, where the flux is determined entirely by the fluid velocity because the neutrinos are trapped. The magnitude of this error is at most comparable to the error induced by the coarse resolution, and is significantly smaller than the error in all components of the second moment predicted by the Levermore closure (Figure 5.17).

Finally, in Figure 5.18, we investigate how these different transport schemes affect the actual heating and cooling rates of the fluid. Once again, we show the results from the 2D_HR DO calculation in the top left quadrant, which outside the core appears visually identical to the 2D_HR_native MC calculation results in the bottom left quadrant. Just as in Figure 5.10, there is significant statistical noise within the

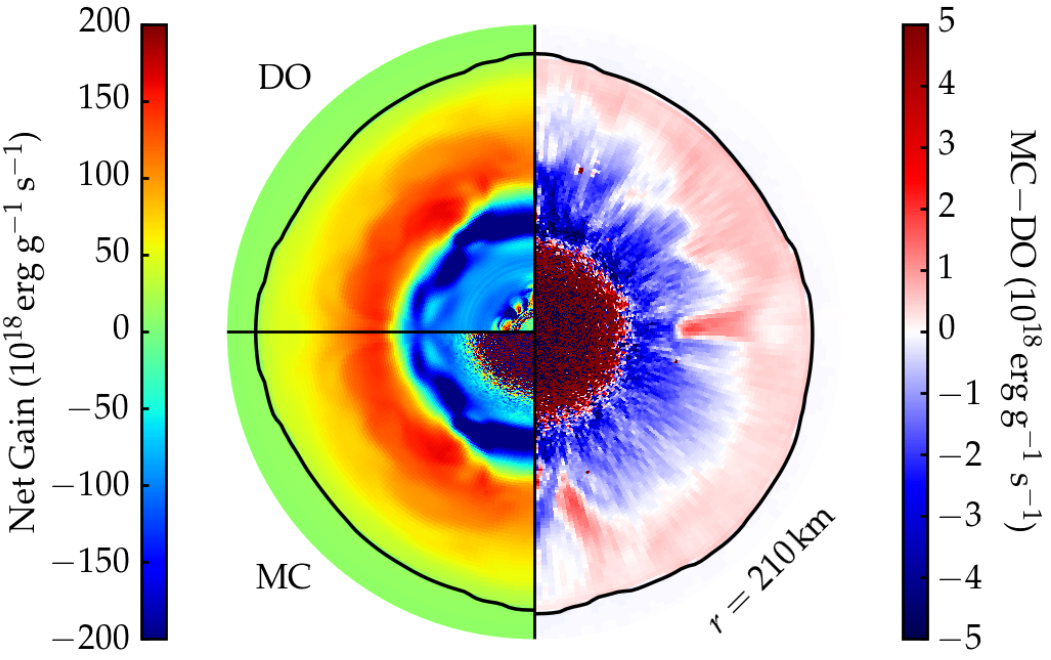

Figure 5.18: **2D net gain.** Net gain ($\mathcal{H} - C$) using the 2D_HR DO calculation (top left, northern hemisphere data) and the 2D_HR_native MC calculation (bottom left, northern hemisphere data). The difference between the two is shown in the right half, and contains data from both hemispheres. The shock front is drawn as a contour at entropy $s = 7\,k_B$ baryon^{-1}. The MC data shows slightly faster cooling in the cooling region, and slightly faster heating in the gain region. The MC data below ~ 70 km is dominated by noise.

core, where neutrinos are largely in equilibrium with the matter. We depict the difference between these results on the right half of the plot. The MC results show more rapid cooling in the cooling region and more rapid heating in the outer regions of the gain region. This is similar to the behavior of the lower-resolution 1D results in Figure 5.10, where MC calculations predict a smaller gain than do the DO calculations at $r \lesssim 125$ km for the 1D_2x calculation and at $r \lesssim 140$ km for the 1D_1x calculations. The 2D MC calculation also predicts larger heating than does the 2D_HR DO calculation in regions of high inward velocity. This is again an effect of the limited momentum-space resolution in the DO calculations that make the two-grid approach somewhat diffusive in angle and energy. This is to be expected given that the average neutrino energies in these regions (Figure 5.12) are higher in the MC calculations. Overall, excluding the noisy region in the core, these errors are at most $\sim 2\%$ of the amplitude of the net gain curve in Figure 5.10.

The volume-integrated gain of the gain region (where there is net heating under the shock) is 9.00×10^{51} erg s^{-1} in the 2D_HR DO calculation and 8.93×10^{51} erg s^{-1} in the 2D_HR MC calculation, which is only a 0.35% difference. Compare to this the relative error of the same quantity between the 2D_LR and 2D_HR DO calculations of 1.3%, which is smaller than in the 1D resolution comparison because our 2D resolutions are much more similar. Even so, the errors from low resolution are significantly larger than the differences between the methods. The difference in integrated heating rate between the 2D_LR and 2D_LR_nonrel DO calculations is 2.0%. This is larger than in the 1D relativity comparison because fluid velocities under the shock are larger in the 2D calculations than in the 1D calculations due to convective motion. Note that the integrated heating rate should not be compared with the 1D results because the fluid profiles are significantly different.

5.6 Conclusions

Neutrinos dominate energy transport in CCSNe and are a vital component of the CCSN explosion mechanism. It is therefore imperative to ensure neutrinos are treated accurately in CCSN simulations. One means of checking the accuracy of a computational method is comparing against another accurate method. The grid-based discrete ordinates (DO) method and particle-based Monte Carlo (MC) method both solve the full transport problem in very different ways. We perform the first detailed multi-dimensional comparison of special relativistic Boltzmann-level neutrino transport codes in the context of CCSNe using the grid-based discrete ordinates (DO) code of Nagakura, Iwakami, Furusawa, Sumiyoshi, et al., 2017 (NSY) and the particle-based Monte Carlo (MC) Sedonu code. We verify that both methods converge to the same result in the limit of large MC packet count and fine DO momentum-space resolution under the assumption of a static fluid background in spherical symmetry and in axisymmetry. This provides confidence in the accuracy of the results from these two completely different approaches.

We demonstrate an agreement of the average neutrino energy to within ~ 0.1 MeV for 1D calculations and ~ 0.5 MeV for coarser 2D calculations everywhere in the simulation domain for all three simulated neutrino species. We also demonstrate exquisite agreement in the local spectra of all three species. We find that numerical diffusion from a coarse momentum-space resolution dominates these small errors, though smaller errors result from finite spatial resolution and from the Monte Carlo random walk approximation.

MC transport computes angular moments of the distribution function with great accuracy when the moments are computed natively during the calculation as opposed to being post-processed from an angular grid. The DO method requires a very high momentum-space angular resolution of about 40 points in the polar direction to compute these moments with similar accuracy in 1D calculations, which is currently not possible in 2D calculations and certainly not possible in 2D time-dependent simulations. The MC method, however, requires a large number of packets to be simulated to reach low noise levels in moments that exhibit subtractive cancellation (i.e., F^i in optically-deep regions, $P^{r\theta}$ in 2D calculations). The present 2D calculation simulated 63 billion packets and still shows some noise in these quantities.

The approximate two moment radiation transport scheme is significantly more efficient than either DO or MC transport by evolving only the energy density and flux. However, this method requires an ad-hoc closure relation to complete the system of equations by making estimates of higher-order moments. We evaluate the performance of the Levermore, Janka, and Minerbo closures in predicting the second angular moments from the zeroth and first. In the 1D calculations, the Levermore closure performs best, with an error comparable to the differences between the highest-resolution DO results and the MC results. In 2D calculations, this closure performs comparably well when predicting diagonal components of the second moment, but this accuracy is not sufficient for determining the very small off-diagonal components. Though careful tests in time-dependent simulations would be required to assess the importance of these small off-diagonal components, they reflect the multi-dimensional nature of CCSN dynamics.

Finally, we find that the difference in local heating and cooling rates between the DO and MC methods is at most 2% of the amplitude of the net gain curve in the cooling region of the CCSN in both 1D and 2D calculations. The volume-integrated gain in the gain region (where there is net heating under the shock), however, differs by only 0.3% in the highest resolution 1D calculations and by 0.4% in the highest resolution 2D calculations. In these cases, the DO and MC schemes share the same energy resolution, but the MC scheme has effectively infinite angular resolution. The differences in the same quantities due to changing the DO energy (and angular) resolution are larger than 1% in both 1D and 2D calculations, indicating that neutrino energy resolution is the dominant source of real error. Since both the MC and DO methods rely on opacities and emissivities discretized into energy bins, both

suffer from this error. The errors in radiation quantities (energy density, angular moments, and average neutrino energies) below the shock is dominated by the finite momentum-space resolution of the DO calculations and statistical noise and limited energy resolution of the MC calculations.

Though it is important to simulate all physics relevant to the CCSN mechanism, the limited numerical resolution can pose a significantly larger threat to simulation accuracy than a lack of physical elements. We test the effects of ignoring special relativistic Lorentz transformation of neutrinos and find it to be severely sub-dominant to errors induced by low momentum-space resolution at the resolutions we use. The diagonal components of the Eddington tensor in the low-resolution DO calculations show resolution-induced errors of $\sim 15\%$, and even the highest-resolution 1D calculations (which would be impossible in 2D) show errors of $\sim 3\%$. This underscores the need for resolution tests in interpreting results of simulation results.

Though this study inspires much more confidence in both methods, we must mention several caveats. The largest is that opacities and emissivities are an extremely important component of radiation transport. In order to facilitate a detailed comparison of the methods themselves, we carefully configure both codes to use identical opacities at each spatial location and neutrino energy bin. However, we do not compare the effects of different approximations and physical processes present in the opacities that may overwhelm the small differences in the results between these codes.

Second, we must emphasize that our calculations are performed under the assumption of an unchanging fluid background and flat metric at one particular stage in the CCSN evolution. At different stages, especially during early postbounce prompt convection and the shock revival phase, the matter distribution and hence neutrino radiation fields are significantly different and would benefit from a similar analysis. We also use an approximate treatment of pair processes and neglect electron scattering. These simplifications are made to bring both codes to the same level, where we could be sure that they are simulating the same physics with the same level of approximation. This allows an isolated evaluation of the relative performance of both transport methods, but neglects many components of physics that should be included in realistic dynamical CCSN simulations.

The impact of the time-dependent features of the radiation field on the fluid dynamics will be the next necessary step in verifying neutrino radiation hydrodynamics codes. A similar careful verification of the choice and implementation of different neutrino interactions, the resolution and discretization scheme (including mesh

geometry and refinement), the treatment of gravity, and the numerical hydrodynamics scheme would also greatly benefit the interpretation of simulation results. We leave this broader task of evaluating multi-dimensional time-dependent radiation hydrodynamics simulations of CCSNe to future work.

We release the data input to and output by both codes at `http://www.stellarcollapse.org/MCvsDO`. The Sedonu code is also open source and available at `https://bitbucket.org/srichers/sedonu.git`, along with a set of ready-to-run input data and parameter files to run the calculations in this chapter. This Sedonu release contains many performance, usability, and flexibility changes implemented since previous releases. In addition, we incorporate a special relativistic, time-independent version of the MC random walk approximation that enables Sedonu to efficiently calculate neutrino transport through regions of arbitrarily large optical depth.

Chapter 6

MAGNETOROTATIONAL CORE COLLAPSE

We present results of new three-dimensional (3D) general-relativistic magnetohydrodynamic simulations of rapidly rotating strongly magnetized core collapse. These simulations are the first of their kind and include a microphysical finite-temperature equation of state and a leakage scheme that captures the overall energetics and lepton number exchange due to postbounce neutrino emission. Our results show that the 3D dynamics of magnetorotational core-collapse supernovae are fundamentally different from what was anticipated on the basis of previous simulations in axisymmetry (2D). A strong bipolar jet that develops in a simulation constrained to 2D is crippled by a spiral instability and fizzles in full 3D. While multiple (magneto-)hydrodynamic instabilities may be present, our analysis suggests that the jet is disrupted by an $m = 1$ kink instability of the ultra-strong toroidal field near the rotation axis. Instead of an axially symmetric jet, a completely new, previously unreported flow structure develops. Highly magnetized spiral plasma funnels expelled from the core push out the shock in polar regions, creating wide secularly expanding lobes. We observe no runaway explosion by the end of the full 3D simulation at 185 ms after bounce. At this time, the lobes have reached maximum radii of ~900 km.

This work was originally published as **Philipp M osta, Sherwood Richers, Christian D. Ott, Roland Haas, Anthony Piro, Kristen Boydstun, Ernazar Abdikamalov, Christian Reisswig and Erik Schnetter (2014). "Magnetorotational Core Collapse Supernovae in Three Dimensions".** ***The Astrophysical Journal Letters*** **785, 2].**

I heavily contributed to data analysis and interpretation of simulations performed by Philipp M osta. I performed much of the visualization (Figure 6.3 and right half of Figure 6.4, along with animations available online). I demonstrated that the magnetic outflows are crippled by $m = 1$ (kink) instabilities that are well-known in the fusion reactor and AGN jet literature.

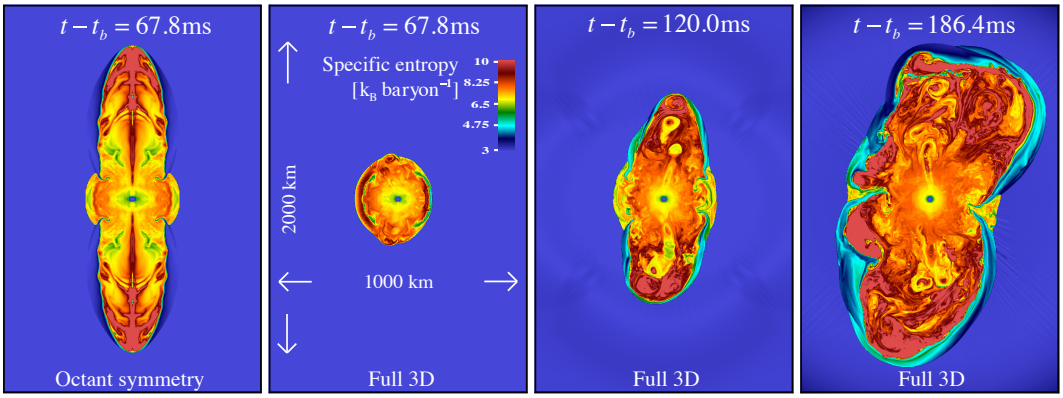

Figure 6.1: Meridional slices ($x - z$ plane; z being the vertical) of the specific entropy at various postbounce times. The "2D" (octant 3D) simulation (leftmost panel) shows a clear bipolar jet, while in the full 3D simulation (3 panels to the right) the initial jet fails and the subsequent evolution results in large-scale asymmetric lobes.

6.1 Introduction

Stellar collapse liberates gravitational energy of order 10^{53} erg s^{-1} (100 B). Most (99%) of that energy is emitted in neutrinos, and the remainder ($\lesssim$ 1 B) powers a core-collapse supernova (CCSN) explosion. However, a small fraction of CCSNe are hyper-energetic ($\sim$ 10 B) and involve relativistic outflows (e.g., Soderberg et al. 2006; Drout et al. 2011). These *hypernovae* come from stripped-envelope progenitors and are classified as Type Ic-bl (H/He deficient, broad spectral lines). Importantly, all SNe connected with long gamma-ray bursts (GRB) are of Type Ic-bl (Modjaz, 2011; Hjorth and Bloom, 2012).

Typical $O(1)$B SNe may be driven by the *n*eutrino mechanism (Bethe, 1990), in which neutrinos emitted from the collapsed core deposit energy behind the stalled shock, eventually driving it outward (e.g., B. Müller, H.-T. Janka, and Marek 2012; Bruenn, Mezzacappa, et al. 2013). However, the neutrino mechanism appears to lack the efficiency needed to drive hyperenergetic explosions. One possible alternative is the *magnetorotational* mechanism (e.g. Bisnovatyi-Kogan 1970; LeBlanc and Wilson 1970; Meier et al. 1976; J. C. Wheeler, Meier, and Wilson 2002). In its canonical form, rapid rotation of the collapsed core (Period $O(1)$ ms, spin energy $O(10)$ B) and magnetar-strength magnetic field with a dominant toroidal component drive a strong bipolar jet-like explosion that could result in a hypernova (Burrows, Dessart, et al. 2007).

The magnetorotational mechanism requires rapid precollapse rotation ($P_0 \lesssim 4$ s;

Ott, Burrows, Thompson, et al. 2006; Burrows, Dessart, et al. 2007) and an efficient process to rapidly amplify the likely weak seed magnetic field of the progenitor. The *magnetorotational instability* (MRI, Balbus and Hawley 1991; Akiyama et al. 2003; Obergaulinger, Cerdá-Durán, et al. 2009) is one possibility. The MRI operates on the free energy of differential rotation and, in combination with dynamo action, has been hypothesized to provide the necessary global field strength on an essentially dynamical timescale (Akiyama et al., 2003; Thompson, Quataert, and Burrows, 2005). The wavelength of the fastest growing MRI mode in a postbounce CCSN core is much smaller than what can currently be resolved in global multi-dimensional CCSN simulations. Under the assumption that MRI and dynamo operate as envisioned, a common approach is to start with a likely unphysically strong precollapse field of $10^{12} - 10^{13}$ G. During collapse and the early postbounce evolution, this field is amplified by flux compression and rotational winding to dynamically important field strength of $B_{\rm tor} \gtrsim 10^{15} - 10^{16}$ G (Burrows, Dessart, et al., 2007). In this way, a number of recent two-dimensional (2D) magnetohydrodynamic (MHD) simulations have found robust and strong jet-driven explosions (e.g., M. Shibata, Liu, et al. 2006; Burrows, Dessart, et al. 2007; Takiwaki and Kotake 2011), while (Sawai and Yamada, 2014) have studied a weakly magnetized progenitor. Only a handful of 3D studies have been carried out with varying degrees of microphysical realism (Mikami et al. 2008; Kuroda and Umeda 2010; Scheidegger, Käppeli, et al. 2010; Winteler et al. 2012) and none have compared 2D and 3D dynamics directly.

These forces are also assembled into a very nonlinear system that is not conducive to traditional analytical techniques. High-performance computation has arisen as the dominant tool for modeling CCSNe and NSMs. The differential equations governing the behavior of the matter are discretized and evolved by a computer. However, the computer resources and computational methods are still too primitive to allow all of these components to be included in the models at sufficient fidelity. Though important conclusions have been drawn from these early simulations, it is necessary to advance these methods with the target of ever more reliable models.

In this chapter, we present new full 3D dynamical-spacetime general-relativistic MHD (GRMHD) simulations of rapidly rotating magnetized CCSNe. These are the first to employ a microphysical finite-temperature equation of state, a realistic progenitor model, and an approximate neutrino treatment for collapse and postbounce evolution. We carry out simulations in full unconstrained 3D and compare with simulations starting from identical initial conditions, but constrained to 2D. Our

results for a model with initial poloidal B-field of 10^{12} G indicate that 2D and 3D magnetorotational CCSNe are fundamentally different. In 2D, a strong jet-driven explosion obtains, while in unconstrained 3D, the developing jet is destroyed by nonaxisymmetric dynamics, caused most likely by an $m = 1$ MHD kink instability. The subsequent CCSN evolution leads to two large asymmetric shocked lobes at high latitudes. Highly-magnetized tubes tangle, twist, and drive the global shock front steadily, but not dynamically outward. A runaway explosion does not occur during the ∼185 ms of postbounce time covered.

6.2 Methods and Setup

We employ ideal GRMHD with adaptive mesh refinement (AMR) and spacetime evolution provided by the open-source EinsteinToolkit (Mösta, Mundim, et al., 2014; Löffler et al., 2012). GRMHD is implemented in a finite-volume fashion with WENO5 reconstruction (Reisswig, Haas, et al., 2013; Tchekhovskoy, McKinney, and Narayan, 2007) and the HLLE Riemann solver (Einfeldt, 1988a) and constrained transport (Tóth, 2000) for maintaining $\mathrm{div}\vec{B} = 0$. We employ the $K_0 = 220$ MeV variant of the equation of state of J. M. Lattimer and Swesty, 1991 and the neutrino leakage/heating approximations described in E. O'Connor and Ott, 2010 and Ott, E. Abdikamalov, et al., 2012. At the precollapse stage, we cover the inner ∼5700 km of the star with four AMR levels and add five more during collapse. After bounce, the protoneutron star is covered with a resolution of ∼370 m and AMR is set up to always cover the shocked region with at least 1.48 km linear resolution.

We draw the 25-$M_\odot$ (at zero-age-main-sequence) presupernova model E25 from Heger, Langer, and Woosley, 2000 and set up axisymmetric precollapse rotation using the rotation law of Takiwaki and Kotake, 2011 (see their Eq. 1) with an initial central angular velocity of $2.8\,\mathrm{rad\,s^{-1}}$. The fall-off in cylindrical radius and vertical position is controlled by parameters $x_0 = 500$ km and $z_0 = 2000$ km, respectively. We set up the initial magnetic field by a vector potential of the form $A_r = A_\theta = 0; A_\phi = B_0(r_0^3)(r^3 + r_0^3)^{-1}\, r \sin\theta$, where B_0 controls the strength of the field.

In this way we obtain a modified dipolar field structure that stays nearly uniform in strength within radius r_0 and falls off like a dipole outside. We set $B_0 = 10^{12}$ G and choose $r_0 = 1000$ km to match the initial conditions of model B12X5β0.1 of the 2D study of Takiwaki and Kotake, 2011, in which a jet-driven explosion is launched ∼20 ms after bounce.

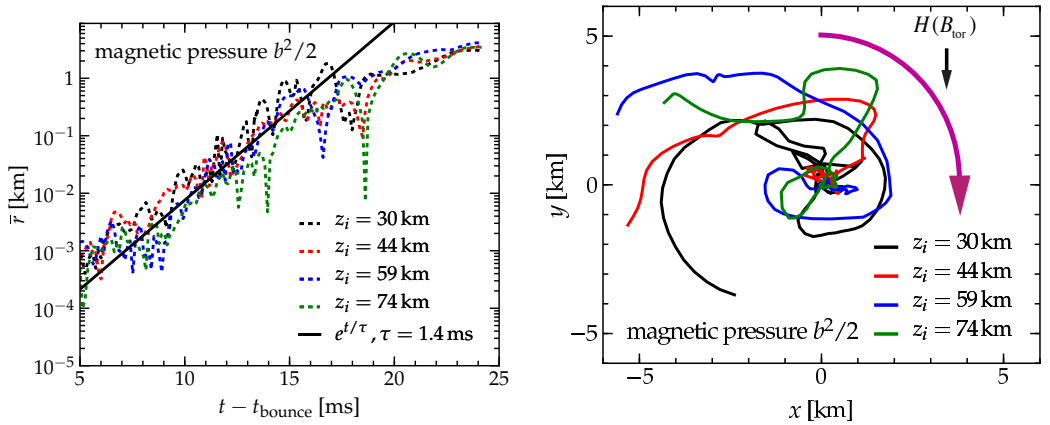

Figure 6.2: **Top panel**: Barycenter displacement $\bar{r}$ of b^2 in $x-y$ planes at different heights z_i. To minimize the influence of material that does not belong to the unstable jet, we include only cells inside a radius of 15 km. We observe exponential growth of the displacement in the early postbounce evolution until saturation at $t - t_b \sim 20$ ms. The growth rate $\tau_{fgm,sim} \approx 1.4$ ms is consistent with estimates for the MHD kink instability. **Bottom panel**: Tracks of the barycenter in the $x-y$ plane at different z_i. They are plotted for the interval shown in the top panel. The tracks trace the spiral nature of the displacement. Note that, as required for the perturbation to be unstable (Begelman, 1998), the helicity of the displacement motion (counter-clockwise in the $x-y$ plane) is opposite to the helicity of the toroidal magnetic field $H(B_{\rm tor})$ (clockwise in the $x-y$ plane, magenta arrow).

We perform simulations both in full, unconstrained 3D and in octant symmetry 3D (90-degree rotational symmetry in the $x-y$ plane and reflection symmetry across the $x-y$ plane) with otherwise identical setups. Octant symmetry suppresses most nonaxisymmetric dynamics, since it allows only modes with azimuthal numbers that are multiples of $m = 4$. In order to study the impact of potential low-mode nonaxisymmetric dynamics on jet formation, we add a 1% $m = 1$ perturbation (random perturbations lead to qualitatively the same results) to the full 3D run. Focusing on a potential instability of the strong toroidal field near the spin axis, we apply this perturbation to the velocity field within a cylindrical radius of 15 km and outside the protoneutron star, 30 km $\leq |z| \leq$ 75 km, at 5 ms after bounce.

6.3 Results

Collapse and the very early postbounce evolution proceed identically in octant symmetry and full 3D. At bounce, ~350 ms after the onset of collapse, the poloidal and toroidal B-field components reach $B_{\rm pol}$, $B_{\rm tor} \sim 10^{15}$ G. The hydrodynamic shock launched at bounce, still approximately spherical, stalls after ~10 ms at a radius of

$\sim$110 km. Rotational winding, operating on the extreme differential rotation in the region between inner core and shock, amplifies the toroidal component to 10^{16} G near the rotation axis within $\sim$20 ms of bounce. At this time, the strong polar magnetic pressure gradient, in combination with hoop stresses excerted by the toroidal field, launches a bipolar outflow. As depicted by the leftmost panel of Fig. 6.1, a jet develops and reaches $\sim$800 km after $\sim$70 ms in the octant-symmetry run. The expansion speed at that point is mildly relativistic ($v_r \simeq 0.1 - 0.15\,c$). This is consistent with the 2D findings of Takiwaki and Kotake, 2011.

The full 3D run begins to diverge from its more symmetric counterpart around $\sim$15 ms after bounce. A nonaxisymmetric spiral ($m = 1$) deformation develops near the rotation axis. It distorts and bends the initially nearly axisymmetrically developing jet, keeping it from breaking out of the stalled shock. The nearly prompt magnetorotational explosion of the octant-symmetry run *fails* in full 3D. The subsequent 3D evolution is fundamentally different from 2D, as evidenced by the three panels of Fig. 6.1 depicting meridional specific entropy slices at different times in the full 3D run. Until 80 ms, the shock remains stalled and nearly spherical. The $m = 1$ dynamics pervade the entire postshock region and cause a spiral-sloshing of the shock front that is reminiscent of the standing-accretion shock instability in rotating 3D CCSNe (cf. Kuroda, Takiwaki, and Kotake 2014). Later, highly-magnetized ($\beta = P_{\rm gas}/P_{\rm mag} \ll 1$) funnels of high-entropy material protrude from polar regions of the core and secularly push out the shock into two dramatic tilted lobes. At the end of our simulation ($\sim$185 ms after bounce) the lobes fill polar cones of $\sim$90° and are only gradually expanding as low-β material is pushed out from below. Accreting material is deflected by these lobes and pushed towards the equator where it accretes through the remainder of the initial nearly spherical shock.

Nonaxisymmetric Instability and Jet Formation

The results discussed in the above suggest that the full 3D run is subject to a spiral instability that grows from $\sim$1% $m = 1$ seeds in the velocity field to non-linear scale within the first $\sim$20 ms after bounce. This instability quenches the jet. Figure 6.2 depicts the linear growth and non-linear saturation of the spiral instability at various locations along the spin axis outside the protoneutron star.

In the rotating CCSN context, rotational shear instabilities in the protoneutron star (e.g., Ott, Dimmelmeier, Marek, H.-T. Janka, Hawke, et al. 2007) and a spiral standing accretion shock instability (SASI; e.g., Kuroda, Takiwaki, and Kotake

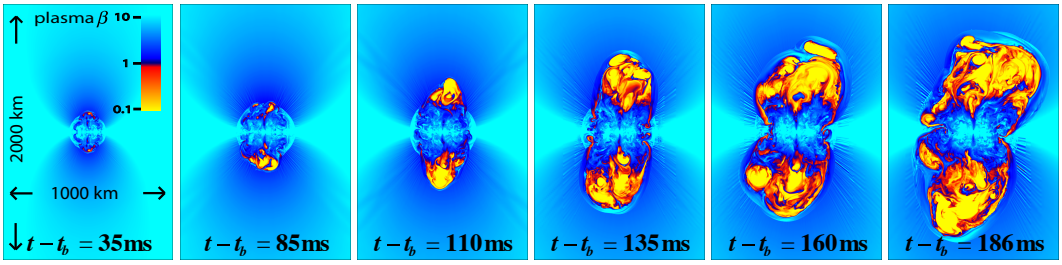

Figure 6.3: Meridional slices ($x - z$ plane; z being the vertical) of the plasma $\beta = P_{\rm gas}/P_{\rm mag}$ at different postbounce times. The colormap is saturated at a minimum $\beta = 0.01$ and a maximum $\beta = 10$. Regions of $\beta < 1$ (warm colors, magnetically dominated) are underdense due to expansion from magnetic pressure, rise buoyantly, and push out the shock front in two prominent polar lobes.

2014) have been discussed to potentially arise already at early postbounce times. It is unlikely that either of these is excited in our simulations, since we choose to perturb a radially and vertically narrow region along the spin axis outside of the protoneutron star and far from the shock, within the region of the highest toroidal magnetic field strength. A spiral MHD instability may thus be the driving agent behind the strong asymmetry in our simulation.

One possible such instability is the screw-pinch kink instability that has been studied in jets from active galactic nuclei (e.g., Begelman 1998; Mignone et al. 2010; McKinney and Blandford 2009). The B-field near the spin axis in our simulation can be roughly approximated by a screw-pinch field configuration. This consists of a non-rotating plasma cylinder and a magnetic field of the form

$$\vec{B} = B_{\rm tor}(r)\hat{\phi} + B_z\hat{z}\,, \tag{6.1}$$

where $\hat{z}$ is along the rotation axis, $\hat{\phi}$ is in the toroidal direction, B_z is a constant vertical component of the B-field, and $B_{\rm tor}(r)$ is the radially-varying toroidal component of the B-field. We can express perturbations to the jet in the form of fluid displacements as a sum of basis elements of the form $\vec{\xi}_{km} \propto e^{i(kz+m\phi-\omega t)}$, where m is an integer, k is the vertical wave number, and ω is the oscillation frequency of the mode. The Kruskal-Shafranov stability criterion states that a plasma cylinder confined to a finite radius a (as in a tokamak) is unstable to kink ($m = \pm 1$) modes if $B_{\rm tor}/B_z > 2\pi a/L$, where L is the length of the cylinder and the sign of m is such that the mode's helicity is opposite to the field helix (Shafranov 1956; Kruskal and Tuck 1958). Unconfined screw-pinch structures with $B_{\rm tor} \gg B_z$ have been shown to be violently unstable to $m = 1$ modes at short vertical wavelengths

($kr \gg 1$) when $d \ln B_{\rm tor}/d \ln r > -1/2$ and the plasma parameter is sufficiently large ($\beta > 2/3\gamma$ where γ is the local adiabatic index). Under these conditions (which are only approximately met in our simulation), the fastest growing unstable mode (fgm) is amplified on a timescale comparable to the Alfvén travel time around a toroidal loop (Begelman, 1998). The expected $m = 1$ growth timescale and vertical wavelength in the most unstable regions of the jet at $\sim 10 - 15$ ms after bounce are

$$\tau_{\rm fgm} \approx \frac{4a\sqrt{\pi\rho}}{B_{\rm tor}} \approx 1\,{\rm ms}, \qquad \lambda_{\rm fgm} \approx \frac{4\pi a B_z}{B_{\rm tor}} \approx 5\,{\rm km},$$

where a is the radius of the most unstable region. The growth time is much shorter than the time it would take for the jet to propagate through the shocked region.

The effect of the kink instability can be most clearly seen in a displacement of the jet barycenter away from the rotation axis of the core. We measure the displacement of the jet in our full 3D run by computing the barycenter displacement (planar "center-of-mass" displacement; Mignone et al. 2010) of the co-moving magnetic field strength b^2 (see, e.g., Mösta, Mundim, et al. 2014) in xy-slices at different heights z_i along the rotation axis (Fig. 6.2). b^2 probes the MHD effects in our simulations most directly, but other variable choices, e.g. the specific entropy s, exhibit similar behavior as flux freezing couples fluid properties to the magnetic field evolution. Figure 6.2 demonstrates that the jet experiences significant displacements from the rotation axis of the core in a spiraling motion with helicity opposite to that of the magnetic field (indicated by the magenta colored arrow in Fig. 6.2), and that the growth rate and dominant instability length scale roughly agree with those predicted by a kink unstable jet in our analysis.

Magnetized Expanding Lobes

Although the initial bipolar jet fails to promptly break out of the stalled shock, MHD becomes dominant tens of milliseconds later. Starting around ~80 ms after bounce, outflows of highly-magnetized material are continuously launched from the protoneutron star and propagate along the rotation axis of the core. This is depicted in Fig. 6.3, which presents meridional slices of the plasma parameter β at a range of postbounce times. The highly-magnetized (low-β) material does not stay neatly confined to the rotation axis.

In Fig. 6.4, we present volume renderings of specific entropy and plasma parameter β at 161 ms after bounce. Only these volume renderings speak the full truth about how severely outflows driven by the core are deformed, sheared, and wound

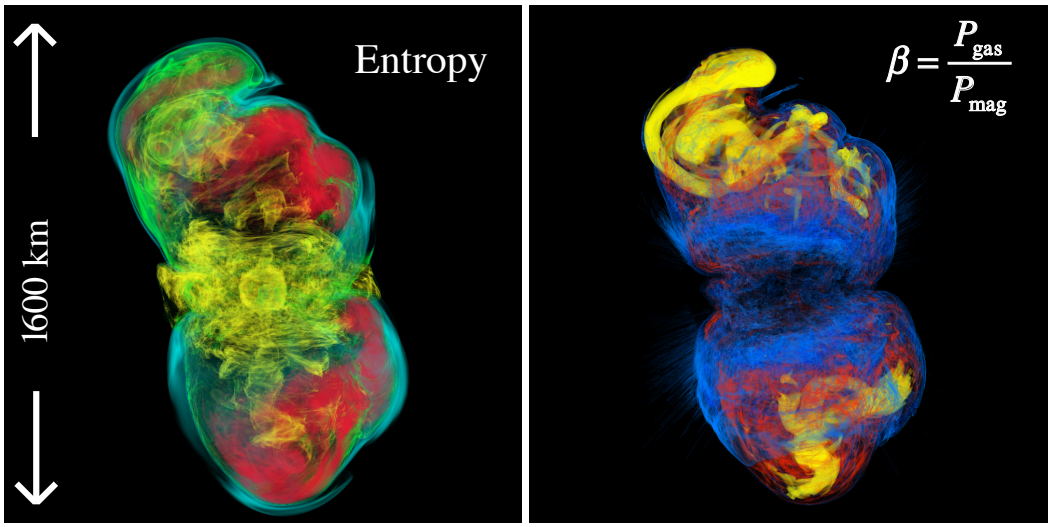

Figure 6.4: Volume renderings of entropy and β at $t - t_b = 161$ ms. The z-axis is the spin axis of the protoneutron star and we show 1600 km on a side. The colormap for entropy is chosen such that blue corresponds to $s = 3.7 k_b$ baryon^{-1}, cyan to $s = 4.8 k_b$ baryon^{-1} indicating the shock surface, green to $s = 5.8 k_b$ baryon^{-1}, yellow to $s = 7.4 k_b$ baryon^{-1}, and red to higher entropy material at $s = 10 k_b$ baryon^{-1}. For β we choose yellow to correspond to $\beta = 0.1$, red to $\beta = 0.6$, and blue to $\beta = 3.5$. Magnetically dominated material at $\beta < 1$ (yellow) is expelled from the protoneutron star and twisted in highly asymmetric tubes that drive the secular expansion of the polar lobes.

up as they propagate in the z-direction. The material that is expelled from the vicinity of the protoneutron star forms tube-like structures that are highly magnetized ($\beta \sim 0.01 - 0.1$), underdense (~1% the density of the surrounding fluid), and rise buoyantly. The overall structure of the shocked region evolves toward strongly prolate-shape with two, roughly 90°-filling tilted lobes at both poles (cf. Figs. 6.1, 6.3, 6.4).

The lobes secularly expand to ~900 km during the simulated time, but their expansion never becomes dynamical. Accreting material is funneled to equatorial regions where it continues to settle onto the protoneutron star. The B-field geometry in the later evolution corresponds to that of a tightly wound coil close to the protoneutron star, but the field lines open up in a spiraling fashion further out, yet still behind the shock. This is consistent with magnetized material moving away from the rotation axis as it propagates in the general z-direction. In 2D simulations, a confining magnetic-tower structure forms instead (Burrows, Dessart, et al., 2007).

6.4 Discussion

Our results show that 3D magnetorotational core-collapse supernovae are fundamentally different from what has been anticipated on the basis of axisymmetric simulations (Burrows, Dessart, et al., 2007; Dessart et al., 2008; Takiwaki and Kotake, 2011). A jet that develops in 2D is disrupted and fizzles in 3D. We suggest that the instability driving this is most likely an MHD kink ($m = 1$) instability to which the toroidally-dominated postbounce magnetic-field configuration is prone. Instead of an axially symmetric jet, a completely new, wide double-lobed flow pattern develops, but we obtain no runaway explosion during the simulated time.

The high precollapse field strength of 10^{12} G yields $\sim 10^{16}$ G in toroidal field and $\beta = P_{\rm gas}/P_{\rm mag} < 1$ within only $\sim 10-15$ ms of bounce, creating conditions favorable for jet formation. Yet, the growth time of the kink instability is shorter than the time it takes for the jet to develop. In a short test simulation with an even more unrealistic, ten times stronger initial field a successful jet is launched promptly after bounce (consistent with Winteler et al. 2012, who used a similarily strong field), but subsequently also experiences a spiral displacement.

Realistic precollapse iron cores are not expected to have magnetic fields in excess of $\sim 10^8 - 10^9$ G, which may be amplified to no more than $\sim 10^{12}$ G during collapse (Burrows, Dessart, et al., 2007). The $10^{15} - 10^{16}$ G of large-scale toroidal field required to drive a magnetorotational jet must be built up after bounce. This will likely require tens to hundreds of dynamical times, even if the magnetorotational instability operates in conjunction with a dynamo. The results of the present and previous full 3D rotating CCSN simulations (Ott, Dimmelmeier, Marek, H.-T. Janka, Hawke, et al., 2007; Kuroda, Takiwaki, and Kotake, 2014) suggest that MHD and also a variety of nonaxisymmetric hydrodynamic instabilities will grow to non-linear regimes on *shorter timescales*, disrupting any possibly developing axial outflow. *This is why we believe that the dynamics and flow structures seen in our full 3D simulation may be generic to the postbounce evolution of rapidly rotating magnetized core collapse that starts from realistic initial conditions.*

If the polar lobes eventually accelerate, the resulting explosion will be asymmetric, though probably less so than a jet-driven explosion. The lobes carry neutron rich ($Y_e \sim 0.1 - 0.2$) material of moderate entropy ($s \sim 10 - 15\, k_B$ baryon^{-1}), which could lead to interesting r-process yields, similar to what Winteler et al., 2012 found for their prompt jet-driven explosion. Even if the lobes continue to move outward, accretion in equatorial regions may continue, eventually (after $2 - 3$ s) leading to

the collapse of the protoneutron star and black hole formation. In this case, the engine supplying the lobes with low-β plasma is shut off. Unless their material has reached positive total energy, the lobes will fall back onto the black hole, which will subsequently hyperaccrete until material becomes centrifugally supported in an accretion disk. This would set the stage for a subsequent long GRB and an associated Type Ic-bl CCSN that would be driven by a collapsar central engine (Woosley, 1993) rather than by a protomagnetar (Metzger, Giannios, et al., 2011).

The results of the present study highlight the importance of studying magnetorotational CCSNe in 3D. Future work will be necessary to explore later postbounce dynamics, the sensitivity to initial conditions and numerical resolution, and possible nucleosynthetic yields. Animations and further details on our simulations are available at `http://stellarcollapse.org/cc3dgrmhd`.

Chapter 7

GRAVITATIONAL WAVES FROM ROTATING CORE COLLAPSE

Gravitational waves (GWs) generated by axisymmetric rotating collapse, bounce, and early postbounce phases of a galactic core-collapse supernova will be detectable by current-generation gravitational wave observatories. Since these GWs are emitted from the quadrupole-deformed nuclear-density core, they may encode information on the uncertain nuclear equation of state (EOS). I examine the effects of the nuclear EOS on GWs from rotating core collapse and carry out 1824 axisymmetric general-relativistic hydrodynamic simulations that cover a parameter space of 98 different rotation profiles and 18 different EOS. I show that the bounce GW signal is largely independent of the EOS and sensitive primarily to the ratio of rotational to gravitational energy, $T/|W|$, and at high rotation rates, to the degree of differential rotation. The GW frequency ($f_{\rm peak} \sim 600 - 1000\,{\rm Hz}$) of postbounce core oscillations shows stronger EOS dependence that can be parameterized by the core's EOS-dependent dynamical frequency $\sqrt{G\bar{\rho}_c}$. I find that the ratio of the peak frequency to the dynamical frequency $f_{\rm peak}/\sqrt{G\bar{\rho}_c}$ follows a universal trend that is obeyed by all EOS and rotation profiles and that indicates that the nature of the core oscillations changes when the rotation rate exceeds the dynamical frequency. I find that differences in the treatments of low-density nonuniform nuclear matter, of the transition from nonuniform to uniform nuclear matter, and in the description of nuclear matter up to around twice saturation density can mildly affect the GW signal. More exotic, higher-density physics is not probed by GWs from rotating core collapse. I furthermore test the sensitivity of the GW signal to variations in the treatment of nuclear electron capture during collapse. I find that approximations and uncertainties in electron capture rates can lead to variations in the GW signal that are of comparable magnitude to those due to different nuclear EOS. This emphasizes the need for reliable experimental and/or theoretical nuclear electron capture rates and for self-consistent multi-dimensional neutrino radiation-hydrodynamic simulations of rotating core collapse.

This work was originally published as **[Sherwood Richers, Christian D. Ott, Ernazar Abdikamalov, Evan O'Connor, and Chris Sullivan (2017). "Equation of State Effects on Gravitational Waves from Rotating Core Collapse".** ***Physical Review D*** **95, 063019].** The discussion of different EOS has been relegaded to Chapter 2.

I ran the simulations using a version of the CoCoNuT code from Nazarbayev University Professor Ernazar Abdikamalov, the GR1D code from North Carolina State University postdoc Evan O'Connor, and detailed electron capture rates from Michigan State University graduate student Chris Sullivan. I performed the data analysis and wrote the text.

7.1 Introduction

Massive stars ($M_{\rm ZAMS} \gtrsim 10\,M_\odot$) burn their thermonuclear fuel all the way up to iron-group nuclei at the top of the nuclear binding energy curve. The resulting iron core is inert and supported primarily by the pressure of relativistic degenerate electrons. Once the core exceeds its effective Chandrasekhar mass (e.g., Bethe, 1990), collapse commences.

As the core is collapsing, the density quickly rises, electron degeneracy increases, and electrons are captured onto protons and nuclei, causing the electron fraction to decrease. Within a few tenths of a second after the onset of collapse, the density of the homologous inner core surpasses nuclear densities. The collapse is abruptly stopped as the nuclear equation of state (EOS) is rapidly stiffened by the strong nuclear force, causing the inner core to bounce back and send a shock wave through the supersonically infalling outer core.

The prompt shock is not strong enough to blow through the entire star; it rapidly loses energy dissociating accreting iron-group nuclei and to neutrino cooling. The shock stalls. Determining what revives the shock and sends it through the rest of the star has been the bane of core-collapse supernova (CCSN) theory for half a century. In the *neutrino mechanism* Bethe and Wilson, 1985, a small fraction ($\lesssim 5-10\%$) of the outgoing neutrino luminosity from the protoneutron star (PNS) is deposited behind the stalled shock. This drives turbulence and increases thermal pressure. The combined effects of these may revive the shock Couch and Ott, 2015 and the neutrino mechanism can potentially explain the vast majority of CCSNe (e.g., Bruenn, Lentz, et al., 2016). In the *magnetorotational mechanism* LeBlanc and Wilson, 1970; Bisnovatyi-Kogan, 1970; Burrows, Dessart, et al., 2007; Takiwaki, Kotake, and Sato, 2009; Moiseenko, Bisnovatyi-Kogan, and Ardeljan, 2006; Mösta, Richers, et al., 2014, rapid rotation and strong magnetic fields conspire to generate bipolar jet-like outflows that explode the star and could drive very energetic CCSN explosions. Such magnetorotational explosions could be essential to explaining a class of massive star explosions that are about ten times more energetic than regular CCSNe and that have been associated with long gamma-ray bursts (GRBs) Smith, W. Li, Filippenko, et al., 2011; Hjorth and Bloom, 2012; Modjaz, 2011. These *hypernovae* make up $\gtrsim$1% of all CCSNe Smith, W. Li, Filippenko, et al., 2011.

The magnetorotational mechanism requires rapid precollapse rotation ($P_0 \lesssim 4\,$s; Ott, Burrows, Thompson, et al. 2006; Burrows, Dessart, et al. 2007) and an efficient process to rapidly amplify the likely weak seed magnetic field of the progenitor. The

magnetorotational instability (MRI, Balbus and Hawley 1991; Akiyama et al. 2003; Obergaulinger, Cerdá-Durán, et al. 2009) is one possibility. The MRI operates on the free energy of differential rotation and, in combination with dynamo action, has been hypothesized to provide the necessary global field strength on an essentially dynamical timescale (Akiyama et al., 2003; Thompson, Quataert, and Burrows, 2005). The wavelength of the fastest growing MRI mode in a postbounce CCSN core is much smaller than what can currently be resolved in global multi-dimensional CCSN simulations. Under the assumption that MRI and dynamo operate as envisioned, a common approach is to start with a likely unphysically strong precollapse field of $10^{12} - 10^{13}$ G. During collapse and the early postbounce evolution, this field is amplified by flux compression and rotational winding to dynamically important field strength of $B_{\rm tor} \gtrsim 10^{15} - 10^{16}$ G (Burrows, Dessart, et al., 2007). In this way, a number of recent two-dimensional (2D) magnetohydrodynamic (MHD) simulations have found robust and strong jet-driven explosions (e.g., M. Shibata, Liu, et al. 2006; Burrows, Dessart, et al. 2007; Takiwaki and Kotake 2011), while (Sawai and Yamada, 2014) have studied a weakly magnetized progenitor. Only a handful of 3D studies have been carried out with varying degrees of microphysical realism (Mikami et al. 2008; Kuroda and Umeda 2010; Scheidegger, Käppeli, et al. 2010; Winteler et al. 2012) and none have compared 2D and 3D dynamics directly.

A key issue for the magnetorotational mechanism is its need for rapid core spin that results in a PNS with a spin-period of around a millisecond. Little is known observationally about core rotation in evolved massive stars, even with recent advances in asteroseismology Dupret et al., 2009. On theoretical grounds and on the basis of pulsar birth spin estimates (e.g., Heger, Woosley, and Spruit, 2005; Ott, Burrows, Thompson, et al., 2006; J. Fuller, Cantiello, et al., 2015), most massive stars are believed to have slowly spinning cores. Yet, certain astrophysical conditions and processes, e.g., chemically homogeneous evolution at low metallicity or binary interactions, might still provide the necessary core rotation in a fraction of massive stars sufficient to explain extreme hypernovae and long GRBs Woosley and Heger, 2006; Yoon, Langer, and C. Norman, 2006; de Mink et al., 2013; C. L. Fryer and Heger, 2005.

Irrespective of the detailed CCSN explosion mechanism, it is the repulsive nature of the nuclear force at short distances that causes core bounce in the first place and that ensures that neutron stars can be left behind in CCSNe. The nuclear force underlying the nuclear EOS is an effective quantum many body interaction

and a piece of poorly understood fundamental physics. While essential for much of astrophysics involving compact objects, we have only incomplete knowledge of the nuclear EOS. Uncertainties are particularly large at densities above a few times nuclear and in the transition regime between uniform and nonuniform nuclear matter at around nuclear saturation density J. M. Lattimer, 2012; Oertel et al., 2017.

The nuclear EOS can be constrained by experiment (see J. M. Lattimer, 2012; Oertel et al., 2017 for recent reviews), through fundamental theoretical considerations (e.g., Hebeler et al., 2010; Hebeler et al., 2013; Kolomeitsev et al., 2016), or via astronomical observations of neutron star masses and radii (e.g., J. M. Lattimer, 2012; Nättilä et al., 2016; Özel and Freire, 2016). Gravitational wave (GW) observations Abbott, 2016b with advanced-generation detectors such as Advanced LIGO LIGO Scientific Collaboration et al., 2015, KAGRA Somiya (for the KAGRA collaboration), 2012, and Advanced Virgo Acernese et al. (Virgo Collaboration), 2009 open up another observational window for constraining the nuclear EOS. In the inspiral phase of neutron star mergers (including double neutron stars and neutron star – black hole binaries), tidal forces distort the neutron star shape. These distortions depend on the nuclear EOS. They measurably affect the late inspiral GW signal (e.g., Bernuzzi, Nagar, et al., 2012; Bernuzzi, Dietrich, and Nagar, 2015; Flanagan and Hinderer, 2008; Read et al., 2009). At merger, tidal disruption of a neutron star by a black hole leads to a sudden cut off of the GW signal, which can be used to constrain EOS properties Vallisneri, 2000; M. Shibata and Taniguchi, 2008; Read et al., 2009. In the double neutron star case, a hypermassive metastable or permanently stable neutron star remnant may be formed. It is triaxial and extremely efficiently emits GWs with characteristics (amplitudes, frequencies, time-frequency evolution) that can be linked to the nuclear EOS (e.g, Radice, Bernuzzi, et al., 2016; Bernuzzi, Radice, et al., 2016; Stergioulas, 2011; Bauswein and H.-T. Janka, 2012; Bauswein, Stergioulas, and H.-T. Janka, 2014).

CCSNe may also provide GW signals that could constrain the nuclear EOS Dimmelmeier, Ott, Marek, et al., 2008; Röver et al., 2009; Marek, H.-T. Janka, and E. Müller, 2009; Kuroda, Kotake, and Takiwaki, 2016. In this chapter, I address the question of how the nuclear EOS affects GWs emitted at core bounce and in the very early post-core-bounce phase ($t - t_{\rm bounce} \lesssim 10\,{\rm ms}$) of rotating core collapse. Stellar core collapse and the subsequent CCSN evolution are extremely rich in multi-dimensional dynamics that emit GWs with a variety of characteristics (see Ott, 2009; Kotake, 2013 for reviews). Rotating core collapse, bounce, and early

postbounce evolution are particularly appealing for studying EOS effects because they are essentially axisymmetric (2D) Ott, Dimmelmeier, Marek, H.-T. Janka, Hawke, et al., 2007; Ott, Dimmelmeier, Marek, H.-T. Janka, Zink, et al., 2007 and result in deterministic GW emission that depends on the nuclear EOS, neutrino radiation-hydrodynamics, and gravity alone. Complicating processes, such as prompt convection and neutrino-driven convection set in only later and are damped by rotation (e.g., Ott, 2009; Dimmelmeier, Ott, Marek, et al., 2008; C. L. Fryer and Heger, 2000). While rapid rotation will amplify magnetic field, amplification to dynamically relevant field strengths is expected only tens of milliseconds after bounce Burrows, Dessart, et al., 2007; Takiwaki and Kotake, 2011; Mösta, Richers, et al., 2014; Mösta, Ott, et al., 2015. Hence, magnetohydrodynamic effects are unlikely to have a significant impact on the early rotating core collapse GW signal Obergaulinger, Aloy, and E. Müller, 2006.

GWs from axisymmetric rotating core collapse, bounce, and the first ten or so milliseconds of the postbounce phase can, in principle, be templated to be used in matched-filtering approaches to GW detection and parameter estimation Dimmelmeier, Ott, Marek, et al., 2008; Ott, E. Abdikamalov, et al., 2012; Engels, Frey, and Ott, 2014; E. Abdikamalov, S. Gossan, et al., 2014. That is, without stochastic (e.g., turbulent) processes, the GW signal is deterministic and predictable for a given progenitor, EOS, and set of electron capture rates. Furthermore, GWs from rotating core collapse are expected to be detectable by Advanced-LIGO class observatories throughout the Milky Way and out to the Magellanic Clouds S. E. Gossan et al., 2016.

Rotating core collapse is the most extensively studied GW emission process in CCSNe. Detailed GW predictions on the basis of (then 2D) numerical simulations go back to Müller (1982) Mueller, 1982. Early work showed a wide variety of types of signals Mueller, 1982; Zwerger and E. Müller, 1997; Mönchmeyer et al., 1991; Yamada and Sato, 1995; Kotake, Yamada, and Sato, 2003; C. D. Ott et al., 2004; Dimmelmeier, Font, and E. Müller, 2002. However, more recent 2D/3D general-relativistic (GR) simulations that included nuclear-physics based EOS and electron capture during collapse demonstrated that all GW signals from rapidly rotating core collapse exhibit a single core bounce followed by PNS oscillations over a wide range of rotation profiles and progenitor stars Ott, Dimmelmeier, Marek, H.-T. Janka, Hawke, et al., 2007; Ott, Dimmelmeier, Marek, H.-T. Janka, Zink, et al., 2007; Dimmelmeier, Ott, Marek, et al., 2008; Dimmelmeier, Ott, H.-T. Janka, et al.,

2007; E. Abdikamalov, S. Gossan, et al., 2014; Ott, E. Abdikamalov, et al., 2012. Ott *et al.* Ott, E. Abdikamalov, et al., 2012 showed that given the same specific angular momentum per enclosed mass, cores of different progenitor stars proceed to give essentially the same rotating core collapse GW signal. Abdikamalov *et al.* E. Abdikamalov, S. Gossan, et al., 2014 went a step further and demonstrated that the GW signal is determined primarily by the mass and ratio of rotational kinetic energy to gravitational energy ($T/|W|$) of the inner core at bounce.

The EOS dependence of the rotating core collapse GW signal has thus far received little attention. Dimmelmeier *et al.* Dimmelmeier, Ott, Marek, et al., 2008 carried out 2D GR hydrodynamic rotating core collapse simulations using two different EOS (LS180 J. M. Lattimer and Swesty, 1991; *Lattimer-Swesty EOS Webpage* n.d. and HShen H. Shen et al., 1998a; H. Shen et al., 1998b; H. Shen et al., 2011; *H. Shen et al. EOS Tables* n.d.), four different progenitors ($11\,M_\odot - 40\,M_\odot$), and 16 different rotation profiles. They found that the rotating core collapse GW signal changes little between the LS180 and the HShen EOS, but that there may be a slight ($\sim$5%) trend of the GW spectrum toward higher frequencies for the softer LS180 EOS. Abdikamalov *et al.* E. Abdikamalov, S. Gossan, et al., 2014 carried out simulations with the LS220 J. M. Lattimer and Swesty, 1991; *Lattimer-Swesty EOS Webpage* n.d. and the HShen H. Shen et al., 1998a; H. Shen et al., 1998b; H. Shen et al., 2011; *H. Shen et al. EOS Tables* n.d. EOS. However, they compared only the effects of differential rotation between EOS and did not carry out an overall analysis of EOS effects.

In this study, I build upon and substantially extend previous work on rotating core collapse. I perform 2D GR hydrodynamic simulations using one 12-$M_\odot$ progenitor star model, 18 different nuclear EOS, and 98 different initial rotational setups. I carry out a total of 1824 simulations and analyze in detail the influence of the nuclear EOS on the rotating core collapse GW signal. The resulting waveform catalog is an order of magnitude larger than previous GW catalogs for rotating core collapse and is publicly available at at https://stellarcollapse.org/Richers_2017_RRCCSN_EOS.

The results of this study show that the nuclear EOS affects rotating core collapse GW emission through its effect on the mass of inner core at bounce and the central density of the postbounce PNS. I furthermore find that the GW emission is sensitive to the treatment of the transition of nonuniform to uniform nuclear matter, to the treatment of nuclei at subnuclear densities, and to the EOS parameterization at around nuclear saturation density. The interplay of all of these elements make it

challenging for Advanced-LIGO-class observatories to discern between theoretical models of nuclear matter in these regimes. Since rotating core collapse does not probe densities in excess of around twice nuclear, very little exotic physics (e.g., hyperons, deconfined quarks) can be probed by its GW emission. I also test the sensitivity of these results to variations in electron capture during collapse. Since the inner core mass at bounce is highly sensitive to the details of electron capture and deleptonization during collapse, these results suggest that full GR neutrino radiation-hydrodynamic simulations with a detailed treatment of nuclear electron capture (e.g., Sullivan et al., 2016; Hix et al., 2003) will be essential for generating truly reliable GW templates for rotating core collapse.

7.2 Methods

As the core of a massive star is collapsing, electron capture and the release of neutrinos drives the matter to be increasingly neutron-rich. The electron fraction Y_e of the inner core in the final stage of core collapse has an important role in setting the mass of the inner core, which, in turn, influences characteristics of the emitted GWs. Multidimensional neutrino radiation hydrodynamics to account for these neutrino losses during collapse is still too computationally expensive to allow a large parameter study of axisymmetric (2D) simulations. Instead, I follow the proposal by Liebendörfer Liebendörfer, 2005 and approximate this prebounce deleptonization of the matter by parameterizing the electron fraction Y_e as a function of only density. Since the collapse-phase deleptonization is EOS dependent, I extract the $Y_e(\rho)$ parameterizations from detailed spherically symmetric (1D) non-rotating GR radiation-hydrodynamic simulations and apply them to rotating 2D GR hydrodynamic simulations. I motivate using the $Y_e(\rho)$ approximation also for the rotating case by the fact that electron capture and neutrino-matter interactions are local and primarily dependent on density in the collapse phase Liebendörfer, 2005. Hence, geometry effects due to the rotational flattening of the collapsing core can be assumed to be relatively small. This, however, has yet to be demonstrated with full multi-dimensional radiation-hydrodynamic simulations. Furthermore, the $Y_e(\rho)$ approach has been used in many previous studies of rotating core collapse (e.g., Dimmelmeier, Ott, H.-T. Janka, et al., 2007; Dimmelmeier, Ott, Marek, et al., 2008; E. B. Abdikamalov et al., 2010; E. Abdikamalov, S. Gossan, et al., 2014) and using it lets us compare with these past results. I ignore the magnetic fields throughout this work, since they are expected to grow to dynamical strengths on timescales longer than the first ~ 10 ms after core bounce that I investigate Burrows,

Dessart, et al., 2007; Takiwaki and Kotake, 2011; Mösta, Richers, et al., 2014; Mösta, Ott, et al., 2015.

1D Simulations of Collapse-Phase Deleptonization with GR1D

I run spherically symmetric GR radiation hydrodynamic core collapse simulations of a nonrotating $12M_{\odot}$ progenitor (Woosley *et al.* Woosley and Heger, 2007, model s12WH07) in the open-source code GR1D E. O'Connor, 2015, once for each of the 18 EOS. The fiducial radial grid consists of 1000 zones extending out to 2.64×10^4 km, with a uniform grid spacing of 200 m out to 20 km and logarithmic spacing beyond that. I test the resolution later in this section.

The neutrino transport is handled with a two-moment scheme with 24 logarithmically-spaced energy groups from 0 to 287 MeV. This allows us to treat the effects of neutrino absorption and emission explicitly and self-consistently. The neutrino interaction rates are calculated by NuLib E. O'Connor, 2015 and include absorption onto and emission from nucleons and nuclei including neutrino blocking factors, elastic scattering off nucleons and nuclei, and inelastic scattering off electrons. I neglect bremsstrahlung and neutrino pair creation and annihilation, since they are unimportant during collapse and shortly after core bounce (e.g., Lentz, Mezzacappa, Messer, Hix, et al., 2012). To ensure a consistent treatment of electron capture for all EOS, the rates for absorption, emission, and scattering from nuclei are calculated using the SNA. To test this approximation, in Section 7.8, I run additional simulations with experimental and theoretical nuclear electron capture rates instead included individually for each of the heavy nuclei in an NSE distribution. I test the neutrino energy resolution and the resolution of the interaction rate table later in this section.

In this study, we use the 18 different EOS described in Table 2.2. We use tabulated versions that are available from https://stellarcollapse.org/equationofstate that also include contributions from electrons, positrons, and photons. Throughout this chapter, we use the SFHo EOS as a fiducial standard for comparison, since it represents the most likely fit to known experimental and observational constraints. While many of the considered EOS do not satisfy multiple constraints, we still include them in this study for two reasons: (1) a larger range of EOS will allow us to better understand and possibly isolate causes of trends in the GW signal with EOS properties and, (2), many constraint-violating EOS likely give perfectly reasonable thermodynamics for matter under collapse and PNS conditions even if they may be

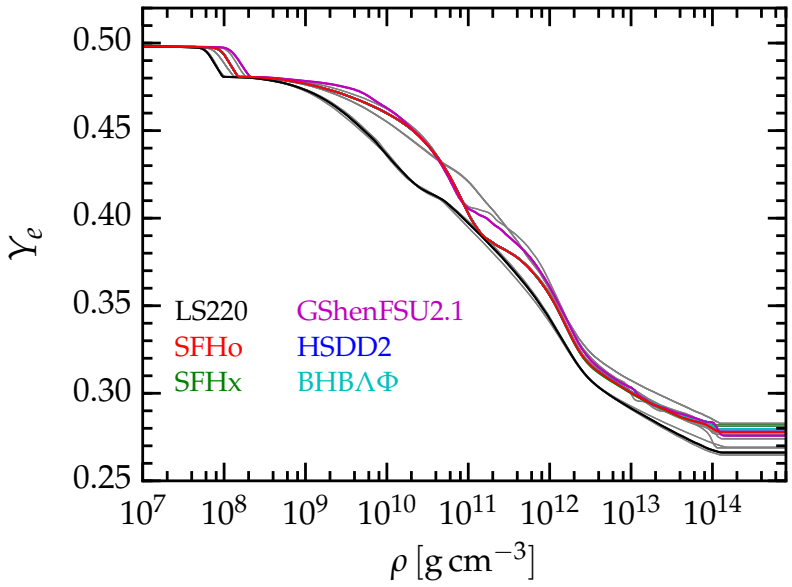

Figure 7.1: **$Y_e(\rho)$ deleptonization profiles.** For each EOS, radial profiles of the electron fraction Y_e as a function of density ρ are taken from spherically-symmetric `GR1D` radiation hydrodynamics simulations using two-moment neutrino transport at the point in time when the central Y_e is smallest (roughly at core bounce) and are plotted here. I manually extend the curves out to high densities with a constant Y_e to ensure that simulations never encounter a density outside the range provided in these curves. In the 2D simulations, Y_e is determined by the density and one of these curves until core bounce.

unrealistic at higher densities or lower temperatures.

To generate the $Y_e(\rho)$ parameterizations, I take a fluid snapshot at the time when the central Y_e is at a minimum (~ 0.5 ms prior to core bounce) and create a list of the Y_e and ρ at each radius. I then manually enforce that Y_e decreases monotonically with increasing ρ. The resulting profiles are shown in Figure 7.1.

A commonly used alternative is to fit a function to this profile and evaluate the function rather than interpolating data in a profile. For convenience and for use in the numerics study later in this section, I also generate functional fits for these profiles. Following Liebendörfer, 2005 with a tweak at high densities, I fit the 1D $Y_e(\rho)$ profiles using the fitting function

$$
Y_e = \begin{cases} \quad 0.5(Y_{e,2} + Y_{e,1}) & \\ +x/2(Y_{e,2} - Y_{e,1}) & \\ \quad +Y_{e,c}[1 - |x| & \rho \leq \rho_2 \\ +4|x|(|x| - 0.5)(|x| - 1)] & \\ Y_{e,2} + m(\log_{10}\rho - \log_{10}\rho_2) & \rho > \rho_2 \ , \end{cases} \tag{7.1}
$$

$$
x = \max\left(-1, \min\left(1, \frac{2\log_{10}\rho - \log_{10}\rho_2 - \log_{10}\rho_1}{\log_{10}\rho_2 - \log_{10}\rho_1}\right)\right) \ ,
$$

$$
m = \frac{Y_{e,H} - Y_{e,2}}{\log_{10}\rho_H - \log_{10}\rho_2} \ .
$$

The parameters $\rho_H = 10^{15}\,\mathrm{g\,cm^{-3}}$ and $Y_{e,1} = 0.5$ are fixed. The parameters $\{\rho_1, \rho_2, Y_{e,2}, Y_{e,c}, Y_{e,H}\}$ are fit using the Mathematica MyFit function, subject to the constraints

$$
\begin{aligned}
10^7 \leq & \frac{\rho_1}{\mathrm{g\,cm^{-3}}} \leq 10^{8.5} \ , \\
10^{12} \leq & \frac{\rho_2}{\mathrm{g\,cm^{-3}}} \leq 10^{14} \ , \\
0.2 \leq & Y_{e,2} \leq 0.4 \ , \\
0.02 \leq & Y_{e,c} \leq 0.055 \ , \\
& \frac{dY_e}{d\rho} < 0 \ .
\end{aligned} \tag{7.2}
$$

The resulting fit parameters are listed in Table 7.1 for each EOS. In Figure 7.2, I plot the $Y_e(\rho)$ profiles for the SFHo EOS used in the SFHo 2D simulations, along with the fit. I also plot the G15 fit from Liebendörfer, 2005, and the $Y_e(\rho)$ profile obtained by tracking the density and electron fraction of the center during collapse in the GR1D simulation and appending this to the $Y_e(\rho)$ at $t = 0$ profile for low densities.

1D Numerics Study

I attempt to quantify the errors resulting from the various numerical and physical approximations in this approach by performing a sensitivity study with various parameters in all simulation phases. I employ the SFHo EOS for these tests and adopt $A3 = 634\,\mathrm{km}$, $\Omega = 5.0\,\mathrm{rad\,s^{-1}}$ as the fiducial rotation setup in rotating test simulations. Key quantitative results from the fiducial 1D and 2D simulations used for comparison are listed in bold at the top of Table 7.2.

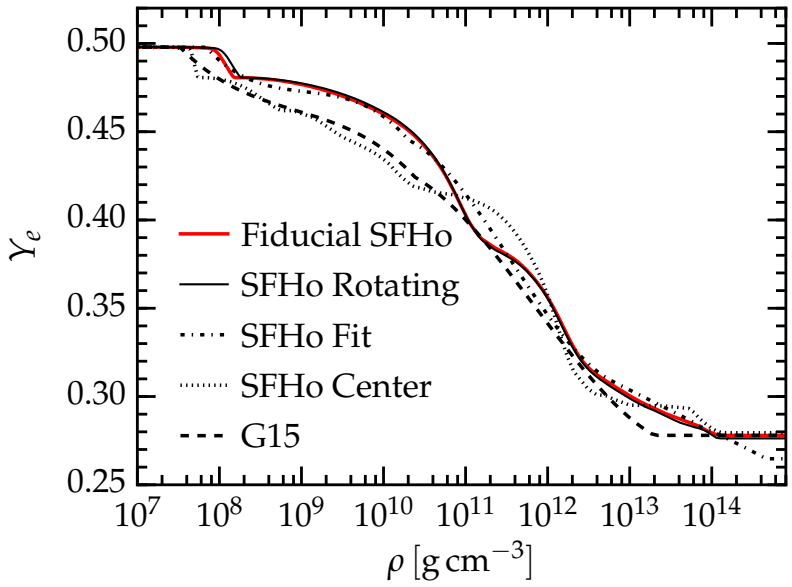

Figure 7.2: **Test $Y_e(\rho)$ profiles.** I plot the different possibilities for deleptonization functions one might input into the 2D GRHD simulations. The solid red line is the $Y_e(\rho)$ directly taken from the radial profile at the moment when the central Y_e is lowest. The solid black line is also directly taken from the radial data of a GR1D simulation using "shellular" rotation with $A = 634\,\mathrm{km}$, $\Omega_0 = 5.0\,\mathrm{rad\,s^{-1}}$. The dot-dashed line is a fit to the nonrotating $Y_e(\rho)$ using the same parameters as Liebendörfer, 2005 in addition to a high-density slope. The dashed line is the G15 fit from Liebendörfer, 2005. The dotted line is a record of the central $Y_{e,c}(\rho_c)$ throughout nonrotating collapse, appended to the $Y_e(\rho)$ profile at $t = 0$.

As described in Section 7.2, I use GR1D simulations to generate $Y_e(\rho)$ profiles for the 2D simulations, and so these profiles encode the effects of the EOS during the collapse phase of the 2D simulations. Here I check the various levels of physical and numerical approximations made in calculating the profiles used in the main text. I also check whether using one of these profiles produces results consistent with full transport. In Table 7.2, I list the time to bounce t_b, the mass of the inner core at bounce $M_{\mathrm{IC,b}}$, and the central density, temperature, and electron fraction at bounce.

Table 7.2 shows that the nonrotating 1D `GR1D` radiation-hydrodynamic simulation and the 2D `CoCoNuT` hydrodynamic simulation agree well in key collapse results and in particular in $M_{\mathrm{IC,b}}$. This confirms that the $Y_e(\rho)$ parameterization captures deleptonization and its effect on the collapsing core well, as previously shown by Liebendörfer, 2005. The difference in the central Y_e at bounce (0.288 in the `GR1D` run vs. 0.278 in the `CoCoNuT` simulation) is due to my use of $Y_e(\rho)$ from the `GR1D` simulation at the time of minimum central Y_e, which occurs just before bounce. Due

EOS	$\log_{10}\rho_1$	$\log_{10}\rho_2$	$Y_{e,2}$	$Y_{e,c}$	$Y_{e,H}$
SFHo	7.795	12.816	0.308	0.0412	0.257
SFHx	7.767	12.633	0.323	0.0380	0.275
SFHo_ecap0.1	8.210	13.053	0.291	0.0493	0.237
SFHo_ecap1.0	8.022	12.882	0.281	0.0528	0.224
SFHo_ecap10.0	7.743	12.405	0.294	0.0473	0.226
LS180	7.738	13.034	0.290	0.0307	0.243
LS220	7.737	12.996	0.292	0.0298	0.245
LS375	7.755	12.901	0.295	0.0279	0.251
HShen	7.754	13.124	0.303	0.0398	0.267
HShenH	7.751	13.124	0.303	0.0397	0.267
GShenFSU1.7	7.939	12.935	0.305	0.0403	0.257
GShenFSU2.1	7.939	12.935	0.305	0.0403	0.257
GShenNL3	7.917	13.104	0.299	0.0412	0.247
HSDD2	7.797	12.813	0.308	0.0411	0.259
HSNL3	7.798	12.808	0.308	0.0409	0.253
HSIUF	7.792	12.777	0.311	0.0403	0.257
HSTMA	7.793	12.787	0.310	0.0408	0.252
HSTM1	7.799	12.812	0.308	0.0411	0.253
HSFSG	7.792	12.784	0.311	0.0404	0.256
BHBΛ	7.794	12.815	0.308	0.0412	0.259
BHBΛΦ	7.794	12.814	0.308	0.0412	0.259
Liebendörfer G15	7.477	13.301	0.278	0.0350	0.278

Table 7.1: **Fitted $\mathbf{Y_e}(\rho)$ profiles.** I provide results for the fitting parameters in Equation 7.2 for each EOS. I provide these fits for convenience, but do not use them in the 2D simulations and instead interpolate from the numerical `GR1D` results.

to shifts in the local beta equilibrium, the central Y_e in the radiations-hydrodynamic simulation increases again after its global minimum.

An important open question is to what extent rotation affects the validity of the $Y_e(\rho)$ for deleptonization during collapse. While I cannot currently carry out detailed multi-D radiation-hydrodynamic simulations to answer this conclusively, rotation is included approximately in `GR1D` 1D radiation-hydrodynamic simulations, using the "shellular rotation" approximation (cf. E. O'Connor and Ott, 2010; Thompson, Quataert, and Burrows, 2005). I employ the fiducial rotation profile specified by $A3 = 634\,\mathrm{km}$ and $\Omega_0 = 5\,\mathrm{rad\,s^{-1}}$ as in the 2D case, though the radial coordinate relevant for the rotational setup is the spherical radius in `GR1D`.

The "`GR1D` Rotating" row in Table 7.2 shows that the effects of rotation on the collapse dynamics are qualitatively similar between 1D "shellular rotation" and 2D

Test	$t_{\rm b}$ (ms)	$M_{\rm IC,b}$ ($M_\odot$)	$\rho_{\rm c,b}$ (g cm^{-3})	$T_{\rm c,b}$ (MeV)	$Y_{\rm e,c,b}$
GR1D Nonrot.	**180**	**0.583**	**4.31**	**14.9**	**0.288**
CoCoNuT Nonrot.	**174**	**0.582**	**4.38**	**14.8**	**0.278**
CoCoNuT Fiducial	**200**	**0.708**	**4.16**	**12.8**	**0.278**
GR1D $n_r = 1500$	180	0.583	4.26	14.9	0.288
GR1D Rotating	202	0.674	3.95	13.9	0.286
GR1D $Y_e(\rho)$ Direct	210	0.583	4.37	14.1	0.278
GR1D $Y_e(\rho)$ Fit	211	0.592	4.43	14.2	0.265
GR1D $Y_e(\rho)$ Center	174	0.610	4.26	17.3	0.279
GR1D $Y_e(\rho)$ G15	189	0.547	4.22	12.5	0.279
NuLib $n_E = 36$	180	0.582	4.25	15.0	0.288
NuLib $n_\rho = 123$	180	0.583	4.27	14.7	0.288
NuLib $n_T = 150$	180	0.582	4.25	14.9	0.288
NuLib $n_{Y_e} = 150$	180	0.583	4.28	14.8	0.288

Table 7.2: **GR1D test results.** Key diagnostic quantities from 1D simulation tests are listed, along with corresponding quantities from select 2D simulations for comparison. $t_{\rm b}$ is the time from simulation start to core bounce. $M_{\rm IC,b}$, $\rho_{c,b}$, $T_{c,b}$, and $Y_{e,c,b}$ are the mass of the inner core, the central density, the central temperature, and the central electron fraction, respectively, at core bounce. Note that I average $\rho_{c,b}$ in the interval $[t_{\rm b}, t_{\rm b} + 0.2\,{\rm ms}]$ to filter out spurious oscillations that are purely numerical in this single-point quantity at the origin. Bolded rows are fiducial simulations, and the two CoCoNuT rows are the same quantities from two of the 2D simulations. In the NuLib block, I vary only the input physics and resolution for the neutrino interaction table used in the 1D simulations. In the GR1D block, I vary only GR1D simulation resolution and rotation. In the $Y_e(\rho)$ block, I experiment with using different prescriptions for the deleptonization profile, including the G15 fit from Liebendörfer, 2005 (see Figure 7.2).

rotation: $t_{\rm b}$ and $M_{\rm IC,b}$ increase and $\rho_{\rm c,b}$ decreases. However, in 1D, the quantitative changes are smaller than in 2D, which is consistent with the findings of Ott, Burrows, Thompson, et al., 2006, who more extensively compared 1D "shellular rotation" with 2D rotation.

Figure 7.2 compares the $Y_e(\rho)$ profile obtained from the rotating `GR1D` simulation with the fiducial $Y_e(\rho)$ profile and other possible profiles. As expected (cf. Section 7.2), rotation in the "shellular" approximation leads to only minor differences in $Y_e(\rho)$ between the nonrotating case and the fiducial rotational setup.

In the first row of the GR1D block of Table 7.2, I list results from a `GR1D` simulation with 1.5 times the standard resolution. The differences with the standard resolution run are very small, giving us confidence that ours `GR1D` simulation results are

numerically converged.

The $Y_e(\rho)$ profiles extracted from the 1D radiation-hydrodynamic simulations should give a good approximation to collapse-phase deleptonization and its impact on collapse and bounce dynamics Liebendörfer, 2005. I test this assertion by re-running the GR1D 1D simulations with various choices for the $Y_e(\rho)$ profiles (see Figure 7.2) rather than using neutrino transport. The results are listed in the third block of Table 7.2.

I find that the fiducial $Y_e(\rho)$ profile (row "GR1D $Y_e(\rho)$ Direct" in Table 7.2) leads to inner core masses, bounce densities, and thermodynamics that approximate the radiation hydrodynamics results very well. Using a fit to the fiducial $Y_e(\rho)$ ("GR1D $Y_e(\rho)$ Fit") or generating the $Y_e(\rho)$ profile from the central value of Y_e ("GR1D $Y_e(\rho)$ Center") leads to larger differences in all quantities (e.g., $\gtrsim$5% in $M_{\mathrm{IC,b}}$). These quantitative differences are of the same order as those due to differences in EOS and electron capture treatment (cf. Section 7.8 and the "GR1D $Y_e(\rho)$ G15" row). For instance, different EOS lead to inner core masses at bounce in the range of $0.549 - 0.618\,M_\odot$. Hence, the $Y_e(\rho)$ parameterization can lead to a systematic error that muddles the interpretation of results from simulations using different EOS. For quantitatively reliable predictions, full 2D radiation-hydrodynamic simulations will be necessary.

The entries in the NuLib block of Table 7.2 give results for test simulations with different resolutions of the neutrino interaction table. These are to be compared with the fiducial neutrino interaction table that has resolution $n_E = 24$ (number of energy groups), $n_\rho = 82$, $n_T = 100$, $n_{Y_e} = 100$. All tables span the range

$$\begin{aligned} 0 &< E/(\mathrm{MeV}) &&< 287\ , \\ 10^6 &< \rho/(\mathrm{g\,cm^{-3}}) &&< 10^{15}\ , \\ 0.05 &< T/(\mathrm{MeV}) &&< 150\ , \\ 0.035 &< Y_e &&< 0.55\ . \end{aligned} \tag{7.3}$$

The energy, density, and temperature points in the table are logarithmically spaced and the electron fraction points are evenly spaced. Increasing the table resolution has negligible impact on the GR1D results.

2D Core Collapse Simulations with CoCoNuT

I perform axisymmetric (2D) core collapse simulations using the CoCoNuT code Dimmelmeier, Font, and E. Müller, 2002; Dimmelmeier, Novak, et al., 2005 with confor-

Name	A [km]	Ω_0 [rad s^{-1}]	# of Profiles
A1	300	0.5 - 15.5	31
A2	467	0.5 - 11.5	23
A3	634	0.0 - 9.5	20
A4	1268	0.5 - 6.5	13
A5	10000	0.5 - 5.5	11

Table 7.3: **Rotation Profiles.** A list of the differential rotation A and maximum rotation rate Ω_0 parameters used in generating rotation profiles. The Ω_0 ranges imply a rotation profile at each 0.5 rad s^{-1} interval. In total, I use 98 rotation profiles.

A [km]	Ω_0 [rad s^{-1}]	EOS
300	15.5	GShenNL3
467	10.0	GShenNL3
	10.5	GShenNL3
	11.0	GShen{NL3,FSU2.1,FSU1.7}
	11.5	GShen{NL3,FSU2.1,FSU1.7}
634	8.0	GShenNL3
	8.5	GShen{NL3,FSU2.1,FSU1.7}
	9.0	GShen{NL3,FSU2.1,FSU1.7}
	9.5	GShen{NL3,FSU2.1,FSU1.7}
		LS{180,220,375}
1268	5.5	GShenNL3
	6.0	GShen{NL3,FSU2.1,FSU1.7}
	6.5	GShen{NL3,FSU2.1,FSU1.7}
		LS{180,220,375}
10000	4.0	GShen{NL3,FSU2.1,FSU1.7}
	4.5	GShen{NL3,FSU2.1,FSU1.7}
	5.0	GShen{NL3,FSU2.1,FSU1.7}
		LS{180,220,375}
	5.5	all but HShen,HShenH

Table 7.4: **No Collapse List**. I list the simulations that do not undergo core collapse within 1 s of simulation time due to sufficiently large centrifugal support already at the onset of collapse. These simulations are excluded from further analysis.

mally flat GR. I use a setup identical to that in Abdikamalov *et al.* E. Abdikamalov, S. Gossan, et al., 2014, but I review the key details here for completeness. I generate rotating initial conditions for the 2D simulations from the same 12 $M_\odot$ progenitor by imposing a rotation profile on the precollapse star according to (e.g., Zwerger and E. Müller, 1997)

$$\Omega(\varpi) = \Omega_0 \left[1 + \left(\frac{\varpi}{A}\right)^2\right]^{-1} , \tag{7.4}$$

where A is a measure of the degree of differential rotation, Ω_0 is the maximum initial rotation rate, and ϖ is the distance from the axis of rotation. Following Abdikamalov *et al.* E. Abdikamalov, S. Gossan, et al., 2014, I generate a total of 98 rotation profiles using the parameter set listed in Table 7.3, chosen to span the full range of rotation rates slow enough to allow the star to collapse. All 98 rotation profiles are simulated using each of the 18 EOS for a total of 1764 2D core collapse simulations. However, the 60 simulations listed in Table 7.4 do not result in core collapse within 1 s of simulation time due to centrifugal support and are excluded from the analysis.

CoCoNuT solves the equations of GR hydrodynamics on a spherical-polar mesh in the Valencia formulation Font, 2008, using a finite volume method with piecewise parabolic reconstruction Colella and Woodward, 1984 and an approximate HLLE Riemann solver Einfeldt, 1988b. The fiducial fluid mesh has 250 logarithmically spaced radial zones out to $R = 3000\,\mathrm{km}$ with a central resolution of 250 m, 40 equally spaced meridional angular zones between the equator and the pole, and reflecting boundary conditions at the equator. The GR CFC equations are solved spectrally using 20 radial patches, each containing 33 radial collocation points and 5 angular collocation points (see Dimmelmeier *et al.* Dimmelmeier, Novak, et al., 2005). I perform resolution tests later in this section.

The effects of neutrinos during the collapse phase are treated with a $Y_e(\rho)$ parameterization as described previously in this section and in Liebendörfer, 2005; Dimmelmeier, Ott, Marek, et al., 2008. After core bounce, the neutrino leakage scheme described in Ott, E. Abdikamalov, et al., 2012 is used to approximately account for neutrino heating, cooling, and deleptonization, though Ott *et al.* Ott, E. Abdikamalov, et al., 2012 have shown that neutrino leakage has a very small effect on the bounce and early postbounce GW signal.

I allow the simulations to run for 50 ms after core bounce, though in order to iso-

Test	$M_{\rm IC,b}$ ($M_\odot$)	$\mathcal{M}_{\rm fid}$	$f_{\rm peak}$ (Hz)	Δh_+ (10^{-21})
CoCoNuT Fiducial	**0.718**	**0**	**793**	**20.9**
NuLib $n_E = 36$	0.717	2.10(-5)	794	20.9
NuLib $n_\rho = 123$	0.718	2.91(-5)	794	21.0
NuLib $n_T = 150$	0.717	4.63(-5)	794	21.0
NuLib $n_{Y_e} = 150$	0.718	1.48(-5)	794	20.9
GR1D $n_r = 1500$	0.716	1.23(-5)	794	21.0
GR1D Rotating	0.711	9.21(-5)	794	20.6
$Y_e(\rho)$ Fit	0.729	9.53(-3)	812	20.6
$Y_e(\rho)$ Center	0.747	4.87(-2)	810	23.3
$Y_e(\rho)$ G15	0.655	7.86(-2)	752	14.1
CoCoNuT $n_r = 500$	0.718	1.79(-3)	795	21.5
CoCoNuT $n_\theta = 80$	0.718	1.03(-4)	794	21.1
CoCoNuT Eq. Bounce	0.714	4.40(-3)	789	21.6
CoCoNuT rk3	0.716	3.34(-3)	797	20.9

Table 7.5: **Waveform test results.** In the NuLib, GR1D, and $Y_e(\rho)$ blocks, I simply run the fiducial CoCoNuT simulation using the $Y_e(\rho)$ profiles extracted from the GR1D tests listed in Table 7.2. In the CoCoNuT block, I only modify 2D simulation parameters. $M_{\rm IC,b}$ is the mass of the inner core at bounce, $\mathcal{M}_{\rm fid}$ is the GW mismatch with the fiducial simulation, $f_{\rm peak}$ is the peak frequency of the GWs from postbounce oscillations, and Δh_+ is the difference between the largest positive and negative GW strain values of the bounce signal.

late the bounce and post-bounce oscillations from prompt convection, I use only about 10 ms after core bounce. Gravitational waveforms are calculated using the quadrupole formula as given in Equation A4 of Dimmelmeier, Font, and E. Müller, 2002. All of the waveforms and reduced data used in this study along with the analysis scripts are available at https://stellarcollapse.org/Richers_2017_RRCCSN_EOS.

2D Numerics Study

I attempt to quantify the errors resulting from the various numerical and physical approximations in this approach by performing a sensitivity study with various parameters in all simulation phases. I employ the SFHo EOS for these tests and adopt $A3 = 634\,\mathrm{km}$, $\Omega = 5.0\,\mathrm{rad\,s^{-1}}$ as the fiducial rotation setup in rotating test simulations. Key quantitative results from the fiducial 1D and 2D simulations used for comparison are listed in bold at the top of Table 7.5.

In Table 7.5, I list the inner core mass at bounce, the GW mismatch (see Section 7.7) with the fiducial 2D simulation, the peak frequency, and the bounce signal amplitude

for several 2D tests. The results of the fiducial 2D simulation are bolded at the top for comparison.

The NuLib and GR1D blocks of Table 7.5 use the $Y_e(\rho)$ profile generated by the corresponding 1D test simulation in a 2D simulation otherwise identical to the fiducial one. These all produce negligible differences in all quantities. Rotation is multidimensional, so the "shellular rotation" approximation in `GR1D` does not take into account multidimensional effects. The lack of impact of approximate 1.5D rotation on the collapse deleptonization suggests that using a $Y_e(\rho)$ profile from a nonrotating 1D simulation in moderately-rapidly rotating 2D collapse simulation is acceptable. The choice of $Y_e(\rho)$ parameterization, however, leads to significant differences, as already pointed out previously in this section. The GW mismatch for the "Fit" and "Center" choices with the fiducial approach is ∼1% and ∼5%, respectively. The peak frequencies differ by ∼2%. Using the G15 $Y_e(\rho)$ fit of Liebendörfer, 2005 leads to even larger mismatch of ∼8% and a peak frequency differing by as much as ∼40 Hz. These differences are as large or larger than differences between many EOS discussed in §7.3. I do not expect this to affect the universal trends I establish in the main text, since differences in EOS already produce different $Y_e(\rho)$ profiles yielding simulation results that consistently follow the universal trends. However, it reaffirms that for quantitatively reliable GW signal predictions, a detailed and converged treatment of prebounce deleptonization with radiation hydrodynamics is vital.

In the final block of Table 7.5, I summarize results of simulations in which I increase the resolution and order of the time integrator in `CoCoNuT` simulations. These lead to waveform mismatches of up to 0.4%, significantly smaller than those from systematic errors induced by the prebounce deleptonization treatment. I transition from the $Y_e(\rho)$ deleptonization prescription to neutrino leakage when the entropy along the polar axis exceeds 3 k_b baryon^{-1}. In rotating models, this is a fraction of a millisecond before this occurs on the equatorial axis, which is my definition of the time of core bounce. The row labeled "`CoCoNuT` Eq. Bounce" shows that having the trigger on the equatorial axis results in negligible differences.

To summarize, the 1D and 2D simulation results are essentially independent of the neutrino interaction table resolution and of the 1D grid resolution. There is a weak dependence on the 2D grid resolution (below 1% mismatch in all resolution tests). However, the results are sensitive to the treatment of prebounce deleptonization at the level of several percent GW mismatch. Again, future GR radiation hydrodynamic

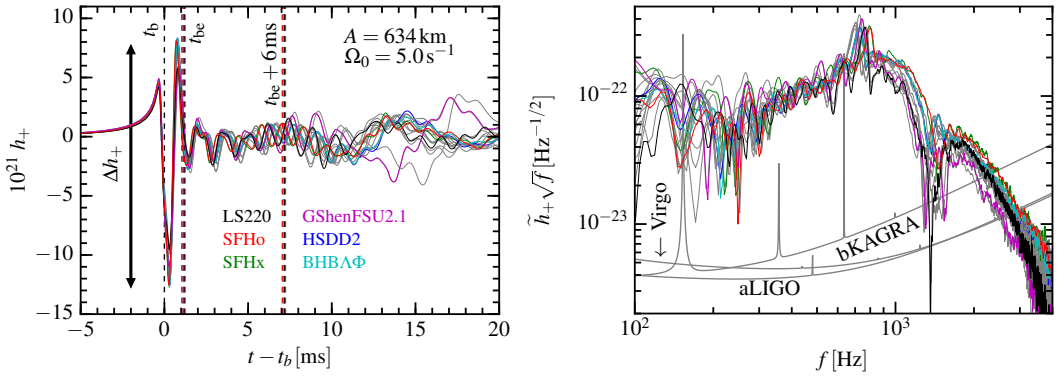

Figure 7.3: **EOS Variability in Waveforms.** The time-domain waveforms (left panel) and Fourier transforms scaled by $\sqrt{f}$ (right panel) of signals from all 18 EOS for the A = 634 km, $\Omega = 5.0\,\mathrm{rad\,s^{-1}}$ rotation profile (moderately rapidly rotating, $T/|W| = 0.069 - 0.074$ at core bounce, depending on the EOS) are plotted assuming a distance of 10 kpc and optimal orientation, along with the Advanced LIGO LIGO Scientific Collaboration et al., 2015; Shoemaker, 2010, VIRGO Acernese et al. (Virgo Collaboration), 2009, and KAGRA in the zero detuning VRSE configuration Somiya (for the KAGRA collaboration), 2012; *KAGRA Detector Sensitivity* 2016 design sensitivity curves. t_b is the time of core bounce, t_{be} is the end of the bounce signal and the beginning of the post-bounce signal. I use data only until $t_{\mathrm{be}} + 6$ ms to exclude the GW signal from prompt convection from the analysis. The differences in post-bounce oscillation rates can be seen both in phase decoherence of the waveform and the peak location of the Fourier transform. The colored curves correspond to EOS that satisfy the constraints depicted in Figure 2.1.

simulations with detailed nuclear electron capture rates will be needed for reliable predictions of gravitational waveforms from rotating core collapse.

7.3 Waveform Morphology

I begin by briefly reviewing the general properties of the GW signal from rapidly rotating axisymmetric core collapse, bounce, and the early postbounce phase. The GW strain can be approximately computed as (e.g., Finn and C. R. Evans, 1990; Blanchet, Damour, and Schaefer, 1990)

$$h_+ \approx \frac{2G}{c^4 D}\ddot{I}\,, \tag{7.5}$$

where G is the gravitational constant, c is the speed of light, D is the distance to the source, and I is the mass quadrupole moment. In the left panel of Figure 7.3 I show a superposition of 18 gravitational waveforms for the $A3 = 634$ km, $\Omega_0 = 5.0\,\mathrm{rad\,s^{-1}}$ rotation profile using each of the 18 EOS and assuming a distance of 10 kpc and

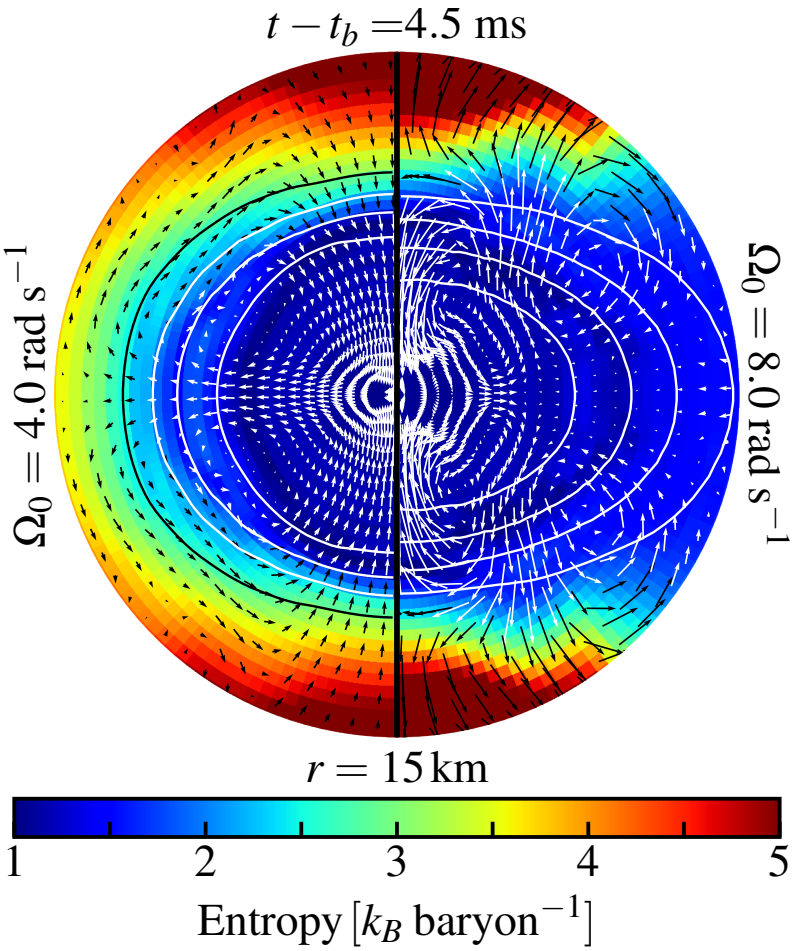

Figure 7.4: **Velocity field.** I plot the entropy, density, and velocity for the $\Omega_0 = 4.0\,\mathrm{rad\,s^{-1}}$ (left) and $\Omega_0 = 8.0\,\mathrm{rad\,s^{-1}}$ (right) simulations with $A = 634\,\mathrm{km}$ at 4.5 ms after core bounce. The color map shows entropy. Blue regions belong to the unshocked inner core. The density contours show densities of $10^{\{13.5,13.75,14.0,14.25\}}\,\mathrm{g\,cm^{-3}}$ from outer to inner. The vectors represent only the poloidal velocity (i.e. the rotational velocity is ignored) and are colored for visibility. At low rotation rates (left) the flow in the inner core is largely quadrupolar. At high rotation rates (right), rotation significantly deforms the inner core and couples $\ell = 2, m = 0$ quadrupole oscillations to other modes.

optimal source-detector orientation.

As the inner core enters the final phase of collapse, its collapse velocity greatly accelerates, reaching values of ∼0.3 c. At bounce, the inner core suddenly (within ∼1 ms) decelerates to near zero velocity and then rebounds into the outer core. This causes the large spike in h_+ seen around the time of core bounce t_b. I determine t_b as the time when the entropy along the equator exceeds 3 k_b baryon^{-1}, indicating the formation of the bounce shock. The rotation causes the shock to form in the equatorial direction a few tenths of a millisecond after the shock forms in the polar direction.

The bounce of the rotationally-deformed core excites postbounce "ring-down" oscillations of the PNS that are a complicated mixture of multiple modes. They last for a few cycles after bounce, are damped hydrodynamically J. Fuller, Klion, et al., 2015, and cause the postbounce oscillations in the GW signal that are apparent in the left panel of Figure 7.3. The dominant oscillation has been identified as the $\ell = 2, m = 0$ (i.e., quadrupole) fundamental mode (i.e., no radial nodes) Ott, E. Abdikamalov, et al., 2012; J. Fuller, Klion, et al., 2015. The quadrupole oscillations can be seen in the postbounce velocity field that I plot in the left panel of Figure 7.4. With increasing rotation rate, changes in the mode structure and nonlinear coupling with other modes result in the complex flow geometries shown in the right panel of Figure 7.4. The density contours in Figure 7.4 also visualize how the PNS becomes more oblate and less dense with increasing rotation rate.

After the PNS has rung down, other fluid dynamics, notably prompt convection, begin to dominate the GW signal, generating a stochastic GW strain whose time domain evolution is sensitive to the perturbations from which prompt convection grows (e.g., Ott, 2009; Marek, H.-T. Janka, and E. Müller, 2009; Kotake, Iwakami, et al., 2009; E. Abdikamalov, S. Gossan, et al., 2014). I exclude the convective part of the signal from the analysis. For the analysis, I delineate the end of the bounce signal and the start of the postbounce signal at t_{be}, defined as the time of the third zero crossing of the GW strain. I also isolate the postbounce PNS oscillation signal from the convective signal by considering only the first 6 ms after t_{be}.

In the right panel of Figure 7.3, I show the Fourier transforms of each of the time-domain waveforms shown in the left panel, multiplied by $\sqrt{f}$ for comparison with GW detector sensitivity curves. The bounce signal is visible in the broad bulge in the range of 200 − 1500 Hz. The postbounce oscillations produce a peak in the spectrum of around 700 − 800 Hz, the center of which I call the peak frequency

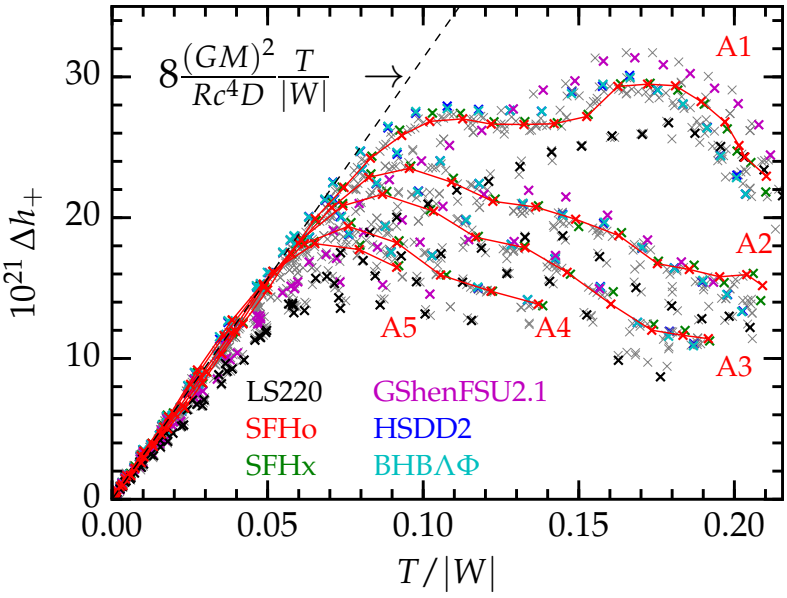

Figure 7.5: **Bounce signal amplitude.** I plot the difference between the maximum and minimum strain Δh_+ before $t_{\rm be}$ assuming $D = 10\,$kpc and optimal source-detector orientation as a function of the ratio of rotational to gravitational energy $T/|W|$ of the inner core at bounce. Each 2D simulation is a single point and the SFHo simulations with the same differential rotation parameter A are connected to guide the eye. $A1 - A5$ corresponds to $A = 300, 467, 634, 1268, 10000\,$km, respectively. Simulations with all EOS and values of A behave similarly for $T/|W| \lesssim 0.06$, but branch out when rotation becomes dynamically important. I plot a dashed line representing the expected perturbative behavior with $T/|W|$, using representative values of $M = 0.6M_\odot$ and $R = 65\,$km. All 1704 collapsing simulations are included in this figure.

$f_{\rm peak}$. Both the peak frequency and the amplitude of the bounce signal in general depend on both the rotation profile and the EOS.

7.4 The Bounce Signal

The bounce spike is the loudest component of the GW signal. In Figure 7.5, I plot Δh_+, the difference between the highest and lowest points in the bounce signal strain, as a function of the ratio of rotational kinetic energy to gravitational potential energy $T/|W|$ of the inner core at core bounce (see the beginning Section 7.3 for details of my definition of core bounce). I assume a distance of 10 kpc and optimal detector orientation. Just as in Abdikamalov *et al.* E. Abdikamalov, S. Gossan, et al., 2014, these results show that at low rotation rates, the amplitude increases linearly with rotation rate, with a similar slope for all EOS. At higher rotation

rates, the curves diverge from this linear relationship due to centrifugal support as the angular velocity Ω at bounce approaches the Keplerian angular velocity. Rotation slows the collapse, softening the violent EOS-driven bounce and resulting in a smaller acceleration of the mass quadrupole moment. However, the value of $T/|W| = 0.06 - 0.09$ at which simulations diverge from the linear relationship depends on the value of the differential rotation parameter A. Stronger differential rotation affords less centrifugal support at higher rotation energies, allowing the linear behavior to survive to higher rotation rates.

The linear relationship between the bounce amplitude and $T/|W|$ of the inner core at bounce can be derived in a perturbative, order-of-magnitude sense. The GW amplitude depends on the second time derivative of the mass quadrupole moment $I \sim M(x^2 - z^2)$, where M is the mass of the oscillating inner core and x and z are the equatorial and polar equilibrium radii, respectively. If we treat the inner core as an oblate sphere, we can call the radius of the inner core in the polar direction $z = R$ and the larger radius of the inner core in the equatorial direction (due to centrifugal support) $x = R + \delta R$. To first order in δR, the mass quadrupole moment becomes

$$I \sim M((R + \delta R)^2 - R^2) \sim MR(\delta R) \ . \tag{7.6}$$

The difference between polar and equatorial radii in this simplified scenario can be determined by noting that the surface of a rotating sphere in equilibrium is an isopotential surface with a potential of $-\varpi^2\Omega^2/2 - GM/r$, where ϖ is the distance to the rotation axis, r is the distance to the origin, Ω is the angular rotation rate, and G is the gravitational constant. Setting the potential at the equator and poles equal to each other yields

$$(R + \delta R)^2\Omega^2 + \frac{GM}{(R + \delta R)} = \frac{GM}{R} \ . \tag{7.7}$$

Assuming differences between equatorial and polar radii are small, we can take only the $O(\delta R/R)$ terms to get $\delta(\varpi^2\Omega^2) \sim R^2\Omega^2 \sim GM(\delta R)/R^2$. Solving for δR,

$$\delta R \sim \Omega^2 R^4/GM \ . \tag{7.8}$$

The timescale of core bounce is the dynamical time $t_{\rm dyn}^{-2} \sim G\rho \sim GM/R^3$. In this order-of-magnitude estimate we can replace time derivatives in Equation 7.5 with division by the dynamical time. We can also approximate $T/|W| \sim R^3\Omega^2/GM$. This results in

$$h_+ \sim \frac{GM\Omega^2R^2}{c^4D} \sim \frac{T}{|W|}\frac{(GM)^2}{Rc^4D} \ . \tag{7.9}$$

EOS	m $[10^{-21}]$	b $[10^{-21}]$	$m_{\rm predicted}$ $[10^{-21}]$	$M_{\rm IC,b,0}$ $[M_\odot]$
BHBL	318	-0.03	321	0.598
BHBLP	317	0.02	322	0.599
HSDD2	316	0.00	322	0.599
SFHo	306	0.03	304	0.582
HSFSG	306	-0.00	325	0.602
SFHx	305	0.09	303	0.581
HSIUF	304	0.06	316	0.593
HSNL3	298	0.07	324	0.600
HSTMA	295	0.15	315	0.593
HSTM1	295	0.18	314	0.591
HShenH	281	0.28	311	0.604
HShen	280	0.29	310	0.604
SFHo_ecap0.1	274	0.22	262	0.562
GShenNL3	267	0.32	298	0.592
GShenFSU1.7	264	0.24	294	0.587
GShenFSU2.1	263	0.24	293	0.587
LS180	242	0.16	245	0.536
LS375	237	0.15	284	0.562
LS220	237	0.20	258	0.543
SFHo_ecap1.0	210	0.08	207	0.506
SFHo_ecap10.0	174	0.03	198	0.482

Table 7.6: **Bounce Amplitude Linear Fits.** I calculate a linear least squares fit for the bounce amplitudes in Figure 7.5 to the function $\Delta h_+ = m(T/|W|) + b$. I only include data with $T/|W| \leq 0.04$. All fitted lines have a y-intercept b of approximately 0 and slopes m in the range of $237 - 315 \times 10^{-21}$. The three LS EOS have the shallowest slopes and the ten Hempel-based EOS (HS, SFH, and BHB) have the steepest. The $m_{\rm predicted}$ column shows the predicted slope of $m_{\rm predicted} = T/|W| \times 8(GM)^2/Rc^4D$ using the mass and radius of the nonrotating inner core at bounce. I choose the arbitrary factor of 8 to make the predicted and actual SFHo slopes match. I list the mass of the nonrotating inner core at bounce ($M_{\rm IC,b,0}$) for each EOS in the last column. The SFHo_ecap{0.1,1.0,10.0} rows use detailed electron capture rates in the GR1D simulations for the $Y_e(\rho)$ profile (see Section 7.8).

Though the mass and polar radius of the PNS depend on rotation as well, the dependence is much weaker (in the slow rotating limit) E. Abdikamalov, S. Gossan, et al., 2014, and $T/|W|$ contains all of the first-order rotation effects used in the derivation. Hence, *in the linear regime, the bounce signal amplitude should depend approximately linearly on* $T/|W|$, which is reflected by Figure 7.5.

Differences between EOS in the bounce signal Δh_+ enter through the mass and

radius of the inner core at bounce (cf. Equation 7.9). Neither M nor R of the inner core are particularly well defined quantities since they vary rapidly around bounce – all quantitative results depend on the definition of the bounce time and Equation 7.9 is expected to be accurate only to an order of magnitude. With that in mind, in order to test how well Equation 7.9 matches the numerical results, I generate fits to functionals of the form $h_+ = m(T/|W|) + b$. b is simply the y-intercept of the line, which should be approximately 0 based on Equation 7.9. m is the slope of the line, which I expect to be $m_{\rm predicted} = 8(GM_{\rm IC,b,0})^2/R_{\rm IC,b,0}c^4D$ based on Equation 7.9, using the mass and radius of the nonrotating PNS at bounce. I include the arbitrary factor of 8 to make the order-of-magnitude predicted slopes similar to the fitted slopes. In Table 7.6 I show the results of the linear least-squares fits to results of slowly rotating collapse below $T/|W| \leq 0.04$ for each EOS. Though $m_{\rm predicted}$ is of the same order of magnitude as m, significant differences exist. This is not unexpected, considering that this model does not account for nonuniform density distribution and the increase of the inner core mass with rotation, which can significantly affect the quadrupole moment.

At a given inner core mass, the structure (i.e. radius) of the inner core is determined by the EOS. Furthermore, the mass of the inner core is highly sensitive to the electron fraction Y_e in the final stages of collapse. In the simplest approximation, it scales with $M_{\rm IC} \sim Y_e^2$ Yahil, 1983, which is due to the electron EOS that dominates until densities near nuclear density are reached. The inner-core Y_e in the final phase of collapse is set by the deleptonization history, which varies between EOS (Figure 7.1). In addition, contributions of the nonuniform nuclear matter EOS play an additional Y_e-independent role in setting $M_{\rm IC}$. For example, we see from Figure 7.1 that the LS220 EOS yields a bounce Y_e of ~0.278, while the GShenFSU2.1 EOS results in ~0.267. Naively, relying just on the Y_e dependence of $M_{\rm IC}$, we would expect LS220 to yield a larger inner core mass. Yet, the opposite is the case: the simulations show that the nonrotating inner core mass at bounce for the GShenFSU2.1 EOS is ~0.59 $M_\odot$ while that for the LS220 EOS is ~0.54 $M_\odot$.

I further investigate the EOS-dependence of the bounce GW signal by considering a representative quantitative example of models with precollapse differential rotation parameter $A3 = 634\,$km, computed with the six EOS identified in Section 2.4 as most compliant with constraints. In Table 7.7, I summarize the results for these models for three precollapse rotation rates, $\Omega_0 = \{2.5, 5.0, 7.5\}\,{\rm rad\,s^{-1}}$, probing different regions in Figure 7.5.

Model	$\rho_{c,b}$ $[10^{14}\,\mathrm{g\,cm^{-3}}]$	$T/\lvert W\rvert$	$M_{IC,b}$ $[M_\odot]$	Δh_+ $[10^{-21}]$
A3Ω2.5-LS220	3.976	0.020	0.589	4.7
A3Ω2.5-SFHo	4.262	0.020	0.624	6.1
A3Ω2.5-SFHx	4.252	0.020	0.610	6.1
A3Ω2.5-GShenFSU2.1	3.612	0.020	0.634	5.2
A3Ω2.5-HSDD2	3.582	0.019	0.629	5.9
A3Ω2.5-BHBΛΦ	3.583	0.019	0.629	6.0
A3Ω5.0-LS220	3.581	0.071	0.673	15.3
A3Ω5.0-SFHo	3.868	0.074	0.708	20.8
A3Ω5.0-SFHx	3.857	0.074	0.705	21.0
A3Ω5.0-GShenFSU2.1	3.376	0.072	0.729	17.1
A3Ω5.0-HSDD2	3.314	0.071	0.712	21.3
A3Ω5.0-BHBΛΦ	3.321	0.071	0.709	21.3
A3Ω7.5-LS220	2.940	0.141	0.784	15.5
A3Ω7.5-SFHo	3.183	0.146	0.829	16.1
A3Ω7.5-SFHx	3.237	0.147	0.831	16.0
A3Ω7.5-GShenFSU2.1	2.878	0.143	0.838	17.3
A3Ω7.5-HSDD2	2.763	0.142	0.835	17.1
A3Ω7.5-BHBΛΦ	2.763	0.142	0.835	17.1

Table 7.7: **Example Quantitative Results for the Bounce Signal.** I present results for the bounce signals of models with differential rotation parameter $A3 = 634\,\mathrm{km}$, a representative set of initial rotation rates (2.5, 5.0, and $7.5\,\mathrm{rad\,s^{-1}}$), and the six EOS in best agreement with current constraints (cf. Section 2.4). The models are grouped by rotation rate. $\rho_{c,b}$ is the central density at bounce (time averaged from t_b to $t_b + 0.2\,\mathrm{ms}$), $T/|W|$ is the ratio of rotational kinetic energy to gravitational energy of the inner core at bounce, and $M_{IC,b}$ is its gravitational mass at bounce. Δh_+ is the difference between the highest and lowest points in the bounce spike at a distance of 10 kpc. Note that ρ_c, $T/|W|$, and M_{IC} all vary rapidly around core bounce and their exact values are rather sensitive to the definition of the time of bounce. The quantities summarized here for this set of models are available for all models at https://stellarcollapse.org/Richers_2017_RRCCSN_EOS.

At $\Omega_0 = 2.5\,\mathrm{rad\,s^{-1}}$, all models reach $T/|W|$ of $\sim$0.02, hence are in the linear regime where Equation 7.9 holds. The LS220 EOS model has the smallest inner core mass and results in the smallest bounce GW amplitude of all EOS (cf. also Figure 7.5). The SFHx and the GShenFSU2.1 EOS models have roughly the same inner core masses ($\sim 0.64 - 0.65\,M_\odot$), but the SFHx EOS is considerably softer, resulting in higher bounce density and correspondingly smaller radius, and thus larger Δh_+, 6.7×10^{-21} (at 10 kpc) vs. 5.4×10^{-21} for the GShenFSU2.1 EOS. Also note that the HSDD2 and the BHB$\Lambda\Phi$ EOS models give nearly identical results. They employ the same low-density EOS and the same RMF DD2 parameterization and their only difference is that $BHB\Lambda\Phi$ includes softening hyperon contributions that appear above nuclear density. However, at the densities reached in the core collapse simulations with these EOS ($\sim 3.6\times10^{14}\,\mathrm{g\,cm^{-3}}$), the hyperon fraction barely exceeds $\sim$1% Banik, Hempel, and Bandyopadhyay, 2014 and thus has a negligible effect on dynamics and GW signal.

The models at $\Omega_0 = 5.0\,\mathrm{rad\,s^{-1}}$ listed in Table 7.7 reach $T/|W| \sim 0.071 - 0.076$ and begin to deviate from the linear relationship of Equation 7.9. However, their bounce amplitudes Δh_+ still follow the same trends with EOS (and resulting inner core mass and bounce density) as their more slowly spinning counterparts.

Finally, the rapidly spinning models with $\Omega_0 = 7.5\,\mathrm{rad\,s^{-1}}$ listed in Table 7.7 result in $T/|W| \sim 0.141 - 0.152$ and are far outside the linear regime. Centrifugal effects play an important role in their bounce dynamics, substantially decreasing their bounce densities and increasing their inner core masses. Increasing rotation, however, tends to decrease the EOS-dependent relative differences in Δh_+. At $\Omega_0 = 5\,\mathrm{rad\,s^{-1}}$, the standard deviation of Δh_+ is $\sim$12.5% of the mean value, while at $\Omega_0 = 7.5\,\mathrm{rad\,s^{-1}}$, it is only $\sim$3%. This is also visualized by Figure 7.5 in which the rapidly rotating models cluster rather tightly around the A3 branch (third from the bottom). In general, for any value of A, the EOS-dependent spread on a given differential rotation branch is smaller than the spread between branches.

Conclusions: In the Slow Rotation regime ($T/|W| \lesssim 0.06$) the bounce GW amplitude varies linearly with $T/|W|$ (Equation 7.9), in agreement with previous works. Small differences in this linear slope are due primarily to differences in the inner core mass at bounce induced by different EOS. In the Rapid Rotation regime ($0.06 \lesssim T/|W| \lesssim 0.17$) the core is centrifugally supported at bounce and the bounce GW signal depends much more strongly on the amount of precollapse differential rotation than on the EOS. In the Extreme Rotation regime ($T/|W| \gtrsim 0.17$) the core

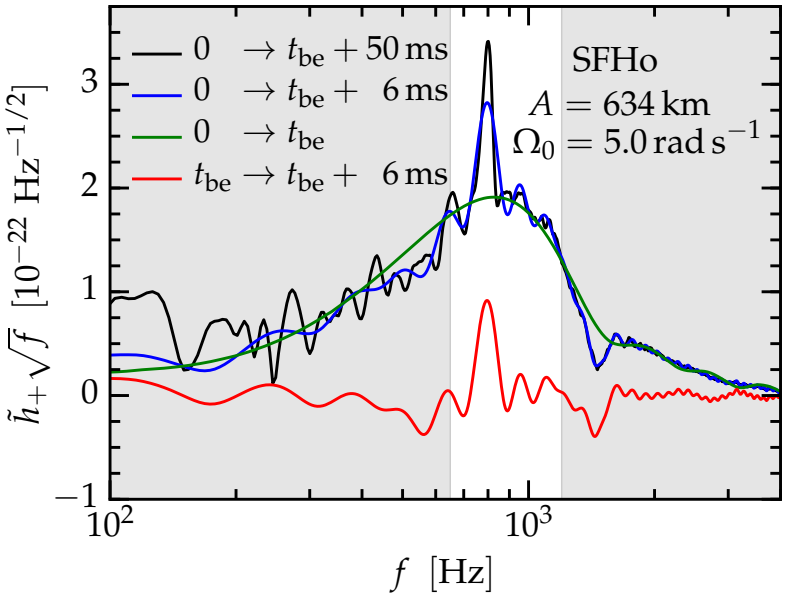

Figure 7.6: **Peak frequency determination.** The full GW spectrum for the $A3$ = 634 km, Ω = 5.0 rad s^{-1} SFHo simulation is plotted in black. To prevent convection contributions from entering into the analysis, I cut the GW signal at 6 ms after the end of core bounce (t_{be} + 6 ms, blue line). The green line is the spectrum for the time series through the end of core bounce. To remove the bounce signal from the spectrum, I subtract the green line from the blue line to get the red line. The maximum of the red line within the depicted window of 600 – 1075 Hz determines the peak frequency f_{peak}.

undergoes a centrifugally-supported bounce and the GW bounce signal weakens.

7.5 The Postbounce Signal from PNS Oscillations

The observable of greatest interest in the postbounce GW signal is the oscillation frequency of the PNS, which may encode EOS information. To isolate the PNS oscillation signal from the earlier bounce and the later convective contributions, I separately Fourier transform the GW signal calculated from GWs up to t_{be} (the end of the bounce signal, defined as the third zero-crossing after core bounce as in Figure 7.3) and from GWs up to t_{be} + 6 ms (empirically chosen to produce reliable PNS oscillation frequencies). I begin with a simulation with intermediate rotation and subtract the former bounce spectrum from the latter full spectrum and I take the largest spectral feature in the window of 600 to 1075 Hz to be the ℓ = 2 f-mode peak frequency f_{peak} Ott, E. Abdikamalov, et al., 2012; J. Fuller, Klion, et al., 2015. The spectral windows for simulations with the same value of A and adjacent values of Ω_0 are centered at this frequency and have a width of 75 Hz. This

process is repeated outward from the intermediate simulation and allows us to more accurately isolate the correct oscillation frequency in slowly and rapidly rotating regimes where picking out the correct spectral feature is difficult. This procedure is visualized in Figure 7.6. Note that there are only around five to ten postbounce oscillation cycles before the oscillations damp, so the peak has a finite width of about 100 Hz. However, the analysis in this section shows that the peak frequency is known far better than that.

In the top panel of Figure 7.7, I plot the GW peak frequency $f_{\rm peak}$ as a function of $T/|W|$ (of the inner core at bounce) for each of the 1704 collapsing cores. I identify three regimes of rotation and $f_{\rm peak}$ systematics in this figure:

(**Slow Rotation** Regime) In slowly rotating cores, $T/|W| \lesssim 0.06$, $f_{\rm peak}$ shows little variation with increasing rotation rate or degree of differential rotation. Note that the analysis is unreliable in the very slow rotation limit ($T/|W| \lesssim 0.02$). There, the PNS oscillations are only weakly excited and the corresponding GW signal is very weak. This is a consequence of the fact that the nonlinear hydrodynamics approach is noisy and not made for the perturbative regime.

(**Rapid Rotation** Regime) In the rapidly rotating regime, $0.06 \lesssim T/|W| \lesssim 0.17$, $f_{\rm peak}$ increases with increasing rotation rate and initially more differentially rotating cores have systematically higher $f_{\rm peak}$.

(**Extreme Rotation** Regime) At $T/|W| \gtrsim 0.17$, bounce and the postbounce dynamics become centrifugally dominated, leading to very complex PNS oscillations involving multiple nonlinear modes with comparable amplitudes. This makes it difficult to unambiguously define $f_{\rm peak}$ in this regime and the analysis becomes unreliable. Excluding all models with $T/|W| \gtrsim 0.17$ leaves us with 1487 simulations with a reliable determination of $f_{\rm peak}$.

Figure 7.7 shows that the different EOS lead to a ~ 150 Hz variation in $f_{\rm peak}$. The peak frequency is expected to scale with the PNS dynamical frequency (e.g., J. Fuller, Klion, et al., 2015). That is,

$$f_{\rm peak} \sim \Omega_{\rm dyn} = \sqrt{G\rho_c}\ , \tag{7.10}$$

where G is the gravitational constant and ρ_c is the central density. In the bottom panel of Figure 7.7, I normalize the observed peak frequency by the dynamical frequency, using the central density averaged over 6 ms after the end of the bounce signal (the same time interval from which I extract $f_{\rm peak}$). The scatter between different EOS

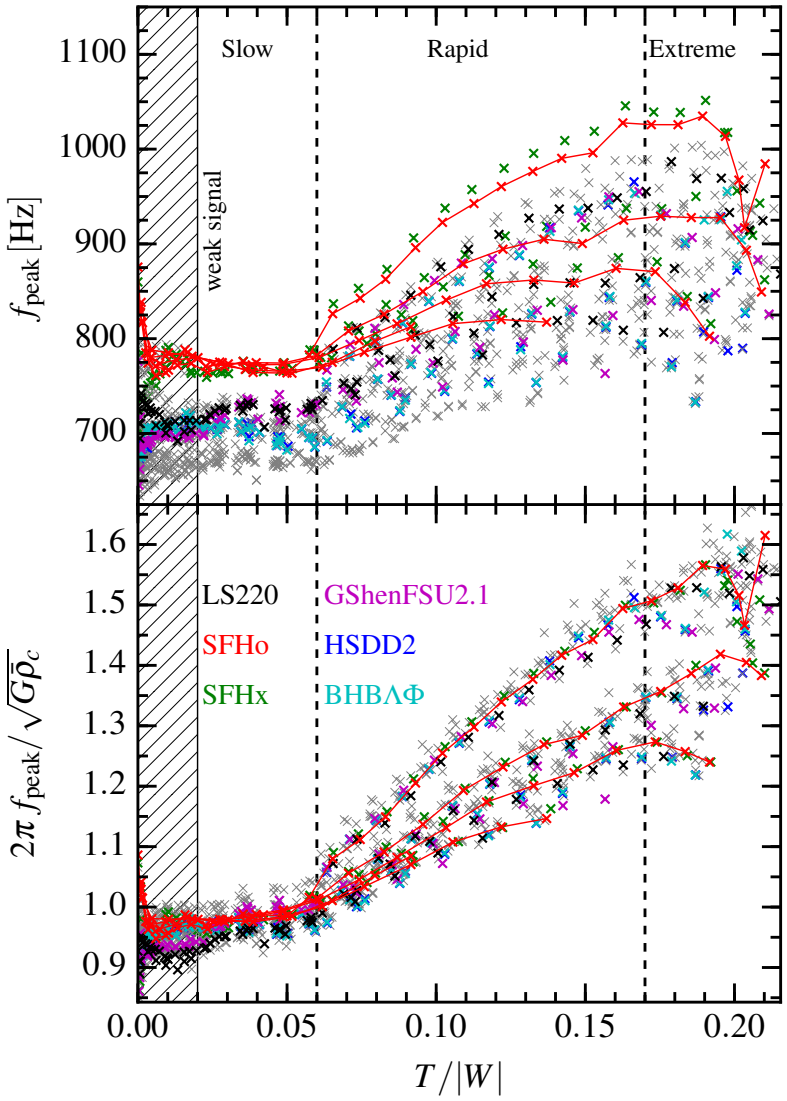

Figure 7.7: **Peak frequencies.** *Top:* The peak frequencies of GWs emitted by postbounce PNS oscillations in all 1704 collapsing simulations are plotted as a function of the ratio of rotational to gravitational energy $T/|W|$ of the inner core at bounce. Red lines connect SFHo simulations with the same differential rotation parameter A. There is a large spread in the peak frequencies due to both the EOS and due to differential rotation. *Bottom:* Most of the effects of the different EOS are removed by normalizing the peak frequency by the dynamical frequency $\sqrt{G\bar{\rho}_c}$ and multiply by 2π to make it an angular frequency. However, significant differences due to differing amounts of differential rotation remain for rapidly spinning models. The transition from slow to rapid rotation regimes occurs at $T/|W| \approx 0.06$ and it becomes difficult for the analysis scripts to find the $\ell = 2$ f-mode peak at $T/|W| \gtrsim 0.17$. Each panel contains 1704 data points, and there are 1487 good points with $T/|W| < 0.17$.

EOS	$\langle f_{\rm peak}\rangle$ [Hz]	$\sigma_{f_{\rm peak}}$ [Hz]	$\langle f_{\rm dyn}\rangle$ [Hz]	$\langle\bar{\rho}_c\rangle$ [$10^{14}\,{\rm g\,cm^{-3}}$]	$\langle M_{\rm IC,b}\rangle$ [$M_\odot$]
SFHo_ecap0.1	871	7.9	795	3.74	0.656
SFHo_ecap1.0	846	9.4	778	3.58	0.573
SFHo_ecap10.0	790	10.5	760	3.42	0.532
SFHo	772	5.6	784	3.64	0.650
SFHx	769	7.3	785	3.64	0.648
LS180	727	7.4	767	3.48	0.611
HSIUF	725	8.6	747	3.30	0.656
LS220	724	6.2	756	3.38	0.616
GShenFSU2.1	723	10.9	734	3.19	0.664
GShenFSU1.7	722	10.6	735	3.20	0.665
LS375	709	8.0	729	3.15	0.626
HSTMA	704	5.6	702	2.91	0.661
HSFSG	702	7.6	731	3.16	0.662
HSDD2	701	8.2	723	3.09	0.660
BHBΛ	700	8.3	723	3.09	0.660
BHB$\Lambda\Phi$	700	8.4	722	3.09	0.659
GShenNL3	699	11.9	691	2.83	0.671
HSTM1	675	5.1	688	2.80	0.659
HShenH	670	6.8	694	2.85	0.678
HShen	670	6.4	694	2.85	0.678
HSNL3	669	3.8	681	2.75	0.660

Table 7.8: **GW Peak Frequencies of PNS Oscillations in the Slow Rotation Regime**. $\langle f_{\rm peak}\rangle$ is the peak frequency for each EOS averaged over all simulations with $0.02 \leq T/|W| \leq 0.06$. $\sigma_{f_{\rm peak}}$ is its standard deviation and provides a handle on how much $f_{\rm peak}$ varies in the Slow Rotation regime. I also provide the average dynamical frequency $\langle f_{\rm dyn}\rangle = \langle\sqrt{G\bar{\rho}_c}/2\pi\rangle$, the averaged central density $\langle\bar{\rho}_c\rangle$, and the averaged gravitational mass of the inner core at bounce $\langle M_{\rm IC,b}\rangle$, all averaged over simulations with $0.02 \leq T/|W| \leq 0.06$. The SFHo_ecap{0.1,1.0,10.0} rows use detailed electron capture rates in the GR1D simulations for the $Y_e(\rho)$ profile (see Section 7.8). Note that despite some outliers there is an overall EOS-dependent trend that softer EOS (producing higher $\bar{\rho}_c$) have higher $f_{\rm peak}$. Also note that $f_{\rm peak}$ is for all EOS quite close to the dynamical frequency of the PNS, $f_{\rm dyn}$.

is drastically reduced, and thus the effect of the EOS on the peak frequency is essentially parameterized by the PNS central density, which is a reflection of the compactness of the PNS core.

In the Slow Rotation regime, the parameterization of $f_{\rm peak}$ with $\sqrt{G\bar{\rho}_c}$ works particularly well, because centrifugal effects are mild and there is no dependence on the precollapse degree of differential rotation. In Table 7.8, I list $f_{\rm peak}$ and $\bar{\rho}_c$

averaged over simulations with $0.02 \leq T/|W| \leq 0.06$ and broken down by EOS. I also provide the standard deviation for $f_{\rm peak}$, average dynamical frequency, average time-averaged central density, and the average inner core mass at bounce for each EOS. These quantitative results further corroborate that $f_{\rm peak}$ and $\bar{\rho}_c$ are closely linked. As expected from the analysis of the bounce signal in Section 7.4, hyperons have no effect: HShen and HShenH yield the same $f_{\rm peak}$ and $\bar{\rho}_c$ and so do HSDD2, BHBΛ, and BHB$\Lambda\Phi$.

The results summarized by Table 7.8 also suggest that the subnuclear, nonuniform nuclear matter part of the EOS may play an important role in determining $f_{\rm peak}$ and PNS structure. This can be seen by comparing the results for EOS with the same high-density uniform matter EOS but different treatment of nonuniform nuclear matter. For example, GShenNL3 and HSNL3 both employ the RMF NL3 model for uniform matter, but differ in their descriptions of nonuniform matter (cf. Section 2.4). They yield $f_{\rm peak}$ that differ by $\sim$30 Hz. Similarly, GShenFSU1.7 (and GShenFSU2.1) produce $\sim$15 Hz higher peak frequencies than HSFSG. Interestingly, the difference between HShen and HSTM1 (both using RMF TM1) in $f_{\rm peak}$ is much smaller even though they have substantially different averaged $\bar{\rho}_c$ and $M_{\rm IC,b}$.

Figure 7.7 shows that $f_{\rm peak}$ is roughly constant in the Slow Rotation regime, but increases with faster rotation in the Rapid Rotation regime. Centrifugal support, leads to a monotonic decrease of the PNS density with increasing rotation (cf. Figure 7.4). Thus, naively and based on Equation (7.10), we would expect a decrease $f_{\rm peak}$ with increasing rotation rate. I observe the opposite and this warrants further investigation.

Figure 7.7 also shows that in the Rapid Rotation regime the precollapse degree of differential rotation determines how quickly the peak frequency increases with $T/|W|$, suggesting that $T/|W|$ may not be the best measure of rotation for the purposes of understanding the behavior of $f_{\rm peak}$. Instead, in Figure 7.8, I plot the normalized peak frequency as a function of a different measure of rotation, $\Omega_{\rm max}$ (normalized by $\sqrt{G\bar{\rho}_c}$), the highest equatorial angular rotation rate achieved at any time outside of a radius of 5 km. I impose this limit to prevent errors from dividing by small radii in $\Omega = v_\phi/r$. This is a convenient way to measure the rotation rate of the configuration without needing to refer to a specific location or time. This produces an interesting result (Figure 7.8): *all the simulations for which I am able to reliably calculate the peak frequency follow the same relationship* in which the normalized peak frequency is essentially independent of rotation at lower rotation

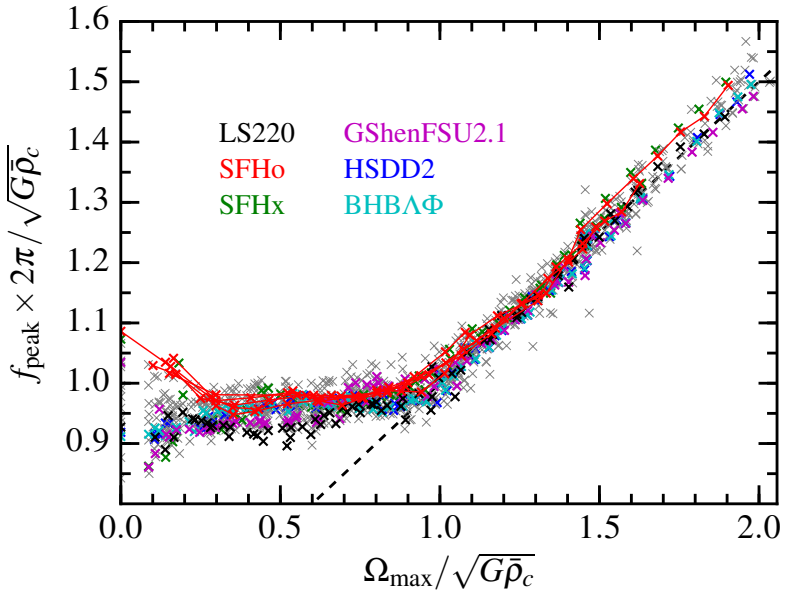

Figure 7.8: **Universal relation:** All differential rotation parameters and EOS result in simulations that obey the same relationship between the normalized peak frequency and the normalized maximum rotation rate $\Omega_{\rm max}$. The kink in the plot where $\Omega_{\rm max} = \sqrt{G\bar{\rho}_c}$ corresponds to $T/|W| \approx 0.06$. The dashed line is described by $2\pi f_{\rm peak}/\sqrt{G\bar{\rho}_c} = 0.5(1 + \Omega_{\rm max}/\sqrt{G\bar{\rho}_c})$. This figure includes all 1487 simulations with $T/|W| < 0.17$.

rates (Slow Rotation), followed by a linear increase with rotation rate at higher rotation rates (Rapid Rotation). Note that the transition between these regimes and the two parts of Figure 7.8 occurs just when $\Omega_{\rm max} \approx \sqrt{G\bar{\rho}_c}$.

We can gain more insight into the relationship of $f_{\rm peak}$ and $\Omega_{\rm max}$ by considering Figure 7.9, in which I plot both $f_{\rm peak}$ (top panel) and $\Omega_{\rm max}$ (bottom panel) against the dynamical frequency $\sqrt{G\bar{\rho}_c}$. Since rotation decreases $\bar{\rho}_c$, rotation rate *increases from right to left* in the figure.

First, consider $f_{\rm peak}$ in the top panel of Figure 7.9. At high $\bar{\rho}_c$ (Slow Rotation regime), all $f_{\rm peak}$ cluster with EOS below the line $2\pi f_{\rm peak} = \sqrt{G\bar{\rho}_c}$ with small differences between rotation rates, just as we saw in Figures 7.7 and 7.8. However, as the rotation rate increases (and $\bar{\rho}_c$ decreases), $f_{\rm peak}$ rapidly increases and exhibits the spreading with differential rotation already observed in Figure 7.7. Notably, this occurs in the region where the peak PNS oscillation frequency exceeds its dynamical frequency, $2\pi f_{\rm peak} > \sqrt{G\bar{\rho}_c}$.

Now turn to the $\Omega_{\rm max} - \sqrt{G\bar{\rho}_c}$ relationship plotted in the bottom panel of Figure 7.9.

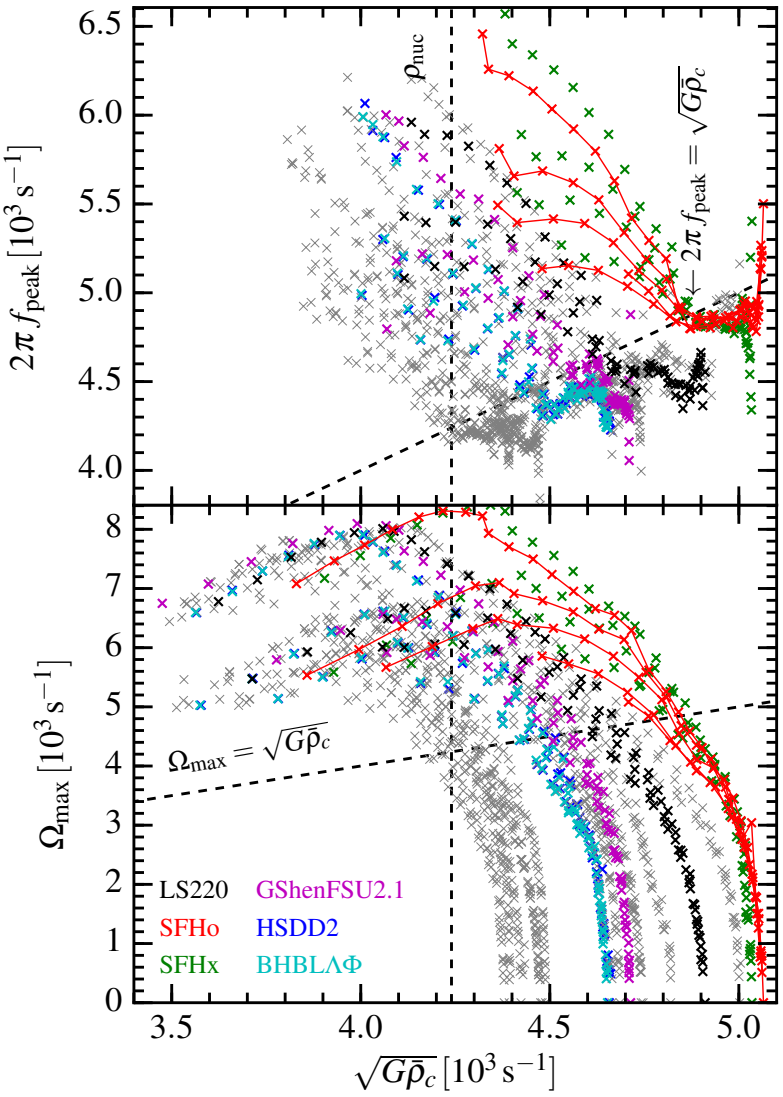

Figure 7.9: **Demystifying the universal relation.** To better understand the relation in Figure 7.8, I plot the peak frequency $f_{\rm peak}$ and the maximum rotation rate $\Omega_{\rm max}$ separately, each as a function of the dynamical frequency. The dramatic kink in Figure 7.8 is due to a sharp change in the behavior of $f_{\rm peak}$ once $2\pi f_{\rm peak} > \sqrt{G\bar{\rho}_c}$. An approximate nuclear saturation density of $\rho_{\rm nuc} = 2.7 \times 10^{14}\,{\rm g\,cm^{-3}}$ is plotted as well for reference. The top panel contains the 1487 simulations with $T/|W| < 0.17$, while the bottom panel contains all 1704 collapsing simulations to show the decrease in $\Omega_{\rm max}$ at extreme rotation rates.

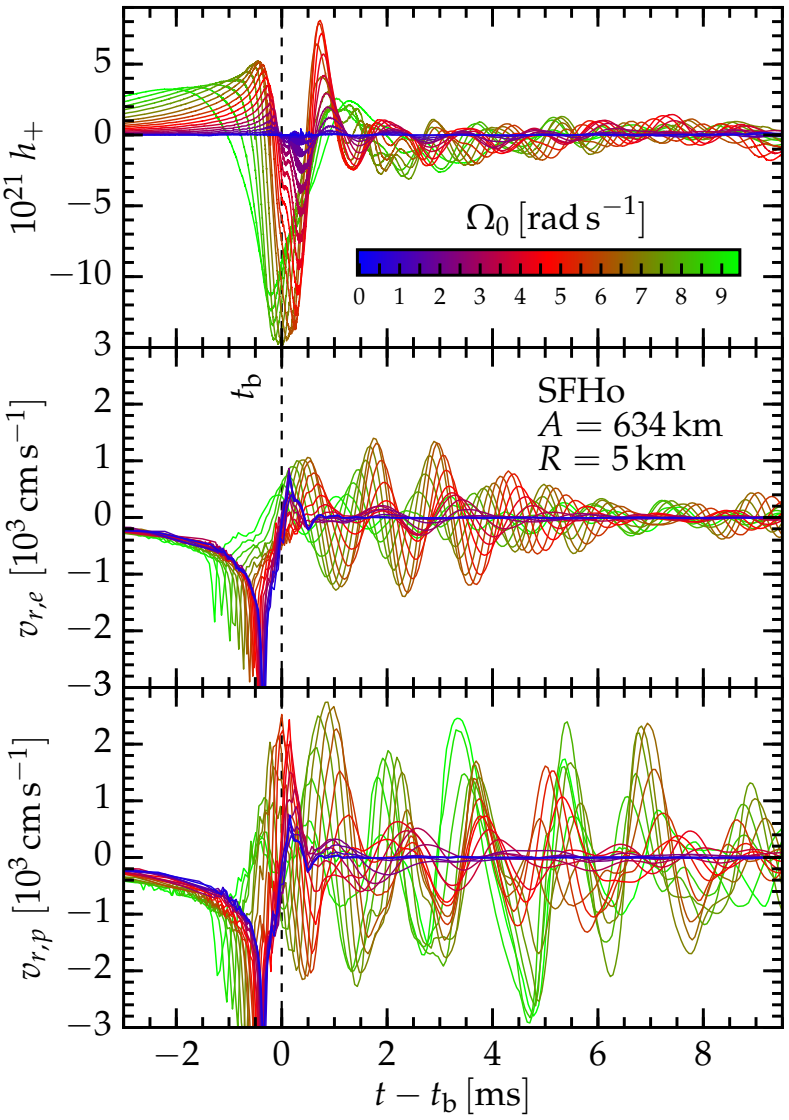

Figure 7.10: **Rotation changes oscillation mode character**. In the top panel, I plot the GW signals for 20 cores collapsed with $A3 = 634\,\mathrm{km}$ and the SFHo EOS, color-coded according to their initial central rotation rate. The center and bottom panel show the radial velocity at 5 km from the origin along the equatorial and polar axis, respectively. I indicate core bounce with a vertical dashed line. In the Rapid Rotation regime (starting at around the transition from red to green color), postbounce GW frequency and velocity oscillation frequency increase visibly. In the same regime, the oscillation mode structure changes. The polar velocities continue to increase, while the oscillations are damped along the equator.

At the lowest rotation rates, this plot simply captures how $\bar{\rho}_c$ varies between EOS. For slowly rotating cores, Ω_{max} is substantially smaller than the dynamical frequency $\sqrt{G\bar{\rho}_c}$, and Ω_{max} points cluster in a line for each EOS. As Ω_{max} surpasses $\sqrt{G\bar{\rho}_c}$, this smoothly transitions to the Rapid Rotation regime, in which $\bar{\rho}_c$ is significantly driven down with increasing rotation rate. At the highest rotation rates (Extreme Rotation regime), Ω_{max} exceeds $\sqrt{G\bar{\rho}_c}$ by a few times and centrifugal effects dominate in the final phase of core collapse, preventing further collapse and spin-up. Faster initial rotation (lower $\bar{\rho}_c$) results in lower Ω_{max} in this regime, consistent with previous work E. Abdikamalov, S. Gossan, et al., 2014.

The bottom panel of Figure 7.9 also allows us to understand the effect of precollapse differential rotation. Stronger differential rotation naturally reduces centrifugal support. Thus it allows a collapsing core to reach higher Ω_{max} before centrifugal forces prevent further spin-up. This causes the spreading branches for the different A values in these models.

Armed with the above observations on differential rotation and the $2\pi f_{peak} - \sqrt{G\bar{\rho}_c}$ and $\Omega_{max} - \sqrt{G\bar{\rho}_c}$ relationships, we now return to Figure 7.8. It depicts a sharp transition in the behavior of f_{peak} at $\Omega_{max} = \sqrt{G\bar{\rho}_c}$. A sharp transition is present in the $2\pi f_{peak} - \sqrt{G\bar{\rho}_c}$ relationship, but not in the $\Omega_{max} - \sqrt{G\bar{\rho}_c}$ relationship shown in Figure 7.9. The variable connected to PNS structure, $\bar{\rho}_c$, instead varies smoothly and slowly with rotation through the $\Omega_{max} = \sqrt{G\bar{\rho}_c}$ line. This is a strong indication that the sharp upturn of f_{peak} at $\Omega_{max} = \sqrt{G\bar{\rho}_c}$ in Figure 7.8 is due to *a change in the dominant PNS oscillation mode rather than due to an abrupt change in PNS structure*. The observation that centrifugal effects do not become dominant until Ω_{max} is several times $\sqrt{G\bar{\rho}_c}$ corroborates this interpretation.

In Figure 7.10, I plot the GW signals along with the equatorial and polar radial velocities 5 km from the origin for all 20 simulations using the SFHo EOS with a differential rotation parameter $A3 = 634$ km. The postbounce GW frequency clearly follows the frequency of the fluid oscillations. Both frequencies begin to significantly increase at around $\Omega_0 \approx 5\,\mathrm{rad\,s^{-1}}$ (corresponding to $T/|W| \approx 0.06$, red-colored graphs). The polar and equatorial velocity oscillation amplitudes initially increase with rotation rate (colors going from blue to red), but when rotation becomes rapid (colors going from red to green) the equatorial velocities decrease and polar velocities continue to grow. This demonstrates that *the multi-dimensional PNS mode structure is altered at rapid rotation and no longer follows a simple $\ell = 2, m = 0$ description*. This is also apparent from comparing the left and right panels of

Figure 7.4.

While the above results show that the increase in $f_{\rm peak}$ is most likely a consequence of changes in the mode structure with rotation, it is not obvious what detailed process is driving the changes. While future work will be needed to answer this conclusively, I can use the work of Dimmelmeier *et al.* Dimmelmeier, Stergioulas, and Font, 2006 as the basis of educated speculation. They study oscillations of rotating equilibrium polytropes and show that the $\ell = 2, m = 0$ f-mode frequency has a weak dependence on both rotation rate and differential rotation. This is consistent with my findings for models in the Slow Rotation regime ($T/|W| \lesssim 0.06$). They also identify several inertial modes whose restoring force is the Coriolis force (e.g., Stergioulas, 2003). The inertial mode frequency increases rapidly with rotation and is sensitive to differential rotation, which is what we see for the PNS oscillations in the Rapid Rotation regime ($T/|W| \gtrsim 0.06$). The PNS cores in this study are also significantly less dense than the equilibrium models of Dimmelmeier, Stergioulas, and Font, 2006, which allows the $\ell = 2$ modes in these simulations to have lower oscillation frequencies that intersect with the frequencies of the inertial modes in Dimmelmeier, Stergioulas, and Font, 2006. It could thus be that in the PNS cores inertial and $\ell = 2$ f-mode eigenfunctions overlap and couple nonlinearly, leading to an excitation of predominantly inertial oscillations as rotation becomes more rapid. The increase of the inertial mode frequency with rotation would explain the trends we see in $f_{\rm peak}$ in Figure 7.7.

Coriolis forces should become dynamically important for oscillations when the oscillation frequency is locally smaller than the Coriolis frequency, given by $2\pi f_{\rm core} = 2\Omega \sin\theta$ (e.g., Saio, 2013), where θ is the latitude from the equator and, for simplicity, Ω is a uniform rotation rate. Thus, we expect Coriolis effects to become locally relevant when $\Omega \gtrsim 2\pi f_{\rm peak}/(2\sin\theta) \approx \sqrt{G\bar{\rho}_c}/(2\sin\theta)$. The kink in Figure 7.8 is at $\Omega_{\rm max} = \sqrt{G\bar{\rho}_c}$, and hence the behavior of the PNS oscillations changes precisely when we expect Coriolis effects to begin to matter. This is supports the notion that the PNS oscillations may be transitioning to inertial nature at high rotation rates.

Conclusions: The effects of the EOS on the postbounce GW frequency can be parameterized almost entirely in terms of the dynamical frequency $\sqrt{G\rho_c}$ of the core after bounce. In the Slow Rotation regime ($T/|W| \lesssim 0.06$), the postbounce frequency depends little on rotation rate. In the Rapid Rotation regime ($0.06 \lesssim T/|W| \lesssim 0.17$), inertial effects modify the nature of the oscillations, causing the frequency to increase with rotation rate. I find that the maximum rotation rate

outside of 5 km is the most useful parameterization of rotation for the purpose of understanding the oscillation frequencies. In the Extreme Rotation regime ($T/|W| \gtrsim 0.17$), the postbounce GW frequency decreases with rotation because centrifugal support keeps the core very extended.

7.6 GW Correlations with Parameters and EOS

We are interested in how characteristics of the GWs vary with rotation, properties of the EOS, and the resulting conditions during core collapse and after bounce. Rather than plot every variable against each other variable, I employ a simple linear correlation analysis. I calculate a linear correlation coefficient C between two quantities U and V that quantifies the strength of the linear relationship between two variables:

$$C_{U,V} = \frac{\sum(\frac{U-\overline{U}}{s_U})(\frac{V-\overline{V}}{s_V})}{(N-1)} \ . \tag{7.11}$$

The summation is over all N simulations included in the analysis. The sample standard deviation of a quantity U is

$$s_U = \sqrt{\frac{1}{N-1}\sum(U-\overline{U})^2} \ , \tag{7.12}$$

where $\overline{U} = \sum U/N$ is the average value of U over all N simulations. The correlation coefficient is always bound between -1 (strong negative correlation) and 1 (strong positive correlation). This only accounts for linear correlations, so even if two variables are tightly coupled, nonlinear relationships will reduce the magnitude of the correlation coefficient and a more involved analysis would be necessary for characterizing nonlinear relationships (see, e.g., Engels, Frey, and Ott, 2014).

I display the correlation coefficients of several relevant quantities in Figure 7.11. L, J, K, $R_{1.4}$, and $M_{\rm max}$ are all innate properties of a given EOS (Section 2.4). A and Ω_0 are the input parameters that determine the rotation profile as defined in Equation 7.4. The rest of the quantities are outputs from the simulations. Quantities defined at the time of core bounce are the inner core mass $M_{\rm IC,b}$, the central electron fraction $Y_{e,\rm c,b}$, the inner core angular momentum $j_{\rm IC,b}$, and the ratio of the inner core rotational energy to gravitational energy $T/|W|$. Rotation is also parameterized by the maximum rotation rate $\Omega_{\rm max}$ and by $\widetilde{\Omega}_{\rm max} = \Omega_{\rm max}/\sqrt{G\bar{\rho}_c}$ (see Section 7.5 for definitions). GW characteristics are quantified in the amplitude of the bounce signal Δh_+, the peak frequency of the postbounce signal $f_{\rm peak}$, and its variant normalized by the dynamical frequency $\widetilde{f}_{\rm peak} = f_{\rm peak}/\sqrt{G\bar{\rho}_c}$. The bottom left half of the plot shows the values of the correlation coefficients for 874 simulations in

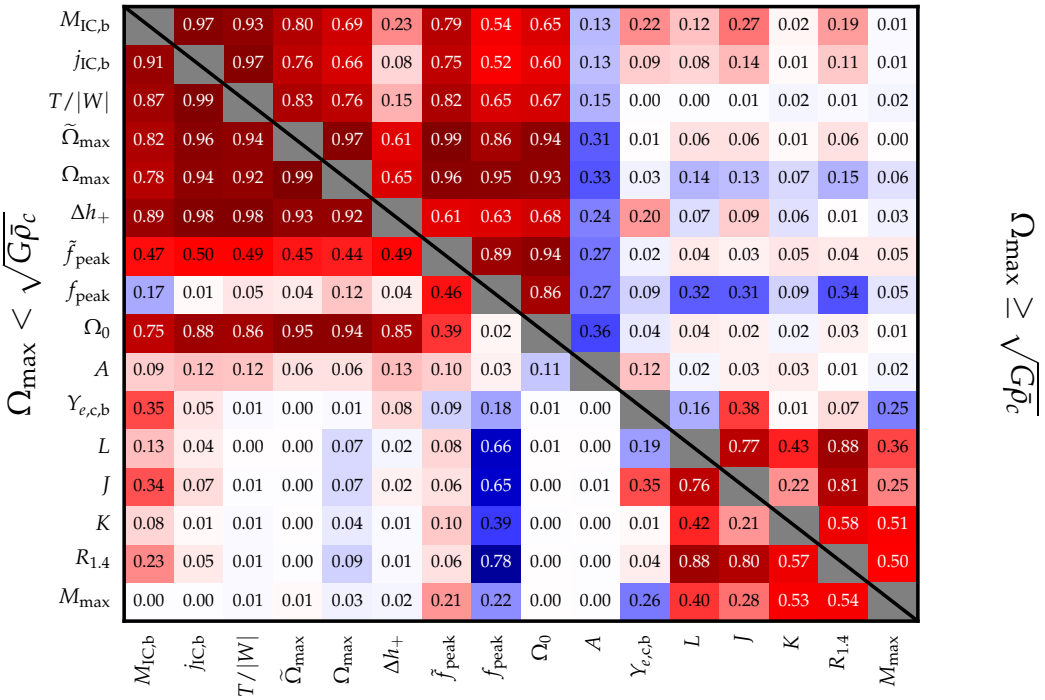

Figure 7.11: **Correlation Coefficients.** I calculate linear correlation coefficients between several parameters and observables in the collapsing simulations. The cell color represents the number within the cell, with positive correlations being red and negative correlations blue. *Bottom Left*: Correlation coefficients for 874 simulations with $\Omega_{\rm max} < \sqrt{G\bar{\rho}_c}$ (i.e. slowly rotating). *Top Right:* Correlation coefficients for 613 simulations with $\Omega_{\rm max} > \sqrt{G\bar{\rho}_c}$ (i.e. rapidly rotating) and $T/|W| < 0.17$. $M_{\rm IC,b}$ is the mass of the inner core, defined by the region in sonic contact with the center, at core bounce. $j_{\rm IC}$ is the angular momentum of the inner core at bounce. $T/|W|$ is the inner core's ratio of rotational kinetic to gravitational potential energy at core bounce. $\Omega_{\rm max}$ is the maximum rotation rate obtained at any time in the simulation outside of $R = 5\,$km and $\widetilde{\Omega}_{\rm max} = \Omega_{\rm max}/\sqrt{G\bar{\rho}_c}$. $f_{\rm peak}$ is the peak frequency of GWs from postbounce PNS oscillations, and $\widetilde{f}_{\rm peak} = f_{\rm peak}/\sqrt{G\bar{\rho}_c}$. Ω_0 is the precollapse maximum rotation rate and A is the precollapse differential rotation parameter. $Y_{e,c}$ is the central electron fraction at core bounce. The incompressibility K, symmetry energy J, density derivative of the symmetry energy L, radius of a $1.4\,M_\odot$ star $R_{1.4}$, and $M_{\rm max}$ are properties of the EOS described in Section 2.4.

the Slow Rotation regime ($\Omega_{\rm max} < \sqrt{G\bar{\rho}_c}$, $T/|W| \lesssim 0.06$) and the top right half shows correlations for 613 simulations in the Rapid Rotation regime ($\Omega_{\rm max} \geq \sqrt{G\bar{\rho}_c}$, $0.06 \lesssim T/|W| \leq 0.17$).

There is a region in the bottom right corner of Figure 7.11 that shows the correlations between EOS parameters L, J, K, $R_{1.4}$, and $M_{\rm max}$. Since I chose to use existing EOS rather than create a uniform parameter space, there are correlations between the input values of L, J, and K that impose some selection bias on the other correlations. In the set of 18 EOS, there is a strong correlation between $R_{1.4}$ and both L and J. The maximum neutron star mass correlates most strongly with K and L. These findings are not new and just reflect current knowledge of how the nuclear EOS affects neutron star structure (e.g., J. M. Lattimer and Prakash, 2001; J. M. Lattimer, 2012; Oertel et al., 2017). The small amount of asymmetry in this corner is the effect of selection bias, as some EOS contribute more data points to one or the other rotation regime.

Next, note that the central Y_e at bounce ($Y_{\rm e,c,b}$) exhibits correlations with EOS characteristics J, L, and $M_{\rm max}$. This encodes the EOS dependence in the high-density part of the $Y_e(\rho)$ trajectories shown in Figure 7.1. The mass of a nonrotating inner core at bounce is sensitive to $Y^2_{\rm e,c,b}$ (though note that it is also sensitive to Y_e at lower densities and to EOS properties). The linear analysis in Figure 7.11 picks this up as a clear correlation between $Y_{\rm e,c,b}$ and $M_{\rm IC,b}$. This correlation is stronger in the slow to moderately rapidly rotating models (bottom left half of the figure) and weaker in the rapidly rotating models (top right half of the figure) since in these models rotation strongly increases $M_{\rm IC,b}$. This can also be seen in the strong correlations of $M_{\rm IC,b}$ with all of the rotation variables.

As discussed in Section 7.4 and pointed out in previous work (e.g., E. Abdikamalov, S. Gossan, et al., 2014), the GW signal from bounce, quantified by Δh_+, is very sensitive to mass $M_{\rm IC,b}$ and $T/|W|$ of inner core at bounce. The correlation analysis confirms this and shows that the Δh_+ is also correlated equally strongly with $j_{\rm IC,b}$ and $\Omega_{\rm max}$ as with $T/|W|$. As expected from Figure 7.5, correlation with the differential rotation parameter A is weak in the slow to moderately rapid rotation regime, but there is a substantial anti-correlation with the value of A in the rapidly rotating regime (the smaller A, the more differentially spinning a core is at the onset of collapse).

Figure 7.11 also shows that the most interesting correlations of any observable from an EOS perspective are exhibited by the peak postbounce GW frequency $f_{\rm peak}$. In the

slow to moderately rapidly rotating regime ($\Omega_{\rm max} \lesssim \sqrt{G\bar{\rho}_c}$), $f_{\rm peak}$ has its strongest correlations with EOS characteristics K, J, L, $R_{1.4}$ through their influence on the PNS central density and is essentially independent of the rotation rate (cf. Figures 7.7 and 7.8). For rapidly rotating models ($\Omega_{\rm max} \gtrsim \sqrt{G\bar{\rho}_c}$) there is instead a clear correlation of $f_{\rm peak}$ with all rotation quantities. Note that the correlations with EOS quantities are all but removed for the normalized peak frequency $\widetilde{f}_{\rm peak} = f_{\rm peak}/\sqrt{G\bar{\rho}_c}$. This supports my claim in Section 7.5 that the influence of the EOS on the peak frequency is parameterized essentially by the postbounce dynamical frequency $\sqrt{G\bar{\rho}_c}$.

Conclusions: Linear correlation coefficients show the interdependence of rotation parameters, EOS parameters, and simulation results. I use these to support my claims that the EOS dependence is parameterized by the dynamical frequency and that rotation is dynamically important for oscillations in the Rapid Rotation regime.

7.7 Prospects of Detection and Constraining the EOS

The signal to noise ratio (SNR) is a measure of the strength of a signal observed by a detector with a given level of noise. I calculate SNRs using the Advanced LIGO noise curve at design sensitivity in the high-power zero-detuning configuration LIGO Scientific Collaboration et al., 2015; Shoemaker, 2010. I assume optimistic conditions where the rotation axis is perpendicular to the line of sight and the LIGO interferometer arms are optimally oriented and 10 kpc from the core collapse event. Following Flanagan and Hughes, 1998; E. Abdikamalov, S. Gossan, et al., 2014, the matched-filtering SNR ρ of an observed GW signal $h(t)$ is defined as

$$\rho = \frac{\langle d, x\rangle}{\langle x, x\rangle^{1/2}} \ , \tag{7.13}$$

where d is observed data and x is a template waveform. When I calculate an SNR for the simulated signals, I take $d = x$ to mimic the GWs from the source matching a template exactly, and this simplifies to $\rho^2 = \langle x, x\rangle$. The inner product integrals are calculated using

$$\langle a, b\rangle = \int_0^\infty \frac{4\widetilde{h}_a^* \widetilde{h}_b}{S_n} df \ , \tag{7.14}$$

where S_n is the one-sided noise spectral density. Fourier transforms are taken according to LIGO convention S. Anderson et al., 2004, namely

$$\widetilde{h}(f) = \int_{-\infty}^{\infty} h(t) e^{-2\pi i f t} dt \ . \tag{7.15}$$

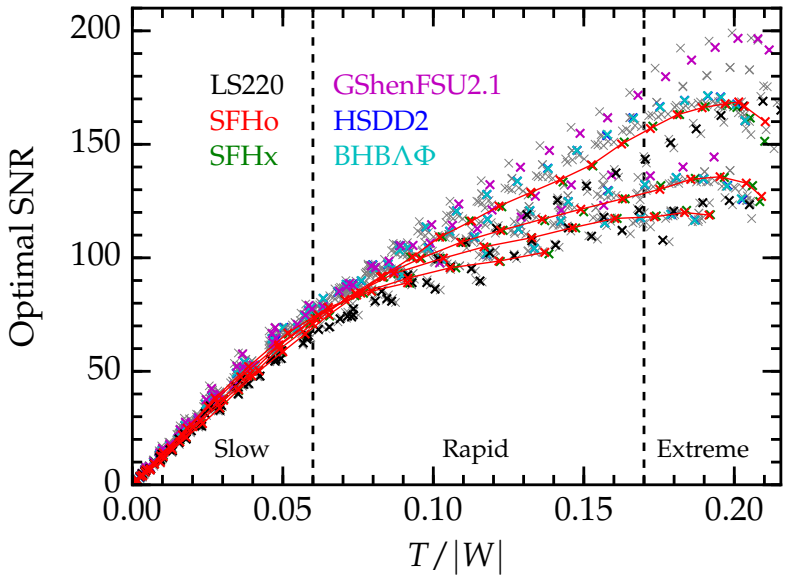

Figure 7.12: **Signal to noise ratios.** The SNR for all 1704 collapsing simulations that result in collapse and core bounce, assuming the rotation axis is perpendicular to the line of sight, the aLIGO interferometer is optimally oriented and at design sensitivity in the high power zero detuning configuration, and the source is 10 kpc away. A SNR of $\gtrsim 10$ is considered detectable. The colors correspond to the EOS in Figure 2.1. A line is drawn through all the SFHo simulations to guide the eye. Each of the five branches corresponds to a different value of the differential rotation parameter A, where $A = 300$ km is the longest branch and $A = 10000$ km is the shortest.

Furthermore, I estimate the difference between two waveforms as seen by Advanced LIGO with the mismatch $\mathcal{M}$ described and implemented in Reisswig & Pollney Reisswig and Pollney, 2011:

$$\mathcal{M} = 1 - \max_{t_A} \left[\frac{\langle x_1, x_2 \rangle}{\sqrt{\langle x_1, x_1 \rangle \langle x_2, x_2 \rangle}} \right] , \tag{7.16}$$

where the latter term is the match between the two waveforms and is maximized over the relative arrival times of the two waveforms t_A. Note that due to the axisymmetric nature of the simulations, the waveforms only have the + polarization, making a maximization over complex phase unnecessary.

The simulated waveforms span a finite time and is sampled at nonuniform intervals. To mimic real LIGO data, I resample the GW time series data at the LIGO sampling frequency of 16384 Hz before performing the discrete Fourier transform.

In Figure 7.12, I show the SNR for the 1704 collapsing cores assuming a distance of 10 kpc to Earth. Faster rotation (higher $T/|W|$ of the inner core at bounce) leads

to stronger quadrupolar deformations, in turn causing stronger signals that are more easily observed, but only up to a point. If rotation is too fast, centrifugal support keeps the core more extended with lower average densities, resulting in a less violent quadrupole oscillation and weaker GWs. This happens at lower rotation rates for the rotation profiles that are more uniformly rotating (e.g., the $A5 = 10000\,\mathrm{km}$ series), since the large amount of angular momentum and rotational kinetic energy created by even a small rotation rate can be enough to provide significant centrifugal support. The more strongly differentially rotating cases (e.g., the $A1 = 300\,\mathrm{km}$ series) require much faster rotation before centrifugal support becomes important at bounce. This also means that they can reach greater inner core deformations and generate stronger GWs.

All of the EOS result in similar SNRs for a given rotation profile. We observe a larger spread with EOS in estimated SNR for the rapid, strongly differentially rotating cases. The bounce part is the strongest part of the GW signal and dominates the SNR. Hence, the EOS-dependent differences in the bounce signal pointed out in Section 7.4 are most relevant for understanding the EOS systematics seen in Figure 7.12. For example, the LS220 EOS yields the smallest inner core masses at bounce and correspondingly the smallest Δh_+. This translates to the systematically lower SNRs for this EOS.

We can get a rough estimate for how different the waveforms are with the simple scalar mismatch (Equation 7.16), which I calculate with respect to the simulations using the SFHo EOS and the same value of A and Ω_0. Simulations using different EOS but the same initial rotation profile will result in slightly different values of $T/|W|$ at bounce, so this measures the difference between waveforms from the same initial conditions rather than from the same bounce conditions. In the context of a matched-filter search, the mismatch roughly represents the amount of SNR lost due to differences between the template and the signal. However, note that searches for core collapse signals in GW detector data have thus far relied on waveform-agnostic methods that search for excess power above the background noise (e.g., Abbott, 2016a).

Figure 7.13 shows the results of the mismatch calculations. The large mismatches at $T/|W| \lesssim 0.02$ are simply due to the small amplitudes of the GWs causing large relative errors. The mismatch results for such slowly spinning models have no predictive power and I do not analyze them further. At higher rotation rates, *the dynamics are increasingly determined by rotation and decreasingly determined by*

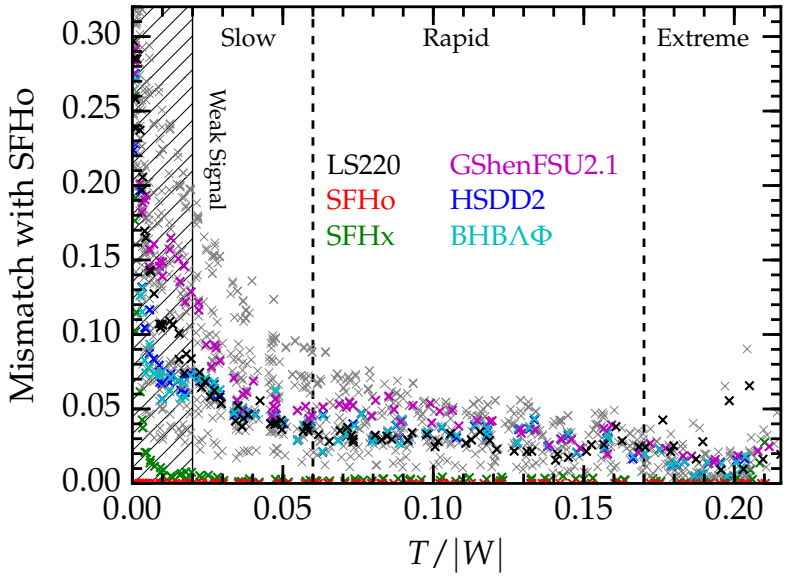

Figure 7.13: **GW differences due to the EOS.** The GW mismatch (see Equation 7.16) integrated between SFHo and each of the other EOS for the same rotation parameters (A,Ω_0) for all 1704 collapsing simulations. Note that $T/|W|$ at bounce will be slightly different between simulations with the same initial rotation parameters due to EOS effects. Only data through 6 ms after the end of the bounce signal are used to avoid contributions from prompt convection. Differences between EOS decrease with faster rotation as the bounce signal becomes stronger and rotational effects become more important. The HShen and HShenH EOS (not identified by color and shown in gray) have the consistently largest mismatches with SFHo in the Slow and Rapid Rotation regimes. Mismatch calculations at $T/|W| \lesssim 0.02$ are unreliable due to a very weak GW signal. In the extreme rotation regime, some EOS develop larger mismatches with SFHo. This occurs because simulations with these EOS transition to a centrifugal bounce at subnuclear density at lower rotation rates than SFHo. The resulting qualitative and quantitative change in the waveforms leads to larger mismatches.

the details of the EOS, and the mismatch generally decreases with increasing rotation rate.

An exception to this rule occurs in the Extreme Rotation regime ($T/|W| \gtrsim 0.17$) where waveforms show increasing mismatches with SFHo simulation results (most notably, LS220 and LS180). In this regime, the bounce dynamics changes due to centrifugal support and bounce occurs below nuclear saturation density for some EOS. Moreover, when centrifugal effects become dominant, bounce is also slowed down, widening the GW signal from bounce and reducing its amplitude. The initial rotation rate around which this occurs differs between EOS and the resulting qualitative and quantitative changes in the waveforms drive the increasing mismatches.

In Figure 7.13, the HShen EOS (included in the gray crosses) consistently shows the highest mismatch with SFHo. These two EOS use different low-density and high-density treatments (see Table 2.2 and Section 2.4). It is insightful to compare mismatches between EOS using the same (or similar) physics in either their high-density or low-density treatments of nuclear matter in order to isolate the origin of large mismatch values. In the following, I again use the example of the $A3 = 634\,\mathrm{km}, \Omega_0 = 5.0\,\mathrm{rad\,s^{-1}}$ rotation profile and compute mismatches between pairs of EOS. HShen and HSTM1 both use the RMF TM1 parameterization for high-density uniform matter, but deal with nonuniform lower-density matter in different ways (see Section 2.4). Their mismatch is $\mathcal{M} = 0.85\%$. GShenNL3 and HSNL3 use the RMF NL3 parameterization for uniform matter and also differ in their nonuniform matter treatment. They have a mismatch of $\mathcal{M} = 5.1\%$. This is comparable to the HShen-SFHo mismatch of $\mathcal{M} = 7.3\%$. I find a mismatch of $\mathcal{M} = 3.2\%$ for the GShenFSU2.1–HSFSG pair. Both use the RMF FSUGold parameterization for uniform nuclear matter and again differ in the nonuniform parts.

The above results suggest that *the treatment of low-density nonuniform nuclear matter is at least in some cases an important differentiator between EOS* in the GW signal of rotating core collapse. While perhaps somewhat unexpected, this finding may, in fact, not be too surprising: Previous work (e.g., Dimmelmeier, Ott, Marek, et al., 2008; E. Abdikamalov, S. Gossan, et al., 2014) already showed that the GW signal of rotating core collapse is sensitive to the inner core mass at bounce (and, of course, its $T/|W|$, angular momentum, or its maximum angular velocity; cf. Section 7.6). The inner core mass at bounce is sensitive to the low-density EOS through the pressure and speed of sound in the inner core material in the final phase of collapse and through chemical potentials and composition, which determine electron capture

rates and thus the Y_e in the final phase of collapse and at bounce.

We can also compare EOS with the same treatment of nonuniform lower-density matter, but different high-density treatments. I again pick the $A3 = 634\,\mathrm{km}, \Omega_0 = 5.0\,\mathrm{rad\,s^{-1}}$ ($T/|W| \sim 0.075$) model sequence as an example for quantitative differences. GShenFSU2.1 and GShenFSU1.7 ($\mathcal{M} = 0.0031\%$) differ only at supernuclear densities, where GShenFSU2.1 is extra stiff in order to support a $2\,M_\odot$ neutron star. HShenH adds hyperons to HShen ($\mathcal{M} = 0.0027\%$), BHBΛ adds hyperons to HSDD2 ($\mathcal{M} = 0.0082\%$), and BHB$\Lambda\Phi$ includes an extra hyperonic interaction over BHBΛ ($\mathcal{M} = 0.014\%$). All of the Hempel-based EOS (HS, SFH, BHB) use identical treatments of low-density nonuniform matter, but parameterize the EOS of uniform nuclear matter differently. For this example rotation profile, the mismatch with SFHo varies from 0.12% (for SFHx) to 7.6% (for GShenNL3). *The results are comparable with the mismatch induced by differences in the low-density regime.*

Conclusions: I expect a maximum SNR of around 200 from a source at a distance of 10 kpc, though this depends both on the amount of differential rotation and the EOS. Using use a simple scalar mismatch to calculate the differences between waveforms generated using different EOS, I find that both the treatment of nonuniform and uniform nuclear matter significantly affect the waveforms, though differences at densities more than about twice nuclear are of little importance.

7.8 Effects of Variations in Electron Capture Rates

Electron capture in the collapse phase is a crucial ingredient in CCSN simulations and influences the inner core mass at bounce ($M_{\mathrm{IC,b}}$) by setting the electron fraction in the final phase of collapse (e.g., Hix et al., 2003; Burrows and J. M. Lattimer, 1983). As pointed out in the literature (e.g., Mönchmeyer et al., 1991; Dimmelmeier, Ott, Marek, et al., 2008; Ott, E. Abdikamalov, et al., 2012; E. Abdikamalov, S. Gossan, et al., 2014), and in this study (cf. Section 7.4), M_{IC} at bounce and ρ_c after bounce has a decisive influence on the rotating core collapse GW signal.

In order to study how variations in electron capture rates affect the GW predictions, I carry out three additional sets of simulations using the SFHo EOS, $A3 = 634\,\mathrm{km}$, and all 20 corresponding values of Ω_0 listed in Table 7.3.

In one set of simulations, SFHo_ecap1.0, I employ a $Y_e(\rho)$ parameterization obtained from `GR1D` simulations using the approach of Sullivan *et al.* Sullivan et al., 2016 that incorporates detailed tabulated electron capture rates for individual nuclei.

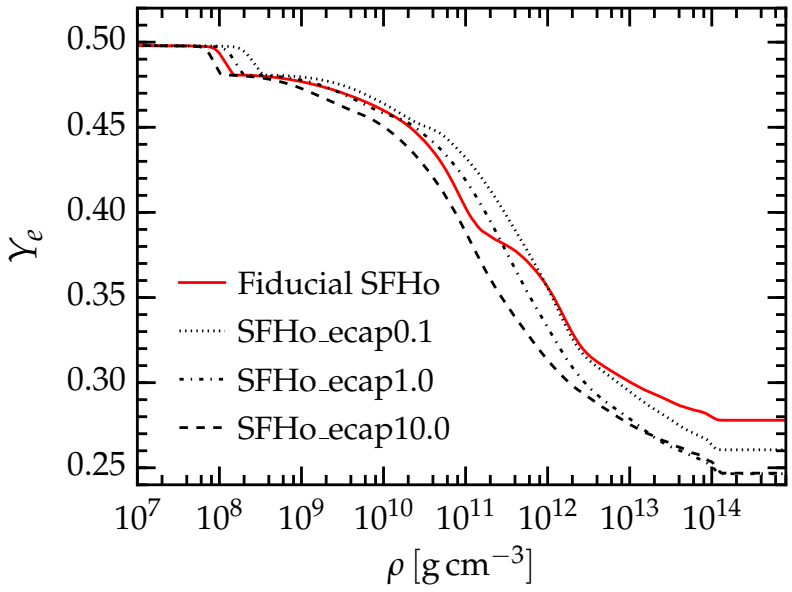

Figure 7.14: **$\mathbf{Y_e}(\rho)$ profiles from variations in electron capture treatment.** I plot the fiducial $Y_e(\rho)$ profile for the SFHo EOS along with $Y_e(\rho)$ profiles obtained with the approach of Sullivan *et al.* Sullivan et al., 2016 for the SFHo EOS using detailed tabulated nuclear electron capture rates (SFHo_ecap1.0) and also rates multiplied by 0.1 (SFHo_ecap0.1) and 10 (SFHo_ecap10.0) as a proxy for systematic uncertainties in the actual rates. Note that these $Y_e(\rho)$ profiles differ substantially from the fiducial profile, leading to different inner core masses and GW signals.

This is an improvement over the prescriptions of Bruenn, 1985; Langanke et al., 2003 that operates on an average $(\bar{A}, \bar{Z})$ nucleus. Sullivan *et al.* Sullivan et al., 2016 found that randomly varying rates for individual nuclei has little effect, but systematically scaling rates by all nuclei with a global constant can have a large effect on the resulting deleptonization during collapse. In order to capture a factor 100 in uncertainty, the other two additional sets of simulations use $Y_e(\rho)$ parameterizations, obtained by scaling the detailed electron capture rates by 0.1 (SFHo_ecap0.1) and 10 (SFHo_ecap10.0).

In Figure 7.14, I plot the three new $Y_e(\rho)$ profiles together with the fiducial SFHo $Y_e(\rho)$ profile. All of the new $Y_e(\rho)$ profiles predict substantially lower Y_e at high densities than the fiducial profiles for the SFHo EOS. However, the SFHo_ecap0.1 profile, and to a lesser extent the SFHo_ecap1.0 profile, have higher Y_e at intermediate densities of 10^{11} – 10^{12} g cm^{-3} than the fiducial profile. This is relevant for the analysis here, since in the final phase of collapse, a large part of the inner core passes this density range less than a dynamical time from core bounce. Thus, the

higher Y_e in this density range can have an influence on the inner core mass at bounce.

In the nonrotating case, the fiducial SFHo inner core mass at bounce is $M_{\rm IC,b} = 0.582\,M_\odot$ and I find $0.562\,M_\odot$, $0.506\,M_\odot$, and $0.482\,M_\odot$, for SFHo_0.1x_ecap, SFHo_1x_ecap, and SFHo_10x_ecap, respectively. Note that SFHo_1x_ecap and SFHo_10x_ecap give the same $Y_e(\rho)$ at $\rho \gtrsim 10^{13}\,{\rm g\,cm^{-3}}$, but SFHo_1x_ecap predicts higher Y_e at $\rho \sim 10^{11} - 10^{12}\,{\rm g\,cm^{-3}}$ (cf. Figure 7.14) and thus has a larger inner core mass at bounce.

In Figure 7.15, I present the key GW observables Δh_+ and $f_{\rm peak}$ resulting from the rotating core collapse simulations with the new $Y_e(\rho)$ profiles. I also plot the fiducial SFHo results for comparison. The top panel shows Δh_+. Note that the differences between the fiducial SFHo simulations and the runs with the SFHo_ecap1.0 base profile are substantial and larger than differences between many of the EOS discussed in Section 7.4 (cf. Figure 7.5). The differences with SFHo_ecap10.0 Δh_+ are even larger. The SFHo_ecap0.1 simulations produce Δh_+ that are very close to the fiducial SFHo results in the Slow Rotation regime. This is a consequence of the fact that the inner core masses of the fiducial SFHo and SFHo_ecap0.1 simulations are very similar in this regime (cf. Section 7.4). SFHo_ecap1.0 and SFHo_ecap10.0 produce smaller Δh_+, because their inner cores are less massive at bounce.

The bottom panel of Figure 7.15 shows $f_{\rm peak}$, the peak frequencies of the GWs from postbounce PNS oscillations. Again, there are large differences in $f_{\rm peak}$ between the fiducial SFHo simulations and those using $Y_e(\rho)$ obtained from detailed nuclear electron capture rates. *These differences are as large as the differences between many of the EOS* shown in Figure 7.7. In the Slow Rotation regime and into the Rapid Rotation regime, the SFHo_ecap1.0 base simulations have $f_{\rm peak}$ that are systematically $50 - 75\,{\rm Hz}$ higher than the fiducial SFHo simulations. For the SFHo_ecap0.1 the difference is $\sim$100 Hz and in the SFHo_ecap10.0 case, the difference is surprisingly only $\lesssim$25 Hz.

For the SFHo_ecap0.1 runs, I find a higher time-averaged postbounce central density $\bar{\rho}_c$ than in the fiducial case. Hence, the higher $f_{\rm peak}$ we observe fits the expectations from Section 7.5. Explaining $f_{\rm peak}$ differences for SFHo_ecap1.0 and SFHo_ecap10.0 is more challenging: I find that SFHo_ecap1.0 runs have $\bar{\rho}_c$ that are similar or slightly lower than those of the fiducial SFHo simulations, yet SFHo_ecap1.0 $f_{\rm peak}$ are systematically higher. Similarly, SFHo_ecap10.0 $\bar{\rho}_c$ are systematically lower than the fiducial $\bar{\rho}_c$, yet the predicted $f_{\rm peak}$ are about the same.

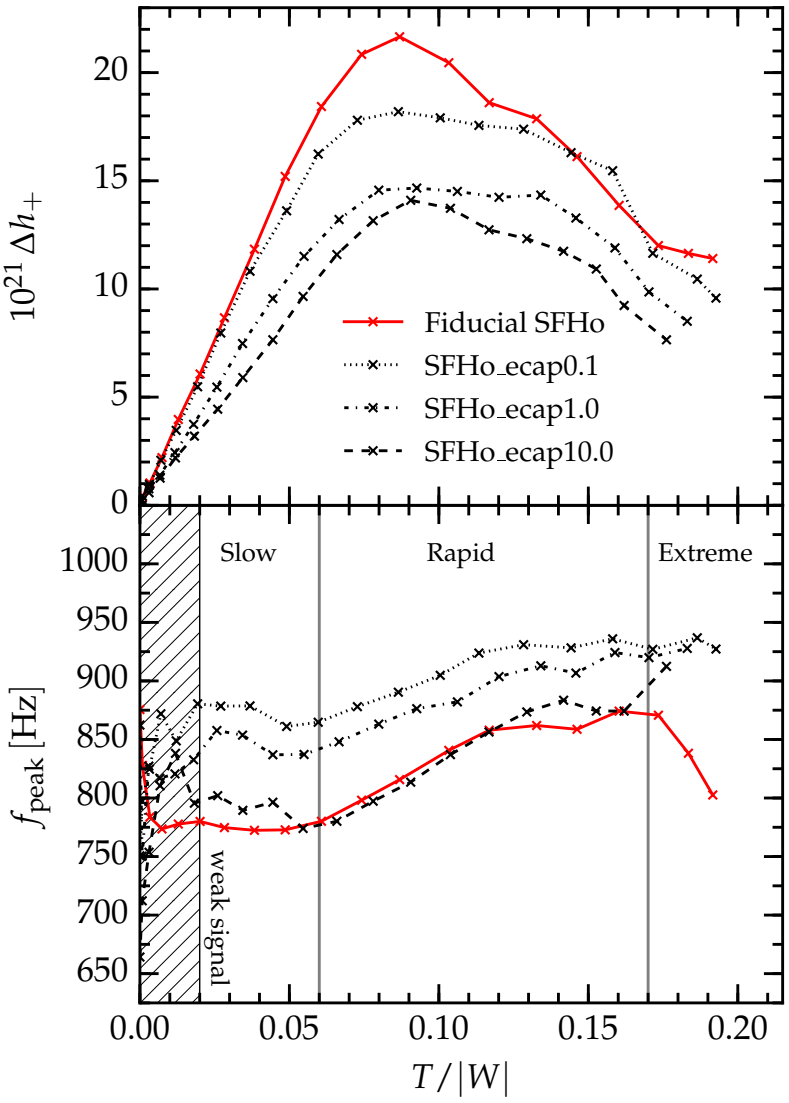

Figure 7.15: **Changes in GW observables with variations in electron capture rates.** I show results for Δh_+ (at 10 kpc, top panel) and $f_{\rm peak}$ for SFHo EOS simulations with $A3 = 634$ km with the fiducial $Y_e(\rho)$ profile and with the new $Y_e(\rho)$ profiles from simulations with detailed tabulated nuclear electron capture rates (cf. Figure 7.14). Differences in electron capture treatment and uncertainties in capture rates lead to differences in the key GW observables that are as large as those induced by switching EOS.

These findings suggest that not only $\bar{\rho}_c$, but also other factors, e.g., possibly the details for the Y_e distribution in the inner core or the immediate postbounce accretion rate play a role in setting $f_{\rm peak}$.

As a quantitative example, I choose the previously considered $\Omega = 5.0\,{\rm rad\,s^{-1}}$ case and compare the fiducial results with those of the detailed electron capture runs. For the fiducial SFHo run, I find $\Delta h_+ = 20.8{\times}10^{-21}$ (at 10 kpc) and $f_{\rm peak} = 798$ Hz, with $M_{\rm IC,b} = 0.708\,M_\odot$ and $\bar{\rho}_c = 3.45{\times}10^{14}\,{\rm g\,cm^{-3}}$. The corresponding detailed electron capture runs yield $\Delta h_+ = \{17.8, 13.2, 11.6\} \times 10^{-21}$, $f_{\rm peak} = \{878, 848, 780\}$ Hz, $M_{\rm IC,b} = \{0.707, 0.611, 0.561\}\,M_\odot$, and $\bar{\rho}_c = \{3.58, 3.43, 3.28\} \times 10^{14}\,{\rm g\,cm^{-3}}$ for SFHo_ecap{0.1, 1.0, 10.0}, respectively. The differences between these fiducial and detailed electron capture runs are comparable to the differences between the fiducial SFHo EOS and the fiducial LS220 EOS simulations discussed in Sections 7.4 and 7.5.

When considering the GW mismatch for the $\Omega_0 = 5.0\,{\rm rad\,s^{-1}}$ case between fiducial SFHo, and SFHo_ecap0.1, SFHo_ecap1.0, and SFHo_ecap10.0, I find 6.2%, 6.2%, and 4.9%, respectively. These values are larger than the mismatch values due to EOS differences shown in Figure 7.13.

Conclusions: The results of this exercise clearly show that the GW signal is very sensitive to the treatment of electron capture during collapse. Differences in this treatment and in capture rates can blur differences between EOS. Though a systematic uncertainty in electron capture rates by a factor as large as 10 in either direction is unlikely, the differences caused by variations in $Y_e(\rho)$ described in this section are major issues if one seeks to extract EOS information from an observed rotating core collapse GW signal.

7.9 Conclusions

I carried out more than 1800 two-dimensional rapidly rotating general-relativistic hydrodynamic core collapse simulations to investigate the effects the nuclear EOS has on GW signals from rapidly rotating stellar core collapse, using 18 microphysical EOS and 98 different rotation profiles.

I distinguish three rotation regimes based on the ratio of rotational kinetic to gravitational energy $T/|W|$ of the inner core at bounce: Slow Rotation ($T/|W| < 0.06$), Rapid Rotation ($0.06 < T/|W| < 0.17$), and Extreme Rotation ($T/|W| > 0.17$). I find that in the Slow Rotation regime, the behavior of the GW bounce signal is nearly independent of the EOS and is straightforwardly explained by an order of magnitude

perturbative analysis. The amplitude of the bounce signal varies linearly with the rotation rate, parameterized by $T/|W|$ of the inner core at bounce, in agreement with previous work (e.g., E. Abdikamalov, S. Gossan, et al., 2014; Dimmelmeier, Ott, Marek, et al., 2008). The differences between bounce signals from different EOS are due largely to corresponding differences in the mass of the inner core at bounce. The GWs from postbounce oscillations of the protoneutron star are almost independent of the rotation rate in the Slow Rotation regime. The effects of the EOS on the GW frequency can be parameterized almost entirely in terms of the dynamical frequency $\sqrt{G\rho_c}$ of the core after bounce.

In the Rapid Rotation regime, the maximum rotation rate at bounce exceeds the dynamical frequency (above $T/|W| \approx 0.06$), and inertial (i.e. Coriolis and centrifugal forces) effects become significant and fundamentally change the character of the oscillations. The bounce amplitudes depart from their linear relationship with $T/|W|$ and depend on both the EOS and the degree of precollapse differential rotation. The variations due to the EOS are significantly smaller than those due to differing rotation profiles. Inertial effects confine oscillations to the poles and increase the oscillation frequency approximately linearly with the maximum rotation rate. Even in this regime, the dynamical time of the postbounce core parameterizes the effects of the EOS on top of the effects of rotation.

In the Extreme Rotation regime ($T/|W| \gtrsim 0.17$) the stellar cores undergo a centrifugally-supported bounce. Increasing the rotation rate in this regime leads to *smaller* rotational kinetic energy at bounce as centrifugal support keeps the collapsed cores more extended. The bounce GW signal correspondingly weakens, and the postbounce GW frequency appears to decrease, though weaker protoneutron star oscillations make positively identifying the peak frequency less reliable.

These results show that EOS differences in the collapse phase are as important as the high-density parameterization in determining characteristics of the GWs. Different treatments of low-density matter produce differences in the bounce signal, postbounce oscillation frequency, and overall signal (as measured by the GW mismatch) that are comparable to those produced by differences in high-density parameterizations or differences in the treatment of the transition from nonuniform to uniform nuclear matter. Densities do not exceed around twice nuclear density in the bounce and brief postbounce phases of core collapse that I study. Hence, the GW signal from these phases does not probe exotic physics or conditions in very massive neutron stars.

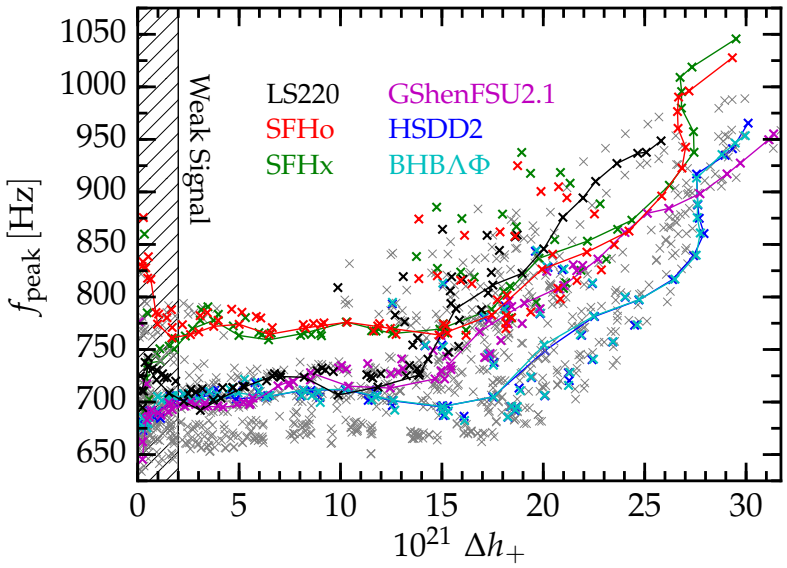

Figure 7.16: **Discerning the EOS.** I plot the GW peak frequency against the bounce signal amplitude for each of the 1704 collapsing cores. Data from the $A1 = 300$ km simulations are connected with lines to guide the eye. I predict a region of parameter space where we can reasonably expect rapidly rotating core collapse GW bounce and early post-bounce signals to lie given uncertainties in the nuclear EOS. For signals with $\Delta h_+ \lesssim 15 \times 10^{-21}$ (at 10 kpc), we may be able to distinguish the EOS from GW signals if the distance and orientation can be accurately determined. Peak frequencies at the slowest rotation rates (corresponding to $\Delta h_+ \lesssim 2 \times 10^{-21}$ in the figure) are unreliable due to extremely weak GW signals.

I demonstrate that using detailed electron capture rates for individual nuclei as opposed to the fiducial single nucleus approach to electron capture results in differences in the bounce and postbounce GWs comparable to those caused by using a different EOS. The GW characteristics are also sensitive to systematic uncertainties in the electron capture rates, producing similarly large variations when scaling the capture rates by a factor of 10 in either direction. I also demonstrate that a density-parameterization of the electron fraction $Y_e(\rho)$ during the collapse phase lacks the precision required for detailed interpretation of observed GW signals. Variations in the way the parameterization is implemented produce changes in the GWs comparable to those produced by different EOS. This leads us to the conclusion that for quantitatively reliable GW predictions full multi-dimensional neutrino radiation-hydrodynamic simulations that include realistic weak interactions will be needed.

In Figure 7.16, I plot the GW bounce signal amplitude against the frequency of

GWs from postbounce oscillations to show that different EOS occupy different, though partially overlapping regions in this observable space. This effectively maps uncertainties in the nuclear EOS to uncertainties in predicted GW signals from rapidly-rotating core collapse. Signals observed from the bounce and early postbounce phases of rotating core collapse outside of this region would be of great interest, since they would indicate unanticipated EOS physics and/or collapse dynamics. It may be possible to use the bounce amplitude to determine how quickly the star is rotating at bounce. The peak frequency could then constrain the EOS if there is enough core rotation to produce a reliable postbounce oscillation peak and little enough for the collapse to be in the Slow Rotation regime.

However, I must note that there are large uncertainties in the measured distances and orientations of nearby core-collapse supernovae, and also in the errors introduced by approximations made in the simulations. GW strain decreases inversely with distance, so the bounce amplitude is known only as well as the distance. Since the observed GW strain varies roughly with $h \sim \sin^2(\theta)$, where θ is the angle between the rotation axis and the line of sight, an accurate determination of the source orientation is required to be able to map the GW strain to a rotation rate. Inferring the peak frequency does not require distance or orientation measurements, but is subject to other observational uncertainties, e.g., the GW detector phase accuracy. Parameter estimation and model selection studies with more sophisticated data analysis tools, like those used by E. Abdikamalov, S. Gossan, et al., 2014; Röver et al., 2009; Logue et al., 2012, are required to evaluate the feasibility of extracting EOS properties given real detector characteristics and noise.

It should also be noted that GWs from rotating core collapse will only be detectable from sources out to the Magellanic Clouds. Furthermore, even those cores that are in the Slow Rotation regime are still very rapidly spinning from a stellar evolution point of view and produce protoneutron stars with spin periods of $\lesssim 5$ ms. Massive stars with rapidly spinning cores are expected to be exceedingly rare. These caveats and the above limitations, combined with the relatively small differences in the GW characteristics and protoneutron star oscillations induced by EOS variations, mean that we are unlikely to be able to use a GW signal from rotating core collapse to discern the EOS with current GW detectors and simulation methods.

The present study has elucidated the various ways in which the nuclear EOS can impact the rotating core collapse GW signal. While I am confident that these qualitative findings are robust, the GW signal predictions are not quantitatively reliable. The

most important limitation to be removed by future work is the lack of 2D neutrino radiation-hydrodynamics in the collapse phase. The results on differences caused by differing treatments of various regimes of the same underlying EOS parameterization also suggest that more work in nuclear theory may be needed. In particular, there is an important need for consistent EOS frameworks with which only differences in EOS physics, but not differences in methods, cause differences in the GW signal. In addition, though previous studies have shown that different progenitors result in only slightly different inner core masses H.-T. Janka, Hanke, et al., 2012 and GW signal characteristics (assuming the same resulting inner core mass and angular momentum) Ott, E. Abdikamalov, et al., 2012, a quantitative understanding of progenitor-induced uncertainties will require a much more exhaustive study of progenitor dependence of GW signals from rotating CCSNe.

While axisymmetry is a good approximation for collapse, bounce, and the early postbounce phase ($\lesssim$ 10 ms after bounce), rotating core collapse is host to rich three dimensional (3D) postbounce dynamics that can drive GW emission, including rotational instabilities and the nonaxisymmetric standing accretion shock instability. 3D simulations of rotating core collapse and postbounce GW emission have been carried out (e.g., Ott, Dimmelmeier, Marek, H.-T. Janka, Hawke, et al., 2007; Scheidegger, Whitehouse, et al., 2010; Kuroda, Takiwaki, and Kotake, 2014), but the EOS dependence of the GWs generated by 3D dynamics has yet to be explored. GWs from prompt and neutrino-driven convection and from the standing accretion shock instability in both rotating and nonrotating core collapse B. Müller, H.-T. Janka, and Marek, 2013; Yakunin et al., 2015; Andresen et al., 2016 have some EOS dependence as well Marek, H.-T. Janka, and E. Müller, 2009; Kuroda, Kotake, and Takiwaki, 2016, but the EOS parameter space has thus far been only sparsely sampled. Future studies of GWs emitted by these dynamics may yet provide alternate means of discerning the nuclear EOS.

GW strain decreases inversely with distance, so the bounce amplitude is known only as well as the distance. There is no established method of measuring accurate distances to galactic supernovae, and methods for existing SN remnants are fairly specific to the source. The distance to SN1987a (in the Large Magellanic Cloud) has been determined to be 51.4 ± 1.2 kpc by measuring the delay of radiation reflected off of different parts of a ring of matter around the supernova that was launched prior to the explosion (Panagia, 1999). This method can be used for the next galactic CCSN only if it shows the same or similar morphology. The distance to the Vela

remnant has been determined to be 250 ± 30 pc by determining which stars with known distances in the line of site exhibit absorption lines from the supernova remnant (Cha, Sembach, and Danks, 1999), but this requires that the remnant expands long enough that it envelops surrounding stars. If we are fortunate enough to watch a known star explode, we can use existing stellar distance measurements from before the explosion. For example, the red supergiant Betelgeuse is known to be 197 ± 45 pc away using VLA radio positions and Hipparcos parallax (Harper, A. Brown, and Guinan, 2008). Future and current parallax missions like Gaia (Gilmore et al., 2012) will map out many more stars. The exterior rotation rate and axis of Betelgeuse is known (e.g., (Uitenbroek, Dupree, and Gilliland, 1998)), but how this maps to interior rotation is not known, and such detailed observations do not exist for most stars. Since the observed GW strain varies roughly with $h \sim \sin(\theta)$, where θ is the angle between the rotation axis and the line of sight, an accurate determination of the source orientation is required to be able to map the GW strain to a rotation rate. Parameter estimation and model selection studies with more sophisticated data analysis tools, like those use E. Abdikamalov, S. Gossan, et al., 2014; S. E. Gossan et al., 2016, are required to evaluate the feasibility of extracting EOS properties given real detector characteristics and noise.

Chapter 8

SUMMARY AND OUTLOOK

Stellar core collapse and neutron star mergers produce brilliant and fascinating explosions, are likely the origin of most of the heavy elements in the universe, and exhibit a beautiful and complicated interplay between many areas of physics.

However, our understanding of these phenomena is incomplete. Their complexity has made computation the dominant means of modeling them; modern simulations account for properties of bulk matter at extreme conditions, general relativity, magnetic fields, and neutrino radiation transport. Though computation enables far more complex models than can be made using analytic techniques, it adds a conceptual layer between the model results and the actual physics. Using computation to understand nature requires understanding of both how well computer algorithms represent physics and how well physics represents nature. In this thesis, I take steps toward bridging both gaps. In this conclusion, I summarize the results presented in previous chapters and indicate how this work sets the stage for many exciting future inquiries.

My primary technical achievement is the open-source relativistic steady-state Monte Carlo neutrino radiation transport code Sedonu. Sedonu is able to solve for the steady-state neutrino radiation field on a fixed fluid background of arbitrary optical depth with a great deal of accuracy. It currently accounts for special relativistic effects in full generality and treats neutrino emission, absorption, pair annihilation, and elastic scattering. To close the gap between the algorithm and the physics, I verify Sedonu's accuracy in the context of core-collapse supernovae with a detailed comparison to a discrete ordinates neutrino transport code that implements the same set of physics. This comparison shows both codes converging to identical results, though the Monte Carlo method has a significant advantage in computing angular moments of the radiation field. Despite the sophistication of both codes, there are still approximations that will be lifted in the near future. Before Sedonu can be used as a verification tool for neutrino transport algorithms with the most sohpisticated set of neutrino interactions available, it will need to account for general relativistic effects and inelastic scattering reactions, both of which are currently in the works. It is my sincere hope that this will help push core-collapse supernova modeling in the direction of independent verification of numerical techniques to make the layer

between algorithms and physics a thinner and a less opaque.

I also use Sedonu to assess the accuracy of a phenomenological leakage treatment of neutrino effects in accretion disks formed from neutron star mergers and find qualitative differences. Though the leakage scheme produces order-of-magnitude accurate disk heating and cooling, I find that accurate transport significantly increases the rate at which the center of the disk cools and at which the edges of the disk are heated. This could cause a larger amount of symmetric ($Y_e \approx 0.5$) outflows and influence the speculative kilonova counterpart to GRBs. I also investigate the possibility of generating a neutrino-driven GRB jet by estimating how much energy would be produced in neutrino pair annihilation in the vacuuous regions above and below the disk. I find that the amount of energy deposited is near the lower limit of the jet kinetic energy, corroborating existing theoretical evidence that such a mechanism is unlikely. However, these results depend on the nature of the accretion disk and central hypermassive neutron star or black hole. Since this work was done, there has been work done to improve estimates of neutrino effects in 3D merger simulations (e.g., Foucart, E. O'Connor, L. Roberts, Kidder, et al. 2016; Fujibayashi et al. 2017. However, these simulations still use two-moment neutrino transport, which struggles with the interesting geometries in neutron star mergers. These results beg for similar Monte Carlo (or other high-order) neutrino transport calculations during first-principles neutron star merger simulations in three dimensions to provide accurate estimates of the amount and composition of ejected matter. This will much more directly approach the question of whether neutron star mergers are in fact the primary source of r-process elements and what optical and infrared kilonova counterparts we might expect to observe.

I harness Sedonu's advantage in calculating angular moments of the radiation field in proof of concept general relativistic dynamical core-collapse simulations with variable Eddington tensor neutrino transport in spherical symmetry. Though this implementation still requires much vetting and optimizing, the ultimate goal is to use it in three-dimensional general relativistic core-collapse and neutron star merger simulations. Doing so will bring CCSN models closer to understanding the explosion mechanism and bring much better estimates of the amount and composition of neutrino-driven winds in neutron star mergers. This is a large, but surmountable technical challenge.

One of the most exciting future possibilities is detecting gravitational waves from a CCSN. Though a suitable event is very rare, if the progenitor star is rapidly rotating

and approximately within the Milky Way galaxy (or perhaps the Large Magellanic Cloud), the gravitational waves could give us a direct insight into the dynamics of exotic CCSNe and a confirmation (or rejection!) of our understanding of the causes of these explosions. I perform a parameter study on the effects of the equation of state on the gravitational waves from such CCSNe, but it unfortunately indicates that LIGO would probably not be able to discern which of the many theoretical equations of state is most correct. The results did, however, demonstrate that the nature of the oscillations that drive the bounce and early post-bounce GWs are very universal with respect to a certain combination of the fluid properties and rotation rate. It will be interesting to see future studies test whether this universality extends to different progenitors as well. These simulations were limited by an assumption of axisymmetry, which prevents the growth of powerful gravitational wave-emitting instabilities on longer timescales than I simulated and which would be perhaps more sensitive to differences in the EOS. The protoneutron star cools and condenses with time, bringing the matter into regions of parameter space where theoretical EOS increasingly differ. A parameter study of these other instabilities might show a stronger, and hence more discernable, effect of the EOS. Just as these two-dimensional simulations used to be, three-dimensional simulations are currently too expensive for such exhaustive parameter studies, but will become possible with future advances in computer hardware and simulation software.

Based in 3D GRMHD simulations of rotating core collapse, I demonstrated that problems vexing fusion reactors and destabilizing active galactic nucleus jets is behind the instabilities that make the canonical magnetorotational mechanism fail, or at least to be delayed. Since then, this work has been followed up by Mösta, Ott, et al., 2015, who showed that, even in the case of a weak seed field, the magnetorotational instability can amplify the magnetic fields to strengths that may dominate the energy deposition for the shock revival. Long-term GRMHD simulations demonstrating this kind of explosion from first principles will be required to make a stronger claim. A collapse to a rapidly rotating black hole may also result from certain magnetorotational core-collapse events that could explain hypernovae and long GRBs, though this poses significant technical challenges.

In the end, the ultimate goal of these modeling efforts is to produce simulations accurate enough that they can be used to interpret past observations and predict future ones. Looking forward, the technical capabilities of simulation codes, in terms of included physics and numerical fidelity, have a long way to grow. This

is, of course, a classic problem that still requires much manpower. However, the main limitation of CCSN and NSM theory is a real dearth of direct natural data. Modern survey telescopes enable hundreds of observations of supernovae and GRBs in other galaxies each year, but the light does not carry much information about the central engines. Observations of the next nearby CCSN, especially in neutrinos, will give a desperately-needed boost to the theory of CCSN engines. Gravitational wave observations would provide a revolutionary insight into the engine dynamics of either, and detections of gravitational waves from mergers may be in our very near future. Until then, we can only watch, wait, and speculate.

BIBLIOGRAPHY

Abadie, J. et al. (2012). "Search for gravitational waves from low mass compact binary coalescence in LIGO's sixth science run and Virgo's science runs 2 and 3". In: *Phys. Rev. D* 85.8, 082002, p. 082002.

Abbasi et al. [IceCube Collaboration], R (2011). "IceCube sensitivity for low-energy neutrinos from nearby supernovae". In: *Astron. Astrophys.* 535, A109.

Abbott, B. P. et al. (2016a). "First targeted search for gravitational-wave bursts from core-collapse supernovae in data of first-generation laser interferometer detectors". In: *Phys. Rev. D* 94.10, 102001, p. 102001.

– (2016b). "Observation of Gravitational Waves from a Binary Black Hole Merger". In: *Phys. Rev. Lett.* 116.6, 061102, p. 061102.

Abdikamalov, E. B. et al. (2010). "Axisymmetric general relativistic simulations of the accretion-induced collapse of white dwarfs". In: *Phys. Rev. D* 81, p. 044012.

Abdikamalov, E., A. Burrows, et al. (2012). "A New Monte Carlo Method for Time-dependent Neutrino Radiation Transport". In: *Astrophys. J.* 755, 111, p. 111.

Abdikamalov, E., S. Gossan, et al. (2014). "Measuring the angular momentum distribution in core-collapse supernova progenitors with gravitational waves". In: *Phys. Rev. D* 90.4, 044001, p. 044001.

Acernese et al. (Virgo Collaboration), F. (2009). *Advanced Virgo Baseline Design*. Tech. rep. VIR-027A-09. Virgo Collaboration. URL: `https://tds.ego-gw.it/itf/tds/file.php?callFile=VIR-0027A-09.pdf`.

Akiyama, S. et al. (2003). "The Magnetorotational Instability in Core-Collapse Supernova Explosions". In: *Astrophys. J.* 584, p. 954.

Anderson, J. L. and E. A. Spiegel (1972). "The Moment Method in Relativistic Radiative Transfer". In: *Astrophys. J.* 171, p. 127.

Anderson, Stuart et al. (2004). *Conventions for data and software products of the LIGO and the LSC*. Tech. rep. LIGO-T010095-00-Z. URL: `%7Bhttps://dcc.ligo.org/LIGO-T010095/public%7D`.

Ando, S., F. Beacom, and H. Yüksel (2005). "Detection of Neutrinos from Supernovae in Nearby Galaxies". In: *Phys. Rev. Lett.* 95, p. 171101.

Andresen, H. et al. (2016). "Gravitational Wave Signals from 3D Neutrino Hydrodynamics Simulations of Core-Collapse Supernovae". In: *Submitted to Mon. Not. Roy. Astron. Soc.; arXiv:1607.05199*.

Antoniadis, J. et al. (2013). "A Massive Pulsar in a Compact Relativistic Binary". In: *Science* 340, p. 448.

Arnould, M., S. Goriely, and K. Takahashi (2007). “The r-process of stellar nucleosynthesis: Astrophysics and nuclear physics achievements and mysteries”. In: *Phys. Rep.* 450, p. 97.

Arnowitt, Richard, Stanley Deser, and Charles W. Misner (1962). “The Dynamics of General Relativity”. In: *Gravitation: An Introduction to Current Research*. Ed. by L. Witten. New York: John Wiley, pp. 227–265.

Asano, K. and T. Fukuyama (2000). “Neutrino Pair Annihilation in the Gravitation of Gamma-Ray Burst Sources”. In: *Astrophys. J.* 531, pp. 949–955.

– (2001). “Relativistic Effects on Neutrino Pair Annihilation above a Kerr Black Hole with the Accretion Disk”. In: *Astrophys. J.* 546, pp. 1019–1026.

Audit, E. et al. (2002). “A radiation-hydrodynamics scheme valid from the transport to the diffusion limit”. In:

Baade, W. and F. Zwicky (1934a). “Cosmic Rays from Super-novae”. In: *Proc. Nat. Acad. Sci.* 20, p. 259.

– (1934b). “On Super-novae”. In: *Proc. Nat. Acad. Sci.* 20, p. 254.

Balbinski, E. (1985). “A new shear instability in rotating, self-gravitating, perfect fluids”. In: *Mon. Not. Roy. Astron. Soc.* 216, p. 897.

Balbus, S. A. and J. F. Hawley (1991). “A powerful local shear instability in weakly magnetized disks. I—Linear analysis. II—Nonlinear evolution”. In: *Astrophys. J.* 376, p. 214.

Banik, S., M. Hempel, and D. Bandyopadhyay (2014). “New Hyperon Equations of State for Supernovae and Neutron Stars in Density-dependent Hadron Field Theory”. In: *Astrophys. J. Suppl. Ser.* 214, 22, p. 22.

Barnes, J. and D. Kasen (2013). “Effect of a High Opacity on the Light Curves of Radioactively Powered Transients from Compact Object Mergers”. In: *Astrophys. J.* 775, 18, p. 18.

Baumgarte, T. W. and S. L. Shapiro (2010). *Numerical Relativity: Solving Einstein’s Equations on the Computer*. Cambridge, UK: Cambridge University Press.

– (1999). “On the numerical integration of Einstein’s field equations”. In: *Phys. Rev. D* 59, p. 024007.

Bauswein, A. and H.-T. Janka (2012). “Measuring Neutron-Star Properties via Gravitational Waves from Neutron-Star Mergers”. In: *Phys. Rev. Lett.* 108.1, p. 011101.

Bauswein, A., N. Stergioulas, and H.-T. Janka (2014). “Revealing the high-density equation of state through binary neutron star mergers”. In: *Phys. Rev. D* 90.2, 023002, p. 023002.

Begelman, M. C. (1998). “Instability of Toroidal Magnetic Field in Jets and Plerions”. In: *Astrophys. J.* 493, p. 291.

Bellini, G. et al. (2014). “Neutrino Oscillations”. In: *Advances in High Energy Physics* 2014, p. 191960.

Berger, E. (2014). “Short-Duration Gamma-Ray Bursts”. In: *Ann. Rev. Astron. Astrophys.* 52, pp. 43–105.

Berger, E., W. Fong, and R. Chornock (2013). “An r-process Kilonova Associated with the Short-hard GRB 130603B”. In: *Astrophys. J. Lett.* 774, L23, p. L23.

Bernuzzi, S., T. Dietrich, and A. Nagar (2015). “Modeling the Complete Gravitational Wave Spectrum of Neutron Star Mergers”. In: *Phys. Rev. Lett.* 115.9, 091101, p. 091101.

Bernuzzi, S., A. Nagar, et al. (2012). “Tidal effects in binary neutron star coalescence”. In: *Phys. Rev. D* 86, p. 044030.

Bernuzzi, S., D. Radice, et al. (2016). “How loud are neutron star mergers?” In: *Phys. Rev. D* 94.2, 024023, p. 024023.

Bethe, H. A. (1990). “Supernova mechanisms”. In: *Rev. Mod. Phys.* 62, p. 801.

Bethe, H. A. and R. F. Bacher (1936). “Nuclear Physics A. Stationary States of Nuclei”. In: *Rev. Mod. Phys.* 8 (2), pp. 82–229. URL: http://link.aps.org/doi/10.1103/RevModPhys.8.82.

Bethe, H. A. and J. R. Wilson (1985). “Revival of a stalled supernova shock by neutrino heating”. In: *Astrophys. J.* 295, pp. 14–23.

Bionta, R. M. et al. (1987). “Observation of a neutrino burst in coincidence with supernova 1987A in the Large Magellanic Cloud”. In: *Phys. Rev. Lett.* 58, p. 1494.

Birkl, R. et al. (2007). “Neutrino pair annihilation near accreting, stellar-mass black holes”. In: *Astron. Astrophys.* 463, p. 51.

Bisnovatyi-Kogan, G. S. (1970). “The Explosion of a Rotating Star As a Supernova Mechanism.” In: *Astron. Zh.* 47, p. 813.

Blanchet, L., T. Damour, and G. Schaefer (1990). “Post-Newtonian hydrodynamics and post-Newtonian gravitational wave generation for numerical relativity”. In: *Mon. Not. Roy. Astron. Soc.* 242, p. 289.

Blandford, R. D. and R. L. Znajek (1977). “Electromagnetic extraction of energy from Kerr black holes”. In: *Mon. Not. Roy. Astron. Soc.* 179, pp. 433–456.

Blondin, J. M., A. Mezzacappa, and C. DeMarino (2003). “Stability of Standing Accretion Shocks, with an Eye toward Core-Collapse Supernovae”. In: *Astrophys. J.* 584, p. 971.

Bloom, J. S. et al. (2006). “Closing in on a Short-Hard Burst Progenitor: Constraints from Early-Time Optical Imaging and Spectroscopy of a Possible Host Galaxy of GRB 050509b”. In: *Astrophys. J.* 638, p. 354.

Brent, R. P. (1973). *Algorithms for Minimization without Derivatives*. Dover Publications, Incorporated. ISBN: 0130223352. URL: https://maths-people.anu.edu.au/~brent/pub/pub011.html.

Bruenn, S. W. (1985). "Stellar core collapse - Numerical model and infall epoch". In: *Astrophys. J. Suppl. Ser.* 58, pp. 771–841.

Bruenn, S. W., E. J. Lentz, et al. (2016). "The Development of Explosions in Axisymmetric Ab Initio Core-collapse Supernova Simulations of 12-25 M Stars". In: *Astrophys. J.* 818, 123, p. 123.

Bruenn, S. W., A. Mezzacappa, et al. (2013). "Axisymmetric Ab Initio Core-collapse Supernova Simulations of 12-25 $M_\odot$ Stars". In: *Astrophys. J. Lett.* 767, L6, p. L6.

Buras, R. et al. (2006). "Two-dimensional hydrodynamic core-collapse supernova simulations with spectral neutrino transport. I. Numerical method and results for a 15 M⊙ star". In: *Astron. Astrophys.* 447, p. 1049.

Burbidge, E. M. et al. (1957). "Synthesis of the Elements in Stars". In: *Rev. Mod. Phys.* 29 (4), p. 547.

Burrows, A. (2000). "Supernova Explosions in the Universe". In: *Nature* 403, p. 727.

– (2013). "Colloquium: Perspectives on core-collapse supernova theory". In: *Rev. Mod. Phys.* 85, p. 245.

Burrows, A., L. Dessart, et al. (2007). "Simulations of Magnetically Driven Supernova and Hypernova Explosions in the Context of Rapid Rotation". In: *Astrophys. J.* 664, pp. 416–434.

Burrows, A., J. Hayes, and B. A. Fryxell (1995). "On the Nature of Core-Collapse Supernova Explosions". In: *Astrophys. J.* 450, p. 830.

Burrows, A. and J. M. Lattimer (1983). "The effect of trapped lepton number and entropy on the outcome of stellar collapse". In: *Astrophys. J.* 270, p. 735.

Burrows, A., S. Reddy, and T. A. Thompson (2006). "Neutrino opacities in nuclear matter". In: *Nuc. Phys. A* 777, p. 356.

Burrows, A. and K. A. van Riper (1995). "A Gamma-Ray Monte Carlo Study of the Clumpy Debris of SN 1987A". In: *Astrophys. J.* 455, p. 215.

Burrows, A., D. Vartanyan, et al. (2016). "Crucial Physical Dependencies of the Core-Collapse Supernova Mechanism". In: *Submitted to Astrophys. J.*

Burrows, A., T. Young, et al. (2000). "A New Algorithm for Supernova Neutrino Transport and Some Applications". In: *Astrophys. J.* 539, p. 865.

C. D. Ott et al. (2004). "Gravitational Waves From Axisymmetric, Rotating Stellar Core Collapse". In: *Astrophys. J.* 600, p. 834.

Calder, A. C. et al. (2002). "On Validating an Astrophysical Simulation Code". In: *Astrophys. J. Suppl. Ser.* 143, p. 201.

Cano, Z. et al. (2017). “The Observer’s Guide to the Gamma-Ray Burst Supernova Connection”. In: *Advances in Astronomy* 2017, 8929054, p. 8929054.

Cappellaro, E., R. Evans, and M. Turatto (1999). “A new determination of supernova rates and a comparison with indicators for galactic star formation”. In: *Astron. Astrophys.* 351, p. 459.

Carbone, A. et al. (2010). “Constraints on the symmetry energy and neutron skins from pygmy resonances in Ni68 and Sn132”. In: *Phys. Rev. C* 81.4, 041301, p. 041301.

Cardall, C. Y., E. Endeve, and A. Mezzacappa (2013). “Conservative 3+1 general relativistic variable Eddington tensor radiation transport equations”. In: *Phys. Rev. D* 87.10, 103004, p. 103004.

Cardall, C. Y., A. Mezzacappa, and M. Liebendoerfer (2001). “NewtonPlus: Approximate Relativity for Supernova Simulations”. In: *arXiv:astro-ph/0106105*.

Castor, J. I. (2004). *Radiation Hydrodynamics*. Radiation Hydrodynamics, by John I. Castor, pp. 368. ISBN 0521833094. Cambridge, UK: Cambridge University Press, November 2004.

Cha, A. N., K. R. Sembach, and A. C. Danks (1999). “The Distance to the Vela Supernova Remnant”. In: *Astrophys. J. Lett.* 515, pp. L25–L28.

Chakraborty, S. et al. (2016). “Collective neutrino flavor conversion: Recent developments”. In: *Nuclear Physics B* 908, pp. 366–381.

Chen, L. (2011). “Higher order bulk characteristic parameters of asymmetric nuclear matter”. In: *Science China Physics, Mechanics, and Astronomy* 54, p. 124.

Colella, P. and P. R. Woodward (1984). “The Piecewise Parabolic Method (PPM) for Gas-Dynamical Simulations”. In: *J. Comp. Phys.* 54, p. 174.

Colgate, S. A. and M. H. Johnson (1960). “Hydrodynamic Origin of Cosmic Rays”. In: *Phys. Rev. Lett.* 5, p. 235.

Couch, S. M. and C. D. Ott (2015). “The Role of Turbulence in Neutrino-driven Core-collapse Supernova Explosions”. In: *Astrophys. J.* 799, 5, p. 5.

Dasgupta, B., E. P. O’Connor, and C. D. Ott (2012). “Role of collective neutrino flavor oscillations in core-collapse supernova shock revival”. In: *Phys. Rev. D* 85, p. 065008.

D’Avanzo, P. (2015). “Short gamma-ray bursts: A review”. In: *Journal of High Energy Astrophysics* 7, pp. 73–80.

de Mink, S. E. et al. (2013). “The Rotation Rates of Massive Stars: The Role of Binary Interaction through Tides, Mass Transfer, and Mergers”. In: *Astrophys. J.* 764, 166, p. 166.

Deaton, M. B. et al. (2013). “Black Hole-Neutron Star Mergers with a Hot Nuclear Equation of State: Outflow and Neutrino-cooled Disk for a Low-mass, High-spin Case”. In: *Astrophys. J.* 776, 47, p. 47.

Densmore, J. D. et al. (2007). “A hybrid transport-diffusion method for Monte Carlo radiative-transfer simulations”. In: *J. Comp. Phys.* 222, p. 485.

Dessart, L., A. Burrows, C. D. Ott, et al. (2006). “Multidimensional Simulations of the Accretion-induced Collapse of White Dwarfs to Neutron Stars”. In: *Astrophys. J.* 644, p. 1063.

Dessart, L., C. D. Ott, et al. (2009). “Neutrino Signatures and the Neutrino-Driven Wind in Binary Neutron Star Mergers”. In: *ApJ* 690, p. 1681.

Dessart, L. et al. (2006). “Multidimensional Radiation/Hydrodynamic Simulations of Proto-Neutron Star Convection”. In: *Astrophys. J.* 645, p. 534.

– (2008). “The Proto-Neutron Star Phase of the Collapsar Model and the Route to Long-Soft Gamma-Ray Bursts and Hypernovae”. In: *Astrophys. J. Lett.* 673, p. L43.

Dimmelmeier, H., J. A. Font, and E. Müller (2002). “Relativistic simulations of rotational core collapse II. Collapse dynamics and gravitational radiation”. In: *Astron. Astrophys.* 393, p. 523.

Dimmelmeier, H., J. Novak, et al. (2005). “Combining spectral and shock-capturing methods: A new numerical approach for 3D relativistic core collapse simulations”. In: *Phys. Rev. D* 71, p. 064023.

Dimmelmeier, H., C. D. Ott, H.-T. Janka, et al. (2007). “Generic Gravitational-Wave Signals from the Collapse of Rotating Stellar Cores”. In: *Phys. Rev. Lett.* 98, p. 251101.

Dimmelmeier, H., C. D. Ott, A. Marek, et al. (2008). “Gravitational wave burst signal from core collapse of rotating stars”. In: *Phys. Rev. D* 78, p. 064056.

Dimmelmeier, H., N. Stergioulas, and J. A. Font (2006). “Non-linear axisymmetric pulsations of rotating relativistic stars in the conformal flatness approximation”. In: *Mon. Not. Roy. Astron. Soc.* 368, p. 1609.

Dolence, J. C., A. Burrows, and W. Zhang (2015). “Two-dimensional Core-collapse Supernova Models with Multi-dimensional Transport”. In: *Astrophys. J.* 800, 10, p. 10.

Dolence, J. C., C. F. Gammie, et al. (2009). “grmonty: A Monte Carlo Code for Relativistic Radiative Transport”. In: *Astrophys. J. Suppl. Ser.* 184, p. 387.

Drout, M. R. et al. (2011). “The First Systematic Study of Type Ibc Supernova Multi-band Light Curves”. In: *Astrophys. J.* 741, 97, p. 97.

Duan, H., G. M. Fuller, J. Carlson, et al. (2007). “Neutrino Mass Hierarchy and Stepwise Spectral Swapping of Supernova Neutrino Flavors”. In: *Phys. Rev. Lett.* 99.24, p. 241802.

Duan, H., G. M. Fuller, and Y.-Z. Qian (2010). “Collective Neutrino Oscillations”. In: *Ann. Rev. Nuc. Part. Sc.* 60, p. 569.

Dubroca, B. and J. Feugeas (1999). “Etude théorique et numérique d’une hiérarchie de modèles aux moments pour le transfert radiatif”. In: *Academie des Sciences Paris Comptes Rendus Serie Sciences Mathematiques* 329, p. 915.

Dupret, M.-A. et al. (2009). “Theoretical amplitudes and lifetimes of non-radial solar-like oscillations in red giants”. In: *Astron. Astrophys.* 506, pp. 57–67.

Eichler, D. et al. (1989). “Nucleosynthesis, neutrino bursts and gamma-rays from coalescing neutron stars”. In: *Nature* 340, p. 126.

Einfeldt, B. (1988a). “On Godunov type methods for the Euler equations with a general equation of state”. In: *Shock tubes and waves; Proceedings of the Sixteenth International Symposium, Aachen, Germany, July 26–31, 1987. VCH Verlag, Weinheim, Germany*, p. 671.

– (1988b). “On Godunov-Type Methods for Gas Dynamics”. In: *SIAM Journal on Numerical Analysis* 25, pp. 294–318.

Engels, W. J., R. Frey, and C. D. Ott (2014). “Multivariate regression analysis of gravitational waves from rotating core collapse”. In: *Phys. Rev. D* 90.12, 124026, p. 124026.

Equation of state tables by Gang Shen. `http://cecelia.physics.indiana.edu/gang_shen_eos/`.

Equation of state tables by Matthias Hempel. `http://phys-merger.physik.unibas.ch/~hempel/eos.html`.

Esteban, I. et al. (2017). “Updated fit to three neutrino mixing: exploring the accelerator-reactor complementarity”. In: *JHEP* 1, 87, p. 87.

Esteban-Pretel, A. et al. (2008). “Role of dense matter in collective supernova neutrino transformations”. In: *Phys. Rev. D* 78, p. 085012.

Etienne, Z. B. et al. (2012). “General relativistic simulations of black-hole-neutron-star mergers: Effects of magnetic fields”. In: *Phys. Rev. D* 85.6, p. 064029.

Faber, J. A. and F. A. Rasio (2012). “Binary Neutron Star Mergers”. In: *Liv. Rev. Rel.* 15, p. 8.

Fernández, R. (2015). “Three-dimensional simulations of SASI- and convection-dominated core-collapse supernovae”. In: *Mon. Not. Roy. Astron. Soc.* 452, pp. 2071–2086.

Fernández, R., D. Kasen, et al. (2015). “Outflows from accretion discs formed in neutron star mergers: effect of black hole spin”. In: *MNRAS* 446, pp. 750–758.

Fernández, R. and B. D. Metzger (2013). “Delayed outflows from black hole accretion tori following neutron star binary coalescence”. In: *Mon. Not. Roy. Astron. Soc.* 435, p. 502.

Fernández, R., E. Quataert, et al. (2015). “The interplay of disc wind and dynamical ejecta in the aftermath of neutron star-black hole mergers”. In: *MNRAS* 449, pp. 390–402.

Finn, L. S. and C. R. Evans (1990). “Determining gravitational radiation from Newtonian self-gravitating systems”. In: *Astrophys. J.* 351, p. 588.

Flanagan, É. É. and T. Hinderer (2008). “Constraining neutron-star tidal Love numbers with gravitational-wave detectors”. In: *Phys. Rev. D* 77.2, 021502, p. 021502.

Flanagan, É. É. and S. A. Hughes (1998). “Measuring gravitational waves from binary black hole coalescences. I. Signal to noise for inspiral, merger, and ringdown”. In: *Phys. Rev. D* 57, pp. 4535–4565.

Fleck, J.A and E.H Canfield (1984). “A random walk procedure for improving the computational efficiency of the implicit Monte Carlo method for nonlinear radiation transport”. In: *J. Comp. Phys.* 54.3, pp. 508–523. ISSN: 0021-9991. URL: http://www.sciencedirect.com/science/article/pii/002199918490130X.

Fleck, J.A., Jr., and J.D. Cummings (1971). “An implicit Monte Carlo scheme for calculating time and frequency dependent nonlinear radiation transport”. In: *J. Comp. Phys.* 8.3, p. 313.

Flowers, E. G. and P. G. Sutherland (1976). “Neutrino-neutrino scattering and supernovae”. In: *Astrophys. J. Lett.* 208, pp. L19–L21.

Flowers, E. and N. Itoh (1976). “Transport properties of dense matter”. In: *Astrophys. J.* 206, pp. 218–242.

– (1979). “Transport properties of dense matter. II”. In: *Astrophys. J.* 230, pp. 847–858.

Foglizzo, T. et al. (2015). “The Explosion Mechanism of Core-Collapse Supernovae: Progress in Supernova Theory and Experiments”. In: *Pub. Ast. Soc. Aus.* 32, e009, e009.

Fong, W. and E. Berger (2013). “The Locations of Short Gamma-Ray Bursts as Evidence for Compact Object Binary Progenitors”. In: *Astrophys. J.* 776, 18, p. 18.

Font, J. A. (2008). “Numerical Hydrodynamics and Magnetohydrodynamics in General Relativity”. In: *Liv. Rev. Rel.* 11, p. 7.

Foucart, F., M. B. Deaton, et al. (2014). “Neutron star-black hole mergers with a nuclear equation of state and neutrino cooling: Dependence in the binary parameters”. In: *Phys. Rev. D* 90.2, 024026, p. 024026.

Foucart, F., R. Haas, et al. (2016). “Low mass binary neutron star mergers : gravitational waves and neutrino emission”. In: *Phys. Rev. D* 93, 044019, p. 044019.

Foucart, F., E. O’Connor, L. Roberts, M. D. Duez, et al. (2015). “Post-merger evolution of a neutron star-black hole binary with neutrino transport”. In: *Phys. Rev. D* 91.12, 124021, p. 124021.

Foucart, F., E. O'Connor, L. Roberts, L. E. Kidder, et al. (2016). "Impact of an improved neutrino energy estimate on outflows in neutron star merger simulations". In: *Phys. Rev. D* 94.12, 123016, p. 123016.

Frail, D. A. et al. (2001). "Beaming in Gamma-Ray Bursts: Evidence for a Standard Energy Reservoir". In: *Astrophys. J. Lett.* 562, pp. L55–L58.

Freiburghaus, C., S. Rosswog, and F.-K. Thielemann (1999). "R-Process in Neutron Star Mergers". In: *Astrophys. J. Lett.* 525, p. L121.

Fruchter, A. S. et al. (2006). "Long γ-ray bursts and core-collapse supernovae have different environments". In: *Nature* 441, pp. 463–468.

Fryer, C. L. and A. Heger (2000). "Core-Collapse Simulations of Rotating Stars". In: *Astrophys. J.* 541, p. 1033.

– (2005). "Binary Merger Progenitors for Gamma-Ray Bursts and Hypernovae". In: *Astrophys. J.* 623, p. 302.

Fryer, C. L. and V. Kalogera (2001). "Theoretical Black Hole Mass Distributions". In: *Astrophys. J.* 554, p. 548.

Fujibayashi, S. et al. (2017). "Properties of Neutrino-driven Ejecta from the Remnant of Binary Neutron Star Merger : Purely Radiation Hydrodynamics Case". In: *ArXiv e-prints*.

Fuller, J., M. Cantiello, et al. (2015). "The Spin Rate of Pre-collapse Stellar Cores: Wave-driven Angular Momentum Transport in Massive Stars". In: *Astrophys. J.* 810, 101, p. 101.

Fuller, J., H. Klion, et al. (2015). "Supernova seismology: gravitational wave signatures of rapidly rotating core collapse". In: *Mon. Not. Roy. Astron. Soc.* 450, p. 414.

Galeazzi, Filippo et al. (2013). "Implementation of a simplified approach to radiative transfer in general relativity". In: *Phys. Rev. D* 88.6, p. 064009. ISSN: 15507998. URL: http://link.aps.org/doi/10.1103/PhysRevD.88.064009.

Gal-Yam, A. et al. (2009). "Supernova 2007bi as a pair-instability explosion". In: *Nature* 462, pp. 624–627.

Gandolfi, S., J. Carlson, and S. Reddy (2012). "Maximum mass and radius of neutron stars, and the nuclear symmetry energy". In: *Phys. Rev. C* 85.3, 032801, p. 032801.

Gilmore, G. et al. (2012). "The Gaia-ESO Public Spectroscopic Survey". In: *The Messenger* 147, pp. 25–31.

Glashow, Sheldon L. (1961). "Partial-symmetries of weak interactions". In: *Nuclear Physics* 22.4, pp. 579–588. ISSN: 0029-5582. URL: http://www.sciencedirect.com/science/article/pii/0029558261904692.

Goriely, S., A. Bauswein, et al. (2015). “Impact of weak interactions of free nucleons on the r-process in dynamical ejecta from neutron star mergers”. In: *Mon. Not. Roy. Astron. Soc.* 452, pp. 3894–3904.

Goriely, S., J.-L. Sida, et al. (2013). “New Fission Fragment Distributions and r-Process Origin of the Rare-Earth Elements”. In: *Phys. Rev. Lett.* 111.24, 242502, p. 242502.

Gossan, S. E. et al. (2016). “Observing gravitational waves from core-collapse supernovae in the advanced detector era”. In: *Phys. Rev. D* 93.4, 042002, p. 042002.

Guillot, S. and R. E. Rutledge (2014). “Rejecting Proposed Dense Matter Equations of State with Quiescent Low-mass X-Ray Binaries”. In: *Astrophys. J. Lett.* 796, L3, p. L3.

H. Shen et al. EOS Tables. http://user.numazu-ct.ac.jp/~sumi/eos/.

Haghighat, Alireza (2015). *Monte Carlo Methods for Particle Transport*. CRC Press, Boca Raton, FL. ISBN: 9781466592537. URL: https://www.crcpress.com/Monte-Carlo-Methods-for-Particle-Transport/Haghighat/p/book/9781466592537.

Hanke, F. et al. (2013). “SASI Activity in Three-dimensional Neutrino-hydrodynamics Simulations of Supernova Cores”. In: *Astrophys. J.* 770, 66, p. 66.

Harikae, S. et al. (2010). “A General Relativistic Ray-tracing Method for Estimating the Energy and Momentum Deposition by Neutrino Pair Annihilation in Collapsars”. In: *Astrophys. J.* 720, p. 614.

Harper, G. M., A. Brown, and E. F. Guinan (2008). “A New VLA-Hipparcos Distance to Betelgeuse and its Implications”. In: *Astronom. J.* 135, p. 1430.

Hayes, J. C. and M. L. Norman (2003). “Beyond Flux-limited Diffusion: Parallel Algorithms for Multidimensional Radiation Hydrodynamics”. In: *Astrophys. J. Suppl. Ser.* 147, p. 197.

Hebeler, K. et al. (2010). “Constraints on Neutron Star Radii Based on Chiral Effective Field Theory Interactions”. In: *Phys. Rev. Lett.* 105, 161102, p. 161102.

– (2013). “Equation of State and Neutron Star Properties Constrained by Nuclear Physics and Observation”. In: *Astrophys. J.* 773, 11, p. 11.

Heger, A., C. L. Fryer, et al. (2003). “How Massive Single Stars End Their Life”. In: *Astrophys. J.* 591, p. 288.

Heger, A., N. Langer, and S. E. Woosley (2000). “Presupernova Evolution of Rotating Massive Stars. I. Numerical Method and Evolution of the Internal Stellar Structure”. In: *Astrophys. J.* 528, p. 368.

Heger, A., S. E. Woosley, and H. C. Spruit (2005). “Presupernova Evolution of Differentially Rotating Massive Stars Including Magnetic Fields”. In: *Astrophys. J.* 626, p. 350.

Hempel, M., T. Fischer, et al. (2012). “New Equations of State in Simulations of Core-collapse Supernovae”. In: *Astrophys. J.* 748, 70, p. 70.

Hempel, M. and J. Schaffner-Bielich (2010). “A statistical model for a complete supernova equation of state”. In: *Nuc. Phys. A* 837, p. 210.

Hillebrandt, W. (1982). “An exploding 10 solar mass star - A model for the Crab supernova”. In: *Astron. Astrophys.* 110, pp. L3–L6.

Hirata, K. et al. (1987). “Observation of a neutrino burst from the supernova SN1987A”. In: *Phys. Rev. Lett.* 58, p. 1490.

Hix, W. R. et al. (2003). “Impact of nuclear reaction rate uncertainties on Nova models”. In: *Nuc. Phys. A* 718, pp. 620–622.

Hjorth, J. and J. S. Bloom (2012). “The Gamma-Ray Burst - Supernova Connection”. In: *Chapter 9 in ”Gamma-Ray Bursts”, Cambridge Astrophysics Series 51, eds. C. Kouveliotou, R. A. M. J. Wijers and S. Woosley, Cambridge University Press (Cambridge)*, pp. 169–190.

Iwamoto, K. et al. (1998). “A hypernova model for the supernova associated with the γ-ray burst of 25 April 1998”. In: *Nature* 395, p. 672.

Janka, H.-T. (1991). *Neutrino transport in type-II supernovae and protoneutron stars by Monte Carlo methods.*

– (1992). “Flux-limited neutrino diffusion versus Monte Carlo neutrino transport”. In: *Astron. Astrophys.* 256, p. 452.

– (2001). “Conditions for shock revival by neutrino heating in core-collapse supernovae”. In: *Astron. Astrophys.* 368, p. 527.

– (2012). “Explosion Mechanisms of Core-Collapse Supernovae”. In: *Ann. Rev. Nuc. Par. Sci.* 62, p. 407.

Janka, H.-T., R. Dgani, and L. J. van den Horn (1992). “Fermion angular distribution and maximum entropy Eddington factors”. In: *Astron. Astrophys.* 265, p. 345.

Janka, H.-T., T. Eberl, et al. (1999). “Black Hole-Neutron Star Mergers as Central Engines of Gamma-Ray Bursts”. In: *Astrophys. J. Lett.* 527, pp. L39–L42.

Janka, H.-T., F. Hanke, et al. (2012). “Core-collapse supernovae: Reflections and directions”. In: *Prog. Th. Exp. Phys.* 2012.1, 01A309, p. 010000.

Janka, H.-T. and W. Hillebrandt (1989a). “Monte Carlo simulations of neutrino transport in type II supernovae”. In: *Astron. Astrophys. Suppl. Ser.* 78, p. 375.

– (1989b). “Neutrino emission from type II supernovae—an analysis of the spectra”. In: *Astron. Astrophys.* 224, p. 49.

Janka, H.-T., K. Langanke, et al. (2007). “Theory of core-collapse supernovae”. In: *Phys. Rep.* 442, p. 38.

Janka, H.-T. and E. Müller (1996). “Neutrino heating, convection, and the mechanism of Type-II supernova explosions.” In: *Astron. Astrophys.* 306, p. 167.

Just, O., A. Bauswein, et al. (2015). “Comprehensive nucleosynthesis analysis for ejecta of compact binary mergers”. In: *Mon. Not. Roy. Astron. Soc.* 448, pp. 541–567.

Just, O., M. Obergaulinger, and H.-T. Janka (2015). “A new multidimensional, energy-dependent two-moment transport code for neutrino-hydrodynamics”. In: *Mon. Not. Roy. Astron. Soc.* 453, pp. 3386–3413.

KAGRA Detector Sensitivity (2016). URL: `http://gwcenter.icrr.u-tokyo.ac.jp/researcher/parameters` (visited on 12/04/2016).

Kaplan, J. D. et al. (2014). “The Influence of Thermal Pressure on Equilibrium Models of Hypermassive Neutron Star Merger Remnants”. In: *Astrophys. J.* 790, 19, p. 19.

Kasen, D., N. R. Badnell, and J. Barnes (2013). “Opacities and Spectra of the r-process Ejecta from Neutron Star Mergers”. In: *Astrophys. J.* 774, 25, p. 25.

Kasen, D., R. Fernández, and B. D. Metzger (2015). “Kilonova light curves from the disc wind outflows of compact object mergers”. In: *Mon. Not. Roy. Astron. Soc.* 450, p. 1777.

Kasen, D., R. C. Thomas, and P. Nugent (2006). “Time-dependent Monte Carlo Radiative Transfer Calculations for Three-dimensional Supernova Spectra, Light Curves, and Polarization”. In: *Astrophys. J.* 651, p. 366.

Keil, M. T., G. G. Raffelt, and H.-T. Janka (2003). “Monte Carlo Study of Supernova Neutrino Spectra Formation”. In: *Astrophys. J.* 590, p. 971.

Kitaura, F. S., H.-T. Janka, and W. Hillebrandt (2006). “Explosions of O-Ne-Mg cores, the Crab supernova, and subluminous type II-P supernovae”. In: *Astron. Astrophys.* 450, p. 345.

Kiuchi, K., K. Kyutoku, et al. (2014). “High resolution numerical relativity simulations for the merger of binary magnetized neutron stars”. In: *Phys. Rev. D* 90.4, 041502, p. 041502.

Kiuchi, K., Y. Sekiguchi, et al. (2012). “Gravitational waves, neutrino emissions and effects of hyperons in binary neutron star mergers”. In: *Class. Quantum Grav.* 29.12, p. 124003.

Kolomeitsev, E. E. et al. (2016). “Unitary Gas Constraints on Nuclear Symmetry Energy”. In: *Submitted to Phys. Rev. Lett.; arXiv:1611.07133*.

Korobkin, O. et al. (2012). “The runaway instability in general-relativistic accretion disks”. In: *Accepted for publication in Mon. Not. Roy. Astron. Soc., ArXiv:1210.1214*.

Kotake, K. (2013). In: *Comptes Rendus Physique* 14, p. 318.

Kotake, K., W. Iwakami, et al. (2009). “Stochastic Nature of Gravitational Waves from Supernova Explosions with Standing Accretion Shock Instability”. In: *Astrophys. J. Lett.* 697, p. L133.

Kotake, K., K. Sato, and K. Takahashi (2006). “Explosion mechanism, neutrino burst and gravitational wave in core-collapse supernovae.” In: *Rep. Prog. Phys.* 69, p. 971.

Kotake, K., K. Sumiyoshi, et al. (2012). “Core-collapse supernovae as supercomputing science: A status report toward six-dimensional simulations with exact Boltzmann neutrino transport in full general relativity”. In: *Prog. Theo. Exp. Phys.* 2012, 01A301, p. 301.

Kotake, K., S. Yamada, and K. Sato (2003). “Gravitational radiation from axisymmetric rotational core collapse”. In: *Phys. Rev. D* 68, p. 044023.

Kouveliotou, C. et al. (1993). “Identification of two classes of gamma-ray bursts”. In: *Astrophys. J. Lett.* 413, pp. L101–L104.

Krumholz, M. R. et al. (2007). “Equations and Algorithms for Mixed-frame Flux-limited Diffusion Radiation Hydrodynamics”. In: *Astrophys. J.* 667, p. 626.

Kruskal, M. and J. L. Tuck (1958). “The Instability of a Pinched Fluid with a Longitudinal Magnetic Field”. In: *Proc. R. Soc. Lond.* 245, pp. 222–237.

Kuroda, T., K. Kotake, and T. Takiwaki (2012). “Fully General Relativistic Simulations of Core-collapse Supernovae with an Approximate Neutrino Transport”. In: *Astrophys. J.* 755, 11, p. 11.

– (2016). “A New Gravitational-wave Signature from Standing Accretion Shock Instability in Supernovae”. In: *Astrophys. J. Lett.* 829, L14, p. L14.

Kuroda, T., T. Takiwaki, and K. Kotake (2014). “Gravitational wave signatures from low-mode spiral instabilities in rapidly rotating supernova cores”. In: *Phys. Rev. D* 89.4, 044011, p. 044011.

– (2016). “A New Multi-energy Neutrino Radiation-Hydrodynamics Code in Full General Relativity and Its Application to the Gravitational Collapse of Massive Stars”. In: *Astrophys. J. Suppl. Ser.* 222, 20, p. 20.

Kuroda, T. and H. Umeda (2010). “Three-dimensional Magnetohydrodynamical Simulations of Gravitational Collapse of a 15 Msun Star”. In: *Astrophys. J. Suppl. Ser.* 191, p. 439.

Langanke, K. et al. (2003). “Electron Capture Rates on Nuclei and Implications for Stellar Core Collapse”. In: *Phys. Rev. Lett.* 90.24, 241102, p. 241102.

Lattimer, J. M. (2012). “The Nuclear Equation of State and Neutron Star Masses”. In: *Ann. Rev. Nuc. Part. Sc.* 62, p. 485.

Lattimer, J. M., C. J. Pethick, et al. (1985). “Physical properties of hot, dense matter: The general case”. In: *Nuc. Phys. A* 432, p. 646.

Lattimer, J. M. and M. Prakash (2000). “Nuclear matter and its role in supernovae, neutron stars and compact object binary mergers”. In: *Phys. Rep.* 333, pp. 121–146.

– (2001). “Neutron Star Structure and the Equation of State”. In: *Astrophys. J.* 550, p. 426.

– (2016). “The equation of state of hot, dense matter and neutron stars”. In: *Phys. Rep.* 621, p. 127.

Lattimer, J. M. and D. N. Schramm (1974). “Black-hole-neutron-star collisions”. In: *ApJ* 192, pp. L145–L147.

Lattimer, J. M. and F. D. Swesty (1991). “A generalized equation of state for hot, dense matter”. In: *Nuc. Phys. A* 535, pp. 331–376.

Lattimer, James M. et al. (1991). “Direct URCA process in neutron stars”. In: *Phys. Rev. Lett.* 66.21, pp. 2701–2704.

Lattimer-Swesty EOS Webpage. `http://www.astro.sunysb.edu/dswesty/lseos.html`.

LeBlanc, J. M. and J. R. Wilson (1970). “A Numerical Example of the Collapse of a Rotating Magnetized Star”. In: *Astrophys. J.* 161, p. 541.

Lee, W. H. and E. Ramirez-Ruiz (2007). “The progenitors of short gamma-ray bursts”. In: *New Journal of Physics* 9, p. 17.

Leng, M. and D. Giannios (2014). “Testing the neutrino annihilation model for launching GRB jets”. In: *Mon. Not. Roy. Astron. Soc.* 445, pp. L1–L5.

Lentz, E. J., S. W. Bruenn, et al. (2015). “Three-dimensional Core-collapse Supernova Simulated Using a 15 $M_\odot$ Progenitor”. In: *Astrophys. J. Lett.* 807, L31, p. L31.

Lentz, E. J., A. Mezzacappa, O. E. B. Messer, W. R. Hix, et al. (2012). “Interplay of Neutrino Opacities in Core-collapse Supernova Simulations”. In: *Astrophys. J.* 760, 94, p. 94.

Lentz, E. J., A. Mezzacappa, O. E. B. Messer, M. Liebendörfer, et al. (2012). “On the Requirements for Realistic Modeling of Neutrino Transport in Simulations of Core-collapse Supernovae”. In: *Astrophys. J.* 747, 73, p. 73.

Levermore, C. D. (1984). “Relating Eddington factors to flux limiters.” In: *J. Quant. Spectrosc. Radiat. Transfer* 31, p. 149.

Levermore, C. D. and G. C. Pomraning (1981). “A flux-limited diffusion theory”. In: *Astrophys. J.* 248, p. 321.

Levinson, Amir and David Eichler (2003). “Baryon Loading of Gamma-Ray Burst by Neutron Pickup”. In: *The Astrophysical Journal Letters* 594.1, p. L19. URL: `http://stacks.iop.org/1538-4357/594/i=1/a=L19`.

Li, L.-X. and B. Paczyński (1998). "Transient Events from Neutron Star Mergers". In: *Astrophys. J. Lett.* 507, p. L59.

Liebendörfer, M. (2005). "A Simple Parameterization of the Consequences of Deleptonization for Simulations of Stellar Core Collapse". In: *Astrophys. J.* 633, p. 1042.

Liebendörfer, M., O. E. B. Messer, et al. (2004). "A Finite Difference Representation of Neutrino Radiation Hydrodynamics in Spherically Symmetric General Relativistic Spacetime". In: *Astrophys. J. Suppl. Ser.* 150, p. 263.

Liebendörfer, M., A. Mezzacappa, and F.-K. Thielemann (2001). "Conservative general relativistic radiation hydrodynamics in spherical symmetry and comoving coordinates". In: *Phys. Rev. D* 63, p. 104003.

Liebendörfer, M., M. Rampp, et al. (2005). "Supernova Simulations with Boltzmann Neutrino Transport: A Comparison of Methods". In: *Astrophys. J.* 620, p. 840.

Liebendörfer, M., S. C. Whitehouse, and T. Fischer (2009). "The Isotropic Diffusion Source Approximation for Supernova Neutrino Transport". In: *Astrophys. J.* 698, p. 1174.

LIGO Scientific Collaboration et al. (2015). "Advanced LIGO". In: *Class. Quantum Grav.* 32.7, 074001, p. 074001.

Lindquist, R. W. (1966). "Relativistic transport theory". In: *Annals of Physics* 37, pp. 487–518.

Lithwick, Y. and R. Sari (2001). "Lower Limits on Lorentz Factors in Gamma-Ray Bursts". In: *Astrophys. J.* 555, pp. 540–545.

Livne, E. et al. (2004). "Two-dimensional, Time-dependent, Multigroup, Multiangle Radiation Hydrodynamics Test Simulation in the Core-Collapse Supernova Context". In: *Astrophys. J.* 609, p. 277.

Lobanov, A. E. (2015). "Particle quantum states with indefinite mass and neutrino oscillations". In: *ArXiv e-prints*.

Löffler, F. et al. (2012). "The Einstein Toolkit: a community computational infrastructure for relativistic astrophysics". In: *Class. Quantum Grav.* 29, p. 115001.

Logue, J. et al. (2012). "Inferring Core-Collapse Supernova Physics with Gravitational Waves". In: *Phys. Rev. D* 86.4, 044023, p. 044023.

MacFadyen, A. I. and S. E. Woosley (1999). "Collapsars: Gamma-Ray Bursts and Explosions in "Failed Supernovae"". In: *Astrophys. J.* 524, p. 262.

Marek, A., H. Dimmelmeier, et al. (2006). "Exploring the relativistic regime with Newtonian hydrodynamics: an improved effective gravitational potential for supernova simulations". In: *Astron. Astrophys.* 445, p. 273.

Marek, A., H.-T. Janka, and E. Müller (2009). "Equation-of-state dependent features in shock-oscillation modulated neutrino and gravitational-wave signals from supernovae". In: *Astron. Astrophys.* 496, p. 475.

Martin, D. et al. (2015). “Neutrino-driven Winds in the Aftermath of a Neutron Star Merger: Nucleosynthesis and Electromagnetic Transients”. In: *Astrophys. J.* 813, 2, p. 2.

McKinney, J. C. and R. D. Blandford (2009). “Stability of relativistic jets from rotating, accreting black holes via fully three-dimensional magnetohydrodynamic simulations”. In: *Mon. Not. Roy. Astron. Soc.* 394, p. L126.

McLaughlin, G. C. and R. Surman (2005). “Prospects for obtaining an r process from Gamma Ray Burst Disk Winds”. In: *Nuc. Phys. A* 758, pp. 189–196.

Meier, D. L. et al. (1976). “Magnetohydrodynamic phenomena in collapsing stellar cores”. In: *Astrophys. J.* 204, p. 869.

Melson, T., H.-T. Janka, R. Bollig, et al. (2015). “Neutrino-driven Explosion of a 20 Solar-mass Star in Three Dimensions Enabled by Strange-quark Contributions to Neutrino–Nucleon Scattering”. In: *Astrophys. J. Lett.* 808, L42, p. L42.

Melson, T., H.-T. Janka, and A. Marek (2015). “Neutrino-driven Supernova of a Low-mass Iron-core Progenitor Boosted by Three-dimensional Turbulent Convection”. In: *Astrophys. J. Lett.* 801, L24, p. L24.

Messer, O. E. B. et al. (1998). “A Comparison of Boltzmann and Multigroup Flux-limited Diffusion Neutrino Transport during the Postbounce Shock Reheating Phase in Core-Collapse Supernovae”. In: *Astrophys. J.* 507, p. 353.

Mészáros, P. (2006). “Gamma-ray bursts”. In: *Rep. Prog. Phys.* 69, p. 2259.

Meszaros, P. and M. J. Rees (1992). “High-entropy fireballs and jets in gamma-ray burst sources”. In: *Mon. Not. Roy. Astron. Soc.* 257, 29P–31P.

Metzger, B. D. and E. Berger (2012). “What is the Most Promising Electromagnetic Counterpart of a Neutron Star Binary Merger?” In: *Astrophys. J.* 746, 48, p. 48.

Metzger, B. D. and R. Fernández (2014). “Red or blue? A potential kilonova imprint of the delay until black hole formation following a neutron star merger”. In: *Mon. Not. Roy. Astron. Soc.* 441, p. 3444.

Metzger, B. D., D. Giannios, et al. (2011). “The protomagnetar model for gamma-ray bursts”. In: *Mon. Not. Roy. Astron. Soc.* 413, p. 2031.

Metzger, B. D., G. Martínez-Pinedo, et al. (2010). “Electromagnetic counterparts of compact object mergers powered by the radioactive decay of r-process nuclei”. In: *Mon. Not. Roy. Astron. Soc.* 406, pp. 2650–2662.

Mezzacappa, A. and S. W. Bruenn (1993). “A numerical method for solving the neutrino Boltzmann equation coupled to spherically symmetric stellar core collapse”. In: *Astrophys. J.* 405, p. 669.

Mignone, A. et al. (2010). “High-resolution 3D relativistic MHD simulations of jets”. In: *Mon. Not. Roy. Astron. Soc.* 402, p. 7.

Mihalas, D. and R. I. Klein (1982). "On the solution of the time-dependent inertial-frame equation of radiative transfer in moving media to O(v/c)". In: *J. Comp. Phys.* 46, p. 97.

Mihalas, D. and B. Weibel-Mihalas (1999). *Foundations of Radiation Hydrodynamics*. Mineola, NY, USA: Dover Publications.

Mikami, H. et al. (2008). "Three-dimensional Magnetohydrodynamical Simulations of a Core-Collapse Supernova". In: *Astrophys. J.* 683, p. 357.

Miller, M. C. and F. K. Lamb (2016). "Observational constraints on neutron star masses and radii". In: *Eur. Phys. J. A* 52, 63, p. 63.

Miller, W. A. et al. (2003). "Off-Axis Neutrino Scattering in Gamma-Ray Burst Central Engines". In: *Astrophys. J.* 583, pp. 833–841.

Minerbo, G. N. (1978). "Maximum entropy Eddington factors." In: *J. Quant. Spectrosc. Radiat. Transfer* 20, p. 541.

Mirizzi, A. et al. (2016). "Supernova neutrinos: production, oscillations and detection". In: *Nuovo Cimento Rivista Serie* 39, pp. 1–112.

Misner, C. W., K. S. Thorne, and J. A. Wheeler (1973). *Gravitation*.

Modjaz, M. (2011). "Stellar forensics with the supernova-GRB connection". In: *Astron. Nachr.* 332, p. 434.

Mohr, Peter J., David B. Newell, and Barry N. Taylor (2016). "CODATA recommended values of the fundamental physical constants: 2014". In: *Rev. Mod. Phys.* 88 (3), p. 035009. URL: https://link.aps.org/doi/10.1103/RevModPhys.88.035009.

Moiseenko, S. G., G. S. Bisnovatyi-Kogan, and N. V. Ardeljan (2006). "A magnetorotational core-collapse model with jets". In: *Mon. Not. Roy. Astron. Soc.* 370, p. 501.

Mönchmeyer, R. et al. (1991). "Gravitational waves from the collapse of rotating stellar cores". In: *Astron. Astrophys.* 246, p. 417.

Mösta, P., B. C. Mundim, et al. (2014). "GRHydro: a new open-source general-relativistic magnetohydrodynamics code for the Einstein toolkit". In: *Class. Quantum Grav.* 31.1, 015005, p. 015005.

Mösta, P., C. D. Ott, et al. (2015). "A Large-Scale Dynamo and Magnetoturbulence in Rapidly Rotating Core-Collapse Supernovae". In: *Nature* 528.7582, p. 376.

Mösta, P., S. Richers, et al. (2014). "Magnetorotational Core-collapse Supernovae in Three Dimensions". In: *Astrophys. J. Lett.* 785, L29, p. L29.

Mueller, E. (1982). "Gravitational radiation from collapsing rotating stellar cores". In: *Astron. Astrophys.* 114, pp. 53–59.

Müller, B. (2016). "The Status of Multi-Dimensional Core-Collapse Supernova Models". In: *Pub. Astron. Soc. Australia* 33, e048, e048.

Müller, B. and H.-T. Janka (2015). “Non-radial instabilities and progenitor asphericities in core-collapse supernovae”. In: *Mon. Not. Roy. Astron. Soc.* 448, pp. 2141–2174.

Müller, B., H.-T. Janka, and H. Dimmelmeier (2010). “A New Multi-dimensional General Relativistic Neutrino Hydrodynamic Code for Core-collapse Supernovae. I. Method and Code Tests in Spherical Symmetry”. In: *Astrophys. J. Suppl. Ser.* 189, p. 104.

Müller, B., H.-T. Janka, and A. Marek (2012). “A New Multi-dimensional General Relativistic Neutrino Hydrodynamics Code for Core-collapse Supernovae. II. Relativistic Explosion Models of Core-collapse Supernovae”. In: *Astrophys. J.* 756, 84, p. 84.

– (2013). “A New Multi-dimensional General Relativistic Neutrino Hydrodynamics Code of Core-collapse Supernovae. III. Gravitational Wave Signals from Supernova Explosion Models”. In: *Astrophys. J.* 766, 43, p. 43.

Murchikova, E. M., E. Abdikamalov, and T. Urbatsch (2017). “Analytic closures for M1 neutrino transport”. In: *Mon. Not. Roy. Astron. Soc.* 469.2, p. 1725. URL: +%20http://dx.doi.org/10.1093/mnras/stx986.

Murphy, J. W. and A. Burrows (2008). “Criteria for Core-Collapse Supernova Explosions by the Neutrino Mechanism”. In: *Astrophys. J.* 688, p. 1159.

Murphy, J. W., J. C. Dolence, and A. Burrows (2013). “The Dominance of Neutrino-driven Convection in Core-collapse Supernovae”. In: *Astrophys. J.* 771, 52, p. 52.

Nagakura, H., W. Iwakami, S. Furusawa, H. Okawa, et al. (2017). “Six-Dimensional Simulations of Core-Collapse Supernovae with Full Boltzmann Neutrino Transport”. In: *ArXiv e-prints*.

Nagakura, H., W. Iwakami, S. Furusawa, K. Sumiyoshi, et al. (2017). “Three-dimensional Boltzmann-Hydro Code for Core-collapse in Massive Stars. II. The Implementation of Moving-mesh for Neutron Star Kicks”. In: *Astrophys. J. Suppl. Ser.* 229, 42, p. 42.

Nagakura, H., K. Sumiyoshi, and S. Yamada (2014). “Three-dimensional Boltzmann Hydro Code for Core Collapse in Massive Stars. I. Special Relativistic Treatments”. In: *Astrophys. J. Suppl. Ser.* 214, 16, p. 16.

Nakamura, T., K. Oohara, and Y. Kojima (1987). “General Relativistic Collapse To Black Holes And Gravitational Waves From Black Holes”. In: *Prog. Theor. Phys. Suppl.* 90, pp. 1–218.

Narayan, R., B. Paczynski, and T. Piran (1992). “Gamma-ray bursts as the death throes of massive binary stars”. In: *Astrophys. J. Lett.* 395, p. L83.

Nättilä, J. et al. (2016). “Equation of state constraints for the cold dense matter inside neutron stars using the cooling tail method”. In: *Astron. Astrophys.* 591, A25, A25.

Neilsen, David et al. (2014). “Magnetized neutron stars with realistic equations of state and neutrino cooling”. In: *Phys. Rev. D* 89.10, p. 104029.

Nissanke, S., M. Kasliwal, and A. Georgieva (2013). “Identifying Elusive Electromagnetic Counterparts to Gravitational Wave Mergers: An End-to-end Simulation”. In: *Astrophys. J.* 767, 124, p. 124.

Nomoto, K. (1984). “Evolution of 8-10 solar mass stars toward electron capture supernovae. I - Formation of electron-degenerate O + NE + MG cores”. In: *Astrophys. J.* 277, p. 791.

– (1987). “Evolution of 8-10 solar mass stars toward electron capture supernovae. II - Collapse of an O + Ne + Mg core”. In: *Astrophys. J.* 322, pp. 206–214.

Nomoto, K. and Y. Kondo (1991). “Conditions for accretion-induced collapse of white dwarfs”. In: *Astrophys. J. Lett.* 367, pp. L19–L22.

Nomoto, K., D. Sugimoto, et al. (1982). “The Crab Nebula’s progenitor”. In: *Nature* 299, pp. 803–805.

Nousek, J. A. et al. (2006). “Evidence for a Canonical Gamma-Ray Burst Afterglow Light Curve in the Swift XRT Data”. In: *Astrophys. J.* 642, pp. 389–400.

Obergaulinger, M., M. A. Aloy, and E. Müller (2006). “Axisymmetric simulations of magneto-rotational core collapse: dynamics and gravitational wave signal”. In: *Astron. Astrophys.* 450, p. 1107.

Obergaulinger, M., P. Cerdá-Durán, et al. (2009). “Semi-global simulations of the magneto-rotational instability in core collapse supernovae”. In: *Astron. Astrophys.* 498, p. 241.

O’Connor, E. (2015). “An Open-source Neutrino Radiation Hydrodynamics Code for Core-collapse Supernovae”. In: *Astrophys. J. Suppl. Ser.* 219, 24, p. 24.

O’Connor, E. and S. M. Couch (2015). “Two Dimensional Core-Collapse Supernova Explosions Aided by General Relativity with Multidimensional Neutrino Transport”. In: *Submitted to Astrophys. J.*

O’Connor, E. and C. D. Ott (2010). “A new open-source code for spherically symmetric stellar collapse to neutron stars and black holes”. In: *Class. Quantum Grav.* 27.11, 114103, p. 114103.

– (2011). “Black Hole Formation in Failing Core-Collapse Supernovae”. In: *Astrophys. J.* 730, 70, p. 70.

– (2013). “The Progenitor Dependence of the Pre-explosion Neutrino Emission in Core-collapse Supernovae”. In: *Astrophys. J.* 762, 126, p. 126.

Oertel, M. et al. (2017). “Equations of state for supernovae and compact stars”. In: *Rev. Mod. Phys.* 89.1, 015007, p. 015007.

Ohnishi, N., K. Kotake, and S. Yamada (2006). “Numerical Analysis of Standing Accretion Shock Instability with Neutrino Heating in Supernova Cores”. In: *Astrophys. J.* 641, p. 1018.

Olson, G. L., L. H. Auer, and M. L. Hall (2000). "Diffusion, P_1, and other approximate forms of radiation transport." In: *J. Quant. Spectrosc. Radiat. Transfer* 64, p. 619.

Ott, C. D. (2007). "Stellar Iron Core Collapse in 3+1 General Relativity and The Gravitational Wave Signature of Core-Collapse Supernovae". PhD thesis. Potsdam, Germany: Universität Potsdam. URL: http://nbn-resolving.de/urn/resolver.pl?urn=urn:nbn:de:kobv:517-opus-12986.

– (2009). "TOPICAL REVIEW: The gravitational-wave signature of core-collapse supernovae". In: *Class. Quantum Grav.* 26, p. 063001.

– (2016). "Massive Computation for Understanding Core-Collapse Supernova Explosions". In: *Computing in Science & Engineering* 18.5, p. 78. ISSN: 1521-9615.

Ott, C. D., E. Abdikamalov, et al. (2012). "Correlated gravitational wave and neutrino signals from general-relativistic rapidly rotating iron core collapse". In: *Phys. Rev. D* 86, 024026, p. 024026.

Ott, C. D., A. Burrows, L. Dessart, et al. (2008). "Two-Dimensional Multiangle, Multigroup Neutrino Radiation-Hydrodynamic Simulations of Postbounce Supernova Cores". In: *Astrophys. J.* 685, pp. 1069–1088.

Ott, C. D., A. Burrows, T. A. Thompson, et al. (2006). "The Spin Periods and Rotational Profiles of Neutron Stars at Birth". In: *Astrophys. J. Suppl. Ser.* 164, p. 130.

Ott, C. D., H. Dimmelmeier, A. Marek, H.-T. Janka, I. Hawke, et al. (2007). "3D Collapse of Rotating Stellar Iron Cores in General Relativity Including Deleptonization and a Nuclear Equation of State". In: *Phys. Rev. Lett.* 98, p. 261101.

Ott, C. D., H. Dimmelmeier, A. Marek, H.-T. Janka, B. Zink, et al. (2007). "Rotating collapse of stellar iron cores in general relativity". In: *Class. Quantum Grav.* 24, p. 139.

Özel, F. (2006). "Soft equations of state for neutron-star matter ruled out by EXO 0748 - 676". In: *Nature* 441, p. 1115.

Özel, F. and P. Freire (2016). "Masses, Radii, and the Equation of State of Neutron Stars". In: *Ann. Rev. Astron. Astrophys.* 54, p. 401.

Özel, F., D. Psaltis, et al. (2016). "The Dense Matter Equation of State from Neutron Star Radius and Mass Measurements". In: *Astrophys. J.* 820, 28, p. 28.

Paczynski, B. (1986). "Gamma-ray bursters at cosmological distances". In: *Astrophys. J. Lett.* 308, pp. L43–L46.

Paczyński, B. (1998). "Are Gamma-Ray Bursts in Star-Forming Regions?" In: *Astrophys. J. Lett.* 494, pp. L45–L48.

Pan, K.-C. et al. (2016). "Two-dimensional Core-collapse Supernova Simulations with the Isotropic Diffusion Source Approximation for Neutrino Transport". In: *Astrophys. J.* 817, 72, p. 72.

Panagia, N. (1999). “Distance to SN 1987 A and the LMC”. In: *New Views of the Magellanic Clouds*. Ed. by Y.-H. Chu et al. Vol. 190. IAU Symposium, p. 549.

Panaitescu, A. and P. Kumar (2001). “Fundamental Physical Parameters of Collimated Gamma-Ray Burst Afterglows”. In: *Astrophys. J. Lett.* 560, pp. L49–L53.

Perego, A., R. M. Cabezón, and R. Käppeli (2016). “An Advanced Leakage Scheme for Neutrino Treatment in Astrophysical Simulations”. In: *Astrophys. J. Suppl. Ser.* 223, 22, p. 22.

Perego, A., S. Rosswog, et al. (2014). “Neutrino-driven winds from neutron star merger remnants”. In: *Mon. Not. Roy. Astron. Soc.* 443, p. 3134.

Peres, B. et al. (2014). “General relativistic neutrino transport using spectral methods”. In: *Classical and Quantum Gravity* 31.4, 045012, p. 045012.

Piekarewicz, J. (2010). “Do we understand the incompressibility of neutron-rich matter?” In: *Journal of Physics G Nuclear Physics* 37.6, 064038, p. 064038.

Piran, T. (2004). “The physics of gamma-ray bursts”. In: *Reviews of Modern Physics* 76, pp. 1143–1210.

Piran, T., E. Nakar, and S. Rosswog (2013). “The electromagnetic signals of compact binary mergers”. In: *Accepted for publication in Mon. Not. Roy. Astron. Soc.; arXiv:1204.6242*.

Pomraning, G. C. (1969). “An extension of the Eddington approximation”. In: *J. Quant. Spectrosc. Radiat. Transfer* 9, p. 407.

– (1983). “Flux-limited diffusion with relativistic corrections”. In: *Astrophys. J.* 266, p. 841.

Pomraning, G.C. (1973). *The Equations of Radiation Hydrodynamics*. International series of monographs in natural philosophy. Pergamon Press, Oxford, UK. ISBN: 9780080168937. URL: `https://books.google.com/books?id=FbLvAAAAMAAJ`.

Pons, J. A., J. M. Ibáñez, and J. A. Miralles (2000). “Hyperbolic character of the angular moment equations of radiative transfer and numerical methods”. In: *Mon. Not. Roy. Astron. Soc.* 317, p. 550.

Popham, R., S. E. Woosley, and C. Fryer (1999). “Hyperaccreting Black Holes and Gamma-Ray Bursts”. In: *Astrophys. J.* 518, p. 356.

Radice, D., E. Abdikamalov, et al. (2013). “A new spherical harmonics scheme for multi-dimensional radiation transport I. Static matter configurations”. In: *J. Comp. Phys.* 242, p. 648.

Radice, D., S. Bernuzzi, et al. (2016). “Probing Extreme-Density Matter with Gravitational Wave Observations of Binary Neutron Star Merger Remnants”. In: *Submitted to Phys. Rev. Lett.; arXiv:1612.06429*.

Radice, D., A. Burrows, et al. (2017). “Electron-Capture and Low-Mass Iron-Core-Collapse Supernovae: New Neutrino-Radiation-Hydrodynamics Simulations”. In: *ArXiv e-prints*.

Radice, D., S. M. Couch, and C. D. Ott (2015). “Implicit large eddy simulations of anisotropic weakly compressible turbulence with application to core-collapse supernovae”. In: *Comp. Astrophy. Cosmol.* 2, 7, p. 7.

Radice, D., C. D. Ott, et al. (2016). “Neutrino-driven Convection in Core-collapse Supernovae: High-resolution Simulations”. In: *Astrophys. J.* 820, 76, p. 76.

Rampp, M. and H.-T. Janka (2002). “Radiation hydrodynamics with neutrinos. Variable Eddington factor method for core-collapse supernova simulations”. In: *Astron. Astrophys.* 396, pp. 361–392.

Read, J. S. et al. (2009). “Measuring the neutron star equation of state with gravitational wave observations”. In: *Phys. Rev. D* 79, p. 124033.

Reisswig, C., R. Haas, et al. (2013). “Three-Dimensional General-Relativistic Hydrodynamic Simulations of Binary Neutron Star Coalescence and Stellar Collapse with Multipatch Grids”. In: *Phys. Rev. D.* 87, p. 064023.

Reisswig, C. and D. Pollney (2011). “Notes on the integration of numerical relativity waveforms”. In: *Class. Quantum Grav.* 28.19, p. 195015.

Rhoads, J. E. (1999). “The Dynamics and Light Curves of Beamed Gamma-Ray Burst Afterglows”. In: *Astrophys. J.* 525, pp. 737–749.

Richers, S. et al. (2015). “Monte Carlo Neutrino Transport through Remnant Disks from Neutron Star Mergers”. In: *Astrophys. J.* 813, 38, p. 38.

Roberts, L. F. (2012). “A New Code for Proto-neutron Star Evolution”. In: *Astrophys. J.* 755, 126, p. 126.

Roberts, L. F., D. Kasen, et al. (2011). “Electromagnetic Transients Powered by Nuclear Decay in the Tidal Tails of Coalescing Compact Binaries”. In: *Astrophys. J. Lett.* 736, L21, p. L21.

Roberts, L. F., C. D. Ott, et al. (2016). “General-Relativistic Three-Dimensional Multi-group Neutrino Radiation-Hydrodynamics Simulations of Core-Collapse Supernovae”. In: *Astrophys. J.* 831, 98, p. 98.

Rosswog, S. and M. Liebendörfer (2003). “High-resolution calculations of merging neutron stars—II. Neutrino emission”. In: *Mon. Not. Roy. Astron. Soc.* 342, p. 673.

Rosswog, S., E. Ramirez-Ruiz, and M. B. Davies (2003). “High-resolution calculations of merging neutron stars—III. Gamma-ray bursts”. In: *Mon. Not. Roy. Astron. Soc.* 345, p. 1077.

Roth, N. and D. Kasen (2015). “Monte Carlo Radiation-Hydrodynamics With Implicit Methods”. In: *Astrophys. J. Suppl. Ser.* 217, 9, p. 9.

Röver, C. et al. (2009). "Bayesian reconstruction of gravitational wave burst signals from simulations of rotating stellar core collapse and bounce". In: *Phys. Rev. D* 80, p. 102004.

Ruffert, M. and H. Janka (1999). "Simulations of Coalescing Neutron Star and Black Hole Binaries". In: *Progress of Theoretical Physics Supplement* 136, pp. 287–299.

Ruffert, M., H.-T. Janka, and G. Schaefer (1996). "Coalescing neutron stars - a step towards physical models. I. Hydrodynamic evolution and gravitational-wave emission." In: *Astron. Astrophys.* 311, p. 532.

Ruffert, M., H.-T. Janka, K. Takahashi, et al. (1997). "Coalescing neutron stars - a step towards physical models. II. Neutrino emission, neutron tori, and gamma-ray bursts." In: *A&A* 319, p. 122.

Ryan, B. R., J. C. Dolence, and C. F. Gammie (2015). "bhlight: General Relativistic Radiation Magnetohydrodynamics with Monte Carlo Transport". In: *Astrophys. J.* 807, 31, p. 31.

Saio, Hideyuki (2013). "Prospects for Asteroseismology of Rapidly Rotating B-Type Stars". In: *Studying Stellar Rotation and Convection: Theoretical Background and Seismic Diagnostics*. Ed. by Mariejo Goupil et al. Berlin, Heidelberg: Springer Berlin Heidelberg, pp. 159–176. ISBN: 978-3-642-33380-4. URL: http://dx.doi.org/10.1007/978-3-642-33380-4_8.

Salam, Abdus (1980). "Gauge unification of fundamental forces". In: *Rev. Mod. Phys.* 52 (3), pp. 525–538. URL: https://link.aps.org/doi/10.1103/RevModPhys.52.525.

Sari, R., T. Piran, and J. P. Halpern (1999). "Jets in Gamma-Ray Bursts". In: *Astrophys. J. Lett.* 519, pp. L17–L20.

Sari, R., T. Piran, and R. Narayan (1998). "Spectra and Light Curves of Gamma-Ray Burst Afterglows". In: *Astrophys. J. Lett.* 497, pp. L17–L20.

Savaglio, S., K. Glazebrook, and D. Le Borgne (2009). "The Galaxy Population Hosting Gamma-Ray Bursts". In: *Astrophys. J.* 691, pp. 182–211.

Sawai, H. and S. Yamada (2014). "Influence of Magnetorotational Instability on Neutrino Heating: A New Mechanism for Weakly Magnetized Core-Collapse Supernovae". In: *Astrophys. J. Lett.* 784, p. L10.

Scheck, L. et al. (2006). "Multidimensional supernova simulations with approximative neutrino transport. I. Neutron star kicks and the anisotropy of neutrino-driven explosions in two spatial dimensions". In: *Astron. Astrophys.* 457, p. 963.

Scheidegger, S., R. Käppeli, et al. (2010). "The influence of model parameters on the prediction of gravitational wave signals from stellar core collapse". In: *Astron. Astrophys.* 514, A51.

Scheidegger, S., S. C. Whitehouse, et al. (2010). “Gravitational waves from supernova matter”. In: *Class. Quantum Grav.* 27, p. 114101.

Sekiguchi, Y. and M. Shibata (2011). “Formation of Black Hole and Accretion Disk in a Massive High-entropy Stellar Core Collapse”. In: *Astrophys. J.* 737, 6, p. 6.

Sekiguchi, Y. et al. (2011). “Gravitational Waves and Neutrino Emission from the Merger of Binary Neutron Stars”. In: *Phys. Rev. Lett.* 107.5, 051102, p. 051102.

– (2012). “Current status of numerical-relativity simulations in Kyoto”. In: *Progress of Theoretical and Experimental Physics* 2012.1, 01A304, 01A304.

– (2015). “Dynamical mass ejection from binary neutron star mergers: Radiation-hydrodynamics study in general relativity”. In: *Phys. Rev. D* 91.6, 064059, p. 064059.

Setiawan, S., M. Ruffert, and H.-T. Janka (2006). “Three-dimensional simulations of non-stationary accretion by remnant black holes of compact object mergers”. In: *Astron. Astrophys.* 458, pp. 553–567.

Shafranov, V. (1956). “The Instability of a Pinched Fluid with a Longitudinal Magnetic Field”. In: *At. Energy* 5, p. 38.

Shen, G., C. J. Horowitz, and E. O’Connor (2011). “Second relativistic mean field and virial equation of state for astrophysical simulations”. In: *Phys. Rev. C* 83, 065808, p. 065808.

Shen, G., C. J. Horowitz, and S. Teige (2010a). “Equation of state of dense matter from a density dependent relativistic mean field model”. In: *Phys. Rev. C* 82.1, 015806, p. 015806.

– (2010b). “Equation of state of nuclear matter in a virial expansion of nucleons and nuclei”. In: *Phys. Rev. C* 82.4, 045802, p. 045802.

– (2011). “New equation of state for astrophysical simulations”. In: *Phys. Rev. C* 83, p. 035802.

Shen, H. et al. (1998a). “Relativistic equation of state of nuclear matter for supernova and neutron star”. In: *Nucl. Phys. A* 637, p. 435. URL: `http://user.numazu-ct.ac.jp/~sumi/eos`.

– (1998b). “Relativistic Equation of State of Nuclear Matter for Supernova Explosion”. In: *Prog. Th. Phys.* 100, p. 1013.

– (2011). “Relativistic Equation of State for Core-collapse Supernova Simulations”. In: *Astrophys. J. Suppl. Ser.* 197, 20, p. 20.

Shibata, M., S. Karino, and Y. Eriguchi (2003). “Dynamical bar-mode instability of differentially rotating stars: effects of equations of state and velocity profiles”. In: *Mon. Not. Roy. Astron. Soc.* 343, p. 619.

Shibata, M., K. Kiuchi, et al. (2011). “Truncated Moment Formalism for Radiation Hydrodynamics in Numerical Relativity”. In: *Progress of Theoretical Physics* 125, p. 1255.

Shibata, M., Y. T. Liu, et al. (2006). "Magnetorotational collapse of massive stellar cores to neutron stars: Simulations in full general relativity". In: *Phys. Rev. D* 74, p. 104026.

Shibata, M. and K. Taniguchi (2008). "Merger of black hole and neutron star in general relativity: Tidal disruption, torus mass, and gravitational waves". In: *Phys. Rev. D* 77, p. 084015.

– (2011). "Coalescence of Black Hole-Neutron Star Binaries". In: *Liv. Rev. Rel.* 14, p. 6.

Shibata, Masaru and Yuichiro Sekiguchi (2012). "Radiation Magnetohydrodynamics for Black Hole-Torus System in Full General Relativity: A Step toward Physical Simulation". In: *Progress of Theoretical Physics* 127.3, pp. 535–559. ISSN: 0033-068X. URL: http://ptp.ipap.jp/link?PTP/127/535/.

Shibata, M. and T. Nakamura (1995). "Evolution of three-dimensional gravitational waves: Harmonic slicing case". In: *Phys. Rev. D* 52, p. 5428.

Shoemaker, D. (2010). *Advanced LIGO anticipated sensitivity curves*. Tech. rep. LIGO-T0900288-v3. LIGO Scientific Collaboration. URL: https://dcc.ligo.org/LIGO-T0900288/public.

Skinner, M. A., A. Burrows, and J. C. Dolence (2016). "Should One Use the Ray-by-Ray Approximation in Core-collapse Supernova Simulations?" In: *Astrophys. J.* 831, 81, p. 81.

Smit, J. M., L. J. van den Horn, and S. A. Bludman (2000). "Closure in flux-limited neutrino diffusion and two-moment transport". In: *Astron. Astrophys.* 356, p. 559.

Smith, N., W. Li, A. V. Filippenko, et al. (2011). "Observed fractions of core-collapse supernova types and initial masses of their single and binary progenitor stars". In: *Mon. Not. Roy. Astron. Soc.* 412, p. 1522.

Smith, N., W. Li, R. J. Foley, et al. (2007). "SN 2006gy: Discovery of the Most Luminous Supernova Ever Recorded, Powered by the Death of an Extremely Massive Star like η Carinae". In: *Astrophys. J.* 666, pp. 1116–1128.

Soderberg, A. M. et al. (2006). "Relativistic ejecta from X-ray flash XRF 060218 and the rate of cosmic explosions". In: *Nature* 442, p. 1014.

Somiya (for the KAGRA collaboration), K. (2012). "Detector configuration of KAGRA-the Japanese cryogenic gravitational-wave detector". In: *Class. Quantum Grav.* 29.12, p. 124007.

Steiner, A. W., S. Gandolfi, et al. (2015). "Using neutron star observations to determine crust thicknesses, moments of inertia, and tidal deformabilities". In: *Phys. Rev. C* 91.1, 015804, p. 015804.

Steiner, A. W., M. Hempel, and T. Fischer (2013). "Core-collapse Supernova Equations of State Based on Neutron Star Observations". In: *Astrophys. J.* 774, 17, p. 17.

Steiner, A. W., J. M. Lattimer, and E. F. Brown (2010). "The Equation of State from Observed Masses and Radii of Neutron Stars". In: *Astrophys. J.* 722, p. 33.

– (2013). "The Neutron Star Mass-Radius Relation and the Equation of State of Dense Matter". In: *Astrophys. J. Lett.* 765, L5, p. L5.

Stergioulas, N. (2011). "Black hole spacetimes with self-gravitating, massive accretion tori". In: *Journal of Physics Conference Series* 283.1, p. 012036.

– (2003). "Rotating Stars in Relativity". In: *Liv. Rev. Rel.* 6, p. 3.

Stone, J. M., D. Mihalas, and M. L. Norman (1992). "ZEUS-2D: A radiation magnetohydrodynamics code for astrophysical flows in two space dimensions. III - The radiation hydrodynamic algorithms and tests". In: *Astrophys. J. Suppl. Ser.* 80, pp. 819–845.

Sullivan, C. et al. (2016). "The Sensitivity of Core-collapse Supernovae to Nuclear Electron Capture". In: *Astrophys. J.* 816, 44, p. 44.

Sumiyoshi, K., T. Takiwaki, et al. (2015). "Multi-dimensional Features of Neutrino Transfer in Core-collapse Supernovae". In: *Astrophys. J. Suppl. Ser.* 216, 5, p. 5.

Sumiyoshi, K. and S. Yamada (2012). "Neutrino Transfer in Three Dimensions for Core-collapse Supernovae. I. Static Configurations". In: *Astrophys. J. Suppl. Ser.* 199, 17, p. 17.

Sumiyoshi, K., S. Yamada, et al. (2005). "Postbounce Evolution of Core-Collapse Supernovae: Long-Term Effects of the Equation of State". In: *Astrophys. J.* 629, p. 922.

Surman, R., G. C. McLaughlin, and W. R. Hix (2006). "Nucleosynthesis in the Outflow from Gamma-Ray Burst Accretion Disks". In: *Astrophys. J.* 643, pp. 1057–1064.

Suwa, Y., K. Kotake, T. Takiwaki, M. Liebendörfer, et al. (2011). "Impacts of collective neutrino oscillations on core-collapse supernova explosions". In: *Astrophys. J.* 738, p. 165.

Suwa, Y., K. Kotake, T. Takiwaki, S. C. Whitehouse, et al. (2010). "Explosion Geometry of a Rotating 13 $M_\odot$ Star Driven by the SASI-Aided Neutrino-Heating Supernova Mechanism". In: *Pub. Astr. Soc. Jap.* 62, p. L49.

Suwa, Y., S. Yamada, et al. (2016). "The Criterion of Supernova Explosion Revisited: The Mass Accretion History". In: *Astrophys. J.* 816, 43, p. 43.

Swesty, F. D. and E. S. Myra (2009). "A Numerical Algorithm for Modeling Multigroup Neutrino-Radiation Hydrodynamics in Two Spatial Dimensions". In: *Astrophys. J. Suppl. Ser.* 181, p. 1.

Takami, K., L. Rezzolla, and L. Baiotti (2015). "Spectral properties of the post-merger gravitational-wave signal from binary neutron stars". In: *Phys. Rev. D* 91.6, 064001, p. 064001.

Takiwaki, T. and K. Kotake (2011). "Gravitational Wave Signatures of Magnetohydrodynamically Driven Core-collapse Supernova Explosions". In: *Astrophys. J.* 743, p. 30.

Takiwaki, T., K. Kotake, and K. Sato (2009). "Special Relativistic Simulations of Magnetically Dominated Jets in Collapsing Massive Stars". In: *Astrophys. J.* 691, p. 1360.

Takiwaki, T., K. Kotake, and Y. Suwa (2012). "Three-dimensional Hydrodynamic Core-collapse Supernova Simulations for an 11.2 Msun Star with Spectral Neutrino Transport". In: *Astrophys. J.* 749, p. 98.

Tammann, G. A., W. Loeffler, and A. Schroeder (1994). "The Galactic supernova rate". In: *Astrophys. J. Suppl. Ser.* 92, p. 487.

Tanvir, N. R. et al. (2013). "A 'kilonova' associated with the short-duration γ-ray burst GRB 130603B". In: *Nature* 500, pp. 547–549.

Tchekhovskoy, A., J. C. McKinney, and R. Narayan (2007). "WHAM: A WENO-based general relativistic numerical scheme I: Hydrodynamics". In: *Mon. Not. Roy. Astron. Soc.* 379, p. 469.

Thompson, T. A., E. Quataert, and A. Burrows (2005). "Viscosity and Rotation in Core-Collapse Supernovae". In: *Astrophys. J.* 620, p. 861.

Thorne, K. S. (1981). "Relativistic radiative transfer—Moment formalisms". In: *Mon. Not. Roy. Astron. Soc.* 194, p. 439.

Timmes, F. X. and D. Arnett (1999). "The Accuracy, Consistency, and Speed of Five Equations of State for Stellar Hydrodynamics". In: *Astrophys. J. Suppl. Ser.* 125, pp. 277–294.

Timmes, F. X. and F. D. Swesty (2000). "The Accuracy, Consistency, and Speed of an Electron-Positron Equation of State Based on Table Interpolation of the Helmholtz Free Energy". In: *Astrophys. J. Suppl. Ser.* 126, p. 501.

Tóth, G. (2000). "The $\nabla \cdot B = 0$ Constraint in Shock-Capturing Magnetohydrodynamics Codes". In: *J. Comp. Phys.* 161, p. 605.

Tsang, M. B. et al. (2009). "Constraints on the Density Dependence of the Symmetry Energy". In: *Phys. Rev. Lett.* 102.12, 122701, p. 122701.

Tubbs, D. L. (1978). "Direct-simulation neutrino transport - Aspects of equilibration". In: *Astrophys. J. Suppl. Ser.* 37, p. 287.

Uitenbroek, H., A. K. Dupree, and R. L. Gilliland (1998). "Spatially Resolved Hubble Space Telescope Spectra of the Chromosphere of alpha Orionis". In: *Astronom. J.* 116, pp. 2501–2512.

Vallisneri, M. (2000). "Prospects for Gravitational-Wave Observations of Neutron-Star Tidal Disruption in Neutron-Star-Black-Hole Binaries". In: *Phys. Rev. Lett.* 84, p. 3519.

van den Bergh, S. and G. A. Tammann (1991). "Galactic and Extragalactic Supernova Rates". In: *Ann. Rev. Astron. Astrophys.* 29, p. 363.

van Paradijs, J. (1979). "Possible observational constraints on the mass-radius relation of neutron stars". In: *Astrophys. J.* 234, pp. 609–611.

Vaytet, N. M. H. et al. (2011). "A numerical model for multigroup radiation hydrodynamics". In: *J. Quant. Spectrosc. Radiat. Transfer* 112, p. 1323.

Wanajo, S. and H.-T. Janka (2012). "The r-process in the Neutrino-driven Wind from a Black-hole Torus". In: *Astrophys. J.* 746, 180, p. 180.

Wanajo, S., Y. Sekiguchi, et al. (2014). "Production of All the r-process Nuclides in the Dynamical Ejecta of Neutron Star Mergers". In: *Astrophys. J. Lett.* 789, L39, p. L39.

Wanajo, S., M. Tamamura, et al. (2003). "The r-Process in Supernova Explosions from the Collapse of O-Ne-Mg Cores". In: *Astrophys. J.* 593, pp. 968–979.

Weinberg, Steven (1967). "A Model of Leptons". In: *Phys. Rev. Lett.* 19 (21), pp. 1264–1266. URL: https://link.aps.org/doi/10.1103/PhysRevLett.19.1264.

– (1972). "Effects of a Neutral Intermediate Boson in Semileptonic Processes". In: *Phys. Rev. D* 5 (6), pp. 1412–1417. URL: https://link.aps.org/doi/10.1103/PhysRevD.5.1412.

Weizsäcker, C. F. v. (1935). "Zur Theorie der Kernmassen". In: *Zeitschrift für Physik* 96.7, pp. 431–458. ISSN: 0044-3328. URL: http://dx.doi.org/10.1007/BF01337700.

Wheeler, J. C., D. L. Meier, and J. R. Wilson (2002). "Asymmetric Supernovae from Magnetocentrifugal Jets". In: *Astrophys. J.* 568, p. 807.

Winteler, C. et al. (2012). "Magnetorotationally Driven Supernovae as the Origin of Early Galaxy r-process Elements?" In: *Astrophys. J. Lett.* 750, L22, p. L22.

Wolfenstein, L. (1978). "Neutrino oscillations in matter". In: *Phys. Rev. D* 17, p. 2369.

Wollaeger, R. T. et al. (2013). "Radiation Transport for Explosive Outflows: A Multigroup Hybrid Monte Carlo Method". In: *Submitted to the Astrophys. J.; arXiv:1306.5700*.

Woosley, S. E. (1993). "Gamma-ray bursts from stellar mass accretion disks around black holes". In: *Astrophys. J.* 405, p. 273.

Woosley, S. E. and J. S. Bloom (2006). "The Supernova Gamma-Ray Burst Connection". In: *Ann. Rev. Astron. Astrophys.* 44, p. 507.

Woosley, S. E. and A. Heger (2006). "The Progenitor Stars of Gamma-Ray Bursts". In: *Astrophys. J.* 637, p. 914.

– (2007). “Nucleosynthesis and remnants in massive stars of solar metallicity”. In: *Phys. Rep.* 442, p. 269.

Woosley, S. E., A. Heger, and T. A. Weaver (2002). “The evolution and explosion of massive stars”. In: *Rev. Mod. Phys.* 74, pp. 1015–1071.

Woosley, S. E. and T. A. Weaver (1995). “The Evolution and Explosion of Massive Stars. II. Explosive Hydrodynamics and Nucleosynthesis”. In: *Astrophys. J. Suppl. Ser.* 101, p. 181.

Yahil, A. (1983). “Self-similar stellar collapse”. In: *Astrophys. J.* 265, p. 1047.

Yakunin, K. N. et al. (2015). “Gravitational wave signatures of ab initio two-dimensional core collapse supernova explosion models for 12 -25 $M_\odot$ stars”. In: *Phys. Rev. D* 92.8, 084040, p. 084040.

Yamada, S., H.-T. Janka, and H. Suzuki (1999). “Neutrino transport in type II supernovae: Boltzmann solver vs. Monte Carlo method”. In: *Astron. Astrophys.* 344, p. 533.

Yamada, S. and K. Sato (1995). “Gravitational Radiation from Rotational Collapse of a Supernova Core”. In: *Astrophys. J.* 450, p. 245.

Yang, B. et al. (2015). “A possible macronova in the late afterglow of the long-short burst GRB 060614”. In: *Nature Communications* 6, 7323, p. 7323.

Yoon, S.-C., N. Langer, and C. Norman (2006). “Single star progenitors of long gamma-ray bursts. I. Model grids and redshift dependent GRB rate”. In: *Astron. Astrophys.* 460, p. 199.

York, James W. (1979). “Kinematics and Dynamics of General Relativity”. In: *Sources of Gravitational Radiation*. Ed. by Larry L. Smarr. Cambridge, UK: Cambridge University Press, p. 83.

Zalamea, I. and A. M. Beloborodov (2011). “Neutrino heating near hyper-accreting black holes”. In: *Mon. Not. Roy. Astron. Soc.* 410, pp. 2302–2308.

Zhang, B. et al. (2006). “Physical Processes Shaping Gamma-Ray Burst X-Ray Afterglow Light Curves: Theoretical Implications from the Swift X-Ray Telescope Observations”. In: *Astrophys. J.* 642, pp. 354–370.

Zhang, W. et al. (2013). “CASTRO: A New Compressible Astrophysical Solver. III. Multigroup Radiation Hydrodynamics”. In: *Astrophys. J. Suppl. Ser.* 204, 7, p. 7.

Zwerger, T. and E. Müller (1997). “Dynamics and gravitational wave signature of axisymmetric rotational core collapse.” In: *Astron. Astrophys.* 320, p. 209.

Appendix A

ANNIHILATION LEGENDRE EXPANSION

In this appendix, I extend the neutrino pair annihilation rates in Bruenn, 1985 to higher moments. I switch notation in this section to be follow that of Bruenn, 1985.

We begin by reformulating Equation A9 of Bruenn, 1985 into a fluid heating rate from both the species and the anti-species, by multiplying by a factor of c and multiplying the distribution functions by the neutrino energy.

$$\begin{aligned} Q^{+}_{\rm ann} &= Q^{+}_{\nu_e\bar{\nu}_e} + Q^{+}_{\nu_\mu\bar{\nu}_\mu} + Q^{+}_{\nu_\tau\bar{\nu}_\tau} \ , \\ Q^{+}_{\nu\bar{\nu}} &= \frac{1}{(hc)^6}\int_0^\infty \omega^2 d\omega \int_0^\infty \bar{\omega}^2 d\bar{\omega} \oint_{4\pi} d\Omega \oint_{4\pi} d\bar{\Omega} f \bar{f} \left(\omega R^{\rm a}(\omega,\bar{\omega},\mu) + \bar{\omega}\bar{R}^{\rm a}(\bar{\omega},\omega,\mu)\right) \ , \\ &= \int_0^\infty d\omega \int_0^\infty d\bar{\omega} \oint_{4\pi} d\Omega \oint_{4\pi} d\bar{\Omega} \frac{f\omega^3}{(hc)^3}\frac{\bar{f}\bar{\omega}^3}{(hc)^3}\frac{\omega+\bar{\omega}}{\omega\bar{\omega}} R^{\rm a}(\omega,\bar{\omega},\mu) \ , \end{aligned} \tag{A.1}$$

where ω is the neutrino energy, μ is the cosine of the angle between the propagation directions Ω of the neutrino and anti-neutrino, and f is the neutrino distribution function. Barred quantities represent those of the anti-neutrino. In the second line, we applied the symmetry of the annihilation kernel $R^a(\omega,\bar{\omega},\mu) = \bar{R}^a(\bar{\omega},\omega,\mu)$. The kernel can be expressed in terms of a transition rate r as (Bruenn, 1985 Equation C6)

$$R^a(\omega,\bar{\omega},\mu) = \int \frac{d^3p_e}{(2\pi)^3}\int \frac{d^3p_{\bar{e}}}{(2\pi)^3}\left[1-F_e(E_e)\right]\left[1-F_{\bar{e}}(E_{\bar{e}})\right] r(\nu+\bar{\nu}\rightarrow e+\bar{e}) \ . \tag{A.2}$$

The transition rate can be obtained from the matrix element for the process using Fermi's golden rule and summing over electron spins. The matrix element for the annihilation and pair production process (including both charged-current and neutral-current processes) is (modified from Bruenn, 1985 Equation C48)

$$M = \frac{G}{\sqrt{2}}\left[\bar{u}_e(p_e)\gamma_\mu(C_v - C_A\gamma_5)v_e(p_{\bar{e}})\right]\left[\bar{u}_\nu(q_\nu)\gamma^\mu(1-\gamma_5)v_\nu(q_{\bar{\nu}})\right] \ . \tag{A.3}$$

The transition rate is then (Bruenn, 1985 Equation C52)

$$\begin{aligned} r(e + \bar{e}+ \rightarrow \nu + \bar{\nu}) =& \frac{G^2(2\pi)^4}{2\omega\bar{\omega}E_e E_{\bar{e}}}\delta(q_\nu + q_{\bar{\nu}} - p_e - p_{\bar{e}}) \times [\\ & (C_v + C_A)^2 \underbrace{(p_{\bar{e}} \cdot q_\nu)(p_e \cdot q_{\bar{\nu}})}_{I} + \\ & (C_v - C_A)^2 \underbrace{(p_e \cdot q_\nu)(p_{\bar{e}} \cdot q_{\bar{\nu}})}_{II} + \\ & (C_v^2 - C_A^2) \underbrace{m_e^2(q_\nu \cdot q_{\bar{\nu}})}_{III}] \ . \end{aligned} \tag{A.4}$$

Since electrons have two spin states and neutrinos are only left-handed, $r(\nu + \bar{\nu} \rightarrow e^- + e^+) = 4r(e^- + e^+ \rightarrow \nu + \bar{\nu})$

Before deriving a closed-form solution, the convention is to separate the annihilation kernel into separate terms according to Equation A.4 and expand in Legendre polynomials in μ so that (Bruenn, 1985 Equations C53 and A42)

$$R^a(\omega, \bar{\omega}, \mu) = \sum P_l(\mu)\Phi_l^a(\omega, \bar{\omega}) \ . \tag{A.5}$$

To find the coefficients $\Phi_l^a(\omega, \bar{\omega})$, we integrate

$$\begin{aligned} \Phi_l^a(\omega, \bar{\omega}) &= \int d\mu P_l(\mu) R^a(\omega, \bar{\omega}, \mu) \\ &= \int d\mu P_l(\mu) \int d^3p_e[1 - F_e(E_e)] \int d^3\bar{p}_e[1 - F_{\bar{e}}(E_{\bar{e}})] \\ &\quad \frac{2G^2}{\omega\bar{\omega}E_e E_{\bar{e}}(2\pi)^2}\delta^4(q_\nu + q_{\bar{\nu}} + p_e + p_{\bar{e}})[\\ &\quad\quad (C_V + C_A)^2(p_{\bar{e}} \cdot q_\nu)(p_e \cdot q_{\bar{\nu}}) \\ &\quad + (C_V - C_A)^2(p_e \cdot q_\nu)(p_{\bar{e}} \cdot q_{\bar{\nu}}) \\ &\quad + (C_V^2 - C_A^2)(m_e c)^2(q_\nu \cdot q_{\bar{\nu}})] \ . \end{aligned} \tag{A.6}$$

If we assume that the electrons and positrons are hyper-relativistic (i.e. $E_e = |p_e|c - m_e c^2 \approx |p_e|c$), the third term is negligible and the integrals can be simplified to (Bruenn, 1985 Equations C62 and C63)

$$\begin{aligned} \Phi_l^a(\omega, \bar{\omega}) =& \frac{2G^2}{2\pi} \int dE_e[1 - F_e(E_e)][1 - F_{\bar{e}}(\omega + \bar{\omega} - E_e)] \\ & \times \left[(C_V + C_A)^2 J_l^I(\omega, \bar{\omega}, E_e) + (C_V - C_A)^2 J_l^{II}(\omega, \bar{\omega}, E_e)\right] \ , \end{aligned} \tag{A.7}$$

where (Bruenn, 1985 Equation C66)

$$
\begin{aligned}
J_l^I(\omega,\bar{\omega},E_e) =& \frac{1}{\omega\bar{\omega}}\Theta(\omega+\bar{\omega}-E_e)\{ \\
& a_l[\Theta(\omega-E_e)\Theta(\bar{\omega}-\omega)+\Theta(\bar{\omega}-E_e)\Theta(\omega-\bar{\omega})] \\
& + b_l[\Theta(E_e-\omega)\Theta(\omega-\bar{\omega})+\Theta(E_e-\bar{\omega})\Theta(\bar{\omega}-\omega)] \\
& + c_l[\Theta(E_e-\omega)\Theta(\bar{\omega}-E_e)] \\
& + d_l[\Theta(E_e-\bar{\omega})\Theta(\omega-E_e)]\} \\
J_l^{II}(\omega,\bar{\omega},E_e) =& J_l^I(\bar{\omega},\omega,E_e)\ .
\end{aligned}
\tag{A.8}
$$

Bruenn, 1985 derived the first set of coefficients:

$$
\begin{aligned}
a_0 &= \frac{4E_e^3}{15\omega\bar{\omega}}[E_e^2-5E_e\bar{\omega}+10\bar{\omega}^2] \\
b_0 &= \frac{4}{15\omega\bar{\omega}}(-E_e+\omega+\bar{\omega})^3\left(E_e^2+3E_e\omega-2E_e\bar{\omega}+6\omega^2-3\omega\bar{\omega}+\bar{\omega}^2\right) \\
c_0 &= \frac{4\omega^2}{15\bar{\omega}}\left(10E_e^2-5E_e(3\omega+4\bar{\omega})+6\omega^2+15\omega\bar{\omega}+10\bar{\omega}^2\right) \\
d_0 &= \frac{4\bar{\omega}^2}{15\omega}\left(10E_e^2-5E_e\bar{\omega}+\bar{\omega}^2\right)
\end{aligned}
\tag{A.9}
$$

and the second:

$$
\begin{aligned}
a_1 &= \frac{4E_e^3}{105\omega^2\bar{\omega}^2}[12E_e^4-21E_e^3(\omega+3\bar{\omega})+7E_e^2\bar{\omega}(13\omega+18\bar{\omega}) \\
&\quad -35E_e\bar{\omega}^2(4\omega+3\bar{\omega})+70\omega\bar{\omega}^3] \\
b_1 &= -\frac{4}{105\omega^2\bar{\omega}^2}(-E_e+\omega+\bar{\omega})^3[-12E_e^4-3E_e^3(5\omega-9\bar{\omega}) \\
&\quad +E_e^2\left(-9\omega^2+17\omega\bar{\omega}-9\bar{\omega}^2\right)+E_e\left(6\omega^3-3\omega^2\bar{\omega}+11\omega\bar{\omega}^2-15\bar{\omega}^3\right) \\
&\quad +30\omega^4-6\omega^3\bar{\omega}+12\omega^2\bar{\omega}^2-13\omega\bar{\omega}^3+9\bar{\omega}^4] \\
c_1 &= -\frac{4\omega^2}{105\bar{\omega}^2}[7E_e^2(9\omega+5\bar{\omega})-7E_e\left(12\omega^2+21\omega\bar{\omega}+10\bar{\omega}^2\right) \\
&\quad +30\omega^3+84\omega^2\bar{\omega}+84\omega\bar{\omega}^2+35\bar{\omega}^3] \\
d_1 &= -\frac{4\bar{\omega}^2}{105\omega^2}\left(7E_e^2(5\omega+9\bar{\omega})-7E_e\bar{\omega}(7\omega+6\bar{\omega})+\bar{\omega}^2(14\omega+9\bar{\omega})\right)\ .
\end{aligned}
\tag{A.10}
$$

The third and *highest* Legendre coefficient is given below.

$$
\begin{aligned}
a_2 &= \frac{4E_e^3}{105\omega^3\bar{\omega}^3}[30E_e^6 - 90E_e^5(\omega + 2\bar{\omega}) + 36E_e^4\left(2\omega^2 + 13\omega\bar{\omega} + 12\bar{\omega}^2\right) \\
&\quad - 63E_e^3\bar{\omega}\left(5\omega^2 + 15\omega\bar{\omega} + 8\bar{\omega}^2\right) + 7E_e^2\bar{\omega}^2\left(73\omega^2 + 126\omega\bar{\omega} + 36\bar{\omega}^2\right) \\
&\quad - 35E_e\omega\bar{\omega}^3(10\omega + 9\bar{\omega}) + 70\omega^2\bar{\omega}^4] \\
b_2 &= \frac{4}{105\omega^3\bar{\omega}^3}(-E_e + \omega + \bar{\omega})^3[30E_e^6 - 90E_e^5\bar{\omega} \\
&\quad - 18E_e^4\left(\omega^2 - \omega\bar{\omega} - 4\bar{\omega}^2\right) - 3E_e^3\left(8\omega^3 - 15\omega^2\bar{\omega} + 15\omega\bar{\omega}^2 - 4\bar{\omega}^3\right) \\
&\quad + E_e^2\left(-18\omega^4 + 27\omega^3\bar{\omega} - 29\omega^2\bar{\omega}^2 + 27\omega\bar{\omega}^3 - 18\bar{\omega}^4\right) \\
&\quad + E_e\bar{\omega}^2\left(3\omega^3 - 5\omega^2\bar{\omega} + 9\omega\bar{\omega}^2 - 18\bar{\omega}^3\right) + 30\omega^6 \\
&\quad + 6\omega^4\bar{\omega}^2 - 6\omega^3\bar{\omega}^3 + 7\omega^2\bar{\omega}^4 - 9\omega\bar{\omega}^5 + 12\bar{\omega}^6] \\
c_2 &= \frac{4\omega^2}{105\bar{\omega}^3}[E_e^2\left(72\omega^2 + 63\omega\bar{\omega} + 7\bar{\omega}^2\right) \\
&\quad - E_e\left(90\omega^3 + 180\omega^2\bar{\omega} + 105\omega\bar{\omega}^2 + 14\bar{\omega}^3\right) \\
&\quad + 30\omega^4 + 90\omega^3\bar{\omega} + 96\omega^2\bar{\omega}^2 + 42\omega\bar{\omega}^3 + 7\bar{\omega}^4] \\
d_2 &= \frac{4\bar{\omega}^2}{105\omega^3}[E_e^2\left(7\omega^2 + 63\omega\bar{\omega} + 72\bar{\omega}^2\right) \\
&\quad - E_e\bar{\omega}\left(35\omega^2 + 90\omega\bar{\omega} + 54\bar{\omega}^2\right) + \bar{\omega}^2\left(16\omega^2 + 27\omega\bar{\omega} + 12\bar{\omega}^2\right)] \ .
\end{aligned}
\tag{A.11}
$$

Incorporating these terms into calculations that already use the zeroth and first step would not be a significant technical difficulty.